

CARDIFF UNIVERSITY

School Of Physics and Astronomy

BLAST: studying cosmic and Galactic star
formation from a stratospheric balloon

PhD in Physics and Astronomy

Academic Year 2010/2011

Author

Lorenzo Moncelsi

Supervisor

Dr. Enzo Pascale

Student Number: 0829637

Co-supervisor

Prof. Philip Mauskopf

Published Work

Refereed Publications

1. **Moncelsi**, L., Ade, P. A. R., et al. 2011, ApJ, 727, 83
2. Viero, M. P., **Moncelsi**, L., et al. 2011, ArXiv 1008.4359
3. Zhang, J., Ade, P. A. R., Mauskopf, P., Savini, G., **Moncelsi**, L., & Whitehouse, N. 2011, Appl. Opt., 50, 3750
4. Chapin, E. L., Chapman, S. C., et al. 2011, MNRAS, 411, 505
5. Braglia, F. G., Ade, P. A. R., et al. 2011, MNRAS, 412, 1187
6. Dye, S., Eales, S., **Moncelsi**, L., & Pascale, E. 2010b, MNRAS, 407, L69
7. Ivison, R. J., Alexander, D. M., et al. 2010a, MNRAS, 402, 245
8. Zhang, J., Ade, P. A. R., Mauskopf, P., **Moncelsi**, L., Savini, G., & Whitehouse, N. 2009, Appl. Opt., 48, 6635
9. Eales, S., Chapin, E. L., et al. 2009, ApJ, 707, 1779
10. Viero, M. P., Ade, P. A. R., et al. 2009, ApJ, 707, 1766
11. Patanchon, G., Ade, P. A. R., et al. 2009, ApJ, 707, 1750
12. Pascale, E., Ade, P. A. R., et al. 2009, ApJ, 707, 1740
13. Marsden, G., Ade, P. A. R., et al. 2009, ApJ, 707, 1729
14. Truch, M. D. P., Ade, P. A. R., et al. 2009, ApJ, 707, 1723
15. Dye, S., Ade, P. A. R., et al. 2009, ApJ, 703, 285
16. Devlin, M. J., Ade, P. A. R., et al. 2009, Nature, 458, 737

Notes on Refereed Publications

Where not explicitly highlighted, **Moncelsi** appears as co-author in alphabetical order, in concordance with BLAST's publication policy, albeit he is not part of the BLAST core team. We point out that **Moncelsi** is a major contributor to the analyses carried out in papers # 1, 2, 9, 12, and 13. As of this thesis' submission date, the refereed publications listed above have been cited 462 times.

Conference Proceedings

17. Fissel, L. M., Ade, P. A. R., et al. 2010, in Proceedings of SPIE, Vol. 7741, Society of Photo-Optical Instrumentation Engineers (SPIE) Conference Series
18. Bintley, D., Macintosh, M. J., et al. 2010, in Proceedings of SPIE, Vol. 7741, Society of Photo-Optical Instrumentation Engineers (SPIE) Conference Series
19. Marsden, G., Ade, P. A. R., et al. 2008, in Proceedings of SPIE, Vol. 7020, Society of Photo-Optical Instrumentation Engineers (SPIE) Conference Series
20. Masi, S., Brienza, D., et al. 2007, in 18th ESA Symposium on European Rocket and Balloon Programmes and Related Research (ESA)

Preface

This thesis is the result of work I have undertaken as a research student in the Astronomy Instrumentation Group, School of Physics and Astronomy, Cardiff University between October 2008 and September 2011. As part of my research, during these three years I have been deployed on observation and instrument integration campaigns three times: at the Anglo-Australian Telescope, Siding Spring Observatory, Australia in November 2008; at the Columbia Scientific Balloon Facility, Palestine, Texas, USA, in June and July 2010; and at the Long Duration Balloon (LDB) facility near McMurdo Station, Antarctica, from November 2010 to January 2011.

Except where otherwise stated and referenced, this thesis solely includes research carried out by myself in its entirety, or for the most part if the work was done in collaboration with the BLAST and BLAST-Pol teams. Neither this thesis nor any similar dissertation has been submitted for a degree, diploma or other qualification at this or any other university. This thesis does not exceed 80,000 words in length.

Chapters 2 and 3 of this thesis are largely based on papers # 1 and 2 (as listed in *Published Work*), respectively. These scientific productions are my intellectual property, as I have conducted the largest part of the analyses described in them. In particular, in paper # 2, I have performed the stacking analysis, SED fitting, noise estimation and propagation, which led to the estimates of SFRs and their uncertainties; I have also been a major contributor to the text.

Finally, where applicable, I adopt American English spelling for consistency with most of the published work.

Lorenzo Monceli

Declaration and Statements

Declaration

This work has not previously been accepted in substance for any degree and is not concurrently submitted in candidature for any degree.

Signed _____ (candidate) Date _____

Statement 1

This thesis is being submitted in partial fulfillment of the requirements for the degree of PhD.

Signed _____ (candidate) Date _____

Statement 2

This thesis is the result of my own independent work/investigation, except where otherwise stated. Other sources are acknowledged by explicit references.

Signed _____ (candidate) Date _____

Statement 3

I hereby give consent for my thesis, if accepted, to be available for photocopying and for inter-library loan, and for the title and summary to be made available to outside organizations.

Signed _____ (candidate) Date _____

Acknowledgments

This work is dedicated to Alceo's son, to whom I am endlessly grateful for being a stainless example of how to be a man and a father. I extend my perpetual gratitude to my mother, my sister, my whole family and Steffi for their never-ending support.

A special appreciation goes to my supervisor Enzo Pascale and to Giorgio Savini, for never allowing my learning curve to flatten and for constituting important role models of scientists and expatriates to me.

I thank Peter Ade for having repeatedly instilled in me knowledge of experimental physics, techniques and crafts. I also wish to thank him for a very effective catalytic action in my process of integration with the British (Welsh in particular) idioms, mores and habits.

I also thank Phil Mauskopf, Jin Zhang, Locke Spencer, Frederick Poidevin, David Nutter, Derek Ward-Thompson, Anthony Whitworth, Peter Coles, Leonid Grishchuk, Luca Cortese, Simon Dye, Steve Eales, Matthew Smith, Rashmi Sudiwala, Peter Hargrave, Will Grainger, Chris North, Ian Walker, Richard Frewin, Nicola Whitehouse, Chris Dunscombe, Brian Kiernan, Julian House, and Chris Dodd.

I am grateful to the members of the BLAST and BLAST-Pol teams, and in particular to Marco Viero, Giles Novak, Mark Devlin, Barth Netterfield, Elio Angile, Jeff Klein, Marie Rex, Matthew Truch, Ed Chapin, Mark Halpern, Gaelen Marsden, Douglas Scott, Don Wiebe, Henry Ngo, Juan Diego Soler, Steve Benton, Natalie Gandilo, Laura Fissel, Jamil Shariff, Guillaume Patanchon, Tristan Matthews, Nick Thomas, Greg Tucker, and Andrei Korotkov.

I thank all my friends that have brightened up my 3-year-and-a-bit stay in Cardiff, and in particular Diego Pizzocaro, Giancarlo Russo, Stefano Larsen, Michele de Benedetti, Riccardo Montana, Piero Volta,

Hillel Raz, Iñaki Grau, Panos Papadopoulos, Nasos Dimopoulos, Achilleas Tziatzios, Tullio Buccellato, Piers Horner, Eduardo Della Pia, Nicolò Accanto, Daniele Pranzetti, Massimo Granata, Daniele Carazzo, Matt Williams, Ahmed Alazzawi, Konrad Borowiecki, Federica Pinto, Baljinder Bains, Barbara Torrisi, Lydia Lagartija, Ieva Bisi-girskaitė, Pilar Clemente-Fernandez, Vanessa Stroud, Carolyn Murphy, Raul Gonzalez, and Yiannis Kouropalatis.

Thanks to all the metal bands I listen to, for the energy they instill in me every day and for sparing me from useless chatters and noisy machines in the lab. A special appreciation goes to Kai Hansen and Gamma Ray for accompanying my “journey through space and time” since 1997.

Thanks to atheists, basketball, ShopRight, coffee, NBA Live 2007, Skype, and VLC. Thanks to Lenovo for my fellow traveler T61, which has endured years of hard work, even if I needed to swap its motherboard a couple of months before finishing.

To my fellow time-travelers

If there's a possible chance for something that can be
called future behind the spiral
the only way to find out is to leave the final frontier
to eternity and fly

I will fly - beyond the gates of space and time
I leave the Universe behind
and I can't wait until tomorrow

Fly - beyond the gates of space and time
I know the Universe is mine
'cause I will dive into the black hole
Ride - and there's a call from deep within
I know I won't return again
'cause I will dive into the black hole

from "Beyond the black hole"

"Somewhere out in space"

Gamma Ray (1997)

Thesis Summary/Abstract

Understanding the history of the formation of stars and evolution of galaxies is one of the foremost goals of astrophysics. While stars emit most of their energy at visible and ultraviolet wavelengths, during the early stages of star formation these photons are absorbed by the dusty molecular clouds that host and fuel the emerging stars, and re-emitted as thermal radiation at infrared and submillimeter wavelengths.

The Balloon-borne Large Aperture Submillimeter Telescope (BLAST) was designed to study the history of obscured star formation in galaxies at cosmological distances and witness the details of the star-formation processes in our own Galaxy, by conducting large-area surveys of the sky at 250, 350, and 500 μm from a long-duration stratospheric balloon platform. Its polarimetric adaptation, BLAST-Pol, will allow us to further probe the strength and morphology of magnetic fields in dust-enshrouded star-forming molecular clouds in our Galaxy. The study of these two diverse, yet highly complementary, topics is the primary scientific motivation for this thesis, which is in two parts.

Part One is concerned with the analysis of a combination of the extragalactic dataset collected by BLAST in the 2006 Antarctic campaign, which comprises maps containing hundreds of distant, highly dust-obscured, and actively star-forming galaxies, with a wealth of ancillary multi-wavelength data spanning the radio to the ultraviolet. The star-formation rates we observe in massive galaxies at high redshift support downsizing and size evolution.

Part Two describes the BLAST-Pol instrument. In particular, we focus on the gondola's primary pointing sensors, the star cameras, and on the design, manufacture and characterization of a polarization

modulation scheme, comprising a cryogenic achromatic half-wave plate and photolithographed polarizing grids, which has been effectively retrofitted on BLAST-Pol.

We report on the construction and deployment of BLAST-Pol, which completed its first successful 9.5-day flight over Antarctica in January 2011 and mapped ten science targets with unprecedented combined mapping speed, sensitivity, and resolution.

List of Abbreviations and Acronyms

AAO: AAOmega, spectrograph at the Anglo-Australian telescope
ADC: analog-to-digital converter
ADM: artificial dielectric metamaterial
ADU: analog-to-digital unit
ARC: anti-reflection coating
AGN: active galactic nucleus
BDA: bolometer detector array
BLAST: balloon-borne large aperture submillimeter telescope
CCD: charge-coupled device
CDFS: Chandra deep-field south
CSBF: Columbia scientific balloon facility
CIB: cosmic infrared background
CMF: prestellar core mass function
COB: cosmic optical background
CMB: cosmic microwave background
Dec: declination, δ
ECDFS: extended Chandra deep-field South
EBL: extragalactic background light
EW: equivalent width
FIR: far-infrared
FOV: field of view
FTS: Fourier transform spectrometer
FUV: far-ultraviolet
FWHM: full width at half maximum
GMC: giant molecular cloud
HWP: half-wave plate
ID: counterpart

IMF: stellar initial mass function
ISM: interstellar medium
 $L_{\odot} = 3.839 \times 10^{26}$ W: solar luminosity
LDB: long duration balloon
LIRG: luminous infrared galaxy
LM: Lorenzo Moncelsi
 M_{\star} : stellar mass
 $M_{\odot} = 1.98892 \times 10^{30}$ kg: solar mass
MIR: mid-infrared
mm: millimeter
NEP: noise equivalent power
NEFD: noise equivalent flux density
NIR: near-infrared
NUV: near-ultraviolet
P10: photolithographed polarizer ($5 \mu\text{m}$ copper strips and $5 \mu\text{m}$ gaps)
PAH: polycyclic aromatic hydrocarbon
PSF: point-spread function
PTFE: polytetrafluoroethylene
QSO: quasi-stellar object
RA: right ascension, α
ROI: region of interest
rms: root mean square
SCUBA: submillimetre common-user bolometer array
SED: spectral energy distribution
SFR: star-formation rate
SNR: signal-to-noise ratio
SSFR: specific star-formation rate
submm: submillimeter
ULIRG: ultra-luminous infrared galaxy

CONTENTS

| | |
|---|------|
| <i>Published Work</i> | I |
| <i>Preface</i> | III |
| <i>Declaration and Statements</i> | IV |
| <i>Acknowledgements</i> | V |
| <i>Thesis Summary/Abstract</i> | VIII |
| <i>List of Abbreviations and Acronyms</i> | X |
| <i>Contents</i> | XII |
| | |
| 1. <i>Introduction</i> | 1 |
| 1.1 <i>Extragalactic Science Case</i> | 5 |
| 1.1.1 <i>The dust-obscured Universe</i> | 5 |
| 1.1.2 <i>Galaxy formation and evolution</i> | 6 |
| 1.1.3 <i>Resolving the FIR background</i> | 8 |
| 1.1.4 <i>A luminous population of submm galaxies at high-z</i> | 9 |
| 1.1.5 <i>The assembly of massive galaxies</i> | 10 |
| 1.2 <i>Galactic Science Case</i> | 12 |
| 1.2.1 <i>Background</i> | 12 |

| | | |
|---------------------------|---|----|
| 1.2.2 | Previous work: Zeeman measurements, stellar polarimetry, FIR and submm–mm polarimetry | 16 |
| 1.2.3 | Mapping the large-scale magnetic fields in star-forming clouds with BLAST-Pol | 20 |
| 1.2.3.1 | Structure lifetimes | 20 |
| 1.2.3.2 | Core morphology | 22 |
| 1.2.3.3 | Magnetic field strength | 22 |
| 1.2.4 | The FIR/submm polarization spectrum | 24 |
| 1.2.5 | Overview of the BLAST-Pol observations | 27 |
| 1.3 | Thesis Overview | 28 |
| 1.3.1 | LM’s contribution to the BLAST and BLAST-Pol projects | 32 |
| 1.3.2 | Other work | 34 |
| <i>Part One</i> | | 36 |
| 2. | <i>A multi-wavelength study of BLAST counterparts</i> | 37 |
| 2.1 | Introduction | 37 |
| 2.2 | Data | 43 |
| 2.2.1 | Submillimeter data | 43 |
| 2.2.2 | Optical spectroscopy | 44 |
| 2.2.3 | UV data | 50 |
| 2.2.4 | SWIRE 70 and 160 μ m MIPS maps | 51 |
| 2.2.5 | MIR/NIR/optical images and catalogs | 51 |
| 2.2.6 | Redshifts | 52 |
| 2.3 | FIR Luminosities and SFRs | 56 |
| 2.3.1 | Deboosting the BLAST fluxes | 56 |
| 2.3.2 | SED fitting and FIR luminosities | 59 |
| 2.3.3 | FIR star-formation rates | 63 |
| 2.4 | UV Luminosities and SFRs | 66 |

| | | |
|-------|---|-----|
| 2.4.1 | UV fluxes and rest-frame luminosities | 66 |
| 2.4.2 | UV star-formation rates | 67 |
| 2.5 | Total SFRs | 69 |
| 2.6 | AGN Fraction and Quasars | 73 |
| 2.7 | Morphology | 75 |
| 2.8 | Stellar Masses | 77 |
| 2.9 | Concluding Remarks | 85 |
| 3. | <i>Measuring star formation in massive high-z galaxies</i> | 89 |
| 3.1 | Introduction | 89 |
| 3.2 | Data | 91 |
| 3.2.1 | Mass-selected catalog | 91 |
| 3.2.2 | Spitzer | 93 |
| 3.2.3 | PACS | 93 |
| 3.2.4 | BLAST | 95 |
| 3.2.5 | LABOCA | 95 |
| 3.3 | Method | 95 |
| 3.3.1 | Stacking formalism | 95 |
| 3.3.2 | Testing the Poisson hypothesis | 97 |
| 3.3.3 | SED fitting, IR luminosities, and star-formation rates | 100 |
| 3.4 | Results | 102 |
| 3.4.1 | Stacking results | 102 |
| 3.4.2 | Contribution of stellar emission | 103 |
| 3.4.3 | Best-fit SEDs and star-formation rates | 104 |
| 3.5 | Discussion | 107 |
| 3.5.1 | Consequences for galaxy growth | 107 |
| 3.5.2 | Potential contribution from other sources of dust heating | 108 |

| | | |
|---------------------------|---|-----|
| 3.5.3 | Red and dead? | 108 |
| 3.6 | Concluding Remarks | 110 |
| <i>Part Two</i> | | 112 |
| 4. | <i>The BLAST-Pol Instrument</i> | 113 |
| 4.1 | Introduction | 113 |
| 4.2 | Optical Design | 115 |
| 4.3 | Detectors | 119 |
| 4.4 | Cryogenics | 121 |
| 4.5 | Polarimetry | 121 |
| 4.5.1 | Polarization recovery strategy | 122 |
| 4.5.2 | Polarimeter design | 124 |
| 4.6 | Gondola | 129 |
| 4.7 | Star Cameras | 132 |
| 4.7.1 | Overview | 132 |
| 4.7.2 | Bad/hot pixels | 139 |
| 4.7.3 | Noise model | 140 |
| 4.7.4 | Post-flight pointing reconstruction | 146 |
| 4.8 | Concluding Remarks | 150 |
| 5. | <i>Half Wave Plate and Polarimetry</i> | 153 |
| 5.1 | Introduction | 153 |
| 5.2 | The BLAST-Pol Half-Wave Plate | 154 |
| 5.2.1 | Birefringent wave plates | 154 |
| 5.2.2 | Achromatic half-wave plate design | 156 |
| 5.2.3 | HWP manufacture | 160 |
| 5.2.4 | Anti-reflection coating | 167 |
| 5.2.4.1 | Old recipes: high- n powders and loaded ceramics | 168 |

| | | |
|---------|---|-----|
| 5.2.4.2 | New recipes: artificial dielectric meta- materials | 169 |
| 5.2.5 | Spectral characterization | 170 |
| 5.2.5.1 | Introduction | 170 |
| 5.2.5.2 | Room-temperature measurements . . . | 171 |
| 5.2.5.3 | Cold measurements | 177 |
| 5.2.6 | Mueller matrix characterization | 187 |
| 5.3 | Polarizing Grids | 205 |
| 5.4 | Concluding Remarks | 209 |
| 6. | <i>The BLAST-Pol map-maker</i> | 214 |
| 6.1 | Introduction | 214 |
| 6.2 | Maximum Likelihood Map-making | 215 |
| 6.3 | Naive Binning | 220 |
| 6.4 | Weights and Uncertainties | 224 |
| 6.5 | Preliminary Maps | 225 |
| 6.6 | Concluding Remarks | 227 |
| 6.7 | Future Work | 228 |
| 7. | <i>Conclusions</i> | 234 |
| 7.1 | Future Work | 238 |
| | <i>Appendix</i> | 239 |
| A. | <i>Stacking Analysis</i> | 240 |
| A.1 | Introduction | 240 |
| A.2 | Mathematical Formalism | 242 |
| A.3 | Aperture Photometry Method | 245 |
| A.4 | Uncertainties | 249 |
| A.5 | Catalogs | 251 |

| | |
|--|------------|
| A.6 Post-flight Pointing Verification | 252 |
| <i>B. Postage Stamps of BLAST Counterparts</i> | <i>256</i> |
| <i>C. Catalogs of BLAST Counterparts</i> | <i>262</i> |
| <i>Bibliography</i> | <i>281</i> |

1. INTRODUCTION

Understanding how the early Universe evolved into the structures that are observed today is one of the foremost goals of astrophysics and experimental cosmology. In particular, the history of the formation of stars and evolution of galaxies is not fully understood yet. While stars emit most of their energy in the visible (optical) and ultraviolet (UV) part of the electromagnetic spectrum, during the early stages of star formation this radiation is absorbed and obscured by the dusty molecular clouds that host and fuel the emerging stars. The dust is heated to tens of kelvin, generating thermal emission at infrared (IR) wavelengths. Regions that are luminous at these wavelengths indicate active in-situ star formation, which in turn is often associated with dynamical stages in galactic evolution. When this thermal IR emission has originated in distant galaxies, the light is stretched by the expansion of the Universe and reaches an observer on Earth as submillimeter (submm) and millimeter (mm) radiation.

From an observational point of view, surveys in the optical have enjoyed a head-start of several decades, and pioneered the field since the derivation of Hubble's (1929) law. However, thanks to the relatively recent advances in IR and submm–mm instrumentation, Galactic and extragalactic observations have started to incorporate these longer wavelengths in the search for a more complete understanding of the formation of structures in the Universe. Impressive headway has been made in the past three decades by conducting surveys of

the sky at IR and submm–mm wavelengths within our Galaxy, in nearby galaxies that populate the local Universe, and in galaxies at cosmological distances. These observations provide a highly complementary picture to those carried out at much shorter wavelengths in the optical, and have been proven to be fundamental to investigate the physical processes associated with star formation and galaxy evolution (e.g., Hildebrand 1983, Helou et al. 1985, Rowan-Robinson et al. 1991, Puget et al. 1996, Smail et al. 1997, Schlegel et al. 1998, Fixsen et al. 1998, Hughes et al. 1998, Genzel et al. 1998, Calzetti et al. 2000).

Most of these ground-breaking findings resulted from data acquired with space-based observatories, namely the *Infrared Astronomical Satellite* (*IRAS*; Neugebauer et al. 1984), the *Cosmic Background Explorer* (*COBE*; Boggess et al. 1992), and the *Infrared Space Observatory* (*ISO*; Kessler et al. 1996). The necessity for geocentrically orbiting telescopes was dictated by the fact that observations from the ground are impaired by the atmosphere being opaque over much of the wavelength range from $20\ \mu\text{m}$ to $1\ \text{mm}$, with only the $850\ \mu\text{m}$ atmospheric window having routine transmission of over 50%. In fact, this band has been effectively exploited with the Submillimetre Common-User Bolometer Array (*SCUBA*; Holland et al. 1999) to discover a population of distant, extremely luminous, heavily dust-enshrouded, starburst galaxies (Hughes et al. 1998, Barger et al. 1998).

In the last decade, three other IR and submm–mm space observatories have started operations in far-Earth orbits, which expose the telescopes much less to Earth’s heat load hence prolonging their mission lifetimes: the *Spitzer Space Telescope* (Werner et al. 2004), placed in heliocentric Earth-trailing orbit since 2003; and the *Herschel Space Observatory* (Pilbratt et al. 2010) along with the *Planck* satellite (Planck Collaboration 2011), which entered a Lissajous orbit

around the second Lagrangian point (L2) of the Earth-Sun system in mid-2009. Some of the data and results obtained by the former two observatories are used and referenced, respectively, in this thesis, as they are highly relevant to our study.

Naturally, space-based missions bring economic burden on the space agencies, and typically require two decades of work between conception and deployment; as a consequence, state-of-the-art technologies and components are not easily implemented aboard these payloads, because they increase the risk of jeopardizing the entire mission. A much less expensive alternative to satellites are long-duration balloon (LDB) platforms, which float for 4–15 days at stratospheric altitudes of ~ 40 km to provide $> 99\%$ atmospheric transparency in the far-IR (FIR) and submm bands. Balloon-borne payloads have been used since the 1960s as precursors to space-based instruments, since the much shorter timescales of realization as well as the limited budget requirements allow greater flexibility in terms of components used and experimental proofs of concept.

The Balloon-borne Large Aperture Submillimeter Telescope (BLAST; Devlin et al. 2004, Pascale et al. 2008), a forerunner of the SPIRE photometer (Griffin et al. 2010) aboard *Herschel*, was designed to conduct confusion-limited and wide-area extragalactic and Galactic surveys at submm wavelengths from a LDB platform. The sky is mapped by BLAST with a 1.8 m primary mirror and re-imaged onto the focal-plane arrays, composed of 280 bolometric detectors; these provide simultaneous photometric measurements at 250, 350, and $500 \mu\text{m}$ with diffraction-limited resolutions of $30\text{--}60''$, over an 88 square arcminute field of view. The recent conversion of BLAST into a polarimeter, BLAST-Pol (see Chapter 4), will allow us to further probe the earliest, highly obscured stages of star formation, and in particular the

inherent role of magnetic fields, via the polarized submm emission from aligned elongated dust grains. As described in more detail in Section 4.1, BLAST has had three LDB flights: a 4-day flight from Kiruna, Sweden in June 2005 (BLAST05); a 11-day flight over Antarctica in December 2006 (BLAST06); and a 9.5-day flight, again over Antarctica, in December 2010 (BLAST-Pol).

BLAST has had and will continue to have a cardinal impact on the scientific community since the publication of its first results in 2008. Not only have the BLAST analyses provided a very valuable benchmark for those that are emerging from space observatories such as *Herschel*, but its results and some of the state-of-the-art technologies implemented on the payload will probably stand the test of time.

The research presented in this thesis combines the reduction and interpretation of astrophysical data with the design, manufacture and characterization of astronomical instrumentation. We therefore divide the thesis in two Parts.

Part One is concerned with the analysis and interpretation of a combination of the BLAST06 primary extragalactic dataset, which comprises maps containing hundreds of distant, highly dust-obscured, and actively star-forming galaxies, with a series of multi-wavelength data spanning the radio to the UV. Part One also reports a challenging mid-IR (MIR) to submm measurement of the level of star formation in optically-selected compact massive galaxies at high redshift.

Part Two describes the experimental work carried out during the construction and deployment of BLAST-Pol, which is aimed at probing the earliest stages of star formation by measuring the strength and morphology of magnetic fields in dust-enshrouded star-forming regions in our own Galaxy. The study of these two diverse, yet highly complementary, topics is the primary scientific motivation for this thesis.

In the following, we outline in greater detail the scientific motivations for the BLAST extragalactic survey (Section 1.1) and the BLAST-Pol Galactic survey (Section 1.2); finally, Section 1.3 gives an overview of the thesis’ structure and content, as well as a brief account of the contribution brought by Lorenzo Moncelsi (LM) to the BLAST and BLAST-Pol projects.

1.1 *Extragalactic Science Case*

1.1.1 *The dust-obscured Universe*

Observational evidence suggests that much of the ongoing star formation in the Universe takes place in a dusty, heavily-obscured interstellar medium (ISM), at all epochs (Rowan-Robinson et al. 1997, Hauser et al. 1998, Dwek et al. 1998, Blain et al. 1999b, Chary & Elbaz 2001, Le Floc’h et al. 2005, Chapman et al. 2005, Dye et al. 2008, Pascale et al. 2009). When the Universe was less than 10% of its current-age, galaxies had already formed from the first generations of stars, which then proceeded to enrich (pollute) the primeval ISM with metals and the other by-products of star formation, such as amorphous silicate and carbonaceous dust grains (Rowan-Robinson 1986, Draine 2003).

The prime observable for understanding galaxy formation and evolution is the star-formation rate (SFR). In particular, the most sensible approach to measure the SFR of a galaxy is to estimate the number of massive stars, as they are short-lived and thus only present during the phases of active star formation in a galactic system. The rest-frame optical–UV emission from young, massive stars is usually “reddened” by dust, often partially extinguished, and sometimes even completely obscured (optically thick; Savage & Mathis 1979, Mathis 1990, Calzetti et al. 2000). On the other hand, observations at rest-frame FIR wave-

lengths provide an almost transparent view (optically thin) into the cores of star-forming molecular clouds by tracing the thermal signature of heated dust. The FIR has opened a new window on the Universe, with its ability to detect violent star-formation activity in dusty and gas¹-rich galaxies (Genzel et al. 1998), which can be missed in even the most sensitive rest-frame optical–UV searches with the *Hubble Space Telescope* (*HST*) and ground-based 10-m class telescopes.

In addition, at high redshift (z) the effect of cosmological dimming is partially compensated in the submm–mm bands by the shift in peak wavelength of a galaxy’s spectral energy distribution (SED), an effect referred to as “negative K-correction” (e.g., Blain et al. 2002; see also Figure 2.7); this allows submm–mm wavelength observations to trace the evolution of star formation in dusty galaxies throughout a large volume of the high-redshift Universe.

1.1.2 Galaxy formation and evolution

In the original optical morphological classification scheme (or sequence) of galaxies introduced by Hubble (1926), there are two main types of galaxies: the ellipticals (or “early-type”) and the spirals (or “late-type”). While elliptical galaxies are typically red, gas-poor and harbor an old, evolved stellar population, spiral galaxies are blue, with a dominant population of young stars, and contain large amounts of gas and dust (“red” and “blue” refer to the galaxy’s optical colors; see e.g., Bell et al. 2004). Although this is a rather simplistic scheme, it does suggest that galaxies of distinct morphologies have different ages and have likely formed and evolved diversely.

The currently most successful picture for galaxy formation and evo-

¹ In the context of galaxy structure, we refer to “gas” as interstellar gas, which by mass is composed of about 75% hydrogen (either in ionic [H II], atomic [H I], or molecular [H₂] form), and of ~23–24% helium plus a few percent of heavier elements (“metals”).

lution is the model of hierarchical structure formation (e.g., Press & Schechter 1974), where galaxies are assembled through mergers and accretion of smaller galaxies. This paradigm is often realized through N-body simulations and “semi-analytic” models, which make assumptions about the astrophysical processes at work in galaxy evolution and then predict the observational consequences. These models were initially developed to explain optical and near-IR (NIR) observations, take a representative set of dark-matter halos that evolve and merge over cosmic time, and determine their star-formation histories using a set of indicators for star formation and feedback from active galactic nuclei (AGN) and supernovae (e.g., White & Frenk 1991, Kauffmann et al. 1993, Guiderdoni et al. 1998, Somerville & Primack 1999, Cole et al. 2000, Khochfar & Burkert 2003, Khochfar & Silk 2006).

Submm astronomy offers unique advantages and opportunities to confront the competing theoretical models (accretion by cold gas streams [Dekel et al. 2009] and minor mergers [e.g., Davé et al. 2010], versus major mergers [e.g., Narayanan et al. 2010, Engel et al. 2010]), refine the empirical relationships (e.g., Ivison et al. 2010a,b), and test the accepted scenarios that compose our current knowledge of the physical processes that drive the initial formation of structure and control its subsequent evolution into the galaxies and clusters that we see today (e.g., Amblard et al. 2011, Marsden et al. 2011). In particular, some authors have recently started to incorporate in their semi-analytic models observables from submm astronomy, such as average galaxy SEDs, luminosity functions, galaxy counts, and redshift distributions (e.g., Hatton et al. 2003, Lacey et al. 2008, Swinbank et al. 2008, González et al. 2011). As more information becomes available, the full capabilities of semi-analytic models will hopefully be applied to derive stronger constraints on dusty galaxy evolution.

1.1.3 Resolving the FIR background

Further constraints to the above models can be imposed by the observational evidence that a major fraction ($\sim 50\%$) of the energy in the Extragalactic Background Light (EBL; excluding the Cosmic Microwave Background [CMB] that permeates the Universe with a photon density of about 410 cm^{-3}) is emitted at MIR to mm wavelengths (Puget et al. 1996, Fixsen et al. 1998). The EBL arises from the integrated luminosity due to star formation and AGN activity within all galaxies over the entire history of the Universe. The IR portion of the EBL, usually referred to as Cosmic Infrared Background (CIB), is broadly interpreted as evidence that half of the total UV–optical emission from stars and nuclear accretion disks, which in turn makes up the Cosmic Optical Background (COB; Bernstein et al. 2002), is effectively absorbed by dust grains in the ISM of galaxies over a wide range of redshifts, and then re-radiated at longer wavelengths (Hauser et al. 1998, Dwek et al. 1998). This produces a broad peak in the SED of the EBL at about $200 \mu\text{m}$, whose integrated energy budget equals that of the COB at shorter wavelengths (e.g., Dole et al. 2006).

One of the main goals of FIR–mm cosmological surveys, including those undertaken with BLAST, is to “resolve” this diffuse extragalactic FIR–mm background by identifying the individual dusty galaxies that contribute to the integrated CIB emission. Studying the sources that make up the CIB can help us determine the evolutionary history of obscured star formation at high- z and the mechanism of the assembly of massive galaxies, their nature and physical properties. As detailed in the introduction to Chapter 2, the analyses performed by the BLAST team by combining submm maps with external multi-wavelength source catalogs have in fact resolved the long-wavelength side of the CIB into individual sources detected at $24 \mu\text{m}$ with flux

density² $\gtrsim 20 \mu\text{Jy}$ (Devlin et al. 2009, Marsden et al. 2009, Pascale et al. 2009). The methodology used to achieve these results goes under the name of “stacking analysis”, for which we extensively describe the mathematical formalism and the perfected technicalities in Appendix A; we also employ this technique in Chapter 3 to make a challenging measurement of the level of star formation in optically-selected massive galaxies at high- z .

1.1.4 A luminous population of submm galaxies at high- z

During the last 15 years, the SCUBA camera on the 15-m James Clerk Maxwell Telescope (JCMT) and the Max Planck Millimetre Bolometer Array (MAMBO; Kreysa et al. 1998) on the 30-m Institut de Radio Astronomie Millimétrique (IRAM) telescope have allowed a series of ground-breaking surveys of the extragalactic sky at $850 \mu\text{m}$ and 1.2 mm , respectively, covering a combined area $< 1 \text{ deg}^2$.

These observations led to the important discovery of a luminous population of high-redshift, optically-obscured, dusty starburst galaxies (e.g., Smail et al. 1997, Hughes et al. 1998, Scott et al. 2002, Greve et al. 2004). Preliminary measurements of the redshift distribution of this new dust-enshrouded submm population, based on optical and IR spectroscopic and rest-frame radio–FIR photometric data (e.g., Chapman et al. 2003, 2005, Aretxaga et al. 2003, 2005), confirmed the expected high-redshifts of these galaxies ($z_{\text{median}} \sim 2.4$, with 50% of the sources between $1.9 < z < 2.8$). The inherent bias in the method by which the faint optical and/or IR counterparts are frequently identified leaves open the possibility that a significant fraction of the submm population could reside at $z \gtrsim 3$. The demonstration that the major-

² Throughout this thesis we make use of the Jansky (Jy) as a (non-SI) unit of flux density, expressed as $\text{Jy} = 10^{-26} \frac{\text{W}}{\text{m}^2 \text{Hz}}$.

ity of the submm population are at $z > 1$ implies that these galaxies are extremely luminous in the rest-frame FIR ($L_{\text{FIR}} \gtrsim 10^{12} L_{\odot}$).

Therefore, these extragalactic submm surveys have identified sites of powerful star formation (with rates $\gg 200 M_{\odot} \text{yr}^{-1}$) in the early Universe, which are believed to be associated with an epoch during which massive galaxies were assembled. The integrated resolved emission from these individual submm sources contributes $\sim 30\text{--}100\%$ of the extragalactic background at $850 \mu\text{m}$ (Blain et al. 1999a) and $20\text{--}30\%$ of the diffuse FIR background that peaks at $\sim 200 \mu\text{m}$ (Coppin et al. 2006, Dye et al. 2007). A key goal of observational cosmology in recent years has been to understand the evolutionary history of this newly discovered high-redshift submm galaxy population.

1.1.5 *The assembly of massive galaxies*

It has become clear in recent years (Marchesini et al. 2009) that about half of the stellar mass (M_{\star}) in galaxies in our Universe has formed over the last 7.5 Gyr ($0 < z < 1$). However, the details of how the mass has been assembled and what physical processes were involved at early stages of galaxy evolution remain unclear. Although models of galaxy formation predict that galaxies form hierarchically, observations in the optical indicate “downsizing”, with high-mass galaxies assembling their stellar mass earlier than low-mass systems, and that the redshift at which star-formation activity peaks is a monotonically increasing function of the final stellar mass (Heavens et al. 2004). The best observable known to date for studying downsizing and mass assembly is the Specific Star-Formation Rate (SSFR; Brinchmann et al. 2004), the ratio between the instantaneous SFR in a galaxy and the stellar mass integrated over the galaxy’s history. The SSFR, as observed in the optical and NIR, increases with z at a rate independent of

mass (Damen et al. 2009). Also, SSFRs of more massive galaxies are typically lower than those of less massive galaxies out to redshift $z \sim 2$.

This behavior has been very recently observed in FIR/submm-selected galaxies with BLAST (see Chapter 2) and *Herschel* (Rodighiero et al. 2010), again out to $z \sim 2$. Therefore, the downsizing pattern seems to be at work up to relatively high redshift, for samples of galaxies selected both in the optical/NIR and in the FIR/submm. We are urged to study whether downsizing still occurs in mass-assembling galaxies at very high redshift ($z \gtrsim 3$). Could it be just a selection effect? How does it relate to the high molecular gas fractions observed in distant massive star-forming galaxies (Genzel et al. 2006, Tacconi et al. 2006, 2008, 2010)?

At slightly higher redshift ($1.7 < z < 2.9$), recent follow-up observations at submm wavelengths of an optically-selected sample of massive galaxies ($M_{\star} \geq 10^{11} M_{\odot}$), detected with the Near Infrared Camera and Multi-Object Spectrometer (NICMOS; Schneider 2004) camera on *HST*, estimate SFRs of the order of a hundred $M_{\odot} \text{yr}^{-1}$. Yet, these SFRs are significantly lower than the ones measured for equally massive and distant, but heavily obscured, submm galaxies. This result has been reported independently, and using different methodologies, by the BLAST (see Chapter 3) and *Herschel* (Cava et al. 2010) teams. In addition, when this sample of optically-selected, massive galaxies is morphologically divided into spheroid-like and disk-like systems, the latter show an average SFR that is at least 3–4 times higher than that of the spheroids. What is the nature of these different populations of massive galaxies at high- z ? Do they really undergo a morphological transition as per the Hubble sequence? Are they linked through dissipative major mergers (Mihos & Hernquist 1994, 1996, Tacconi et al. 2008, Bournaud et al. 2011), or are they following separate evolution-

ary paths leading to differences in the structural parameters?

There are indications that massive galaxies at high redshift are the cores of present-day massive ellipticals (Hopkins et al. 2009, Bezanson et al. 2009), and that the growth of these galaxies takes place mostly in the outskirts via star formation and minor mergers (Hopkins et al. 2009, van Dokkum et al. 2010) — a process sometimes referred to as “inside-out” growth, which has also been observed in hydrodynamical cosmological simulations (Naab et al. 2009, Johansson et al. 2009, Oser et al. 2010). In Chapter 3, we discuss how our findings are qualitatively consistent with a picture of gradual growth in the outer regions.

1.2 Galactic Science Case

1.2.1 Background

The extragalactic emission detected by BLAST, whether from starburst galaxies, buried AGNs, or the diffuse CIB, results from higher-frequency photons reprocessed by dust. In the previous section, we have outlined how measurements of the global level of star formation in galaxies at cosmological distances can lead to a better understanding of the formation and evolution of the structures in our Universe.

In our Galaxy, we have the opportunity to witness the details of how starlight is reprocessed and thereby probe the physics of diverse environments. Star formation in the Milky Way takes place in clouds of dense dust and gas (sometimes called “stellar nurseries”) with temperatures of 10–30 K, which glow at FIR and submm wavelengths. The dynamics, temperature distribution and masses of the prestellar regions, as well as the strength and morphology of the local magnetic fields provide a probe of the earliest stages of star formation.

These stellar nurseries are overdensities in the cold ISM where the

gas is mostly found in molecular form; hence they go under the name of molecular clouds³. Vast assemblages of molecular gas with masses of 10^4 – $10^6 M_\odot$ are called giant molecular clouds (GMCs). These clouds can reach tens of parsecs⁴ in diameter and have an average particle density of $n \sim 10^2$ – 10^3 cm^{-3} (see e.g., Lada 2005). GMCs are highly structured; in particular, they contain dense gas in the form of identifiable clumps, called “pre-protostellar” (or “prestellar”) cores, which are gravitationally-bound and have mean particle densities of $n \sim 10^4 \text{ cm}^{-3}$, with peaks as high as $\sim 10^6 \text{ cm}^{-3}$. These dense cores have masses ranging from ~ 1 – $1000 M_\odot$, and typically spawn one or more young protostars, which eventually develop into main sequence stars. However, the quantitative details of these early stages of star birth are far from being well understood.

Significant progress has been made in recent years on the knowledge of the spectrum of masses of prestellar cores, and its apparent connection to the distribution of stellar masses. Observations of dust emission and extinction (e.g., Motte et al. 1998, Johnstone et al. 2000, Reid & Wilson 2006, Alves et al. 2007, Nutter & Ward-Thompson 2007, André et al. 2010, Könyves et al. 2010) show that the overall distribution of core masses (usually referred to as “prestellar core mass function” [CMF]) bears a striking resemblance to the stellar initial mass function (IMF; Salpeter 1955, Miller & Scalo 1979, Kennicutt 1983, Kroupa 2001, Chabrier 2003). This suggests that the origin of the IMF lies in the power spectrum of density fluctuations in turbulent molecular clouds (e.g., Hennebelle & Chabrier 2008).

³ Besides the vast majority of cold molecular hydrogen (H_2), a notable constituent in molecular clouds is carbon monoxide (CO). CO is the species most easily detected through its rotational emission lines, and is a reliable tracer of H_2 because the ratio between CO luminosity and H_2 mass is observed to be nearly constant.

⁴ Throughout this thesis we make use of the parsec [pc] as a (non-SI) unit of distance, expressed as $1 \text{ pc} = 3.0857 \times 10^{16} \text{ m} = 3.26156 \text{ light years} [\text{ly}] = 206.26 \times 10^3 \text{ astronomical units} [\text{AU}]$.

GMCs generally host many Jeans (1902) masses ($M_J \approx 20\text{--}80 M_\odot$) and have free-fall (or dynamical) timescales of 1–3 Myr. The actual lifetimes of GMCs have been a matter of long debate, with estimates ranging from one to ten or more free-fall times (e.g., Murray 2011). If GMCs are long-lived, the question arises as to what holds them up. The thermal pressure, along with either the energy stored in the local magnetic field or carried by supersonic turbulent gas motions, can provide the necessary support against gravitational collapse.

A small fraction, typically 10^{-6} , of gas particles ionized by cosmic rays provide strong coupling between the cold gas and the magnetic field within molecular clouds. Thus, magnetic fields might play an important role in the evolution of star-forming clouds, perhaps controlling the rate at which stars form and even determining the masses of stars (Crutcher 2004, McKee & Ostriker 2007). Many theories and models have been developed in which magnetism plays a crucial role in star formation (e.g., Galli & Shu 1993a,b, Allen et al. 2003).

On the other hand, the last decade has seen models leaning more towards the control of star formation by supersonic, super-Alfvénic turbulent gas flows (Elmegreen & Scalo 2004, Mac Low & Klessen 2004, Padoan et al. 2004), in which case the local magnetic field is too weak to have a decisive influence. Impressive advances in computer hardware and magnetohydrodynamic (MHD) algorithms have led to the widespread use of detailed numerical simulations of turbulent molecular clouds (e.g., Ostriker et al. 2001, Nakamura & Li 2008), which are highly dynamical structures and not necessarily long-lived.

Recent observations undertaken with *Herschel* reveal the presence of highly filamentary structures in the ISM (Men'shchikov et al. 2010, André et al. 2010, Ward-Thompson et al. 2010, Molinari et al. 2010); several possible models for the formation of filamentary cloud struc-

tures have been proposed in the literature. In particular, numerical simulations of supersonic MHD turbulence in weakly magnetized clouds always generate complex systems of shocks, which fragment the gas into high-density sheets, filaments, and cores (e.g., Padoan et al. 2001). Filaments are also produced in turbulent simulations of more strongly magnetized molecular clouds, whereby the gas can be channeled and collapse along the field lines (Nakamura & Li 2008).

Since Galactic magnetic fields are difficult to observe, especially in obscured molecular clouds (see e.g., Crutcher et al. 2004, Whittet et al. 2008), it has not yet been possible to clearly establish the influence of magnetic fields on GMCs and star formation. One promising method for probing them is to observe clouds with a far-IR/submm polarimeter (Hildebrand et al. 2000, Ward-Thompson et al. 2000). By tracing the linearly polarized thermal emission from dust grains aligned with respect to the local magnetic fields, we can measure direction and strength of the plane-of-the-sky component of the field within the cloud. FIR/submm polarimetry is an emerging area of star formation research, with many upcoming experiments that have already and will map fields on different scales.

Ground-based observations with the SCUBA polarimeter (Murray et al. 1997) and the Submillimeter Polarimeter for Antarctic Remote Observations (SPARO; Novak et al. 2003) show that the submm emission from, respectively, prestellar cores and GMCs is indeed polarized to a few percent (Ward-Thompson et al. 2000, Li et al. 2006). *Planck* (Planck Collaboration 2011) will provide coarse resolution (FWHM $\sim 5'$) submm polarimetry maps of the entire Galaxy. The Atacama Large Millimeter/submillimeter Array (ALMA; Wootten & Thompson 2009) will provide sub-arcsecond resolution mm/submm polarimetry, capable of resolving fields within cores and circumstellar disks, but

will not be sensitive to cloud-scale fields.

BLAST-Pol, with its arcminute resolution, will be the first submm polarimeter to map the large-scale magnetic fields within molecular clouds with high sensitivity and mapping speed, and sufficient angular resolution to observe into the dense cores (~ 0.1 pc). BLAST-Pol will produce maps of polarized dust emission over a wide range of column densities corresponding to $A_v \gtrsim 4$ mag (see Table 4.2), yielding hundreds of independent polarization vectors per cloud, for a dozen clouds (see Table 1.1). Moreover, the polarimetric observations of BLAST-Pol complement those planned for SCUBA-2 (Bastien et al. 2005, Holland et al. 2006). In particular, BLAST-Pol will have better sensitivity to degree-scale polarized emission. Core maps to be obtained using SCUBA-2 can be combined with those produced by BLAST-Pol to trace magnetic structures in the cold ISM from scales of 0.01 pc out to 5 pc, thus providing a much needed bridge between the large-area but coarse-resolution polarimetry provided by *Planck* and the high-resolution but limited field-of-view maps of ALMA.

Although the reduction of the dataset collected by BLAST-Pol during its 2010 Antarctic campaign (see Section 1.2.5) has not yet been finalized, we show a sample of preliminary polarization maps in Chapter 6, which result as the culmination of the whole data analysis process and qualitatively demonstrate the overall success of the mission.

1.2.2 Previous work: Zeeman measurements, stellar polarimetry, FIR and submm–mm polarimetry

We have mentioned that Galactic magnetic fields are difficult to measure, especially those embedded in dark clouds. In the following, we briefly describe the three main methods that have been used in the literature to measure magnetic fields in molecular clouds.

Measurements of the Zeeman (1897) effect in molecular clouds allow one to estimate the line-of-sight field properties using the line splitting of different electronic magnetic moment states in the presence of a magnetic field. In particular, radio observations of Zeeman splitting in atomic (H I 21 cm line) or thermally excited molecular lines (such as the hydroxyl [OH], cyano [CN], and sulfur monoxide [SO] radicals) provide the strength and direction of the line-of-sight component of the field (Crutcher 1999). However, most measurements with H I and OH transitions are restricted to low or moderate densities ($n(\text{H}_2) \lesssim 10^3 \text{ cm}^{-3}$); on the other hand, successful measurements on the dense core gas using suitable molecules like CN and SO are still rare (see reviews by Crutcher 1999, 2004). Thus, Zeeman measurements do not reliably probe the density range $n(\text{H}_2) \sim 10^3\text{--}10^6 \text{ cm}^{-3}$, within which the most important phenomena in star formation take place.

The FIR/submm thermal emission from magnetically aligned dust grains (see later in this section and Section 1.2.4 for more details on the possible alignment mechanisms) is partially polarized in a direction perpendicular to that of the sky-plane projection of the aligning field (e.g., Hildebrand et al. 2000, Ward-Thompson et al. 2000). Polarized dust emission has been mapped in dozens of clouds, with up to a few hundred points per cloud. Moreover, field strength estimates can be obtained from the dispersion of measured dust emission polarization angles (Chandrasekhar & Fermi [CF; 1953] technique; see Section 1.2.3 for details). However, most dust polarization studies have been limited so far to dense cloud cores (e.g., Crutcher et al. 2004, Kirk et al. 2006).

Crutcher (2004) compares these CF estimates with those obtained with the Zeeman measurements, finding that molecular cloud cores are in approximate equipartition between magnetic flux density and turbulent kinetic energy. He writes that “a strong conclusion does

come from the observations: both turbulence and strong magnetic fields are important in the physics of molecular clouds. There does not seem to be a single driver of star formation.” He further notes that the fields in the cloud envelopes are almost completely unexplored. In particular, it remains to be determined how the field in the cores connects with that in its surroundings.

We have said that the collisional coupling between the neutral gas and the ions frozen into the magnetic field lines may provide support against the gravitational collapse of a cloud. A class of theoretical models invokes ambipolar diffusion as the mechanism that acts to change the mass distribution against the magnetic flux tube; because the ambipolar diffusion timescale is several times longer than the dynamical contraction (or free-fall) timescale, neutral particles can drift into the core without significant increase in the magnetic flux, eventually leading to a gravitational instability and dynamical collapse of the core (see e.g., Mouschovias 1976, Shu et al. 1987, Basu & Mouschovias 1994, Tassis & Mouschovias 2004). Evidence for an increase in ratio of the mass in a magnetic flux tube to the magnitude of the magnetic flux (mass-to-flux ratio) from envelope to core would support these ambipolar diffusion models.

In principle, such large-scale cloud fields can be probed by optical/NIR polarimetry of background stars; starlight experiences differential extinction by aligned dust grains and hence becomes partially polarized in a direction parallel to that of the sky-plane projection of the aligning field (see e.g., Draine 2003). In practice, however, stellar polarization measurements seem to be primarily sensitive to fields in the clouds’ outermost skins, because the grain alignment efficiency is high at the cloud’s surface, but much lower in the interiors of clouds (Lazarian 2007); in fact, in even moderately obscured regions

($A_v \gtrsim 1\text{--}2$ mag) the polarization efficiency (an observational tracer of the alignment efficiency) at NIR and optical wavelengths is found to be very much reduced (Whittet et al. 2001, 2008). On the other hand, the submm emission from highly obscured ($A_v \sim 30$ mag) quiescent cores is indeed polarized (Crutcher et al. 2004, Kirk et al. 2006).

A possible explanation for this apparent inconsistency is provided by the theoretical studies of Cho & Lazarian (2005) and Lazarian & Cho (2005), who calculate alignment efficiencies under the assumption that grains are brought into alignment with magnetic fields via the radiative torque mechanism: anisotropic and unpolarized starlight can both spin the grains up and align them, provided that the dust grains have some degree of helicity, i.e. they possess a well defined rotation axis but are irregular in shape. When a helical grain is subject to an unpolarized and anisotropic radiation field, it undergoes a systematic torque such that its longer axis aligns perpendicularly to the magnetic field (see review by Lazarian 2007). This mechanism has gained significant observational support (e.g., Hildebrand et al. 1999), and has superseded the Davis–Greenstein (1951) mechanism, which is based on the paramagnetic dissipation that is experienced by a rotating grain. Paramagnetic materials contain unpaired electrons that get oriented by the interstellar magnetic field. The orientation of the electron spins causes grain magnetization, which varies as the vector of magnetization rotates in the grain body coordinates. This causes paramagnetic losses at the expense of the grain rotation energy. Thus paramagnetic dissipation acts to decrease the component of the grain rotational velocity perpendicular to the local magnetic field, eventually causing the grains to rotate with velocity parallel to the field lines, provided that the Davis–Greenstein relaxation time is much shorter than the time of randomization through chaotic gaseous bombardment. In

practice, this condition is difficult to satisfy for typical ISM grains (of size $\sim 0.1 \mu\text{m}$), and paramagnetic alignment becomes inefficient.

For regions that are shielded from the interstellar radiation field, Lazarian and Cho find that the efficiency of radiative torques increases rapidly with grain size. Because submillimeter emission is relatively more sensitive to large grains (emission is proportional to grain volume) while optical/NIR extinction is relatively more sensitive to small grains (extinction is proportional to grain cross-section), one sees that the long-wavelength technique is more sensitive to the grain population that is better aligned. Grains that are near the upper end of the size distribution can become aligned even for cloud optical depths as high as $A_v \sim 10 \text{ mag}$ (Whittet et al. 2008). Because clouds are likely to be inhomogeneous and thus partially permeable to outside radiation, the results of Cho & Lazarian (2005) can also explain the observed grain alignment for clouds with $A_v \lesssim 30 \text{ mag}$ (Crutcher et al. 2004).

Finally, we also mention for completeness that a different manifestation of the magnetic field can be directly observed by means of a comparison of the spectra of molecular ions with those of neutral molecules (Li & Houde 2008).

1.2.3 Mapping the large-scale magnetic fields in star-forming clouds with BLAST-Pol

1.2.3.1 Structure lifetimes

Despite the recent advances discussed in the previous sections, fundamental questions regarding molecular cloud structure are still open. We have mentioned that GMC lifetimes have been a subject of long debate; in fact, the problem extends also to cloud sub-structures. Some authors argue that molecular clouds, as well as cores, clumps,

and filaments inside the clouds, are dynamical structures, with lifetimes approximately equal to their turbulent crossing times (Vázquez-Semadeni et al. 2006; and references therein). This relatively recent point of view is opposed by those who favor longer lifetimes, of the order of several crossing times, which has recently gained some observational support (e.g., Goldsmith & Li 2005, Netterfield et al. 2009; the latter find core lifetimes of ~ 4 Myr, whereas typical core dynamical times are of the order of 0.1–0.3 Myr). If clouds and cloud substructures do live longer than a crossing time, they may be supported against gravity by large-scale magnetic fields (e.g., Basu 2000).

However, the 1980’s view of star formation, in which magnetically supported cores were presumed to live for about ten dynamical times (e.g., Shu et al. 1987) is not well supported by all current observations (see review by Mac Low & Klessen 2004). Nevertheless, a version of this theoretical picture can be salvaged by invoking a faster rate of ambipolar diffusion, thereby shortening core lifetimes (Basu 2000). Indeed, very high angular resolution submillimeter polarimetry obtained using the Submillimeter Array (SMA; Ho et al. 2004) interferometer on Mauna Kea has revealed hourglass-shaped field lines (Girart et al. 2006; see also the complementary observations by Attard et al. 2009, obtained with the Submillimeter High Angular Resolution Polarimeter [SHARP; Li et al. 2008]), a key prediction of magnetically-regulated models (Galli & Shu 1993a,b, Allen et al. 2003).

A combination of the polarimetric observations from BLAST-Pol and SCUBA-2 will allow us to trace magnetic structures in the cold ISM from scales of 0.01 pc out to 5 pc, and hence investigate the rates of ambipolar diffusion by searching for an increase in the mass-to-flux ratio from envelope to core.

1.2.3.2 Core morphology

Another prediction of models invoking magnetic support for the cores is the predominance of oblate cores in molecular clouds, which seems to be endorsed by observations (e.g., Jones & Basu 2002). In addition, such models also require that the core be embedded in a large-scale cloud field running parallel to the core minor axis. Submm polarimetry of quiescent cloud cores by Ward-Thompson et al. (2000), Kirk et al. (2006), and Ward-Thompson et al. (2009) shows significant offsets between core minor axes and core fields ($\sim 30 \pm 3^\circ$), confirming that turbulence and magnetic fields play roughly equal roles in the dynamics of molecular clouds. From a theoretical point of view, while Basu (2000) predicts such large offsets for triaxial cores, none of the current models can explain how a triaxial core would collapse in the presence of a magnetic field.

BLAST-Pol and SCUBA-2 will probe the linkages between core and cloud fields predicted by the magnetically-regulated models. Such tests will complement the smaller-scale ones carried out at SMA and ALMA. These observations will address the formation mechanism for the cores themselves: are they just density peaks in a turbulent medium, or are they formed in a more quiescent, magnetically-controlled manner?

1.2.3.3 Magnetic field strength

In order to assess what are the relative contributions of magnetic fields and turbulent motions to the total energy budget of molecular clouds, we need to quantify the magnetic flux density in GMCs and cores. As previously mentioned, the field strength can be estimated by measuring a specific observable via the Chandrasekhar-Fermi (CF; 1953) technique, the degree of order of cloud-scale magnetic fields; the mean

plane-of-sky magnetic field strength, $|B_{\text{pos}}|$, can be written as:

$$|B_{\text{pos}}| = \sqrt{\frac{4\pi\rho}{3}} \frac{v_{\text{turb}}}{\sigma_{\theta}}, \quad (1.1)$$

where ρ is the density of the diffuse ISM, σ_{θ} is the mean dispersion in the measured dust emission polarization angles, and v_{turb} is rms velocity of the gas turbulent motion. This method has been employed by many authors in the literature (see e.g., Crutcher et al. 2004, Girart et al. 2006, Novak et al. 2009); indeed, submillimeter CF estimates have been obtained for molecular cloud cores, and the results are in rough agreement with values given by Zeeman observations (Crutcher 2004). Novak et al. (2009) used SPARO data to obtain field strength estimates for large-scale GMC fields, but were hampered by small survey size (four clouds) and poor spatial resolution (4').

Numerical MHD turbulence simulations have been used to confirm the reliability of molecular cloud CF estimates (Ostriker et al. 2001, Padoan et al. 2001, Pelkonen et al. 2007, Falceta-Gonçalves et al. 2008). These simulations indicate that clouds having magnetic fields that are strong enough to play an important role in supporting them against gravitational collapse tend to have aligned polarization angles, whereas clouds with weaker fields show more randomly oriented polarization angles. In particular, Figure 1.1 (from Ostriker et al. 2001) shows the result of 3D MHD simulations of turbulent, self-gravitating molecular clouds, one with strong magnetic field ($14 \mu\text{G}^5$), the other with a weak field ($1.4 \mu\text{G}$); the former has a dispersion of only $\delta\phi \sim 9^\circ$ in the distribution of polarization angles, while the latter has $\delta\phi \sim 45^\circ$ (for a magnetic field that is parallel to the plane of the sky).

Observations of large-scale molecular cloud fields with BLAST-Pol

⁵ Throughout this thesis we make use of the gauss [G] as a (non-SI) unit of magnetic flux density, expressed as $1 \text{ G} = 10^{-4} \text{ kg C}^{-1} \text{ s}^{-1} = 10^{-4} \text{ tesla [T]}$.

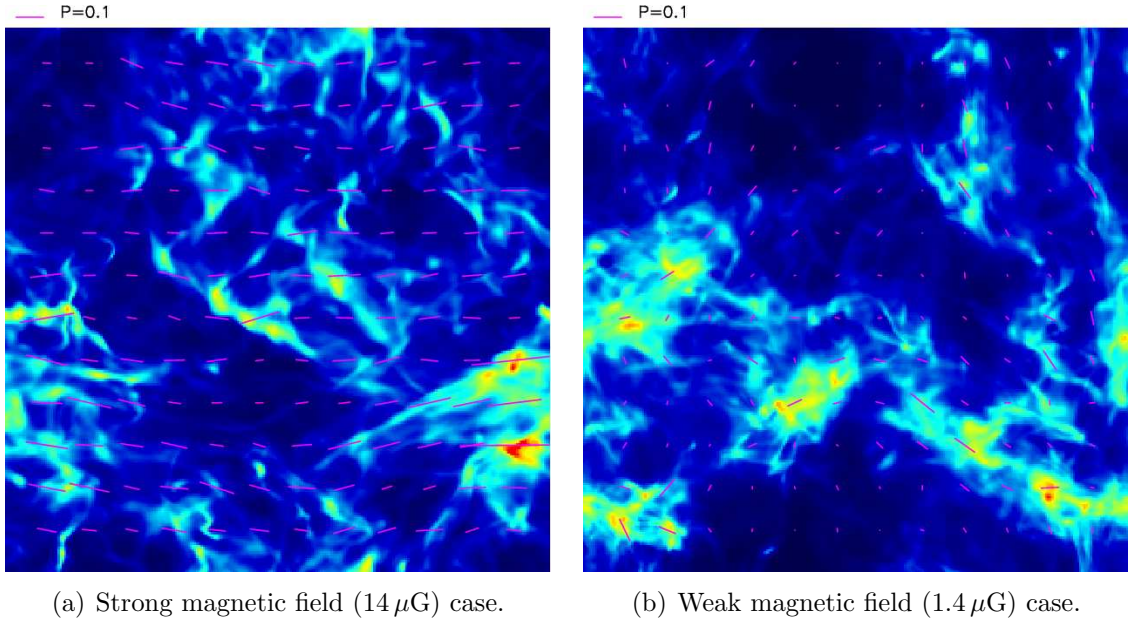


Fig. 1.1 Column density and simulated polarization map, projected along a direction perpendicular to the mean magnetic field. The fractional polarization at each point is proportional to the value of a fiducial polarization P corresponding to a uniform medium and uniform magnetic field perpendicular to the line of sight, arbitrarily set here to $P = 0.1$ as shown in the key. (from Ostriker et al. 2001).

will allow us to conclusively rule out one of these models.

1.2.4 The FIR/submm polarization spectrum

We have discussed in the previous section how the dispersion in the polarization angle is an indicator of magnetic field strength. Another fundamental observable is the polarization amplitude and its dependence on the wavelength (usually referred to as “polarization spectrum”); here we briefly discuss some observational results and how additional and improved measurements of the polarization spectrum at submm wavelengths may help constrain cloud and dust models as well as grain alignment theories.

At visible wavelengths, much has been inferred about the physical properties of dust grains from spectropolarimetry (Whittet et al. 2001, 2008): in particular, large grains (radii $\gtrsim 0.1 \mu\text{m}$) are more effi-

cient polarizers than small grains (radii $\lesssim 0.01 \mu\text{m}$), which are apparently minimally aligned; amorphous silicate grains are better aligned than carbonaceous grains (including polycyclic aromatic hydrocarbons [PAHs]); and the shape of aligned grains is more that of an oblate (disc-like) rather than prolate (needle-like) spheroid, with its short axis aligned with the magnetic field (see also Draine 2003, Draine & Fraisse 2009).

Observations at FIR and submm–mm wavelengths have found that in the densest cores of molecular clouds the polarization spectrum increases with wavelength (in the range $100 \mu\text{m}$ – 1mm ; Schleuning 1998, Coppin et al. 2000). This rise is consistent with an opacity effect; as the opacity increases towards shorter wavelengths the emitted polarization must decrease, approaching zero as the emission becomes optically thick (Vaillancourt 2009). In cloud envelopes, where the emission is typically optically thin, the spectrum falls with wavelength below $350 \mu\text{m}$, but rises at longer wavelengths (Hildebrand et al. 2000, Vaillancourt 2002, Vaillancourt et al. 2008).

The submm rise can be explained by a model in which the colder grains are better aligned than the warmer grains. Bethell et al. (2007) have shown that this can be achieved by applying the radiative torque model of grain alignment (Lazarian 2007) to starless clouds. In their model the cloud structure is clumpy, such that external photons can penetrate deep into the cloud. These photons heat all grains, but the larger grains tend to be cooler as they are more efficient emitters. At the same time, the alignment mechanism is more efficient at aligning the larger grains (Cho & Lazarian 2005). Therefore, their model predicts that the cooler grains are better aligned and that the polarization spectrum rises with wavelength. Similarly, Draine & Fraisse (2009) reproduce the submm rise, under the assumption that carbonaceous

grains are not aligned. Their explanation is that the silicate grains contribute an increasing fraction of the emission as the wavelength increases, in part because the silicate grains are slightly cooler than the carbonaceous grains ($\lambda \lesssim 200 \mu\text{m}$), and in part because the ratio of the silicate opacity to the graphite opacity increases with increasing wavelength for $\lambda \gtrsim 100 \mu\text{m}$.

Nevertheless, to our knowledge the FIR fall and the submm rise have yet to be connected by a theoretical dust model. Hildebrand et al. (1999) and Vaillancourt et al. (2008) claim that the observed behavior is not consistent with a simple isothermal dust model but requires multiple grain populations, where each population's polarization efficiency is correlated with either the dust temperature or spectral index. While Bethell et al. (2007) work under the assumption of starless clouds, in real molecular clouds there exist embedded stars that provide an additional source of photons, which will both heat and align dust grains. One can expect that grains closer to these stars will be warmer and better aligned than grains that are either further from stars or shielded from photons in optically thick clumps. This naturally produces grain populations in which the warmer grains are better aligned (Hildebrand et al. 1999). The result is a polarization spectrum that falls with wavelength. The observed polarization spectrum with a minimum between 100 and 850 μm can in fact be modeled by incorporating embedded stars into the models of starless cores (Vaillancourt 2009, Hildebrand & Vaillancourt 2009).

BLAST-Pol will measure polarization spectra at 250, 350, and 500 μm (bracketing the minimum) for a number of cloud envelopes, and will map its spatial variations. By testing the simulations against such observational data sets, we will help improve the models, leading also to a greater reliability of the CF field strength estimates.

Table 1.1. BLAST-Pol 2010 targets

| Name | Area [deg ²] | Integration time [hr] |
|---|--------------------------|-----------------------|
| Lupus I | 0.69 | 55 |
| Lupus IV | 0.17 | 15 |
| Vela Molecular Ridge ^a (“AxeHead”) | 1.4 | 50 |
| Vela Molecular Ridge ^a (“SpearHead”) | 0.14 | 5 |
| Carina Nebula | 0.2 | 3 |
| GMCs in Carina | 1.0 | 13 |
| IRDC G321.934-0.052 | 0.5 | 5 |
| Centaurus A | 0.07 | 2.5 |
| SPARO ^b calibrators | 0.2 | 5 |
| NANTEN ^c selected region | 0.32 | 23 |

Note. — Targets observed by BLAST-Pol during the 2010 Antarctic flight, with approximate extent of area mapped and integration time. ^aNetterfield et al. (2009); ^bLi et al. (2006) ; ^cTakeuchi et al. (2010a).

1.2.5 Overview of the BLAST-Pol observations

With the addition of a polarimeter, BLAST has now been transformed into BLAST-Pol (see Chapter 4), a uniquely sensitive instrument for probing linearly polarized Galactic dust emission. In January 2011, BLAST-Pol completed its first successful 9.5-day flight over Antarctica; in Figure 1.2, we show the GPS trace of the path cruised by the $1.1 \times 10^6 \text{ m}^3$ helium balloon, which BLAST-Pol was suspended from.

Ten science targets, comprising filamentary dark clouds as well as massive GMCs, were mapped with unprecedented combined mapping speed and resolution; the data are currently being analyzed. Figure 1.3 depicts the regions of the sky observed by BLAST-Pol in the Southern Hemisphere; the complete list of targets is given in Table 1.1.

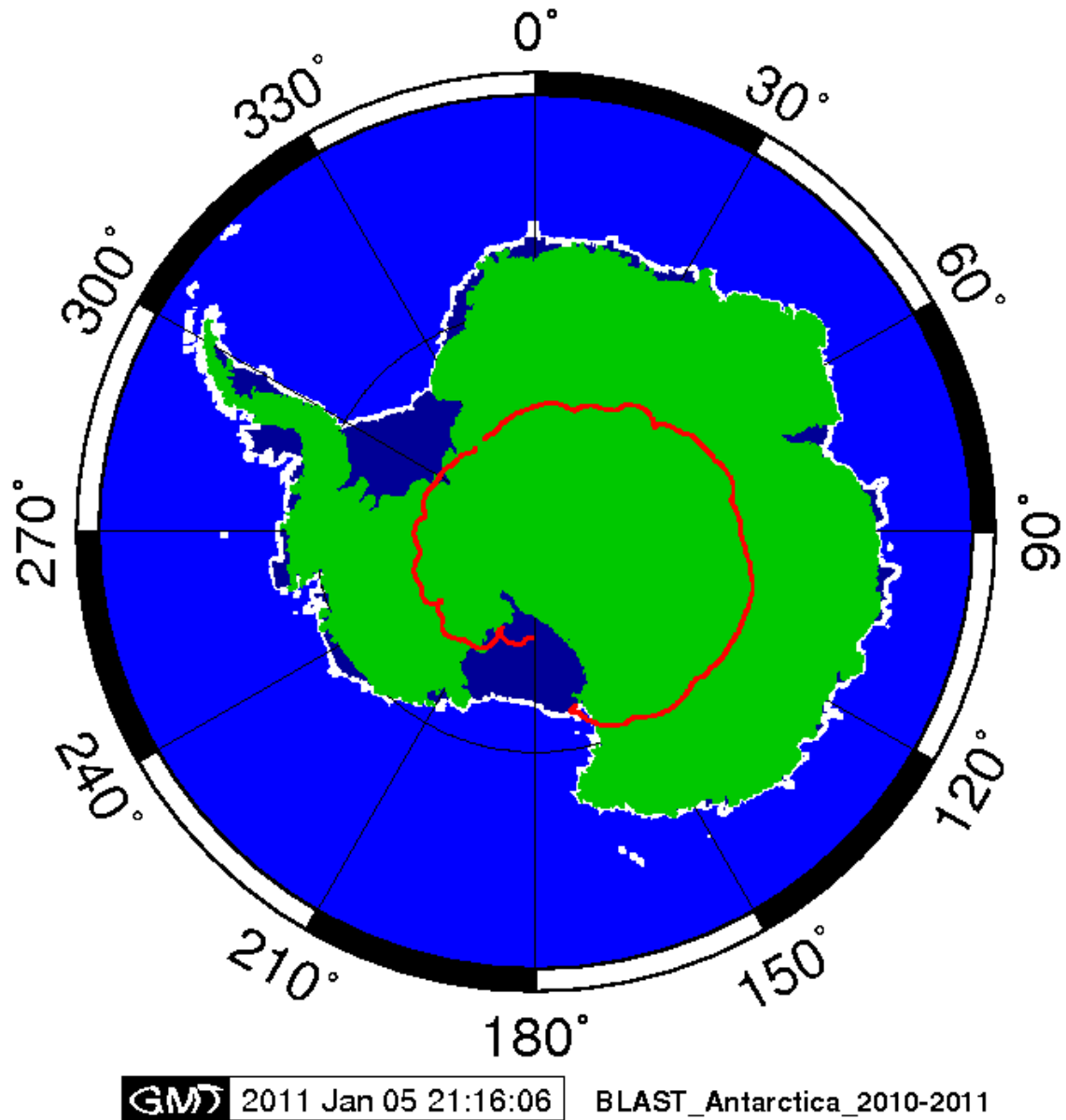


Fig. 1.2 GPS path for the BLAST-Pol science flight. BLAST-Pol was launched on December 27th 2010, and flew over the Antarctic continent, landing after 9.5 days. The coordinates of landing were: latitude $82^{\circ} 48.67\text{S}$; longitude $178^{\circ} 18.28\text{W}$; altitude: 4m. Image credits: Columbia Scientific Balloon Facility.

1.3 Thesis Overview

This thesis presents a multi-wavelength study of the primary extragalactic dataset from the Balloon-borne Large Aperture Submillimeter Telescope, as well as the design, manufacture and characterization of

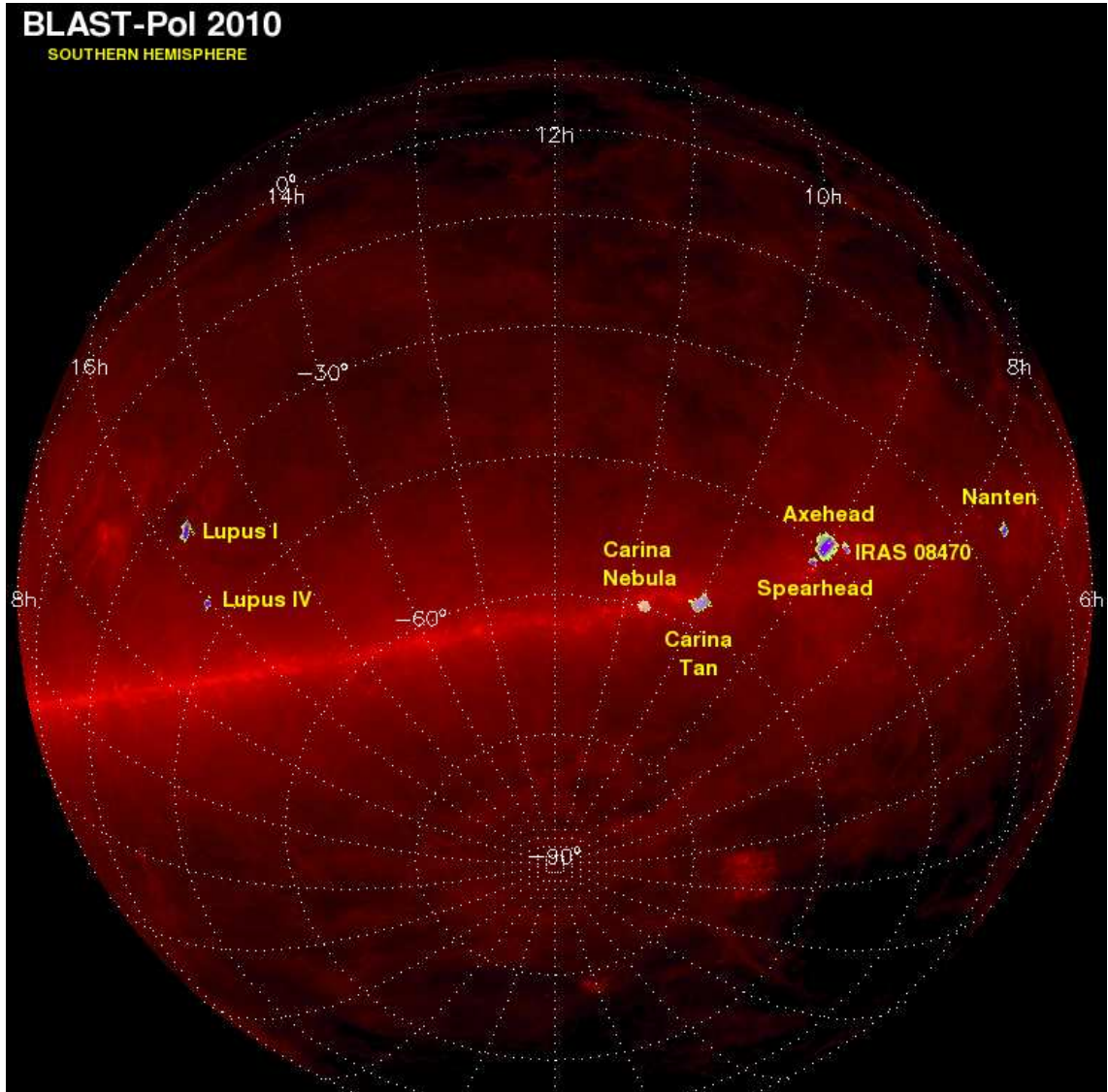


Fig. 1.3 Areas of the sky observed by BLAST-Pol during the 2010 flight. Scans are superimposed onto a combined *IRAS/DIRBE* map of the $100\ \mu\text{m}$ dust emission (from Schlegel et al. 1998). A few targets are missing from this figure; a complete list is given in Table 1.1. Image credits: Matthew Truch, Tristan Matthews, LM.

astronomical instrumentation for the polarimetric upgrade of the same experiment, BLAST-Pol. BLAST has conducted large-area submm surveys that have helped constrain the star formation history of the high-redshift Universe. BLAST has also probed the earliest stages of star formation within our own Galaxy; the addition of a polarimeter will further this goal by measuring the strength and morphology of

magnetic fields in nearby star-forming regions. The study of these two diverse, yet highly connected, topics is the main scientific motivation for this thesis.

In this chapter, we have introduced the reader to submm Galactic and extragalactic astronomy, highlighting the state-of-the-art theoretical models and observational findings, pinpointing the questions and problems that are still open, and defining the role that BLAST and BLAST-Pol, respectively, has played and will play in advancing our current understanding of the cosmic and Galactic star-formation processes, through observations that uniquely combine elevated mapping speed, sensitivity and resolution.

Chapter 2 (Part One) describes a multi-wavelength study of the extragalactic sources detected by BLAST in its survey of the Extended Chandra Deep-Field South (ECDFS), using data spanning the radio to the UV. We develop a Monte Carlo method to account for flux boosting, source blending, and correlations among bands, which we use to derive deboosted FIR luminosities for our sample. We estimate total (obscured plus unobscured) star-formation rates for the BLAST counterparts by combining their FIR and UV luminosities. We capitalize on the multi-wavelength data at our disposal to derive a broad morphological classification of our galaxies, their AGN fraction and stellar masses. We use the combined estimates of SFRs and stellar masses to compare our sample to those selected with other submm facilities such as SCUBA and *Herschel*. Finally, we contextualize our results in the current framework of galaxy formation and evolution.

Chapter 3 (Part One) presents a challenging measurement of the star-formation level in massive, high-redshift galaxies selected in the optical with the NICMOS camera on *HST*. Because the emission from each galaxy is too faint to be individually detected in the BLAST

maps, we use a technique that goes under the name of “stacking analysis” (extensively described in Appendix A of this thesis) to estimate the average brightness of our externally-selected population of galaxies at the BLAST frequencies. Subsequently, the galaxies are divided into two groups, disk-like and spheroid-like, according to their surface brightness profile, and separate measurements of SFR are performed. We show that star formation is a plausible mechanism for size evolution in this population as a whole, but find only marginal evidence that it is what drives the expansion of the spheroid-like galaxies.

Chapter 4 (Part Two) describes the BLAST-Pol instrument. We focus on the important subsystems of the gondola, including the optics, cryogenic system, bolometric detectors, polarization-sensitive elements, readout electronics, pointing sensors and control. We also provide the nominal sensitivities for BLAST-Pol, and describe the scanning strategy adopted to optimally recover the Stokes Q and U in the sky. The second part of the chapter is devoted specifically to the primary pointing sensors for BLAST-Pol, two redundant optical star cameras. The principles of operation, design, control software, and preliminary in-flight performance are presented.

Chapter 5 (Part Two) illustrates in full detail the theoretical framework, principles of operation and manufacturing process for the optical components of the BLAST-Pol polarimeter, an achromatic cryogenic half-wave plate (HWP) and photolithographed polarizing grids acting as analyzers, as well as their pre-flight performance. We identify and measure the parameters that characterize the optical properties and efficiency of these polarizing elements. In particular, we perform a full spectral characterization, both at room and cryogenic temperatures, of the five-plate sapphire HWP, which is, to our knowledge, the most achromatic ever built at mm and submm wavelengths.

Chapter 6 (Part Two) focuses on the most important aspect of the BLAST-Pol data analysis pipeline that is used to transform raw detector time streams into usable sky maps of Stokes parameter $[I, Q, U]$: the map-maker. We develop the mathematical formalism of map-making, and describe the algorithmic implementation of a naive binning technique for the case of BLAST-Pol. As a proof of concept, we present a sample of preliminary polarization maps, which result as the culmination of the whole data analysis process and demonstrate the overall success of the mission.

Chapter 7 concludes the thesis with an outlook on future work.

1.3.1 *LM's contribution to the BLAST and BLAST-Pol projects*

LM joined the BLAST team at the beginning of 2008. Here we briefly summarize the main contributions brought by LM to the BLAST and BLAST-Pol projects.

The very first task has been the design, optimization and implementation of a whitening filter for the BLAST extragalactic maps of the ECDFS, which is not explicitly reported in this thesis. The raw maps present large-scale noise that hampers the detection of individual point sources. It is common habit to apply to the maps a whitening filter in order to suppress such large-scale structure, which in our case is primarily noise. The bi-dimensional Fourier transform of the maps is thus filtered on spatial scales larger than the size of the BLAST array projected onto the sky (roughly $14' \times 7'$). The filtered BLAST maps reveal the presence of hundreds of $\geq 5\sigma$ submm galaxies, the largest sample in the pre-*Herschel* era (Devlin et al. 2009).

The second important task within the context of the analysis of the BLAST extragalactic dataset has been developing the algorithm and perfecting the technicalities of the stacking methodology (see Ap-

pendix A), as well as optimizing and implementing a large number of simulations to evaluate stacking as an unbiased technique to estimate the average brightness of an externally-selected population of galaxies at submm wavelengths. Stacking analyses have enabled the statistical resolution of the full CIB intensity into flux density produced by identifiable $24\ \mu\text{m}$ -selected galaxies (Marsden et al. 2009), and the measurement of the history of obscured star formation in the Universe (Pascale et al. 2009), as well as the results presented in Chapter 3.

In November 2008, LM carried out follow-up observations of the BLAST galaxies with AAOmega, the spectrograph on the Anglo-Australian telescope. LM has been heavily involved in the subsequent data reduction, which resulted in spectroscopic redshifts for about two hundred BLAST sources. The BLAST redshift survey has enabled the first direct measurement of the luminosity function at 250, 350, and $500\ \mu\text{m}$ (Eales et al. 2009), as well as the results presented in Chapter 2.

These contributions to the BLAST data analysis have granted LM co-authorship in most of the BLAST extragalactic scientific production (including a paper on the *Nature* journal; see *Published Work*), albeit he is not part of the BLAST core team.

On the instrumentation front, LM has been part of the BLAST-Pol team since the very beginning in 2008.

The first task has been to manufacture, test, and fully characterize the BLAST-Pol cryogenic HWP, the most achromatic ever built to date. In the same context, LM has participated in the tests and spectral measurements of a novel artificial dielectric metamaterial (Zhang et al. 2009), which has found its first successful application as anti-reflection coating for the BLAST-Pol HWP. In addition, the BLAST-Pol photolithographed analyzers, have been designed, manufactured and extensively tested in Cardiff; LM has been directly involved in

every step of their deployment.

The second important task has been the hardware/software optimization, testing and deployment of two optical star cameras, which constitute BLAST-Pol’s primary pointing sensors. The star cameras have performed successfully during BLAST-Pol’s first flight over Antarctica in December 2010. LM is also in charge of the post-flight pointing reconstruction; preliminary analysis suggests that the absolute pointing accuracy will equal that of BLAST06 ($\lesssim 3''$ rms).

The third major task has been the design, optimization and implementation of the BLAST-Pol polarized map-maker. A big challenge has been to finalize this fundamental piece of software before the deployment to Antarctica for the flight campaign. LM has been using the map-maker during the first two days of the BLAST-Pol flight to produce “on-the-fly” maps of the bright calibrators to assess the overall performance of the telescope.

LM has participated in the two BLAST-Pol integration campaign, at the University of Toronto in April 2010 and at the Columbia Scientific Balloon Facility, Palestine, Texas, USA, in June and July 2010. Finally, LM has partaken in the BLAST-Pol flight campaign at the Long Duration Balloon (LDB) facility near McMurdo Station, Antarctica, from November 2010 to January 2011.

1.3.2 Other work

During the three years at Cardiff University, LM has gained valuable laboratory experience in several occasions beyond the PhD project.

Most notably, LM has participated in tests of the SCUBA-2 arrays (both electronics modules and science grade) in the Cardiff test-bed cryostat, which earned LM co-authorship in Bintley et al. (2010).

LM has also participated in the anechoic-chamber measurements of

the beam patterns of the multi-mode *Planck* High Frequency Instrument (HFI) horns at 857 and 545 GHz.

In addition, LM has participated in the spectral measurements of a novel prototype of polypropylene-embedded metal-mesh broadband achromatic HWP for millimeter wavelengths, which earned LM co-authorship in Zhang et al. (2011).

The design and manufacture of the HWP for the PILOT experiment (with similar photometric bands to BLAST-Pol; Bernard et al. 2007) has gone hand in hand with that of BLAST-Pol; LM has participated in its fabrication, spectral characterization and cryogenic testing.

Finally, LM has participated in the software deployment and performance characterization of one star camera for the E and B Experiment (EBEX; Reichborn-Kjennerud et al. 2010).

Part One

2. A MULTI-WAVELENGTH STUDY OF BLAST COUNTERPARTS

2.1 Introduction

The physical processes associated with the evolution of the Universe have left an imprint in the extragalactic background light. The far-infrared (FIR) portion of the background is associated with forming galaxies in which the ultraviolet (UV) photons emitted by newborn stars are absorbed and re-radiated by dust in the IR. Roughly half of the energy content of the starlight integrated over the age of the Universe is stored in the Cosmic Infrared Background (CIB), glowing with a broad peak at around $200\ \mu\text{m}$ (Puget et al. 1996, Fixsen et al. 1998, Hauser et al. 1998, Dwek et al. 1998). The tight connection between star formation and FIR luminosity provides a route to understanding the history of star formation in the Universe, by means of studying the CIB at wavelengths close to its peak (Gispert et al. 2000, Rowan-Robinson 2001, Chary & Elbaz 2001, Hauser & Dwek 2001).

The first leg on this route is to identify the sources contributing to the CIB. Ground-based surveys with the Submillimetre Common-User Bolometer Array (SCUBA; Holland et al. 1999) have revealed the existence of a population of distant, highly dust-obscured galaxies, similar to the Ultra Luminous Infrared Galaxies (ULIRGs) detected by *IRAS* (Smail et al. 1997, Hughes et al. 1998, Barger et al. 1998), which make up all the background at $850\ \mu\text{m}$ (Blain et al. 1999a). However, at these wavelengths the energy in the CIB is only one-thirtieth of the

value at its peak, and the SCUBA population only contributes 20–30% to the CIB at its peak (Coppin et al. 2006, Dye et al. 2007).

Recent progress has been made through new observations obtained at 24, 70, and 160 μm by the MIPS instrument aboard the *Spitzer Space Telescope* (Rieke et al. 2004), and at 250, 350, and 500 μm by the Balloon-borne Large Aperture Submillimeter Telescope (BLAST; Devlin et al. 2004, Pascale et al. 2008), a forerunner of the SPIRE photometer (Griffin et al. 2010) on the *Herschel Space Observatory* (Pilbratt et al. 2010). These wavelengths bracket the CIB peak; several authors have shown through stacking analyses that 24 μm -selected galaxies resolve the CIB background, both on the short-wavelength side of the peak (Dole et al. 2006) and on its long-wavelength side (Devlin et al. 2009, Marsden et al. 2009).

Sources identified at 24 μm are mostly unresolved in the FIR, and have a redshift distribution with a median of 0.9 (Pascale et al. 2009). A detailed multi-wavelength study of these sources is the necessary next step. Starting from a catalog of $\geq 5\sigma$ BLAST sources, Dye et al. (2009; hereafter D09) identify counterparts in 24 μm and radio catalogs (BLAST IDs). These tend to be relatively nearby sources (median z of 0.6, interquartile range of 0.2–1.0), with a median dust temperature of 26 K and a median bolometric FIR luminosity of $4 \times 10^{11} L_{\odot}$, which contribute 20% to the CIB at 250 μm . Identified BLAST sources typically lie at lower redshifts and have lower rest-frame dust temperatures compared to submillimeter (submm) sources detected in surveys conducted with SCUBA (Chapman et al. 2005, Pope et al. 2005). However, D09 also note that the $\sim 40\%$ of BLAST sources without identified counterparts probably lie at higher redshifts on average. Finally, D09 illustrate how the apparent increase in dust temperature and FIR luminosity with redshift occurs as a result of selection effects.

We also note that three other multi-wavelength studies of fainter BLAST sources discovered in the deepest part of the map have been undertaken. Dunlop et al. (2010) concentrate on 250 μm radio-identified sources within Great Observatory Origins Deep Survey-South (GOODS-S; Dickinson et al. 2003; see Section 2.2.1) where the deepest ancillary data coincide. Chapin et al. (2011) use overlapping BLAST 250–500 μm and LABOCA 870 μm (Weiß et al. 2009) data in the larger Extended Chandra Deep-Field South (ECDFS) to constrain the Rayleigh–Jeans tail more accurately than is possible in D09. Finally, Ivison et al. (2010a) study the FIR/radio correlation for a catalog of BLAST 250 μm -selected galaxies in the ECDFS; this sample is deeper than the D09 one, and yet slightly shallower than the selection in Dunlop et al. (2010). There is little overlap between the sources used in these studies and the shallower/wider area sample from D09.

The basis of our present study is the D09 sample as its brighter, and lower-redshift objects are most easily followed-up in the optical and UV. However, we first extend the submm analysis of D09 by accounting for flux boosting, source blending, and correlations among BLAST bands that inevitably arise in IR surveys as a consequence of finite instrumental angular resolution and source confusion (Coppin et al. 2005). We then identify counterparts to the BLAST IDs in the near- and far-UV *Galaxy Evolution Explorer* (*GALEX*) maps, in order to quantify the total dust-obscured and unobscured star formation, as described by several authors (Bell 2003, Hirashita et al. 2003, Iglesias-Páramo et al. 2006, Buat et al. 2007). We also extend the analysis of Eales et al. (2009; hereafter E09) to combine spectroscopic data of BLAST IDs with optical, near-IR (NIR) and mid-IR (MIR) photometry in order to place firmer constraints on source redshifts, morphology, active galactic nucleus (AGN) fraction, and stellar

masses.

We are able to assign spectroscopic and photometric redshifts to $\sim 62\%$ of the BLAST IDs. We use this information to estimate the rest-frame total FIR luminosity from the combined BLAST and MIPS photometry. We compare our FIR luminosities with those obtained from MIPS photometry only, finding a significant discrepancy for high luminosity sources ($L_{\text{FIR}} \gtrsim 5 \times 10^{11} L_{\odot}$) at $z \gtrsim 0.5$. The BLAST and SPIRE wavebands are therefore fundamental in constraining the peak of hidden star formation at high redshift (see also e.g., Schulz et al. 2010, Elbaz et al. 2010).

In addition, UV counterparts are found for about 60% of the BLAST IDs. This allows us to estimate the fraction of UV photons that manage to escape the dust shroud, which is then combined with FIR data to build an estimator of the total star-formation rate (SFR_{tot}) ongoing in these sources. Recent observations at the same wavelengths (Rodighiero et al. 2010) delineate the UV contribution as marginal at all redshifts. We find that star formation is heavily obscured at $L_{\text{FIR}} \gtrsim 10^{11} L_{\odot}$, $z \gtrsim 0.5$, but unobscured starlight plays an important role in low-redshift, low FIR luminosity sources ($z \lesssim 0.25$, $L_{\text{FIR}} \lesssim 10^{11} L_{\odot}$), in agreement with Buat et al. (2010).

We reanalyze the optical spectroscopy data from the AAOmega survey presented in E09 to obtain $\text{H}\alpha$ equivalent widths (EWs) and $[\text{N II}]/\text{H}\alpha$ line ratios. This spectral analysis, combined with a qualitative study of the radio, MIR, and optical emission, allows us to assess whether or not a BLAST galaxy is hosting an active nucleus: roughly 20% of the objects in our sample show evidence of AGN presence. Recent observations of FIR-selected samples (Wiebe et al. 2009, Coppin et al. 2010, Muzzin et al. 2010, Hatziminaoglou et al. 2010, Shao et al. 2010, Elbaz et al. 2010) show that the submm emission

of such objects is mainly due to star formation ongoing in the host galaxy, rather than due to the AGN. Therefore, we do not explicitly exclude AGNs from our analysis, unlike other authors (Bell 2003, Iglesias-Páramo et al. 2006, Buat et al. 2007), but rather flag them as such. Visual examination of BLAST IDs in UV, optical, and MIR images (see Appendix B) is used to derive a broad morphological classification of these objects: at low redshift we find predominantly spirals, whereas most of the BLAST sources identified at high redshift are compact and show AGN signatures. This is probably a selection bias, as the fraction of submm sources identified at other wavelengths gradually decreases with z (see D09), and the farthest objects can often be identified only if they are particularly bright in the radio or in the optical, frequently an indication of AGN presence. As a matter of fact, the analysis carried out by Dunlop et al. (2010) shows that a deep survey at $250\ \mu\text{m}$ not only contains low- z spirals, but also extreme dust-enshrouded starburst galaxies at $z \sim 2$. Our analysis tends to miss the latter because they are typically extremely faint in the optical/UV, unless they also host an AGN.

Finally, stellar masses (M_\star) are estimated using the method detailed in Dye (2008), in order to study whether or not specific star-formation rates ($\text{SSFR} \equiv \text{SFR}/M_\star$) depend on stellar mass and L_{FIR} . The SSFR plays an important role as it measures the timescale of recent star formation in a galaxy, as compared to the star-formation rate integrated over the galaxy's history. Several studies (Santini et al. 2009, Rodighiero et al. 2010; and references therein) report that the SSFR increases with redshift at all masses, whereas the dependence of SSFR on mass is one of the most debated questions. In particular, we aim to understand whether or not sources selected at wavelengths longward of $200\ \mu\text{m}$ are experiencing a major episode of star

formation, forming stars more actively than in their recent past and building up a substantial fraction of their final stellar mass. We highlight a dichotomy in the BLAST population: sources at $z \lesssim 1$ appear to be run-of-the-mill star-forming galaxies with intermediate stellar masses (median $M_\star \sim 7 \times 10^{10} M_\odot$) and approximately constant SSFRs, whereas the high- z tail of the BLAST counterparts significantly encroaches on the SCUBA population detected in the SHADES survey (Dye et al. 2008), in terms of both stellar masses and SSFRs. This is expected since there is good overlap between fainter BLAST sources and $870 \mu\text{m}$ -selected galaxies (Dunlop et al. 2010, Chapin et al. 2011), but it is also important to establish an additional link with a shallower BLAST sample, using a methodology equivalent to that of SHADES. In addition, since the more massive BLAST galaxies at intermediate redshifts ($0 < z < 1$) seem to form stars more vividly than the equally massive and aged $24 \mu\text{m}$ sources detected in the GOODS survey, we suggest that the BLAST counterparts may act as linking population between the $24 \mu\text{m}$ -selected sources and the SCUBA starbursts.

The layout of this chapter is as follows. In Section 2.2, we describe in detail the maps, images, and catalogs used throughout this work. Sections 2.3 and 2.4 are concerned with luminosities and SFRs in the FIR and UV, respectively. In Section 2.5, we build a unified estimator of total star formation and discuss the first results. In Section 2.6, we estimate the AGN content of our sample, while in Section 2.7 we outline a broad morphological scheme for our sources. In Section 2.8, we compute the stellar masses and present the main results. Section 2.9 contains our conclusions. Throughout this thesis, we adopt the concordance flat Λ CDM cosmological model, with $\Omega_M = 0.274$, $\Omega_\Lambda = 0.726$, and $H_0 = 70.5 \text{ km s}^{-1} \text{ Mpc}^{-1}$ (Hinshaw et al. 2009).

2.2 *Data*

This section describes the data sets used for our analysis, spanning from the UV to the submillimeter.

2.2.1 *Submillimeter data*

We use data from the wide-area extragalactic survey of BLAST described by Devlin et al. (2009), and centered on the GOODS-S (Dickinson et al. 2003; which in turn is centered on the Chandra Deep-Field South, CDFS) region. The maps¹ cover an area of 8.7 deg^2 with a 1σ depth of 36, 31, and 20 mJy at 250, 350, and $500 \mu\text{m}$, respectively. We refer to this region as the BLAST GOODS-S Wide (BGS-Wide). A smaller region of 0.8 deg^2 , nested inside BGS-Wide and referred to as BLAST GOODS-S Deep (BGS-Deep), has a 1σ depth of 11, 9, and 6 mJy at 250, 350, and $500 \mu\text{m}$, respectively; these depths account for the instrumental noise only. Due to large instrumental beams (36, 42, and $60''$) and steep source counts (approximately following $dN/dS \propto S^{-3}$; Patanchon et al. 2009), source confusion contributes substantially to the noise in these maps. Marsden et al. (2009) estimate that fluctuations arising from unresolved sources in BGS-Deep are $\sigma_{\text{confusion}} \approx 21, 17, \text{ and } 15 \text{ mJy}$ at 250, 350, and $500 \mu\text{m}$, respectively. The BLAST maps are made using both an optimal mapmaker (Patanchon et al. 2008) and a naive mapmaker (Pascale et al. 2011), and are found to be in excellent quantitative agreement. Further details on the instrument may be found in Pascale et al. (2008), while flight performance and calibration are provided in Truch et al. (2009). Catalogs of sources detected at each wavelength in BGS-Deep and BGS-Wide are presented by Devlin et al. (2009).

¹ Available at: <http://blastexperiment.info/results.php>

D09 combine these single-wavelength catalogs by selecting sources with a $\geq 5\sigma$ (instrumental only, no confusion noise) significance in at least one of the bands. They use this multi-band catalog to identify counterparts (BLAST primary IDs) in deep radio (ACTA and Very Large Array, VLA; Norris et al. 2006, Miller et al. 2008) and $24\mu\text{m}$ (SWIRE and FIDEL; Lonsdale et al. 2004, Dickinson & FIDEL team 2007, Magnelli et al. 2009) surveys. The BLAST primary IDs all have $\leq 5\%$ probability of being a chance alignment. They also compile a list of secondary IDs, with different counterparts associated with the same BLAST source as the primary ID, but with larger probability of being a chance alignment.

In this work, we present an extended version of the D09 catalog of the BLAST primary IDs which contains 227 BLAST sources. In the following sections, we update this list to include UV data, recent redshifts, corrections for submm flux boosting and blending, morphology, AGN features, and SFRs (see Appendix C for data tables). The list of secondary IDs is extensively discussed in E09, and we do not investigate them further.

We emphasize again that the sample studied in this work comprises the subset of BLAST-selected bright sources for which optical spectroscopy/photometry is available, and/or for which we find a clear counterpart in the UV. Naturally, this is only a fraction of sources that would be in a purely BLAST-selected catalog, skewed toward lower redshifts and strong optical/UV fluxes.

2.2.2 *Optical spectroscopy*

A spectroscopic follow-up of the BLAST IDs is carried out with the AAOmega optical spectrograph at the Anglo-Australian Telescope. The BLAST spectroscopic redshift survey is discussed in E09, as well

as the reduction of the spectral data; here we extend their analysis and results (see Sections 2.6, 2.7 and Tables 2.2, C1).

AAOmega (AAO; Sharp et al. 2006) consists of 392, 2''-wide fibers feeding light from targets within a 2° field of view; the configuration of diffraction gratings is chosen to yield a wavelength coverage from 370 to 880 nm, with spectral resolution $\lambda/\delta\lambda \simeq 1300$. At redshifts lower than 1, this allows us to detect two or more of the following lines: [O II] 372.7, calcium H and K, H β , [O III] 495.9 and 500.7, H α , [N II] 658.3, and [S II] 671.6 and 673.1. At redshifts greater than 1, we only rely on broad emission lines, such as Lyman α , Si IV 140.3, C III] 190.9, and C IV 154.9.

We have produced two prioritized lists of targets. The first list comprises $\geq 3.5\sigma$ BLAST sources with primary radio or 24 μm counterparts². Sources selected at 24 μm are also included in the target list to use all the available fibers. The second list contains the secondary BLAST IDs, plus 24 μm sources. The positions of the primary and secondary targets are shown in Figure 2.1.

The net observing time for the list of primary targets is 7 hr, obtaining spectra for 669 sources (316 BLAST IDs and 356 SWIRE sources). The list of secondary targets is observed for only 1 hr (due to poor weather), obtaining 335 spectra (77 BLAST IDs, and 258 SWIRE sources). Spectroscopic redshifts are consequently obtained by E09 for 212 BLAST IDs in the primary list, 193 of which have $\geq 75\%$ confidence level (c.l.), and for 11 BLAST IDs in the secondary list (all with $\geq 75\%$ c.l.). Figure 2.2 shows three representative spectra of primary BLAST counterparts, while Figure 2.3 (which we choose to display full-page and rotated for visual clarity) compares the spectroscopic redshifts of primary and secondary targets measured with AAOmega

² If only the 24 μm counterpart is present, we refine the position of the source by matching it with optical or IRAC 3.6 μm coordinates.

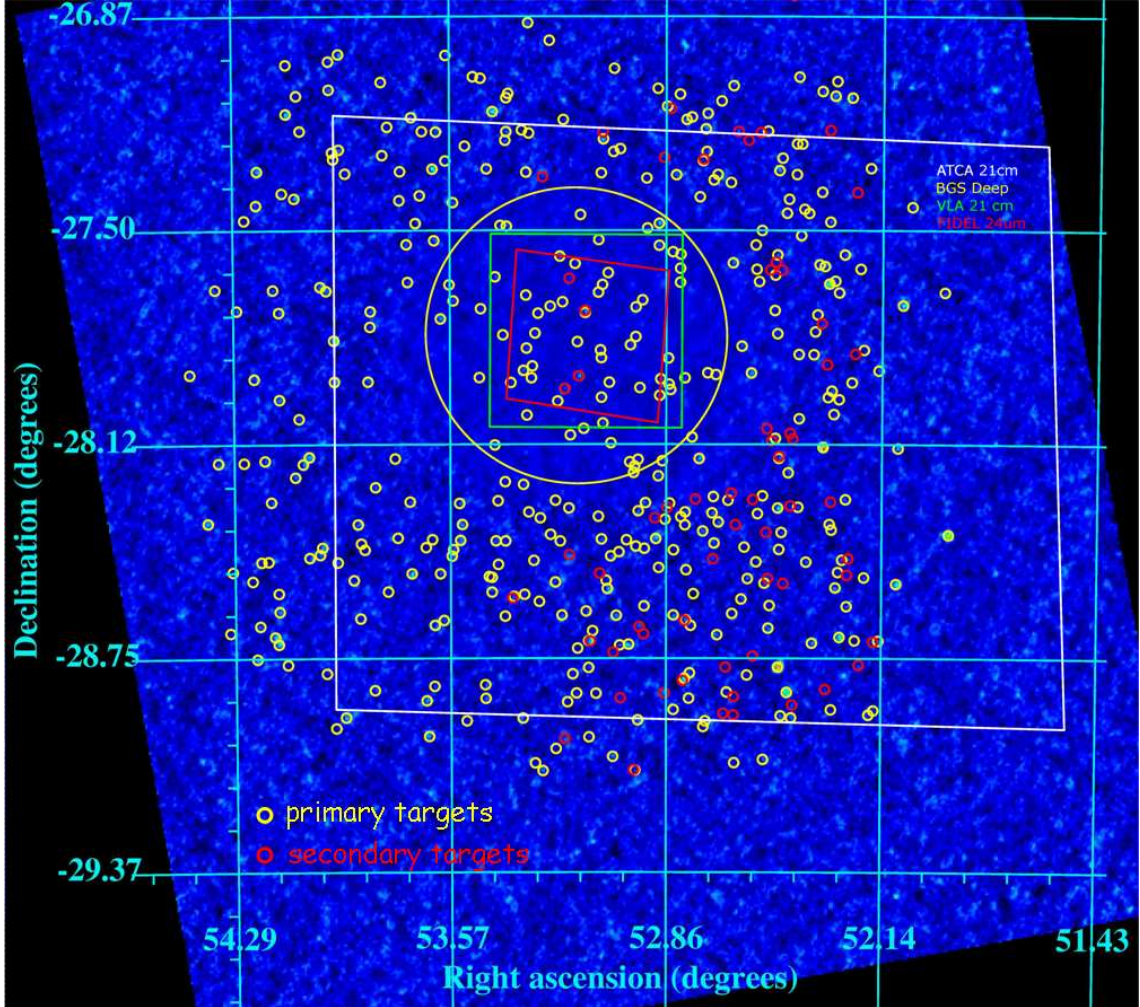


Fig. 2.1 Positions of the primary (yellow circles) and secondary (red circles) AAO targets. The underlying map is the 250 μm BLAST map of the GOODS-South field. Also shown are the regions covered by ancillary radio and 24 μm catalogs (see Section 2.2.1).

with a mixture of photometric redshifts collected from the literature.

It is important to clarify here that the two lists used for the AAO observations are not fully coincident with the D09 list discussed in the previous section and used in this work. However, a large overlap among sources in these lists is present and 82 sources from the D09 catalog of BLAST IDs have AAO redshifts, all with $\geq 95\%$ c.l. (see Table C1).

Using the available spectra we estimate $\text{H}\alpha$ EWs and $[\text{N II}]/\text{H}\alpha$ line

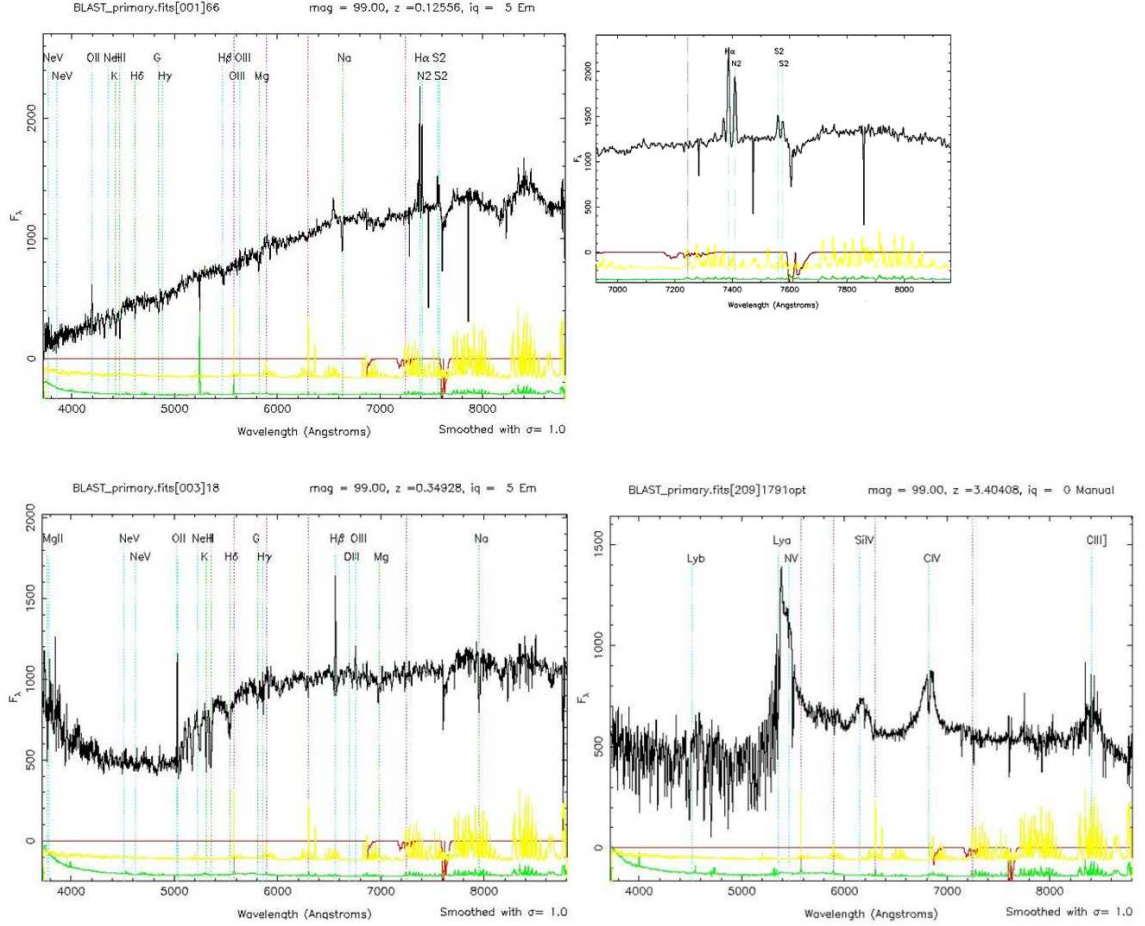


Fig. 2.2 Spectra of three representative primary BLAST counterparts, plotted in the rest frame of each galaxy (black solid line); the spectra are uncalibrated in flux, therefore the y -axis is in arbitrary units. The other solid lines represent the error spectrum (green), sky spectrum (yellow) and the telluric absorption spectrum (red). The vertical dotted lines indicate the positions of the main emission (cyan) and absorption (green) features at the measured redshift. Also shown are the strongest of the night sky emission lines (dotted magenta lines). *Top*: spectrum of a star-forming galaxy at $z = 0.1256$, with a zoom-in around the $H\alpha$, N II lines, and the S II doublet. *Bottom left*: spectrum of an irregular galaxy at $z = 0.3493$. *Bottom right*: spectrum of quasar at $z = 3.404$.

ratios for 56 of these 82 sources. The remaining 26 sources either are at too high redshift for the $H\alpha$ line to fall in our spectral coverage ($z \gtrsim 0.33$), or have spectra with a poor signal-to-noise ratio.

We implement a bootstrapping technique for estimating the measurement error on the $H\alpha$ EWs: we add to every individual spectrum a

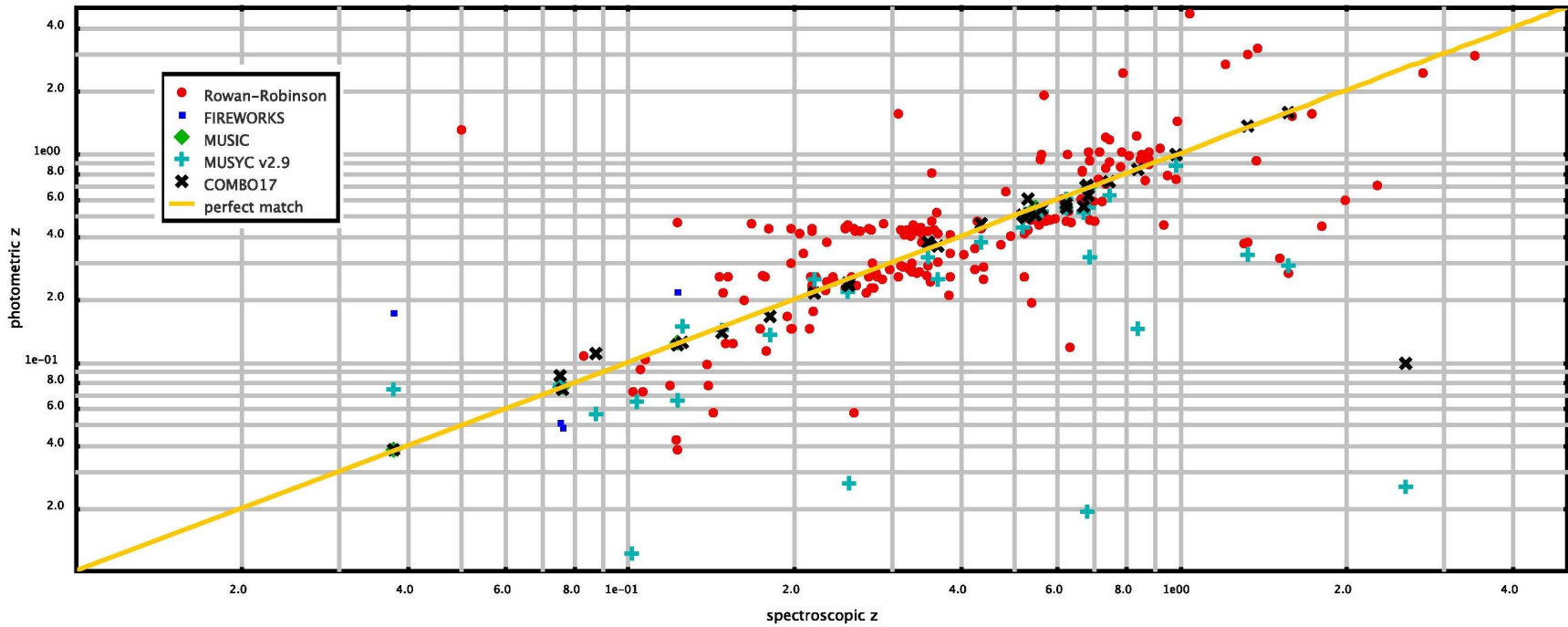


Fig. 2.3 Comparison between the spectroscopic redshifts of primary and secondary targets measured with AAOmega and a mixture of photometric redshifts collected from the literature. Of all the BLAST and SWIRE targets with a spec- z from AAO: 191 have a photometric z from Rowan-Robinson et al. (2008; red filled circles); 39 from Brammer et al. (2008), who apply a new photo- z algorithm named EAZY to the FIREWORKS (Wuyts et al. 2008; blue filled squares, five sources) and MUSYC (Taylor et al. 2009; cyan crosses, 34 sources) catalogs; six from MUSIC Grazian et al. (2006; green filled diamonds); and 32 sources have photo- z from Wolf et al. (2004, 2008; black exs).

realization of white noise, scaled to the 1σ uncertainty of the spectrum itself, and compute the EW again using this newly generated spectrum. This is repeated 1000 times per spectrum, yielding a histogram of values for the EW. Provided that the histogram has Gaussian shape (an example is given in Figure 2.4), we can safely use the value of σ in the Gaussian fit to the histogram as the estimated measurement error on the EW. We calculate the final uncertainties on the EWs as the quadrature sum of the measurement error, estimated with above bootstrapping technique, and the Poisson noise, estimated following Vollmann & Eversberg (2006; Equation 7).

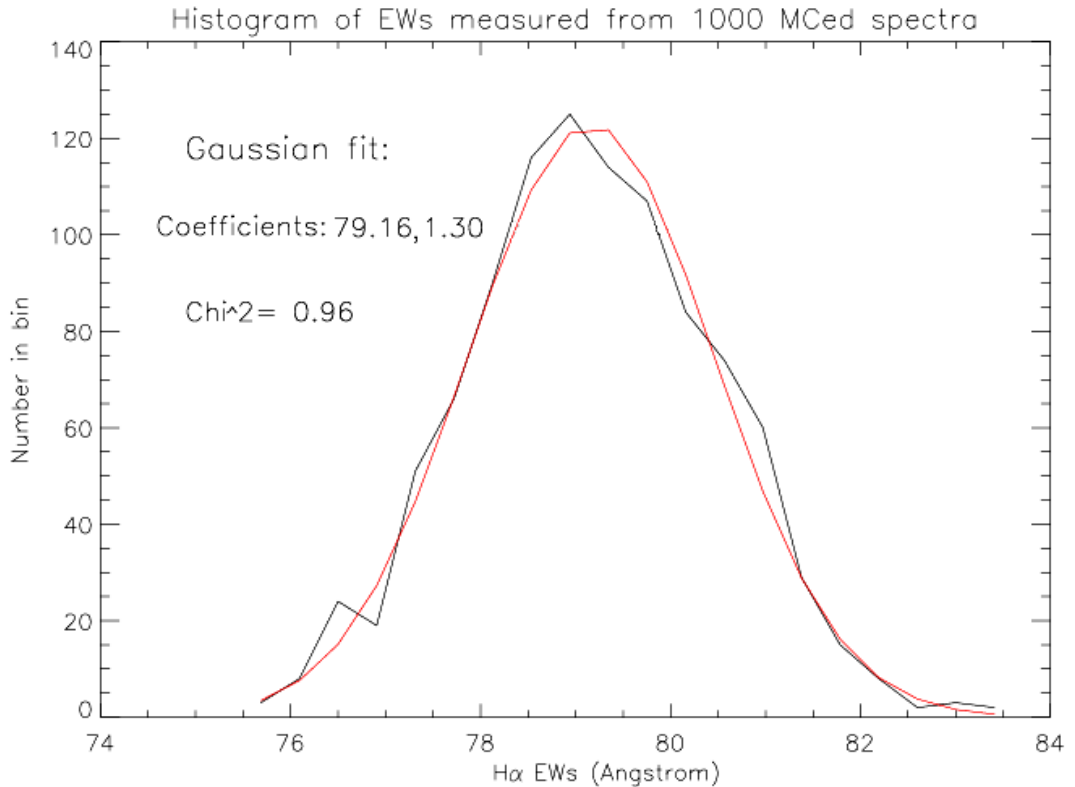


Fig. 2.4 Histogram of measured H α equivalent widths for the source PKS 0326-288, located at redshift $z = 0.109$. The bootstrapping technique used to generate the histogram is described in the text. The value of σ in the Gaussian fit (red) to the histogram is a good estimate of the measurement error.

We list the rest-frame EWs, $EW_{\text{rf}} = EW/(1+z)$, in Table C1, along

with their uncertainties and the $[\text{N II}]/\text{H}\alpha$ line ratios. Note that we apply a 1 \AA correction to the $\text{H}\alpha$ EW_{rf} for underlying stellar absorption (Hopkins et al. 2003, Balogh et al. 2004).

2.2.3 UV data

We identify near-UV (NUV) and far-UV (FUV) counterparts to BLAST IDs by searching for *GALEX* sources in the Deep Imaging Survey (DIS; Martin et al. 2005; data release GR-4/5) within $6''$ of the radio or $24 \mu\text{m}$ counterpart³, a separation just slightly larger than the *GALEX* point-spread function (PSF) FWHM (Morrissey et al. 2007). This choice is justified by the presence of a few extended objects, unresolved by the submillimetric beam, that contribute to the same BLAST source (see Section 2.7). After visual inspection of the UV images, we add one additional interacting system extending beyond $6''$ from the BLAST ID (#2); in this case we integrate the UV magnitude from both the interacting objects, because they fall within the same BLAST beam. We estimate FUV and NUV magnitudes using the standard *GALEX* pipeline (Morrissey et al. 2007) for most IDs, whereas we perform aperture photometry on 13 extended objects. A magnitude is considered to be unreliable if the source is either confused or blended with a star.

We find that 144 BLAST IDs have an NUV counterpart (136 with reliable magnitude), and 113 have an FUV counterpart (107 with reliable magnitude). Three sources are outside the area covered by the DIS, and the remaining 80 BLAST IDs have no obvious counterpart. By comparing the flux estimates for objects detected in more than one *GALEX* tile (pointing), we find that the average uncertainty associ-

³ If both counterparts are present, we use the arithmetic mean between the two sets of coordinates: $[\alpha_{\text{BLAST}}, \delta_{\text{BLAST}}]$.

ated with the reproducibility of the measurement is 0.06 and 0.11 mag in NUV and FUV, respectively. For bright galaxies, these values are larger than the uncertainty in the calibration (0.03 and 0.05 mag in the NUV and FUV, respectively; Morrissey et al. 2007), and in the source extraction procedure (≤ 0.02 mag). The uncertainty on a quoted UV magnitude is therefore the sum in quadrature of these three terms, and it lies in the 1σ range of 0.07–0.25 mag and 0.12–0.5 mag in NUV and FUV, respectively.

GALEX postage-stamp images, $2' \times 2'$ wide, are used to study the UV morphology of the BLAST IDs; a selection⁴ of these is shown in Figure B1. UV magnitudes and uncertainties are listed in Table C2.

2.2.4 SWIRE 70 and 160 μm MIPS maps

We use 70 and 160 μm fluxes extracted from SWIRE maps (Lonsdale et al. 2004) at positions $[\alpha_{\text{BLAST}}, \delta_{\text{BLAST}}]$ to constrain the spectral energy distribution (SED) of each BLAST source at wavelengths shorter than the emission peak (see Section 2.3.2). These maps overlap almost completely with BGS-Wide, and all the $\geq 5\sigma$ BLAST sources investigated in this work lie within them. The 1σ depth of the maps is 3.6 and 20.8 mJy at 70 and 160 μm , respectively.

2.2.5 MIR/NIR/optical images and catalogs

In addition to the aforementioned UV *GALEX* images, we investigate BLAST source morphology using optical and IR images. The latter are 3.6, 4.5, 5.8, and 8 μm IRAC (Fazio et al. 2004) images from the SWIRE survey. In the optical, we examine (*Ugr*)-band images, acquired with the 4m Cerro Tololo Inter-American Observatory (CTIO)

⁴ The complete set of full-color cutouts can be found at http://blastexperiment.info/results_images/moncelsi/

as part of the SWIRE survey, and R -band images from the COMBO–17 survey (Wolf et al. 2004, 2008). In Figure B1, we show $2' \times 2'$ cutouts for a selection⁴ of BLAST IDs.

For the purpose of studying the morphology, AGN fraction and stellar mass, we also match, using a search radius of $3''$ as in D09, the catalog of BLAST IDs to the following catalogs:

1. the SWIRE band-merged catalog consisting of optical ($U g r i z$) and MIR IRAC fluxes⁵ (Surace & SWIRE Team 2005);
2. the 17 band COMBO–17 optical catalog (Wolf et al. 2004, 2008);
3. the Multi-wavelength Survey by Yale-Chile (MUSYC; Gawiser et al. 2006) catalog for NIR photometry (J and K bands).

As a result of this analysis, out of 227 BLAST IDs:

- 205 (90%) have an IRAC counterpart from the SWIRE survey;
- 114 (50%) have an optical (SWIRE and/or COMBO–17), *and* either an NIR (MUSYC) or MIR (3.6 or $4.5 \mu\text{m}$, IRAC) counterpart⁶;
- 102 of the above 114 are detected in a minimum of five bands (optical, NIR, and MIR);
- 52 of the above 102 have J - and K -band photometry from MUSYC.

We use the wealth of ancillary information for a variety of purposes: we refer to Sections 2.6, 2.7, and 2.8 for discussions on AGN fraction, morphology, and stellar masses.

2.2.6 Redshifts

In addition to the 82 spectroscopic redshifts obtained with AAO for the BLAST primary IDs, we find five additional spectroscopic red-

⁵ The lower limits for inclusion in the catalog are 7 (10σ), 7 (5σ), 41.8 (5σ) and $48.6 \mu\text{Jy}$ (5σ) at 3.6 , 4.5 , 5.8 and $8 \mu\text{m}$, respectively.

⁶ We note that the sky overlap among BGS, SWIRE, COMBO–17, and MUSYC is limited to a $\sim 4.15 \text{ deg}^2$ region.

shifts by exploring the NASA/IPAC Extragalactic Database (NED) with a $1''$ search radius around each ID. For the other sources, we use photometric redshifts from the MUSYC-EAZY (Brammer et al. 2008, Taylor et al. 2009), COMBO-17 (Wolf et al. 2004, 2008; only sources with $R \leq 24$) and Rowan-Robinson et al. (2008; RR08) catalogs, using again a $1''$ search radius. We carefully inspect each individual alignment by taking into account the imaging data in Figure B1, the UV photometry, the SED in the FIR/submm, and any additional information available from NED. In the cases of BLAST IDs with more than one associated photometric redshift, priority is given in the order: EAZY, COMBO-17, and RR08. We thereby acquire 53 additional photometric redshifts, of which 20 are from EAZY, six from COMBO-17, and 27 from RR08.

We have succeeded in assigning 140 redshifts out of 227 ($\sim 62\%$) objects in our sample. The redshifts are listed in Table C1, along with their provenance. Figure 2.5 shows the redshift distribution of the whole BLAST ID catalog, and of the UV subset used in Section 2.5 for the discussion on the total SFRs. The number of sources with redshift is doubled with respect to the robust sample of D09,⁷ but the median redshift is roughly halved. This apparent pronounced discrepancy, limited to the $z \lesssim 0.2$ bin, amounts to 40 sources and is due to the combination of two selection effects. First, roughly 15 sources in D09 with $z \lesssim 0.2$ (mostly from RR08) do not make it into the robust sample, mainly because the photometric redshift is intrinsically unreliable or, in a handful of cases, because the BLAST source has been spuriously identified with the counterpart. Second, 27 other sources with redshifts estimated in this work have no redshift in D09, because they have neither sky coverage from COMBO-17 nor from RR08; of

⁷ The robustness of a source is assessed by D09 based solely on the goodness of the SED fit.

these 27, 21 are from AAO, and 24 have $z \lesssim 0.25$. Therefore, the apparent excess of low- z sources with respect to D09 partly reflects the inclusion of the AAO spectroscopic redshifts (naturally skewed towards low- z) and partly lies in the intrinsic robustness in D09 of either the photometric redshift or the counterpart itself.

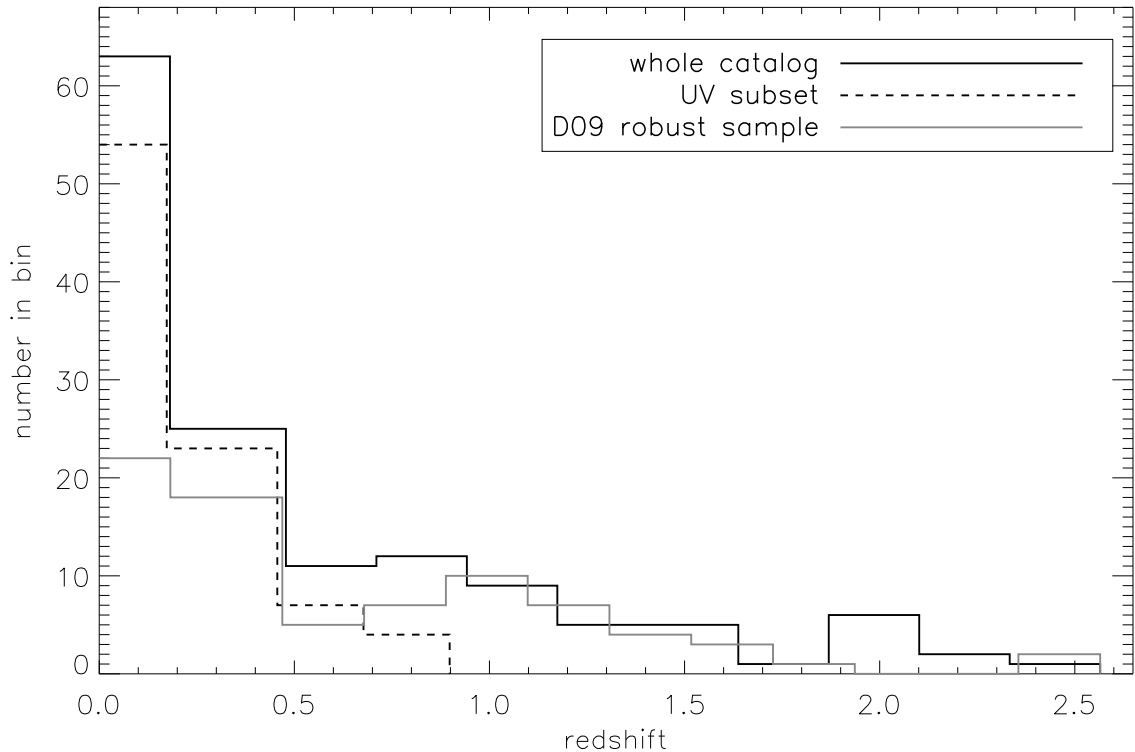


Fig. 2.5 Redshift distributions for the whole catalog of BLAST IDs and for the subsample with UV data. The former has a median of 0.29 and an interquartile range of 0.12–0.84; the latter has a median of 0.18 and an interquartile range of 0.10–0.34. We also show the redshift distribution for the robust sample of D09, with median of 0.6 and an interquartile range of 0.2–1.0.

It is worth noting here that this study misses a large fraction of the high- z BLAST sources that are known to constitute an important part of the BLAST population (Devlin et al. 2009, Marsden et al. 2009, Pascale et al. 2009). This is again due to the combination of two factors. First, $\sim 38\%$ of the BLAST IDs presented in this work do not have a redshift estimate; using information about the UV identification rate (similarly to D09), we can argue that more than half of the sources

without a redshift estimate lie at $z \gtrsim 0.7$. In fact, 90 out of 99 (91%) sources at $z \leq 0.7$ (and 96 out of 115, 83%, sources at $z \leq 1$) have a *GALEX* counterpart; now, of the 87 sources with no redshift estimate, 57 (66%) do not have a *GALEX* counterpart. Under the assumption that the UV identification rate is a reasonable (if coarse) estimator of redshift, arguably more than half of the sources without a redshift estimate lie at $z \gtrsim 0.7$ and roughly half lie at $z \gtrsim 1$. Second, D09 start with a catalog composed of bright, $\geq 5\sigma$ sources with flux densities ≥ 33 mJy at $250\ \mu\text{m}$, ≥ 27 mJy at $350\ \mu\text{m}$, and ≥ 19 mJy at $500\ \mu\text{m}$; Dunlop et al. (2010) and Chapin et al. (2011) clearly show the necessity of digging deeper into the BLAST maps, with the aid of the deepest available multi-wavelength data, in order to identify the faintest, high- z BLAST galaxies. Of course, this is done at the expense of the size of the submm sample, which inevitably drops to a few tens of sources.

Nonetheless, the present study is still unique in terms of size of the sample, wavelength coverage, depth, and quality of the ancillary data. Indeed, *IRAS* sources have been studied at many wavelengths (e.g., Della Valle et al. 2006, Mazzei et al. 2007), but with little knowledge of the details of the cold dust emission from which the FIR SFR estimates come. Some improvements have been made with the SCUBA Local Universe and Galaxy Survey (SLUGS; Dunne et al. 2000, Vlahakis et al. 2005), but still with limited ability to estimate the bolometric FIR luminosity. The results in this work probably will not be immediately replaced by deeper surveys undertaken by *Herschel*; in fact, even the much more sensitive observations carried out with SPIRE will have to face the lack of deeper ancillary data. This is especially true in the optical/NIR, where most of the $z > 2$ submm galaxies are much too faint to be detected by instruments like AAOmega, and in the radio, where the identification rate of the faintest $z > 2$ sources

drops drastically, even when using the deepest available data (VLA).

2.3 *FIR Luminosities and SFRs*

2.3.1 *Deboosting the BLAST fluxes*

The sources in the BLAST catalog used by D09 to identify counterparts in the radio and $24\ \mu\text{m}$ are detected directly from the maps of BGS-Deep and BGS-Wide. While the details of the catalog are discussed there, it is useful to summarize here the procedure to clarify what are the potential biases.

First, a catalog of BLAST sources with detection significance higher than 3σ is made at each wavelength, independently. Each entry in the catalog is then positionally matched across the three bands, with the requirement of a 5σ detection in at least one band. The significance here is relative to instrumental noise, and does not include confusion noise. A new position is assigned to the source by averaging its positions in the original single-wavelength catalogs, with weights estimated by taking into account the beam sizes and the signal-to-noise ratios (SNRs) of the detections at each wavelength. This combined catalog is then used to identify counterparts in the radio and at $24\ \mu\text{m}$, and a new flux density is measured from the 70 to $500\ \mu\text{m}$ maps at the accurate position of the counterpart.

The BLAST differential source counts fall very rapidly with flux density (approximately following $dN/dS \propto S^{-3}$; Patanchon et al. 2009), thus Eddington bias as well as source confusion will cause the fluxes to be boosted. This effect has to be estimated to properly compute the FIR luminosity of each source. Coppin et al. (2005) have proposed a Bayesian approach that can be applied to estimate the most likely flux distribution when the noise properties of the detection

and the underlying source distribution are known. Their method is derived under the assumption that the flux density comes from just one source, plus noise. This cannot be applied to BLAST sources because of blending: the measured flux density can either come from just one source, or more likely from several sources blended together by the beam, which then appear as one single source of larger flux density.

We develop a different method to account for boosting of BLAST fluxes, which is entirely based on Monte Carlo simulations. We generate 100 noiseless sky maps using the BLAST measured count models (Patanchon et al. 2009), and no clustering⁸. Noise is added to each simulated map to a realistic level for the BGS-Deep and BGS-Wide regions. Sources are then retrieved with the same method used on the real maps (Devlin et al. 2009). Considering all the input components within an FWHM beam distance from each retrieved source, we stipulate that the input component with largest flux density is the actual counterpart⁹ (ID). The source flux density is then remeasured at the position of the ID. Finally, we compare this flux density with that of the input source. By repeating this for each source detected in each simulation, we generate distributions of input/output SNR, where the relevant noise is the instrumental noise at the position of the ID. These simulations are similar to those used in Chapin et al. (2011) to study the effects of confusion for their deeper sample.

Figure 2.6 shows the result of this analysis. In each bin, we display the median of the distribution of input SNR (labeled SNR_{ID}) corresponding to the measured SNR. The error bars define the first and third interquartiles. To obtain the deboosted flux density likelihood,

⁸ Here we refer to the source clustering detected in the BLAST maps by Viero et al. (2009).

⁹ We know that this assumption is always verified in BGS-Wide but less so in BGS-Deep, where in 21% of the cases the second brightest component contributes to more than 50% of the retrieved flux (see E09, Appendix B).

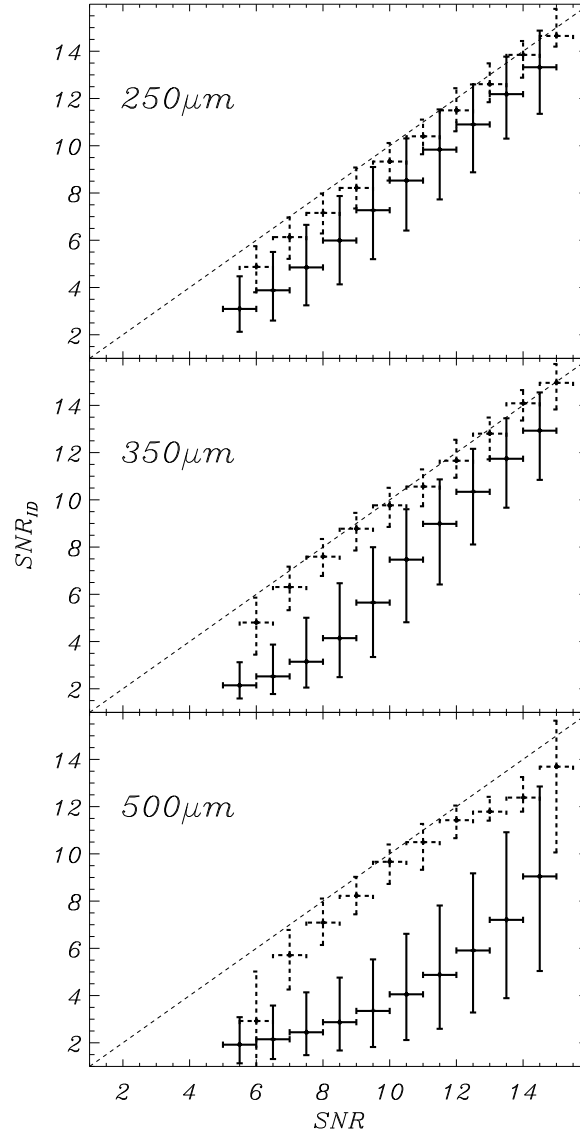


Fig. 2.6 Effects of flux boosting, and source blending at BLAST wavelengths in BGS-Deep (solid error bars) and in BGS-Wide (dashed bars). For a source with a measured SNR at a given wavelength, the points show the distribution of the SNR_{ID} retrieved from simulations, binned in 1-SNR wide bins. Each point indicates the median value of the distribution in each bin, and the low and high error bars are the first and third interquartiles, respectively. The dashed line indicates where the points would lie in the absence of biases. The effects are mild in the wide region, where instrumental noise dominates, and become more severe in BGS-Deep, where confusion noise dominates, and source blending is more important. At the longest wavelength, the beam size blends fluxes from many adjacent sources, giving a strong bias. This is not a major problem for our analysis, which deals with sources identified at low, or moderate redshifts.

it suffices to multiply the y -axis by the corresponding instrumental noise. It is clear from this figure that sources in the BGS-Wide region are only moderately affected by boosting. The situation is substantially different for BGS-Deep, and the effect of boosting increases with wavelength, as expected, due to the telescope PSF becoming larger. At the longest BLAST wavelength, the fluxes are severely affected by boosting: a source detected even with a 10σ significance level has a deboosted flux only about half of what is measured directly from the map. By comparing the deboosted values for BGS-Wide at 250 and 350 μm , we notice that the longer wavelength appears to be slightly less biased. This arises from the fact that the two PSFs are not very different in size (36 and 42'', respectively), but the 250 μm PSF has larger sidelobes (Truch et al. 2009).

2.3.2 *SED fitting and FIR luminosities*

In order to estimate the rest-frame FIR luminosity (L_{FIR}) of each BLAST source in our sample, we perform SED fitting using the MIPS flux densities (70 and 160 μm only) and the deboosted BLAST flux densities; the model template is a modified blackbody spectrum (with spectral index $\beta = 1.5$; Hildebrand 1983), with a power law $\nu^{-\alpha}$ replacing the Wien part of the spectrum, to account for the variability of dust temperatures within a galaxy (we choose $\alpha = 2$; Blain 1999, Blain et al. 2003). Pascale et al. (2009) show that the estimated FIR luminosities depend weakly on the choice of α , whereas the estimated dust temperatures are more sensitive to the template used. Since our analysis does not employ temperature measurements, the value of α we adopt is not critical. We also note here that the SED template chosen is the one that best performs in fitting the spectrum of two often-used IR-luminous local galaxies, Arp 220 (shown in Figure 2.7)

and M82; by sampling their SEDs at the five observed wavelengths in question, the nominal FIR luminosities and dust temperatures are correctly retrieved (within uncertainties) not only at $z \sim 0$, but also when their spectra are redshifted up to $z = 2$.

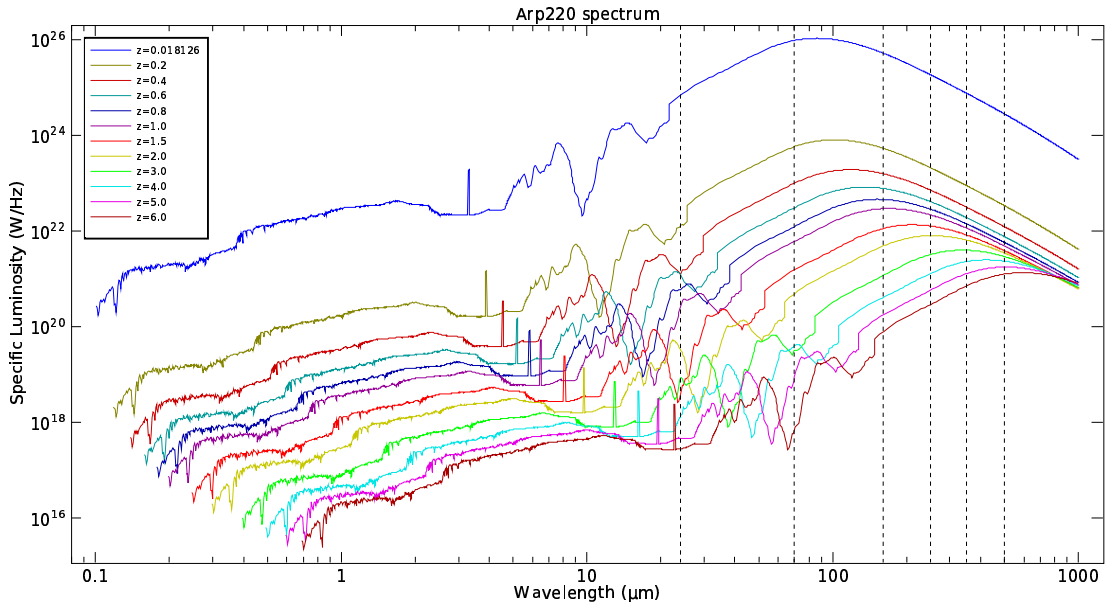


Fig. 2.7 Observed UV-to-FIR spectrum of the local ($z = 0.018126$) ULIRG Arp 220. The spectrum is plotted in the galaxy’s rest frame, and at increasingly higher redshift, to visually render the effect of cosmological dimming combined with the shift in peak wavelength in the submm. The partial compensation of these two counteracting effects is often referred to as “negative K-correction” (e.g., Blain et al. 2002). We also show for reference, as dotted vertical lines, the central wavelength of the MIPS (24, 70, and 160 μm) and BLAST (250, 350, and 500 μm) bands.

The way each BLAST flux density is deboosted depends on its SNR. If this is larger than 15, no correction is applied. If the measured flux density is smaller than twice the square root of the sum in quadrature of instrumental and confusion noise (as reported in Marsden et al. 2009), the detection is treated as an upper limit. In all other cases, the above deboosting distributions are used. For sources in BGS-Deep, the deboosting likelihood distribution is well approximated by a Gaussian function, but this is less true in BGS-Wide (especially at low SNR). Therefore, we use the sampled distribution for sources in

Table 2.1. Correlations among BLAST bands

| Band [μm] | Pearson Correlation Matrix | | | | | |
|---------------------------|----------------------------|-------------------|-------------------|-------------------|-------------------|-------------------|
| | BGS-Deep | | | BGS-Wide | | |
| | 250 μm | 350 μm | 500 μm | 250 μm | 350 μm | 500 μm |
| 250 | 1 | 0.68 | 0.66 | 1 | 0.26 | 0.29 |
| 350 | | 1 | 0.69 | | 1 | 0.29 |
| 500 | | | 1 | | | 1 |

BGS-Wide, and a Gaussian approximation in BGS-Deep.

The portion of noise arising from confusion is highly correlated among bands. The Pearson coefficients of the correlation matrix are listed in Table 2.1, and are estimated from the (beam-convolved) BGS-Deep and BGS-Wide maps. As expected, the correlation effects are more important for sources in BGS-Deep, and we do take this into account in the SED fitting algorithm, whereas no correlations among bands are considered for sources in BGS-Wide. This turns out to be convenient, as in BGS-Deep the distributions are Gaussian, and a correlation analysis is relatively straightforward. This would not be the case for the sources in BGS-Wide.

MIPS fluxes at 70 and 160 μm are also used in the fitting routine to constrain the SED at wavelengths shorter than the emission peak. Deboosting these bands is beyond the scope of this work, and it is less necessary because the source counts are shallower than the BLAST ones (see Frayer et al. 2009, Béthermin et al. 2010). The SED fitting procedure (described in Chapin et al. 2008) copes with the size of the photometric bands (color correction), and the instrumental plus photometric uncertainties (Truch et al. 2009). Correlations are properly taken into account via a Monte Carlo procedure.

In Figure 2.8, we show the fitted FIR SED for three representa-

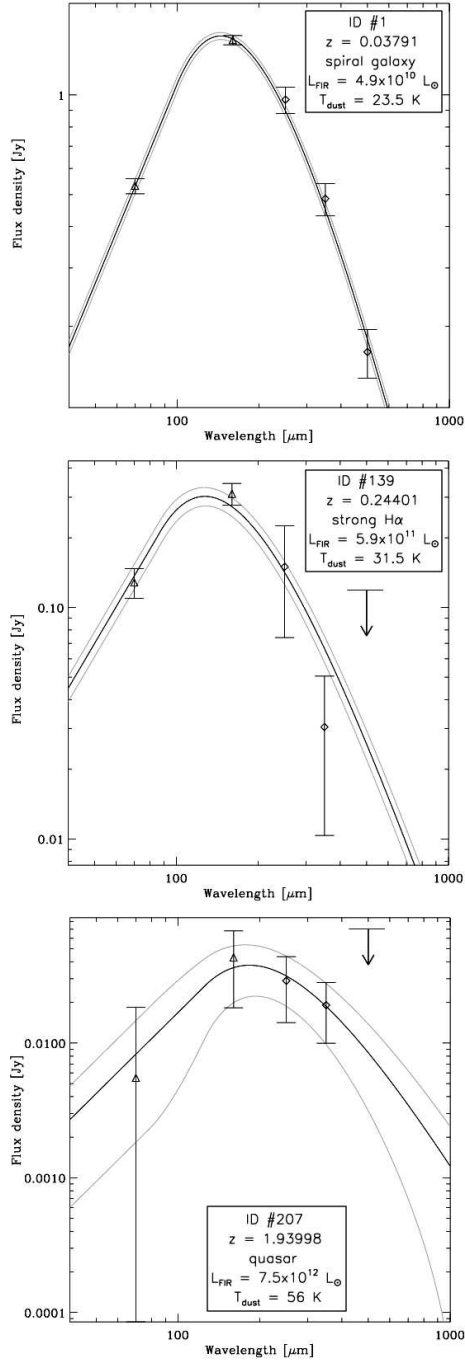


Fig. 2.8 SED fitting of the FIR flux densities for three representative objects in our sample. Points with error bars are from BLAST (deboosted, color-corrected 250, 350, and 500 μm) and MIPS (70 and 160 μm); arrows indicate upper limits (see text). Black solid lines show the best-fit curves, with 68% confidence levels displayed as gray solid lines. The fitting routine accounts for the finite BLAST bandwidths and for the correlated calibration uncertainties. The model template is a modified graybody with an emissivity law $\beta = 1.5$ (Hildebrand 1983) and a power law $\nu^{-\alpha}$ replacing the Wien part of the spectrum ($\alpha = 2$; Blain et al. 2003).

tive objects in our sample: a low-redshift spiral galaxy; a mid-redshift strong $H\alpha$ emitter; and a high- z quasar. The resulting FIR luminosities, listed in Table C2, are the rest-frame SED integral between 8 and $1000\ \mu\text{m}$ (Kennicutt 1998).

In Figure 2.9, we compare our estimates of rest-frame FIR luminosity with those obtained using only MIR flux densities to investigate the level of uncertainty when data are not available in the submm. Following the prescription of Dale & Helou (2002), we calculate the FIR luminosities using only MIPS flux densities (24, 70, and $160\ \mu\text{m}$) for a $z \leq 2$ subset of 93 sources with $24\ \mu\text{m}$ counterpart. There is considerable agreement up to $L_{\text{FIR}} \lesssim 5 \times 10^{11} L_{\odot}$ and $z \lesssim 0.5$. At higher redshifts (and luminosities) we find a poorer concordance; the MIPS-only estimates tend to overestimate the FIR luminosity, by as much as a factor of two in some cases. Other authors (Pope et al. 2006, Papovich et al. 2007, Kriek et al. 2008, Murphy et al. 2009, Muzzin et al. 2010, Elbaz et al. 2010, Nordon et al. 2010) find similar trends; this is expected as the MIPS bands sample the SED peak progressively less and less as redshift increases, thus pulling the SED toward shorter wavelengths, and resulting in a higher L_{FIR} . This emphasizes how essential the BLAST and SPIRE wavebands are to constrain the IR emission peak of star-forming galaxies at high redshift (see also e.g., Schulz et al. 2010, Elbaz et al. 2010).

2.3.3 *FIR star-formation rates*

The FIR luminosities are a sensitive tracer of the young stellar population and, under some reasonable assumption, can be directly related to the star-formation rates (SFRs). This is particularly true for dusty starburst galaxies, because the optically thick dust surrounding star-forming regions is very effective in absorbing the UV photons emitted

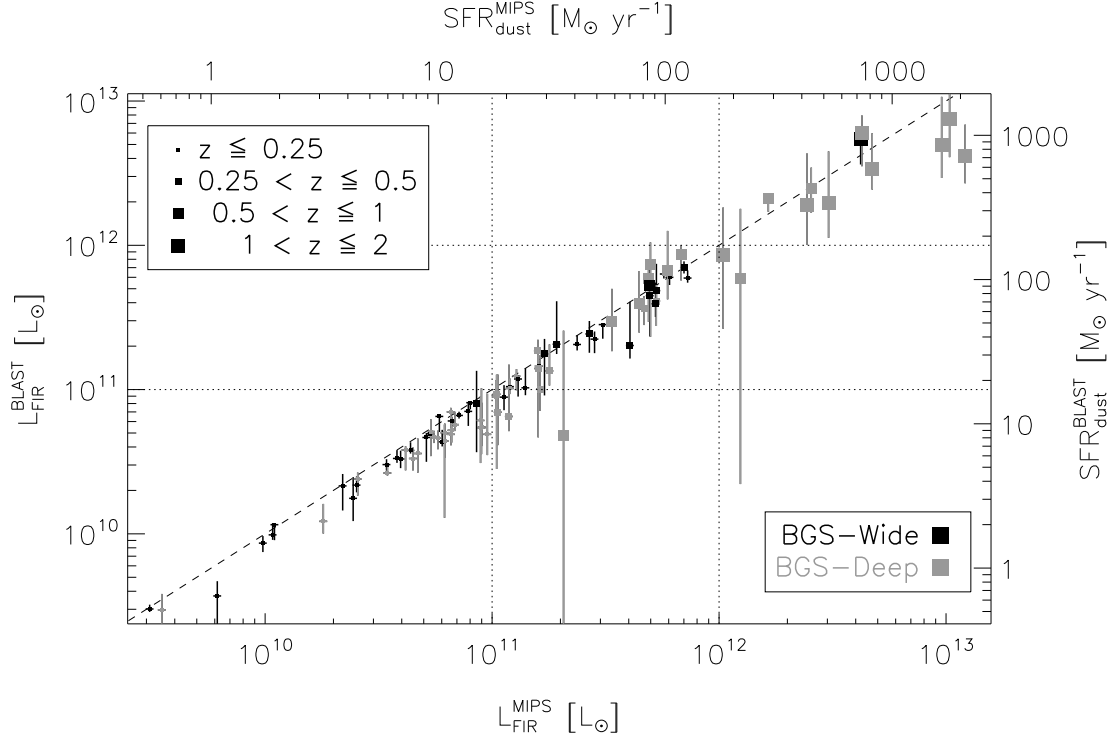


Fig. 2.9 Comparison of estimates of total FIR luminosity for a $z \leq 2$ subset of 93 sources with $24 \mu\text{m}$ counterpart. On the x -axis we used the prescription of Dale & Helou (2002; Equation 4) based on 24 , 70 and $160 \mu\text{m}$ MIPS fluxes; the error bars are set to 4%, which represents the mean discrepancy between their prescription and their model bolometric IR luminosities. On the y -axis we used the FIR luminosity estimates and uncertainties described in Section 2.3.2. Sources lying in the BGS-Wide region are in black and sources in BGS-Deep are in gray. Symbol sizes increase with redshift as shown in the legend. The secondary axes are both calculated using Equation (2.1). The dashed line shows $y = x$, for reference.

by young, massive stars and converting this energy into IR emission.

Under the assumption that the above is the only physical process heating up the dust, Kennicutt (1998) derives the following relation between SFR and bolometric FIR luminosity:

$$\text{SFR}_{\text{dust}} \left[\frac{M_{\odot}}{\text{yr}} \right] = 1.73 \times 10^{-10} \times L_{\text{FIR}} [L_{\odot}]. \quad (2.1)$$

Our sample includes sources with a wide range of FIR luminosities. On one end, the FIR energy output is similar to the one found in

Luminous IR galaxies (LIRGs, $L_{\text{FIR}} > 10^{11} L_{\odot}$), and Ultra Luminous IR galaxies (ULIRGs, $L_{\text{FIR}} > 10^{12} L_{\odot}$). In this type of source, AGN can play an important role in heating up the dust, resulting in a bias in the SFR calculation (an effect discussed further in Section 2.6). At lower FIR luminosities, we have strong additional evidence indicating that most of the galaxies sampled by BLAST are actively star-forming. This is shown in Figure 2.10: available $\text{H}\alpha$ rest-frame equivalent widths (EW_{rf}) are plotted against FIR luminosity for 56 sources at $z \lesssim 0.33$ (see Section 2.2.2). The horizontal dashed line at 4 \AA separates galaxies with ongoing star formation from quiescent ones (Balogh et al. 2004). All sources but one have $\text{H}\alpha$ signature of ongoing star formation. It is highly unlikely that, despite the poor statistics of this plot, we could be missing a population of quiescent objects with $L_{\text{FIR}} \lesssim 10^{10} L_{\odot}$, whose FIR emission is due to a different physical process than the one described above.

Nonetheless, as the FIR luminosity decreases, our sources approach more normal star-forming galaxies. In this type of source a non-negligible contribution to dust heating comes from older stellar populations, which would bias the SFR estimate high (Bell 2003, Hirashita et al. 2003, Iglesias-Páramo et al. 2004, 2006). The reduced optical depth of dust also needs to be taken into account or it would result in a lower estimate of SFR (Inoue 2002). Both these effects are considered in the following discussion (Section 2.5) on the total SFR in our sample.

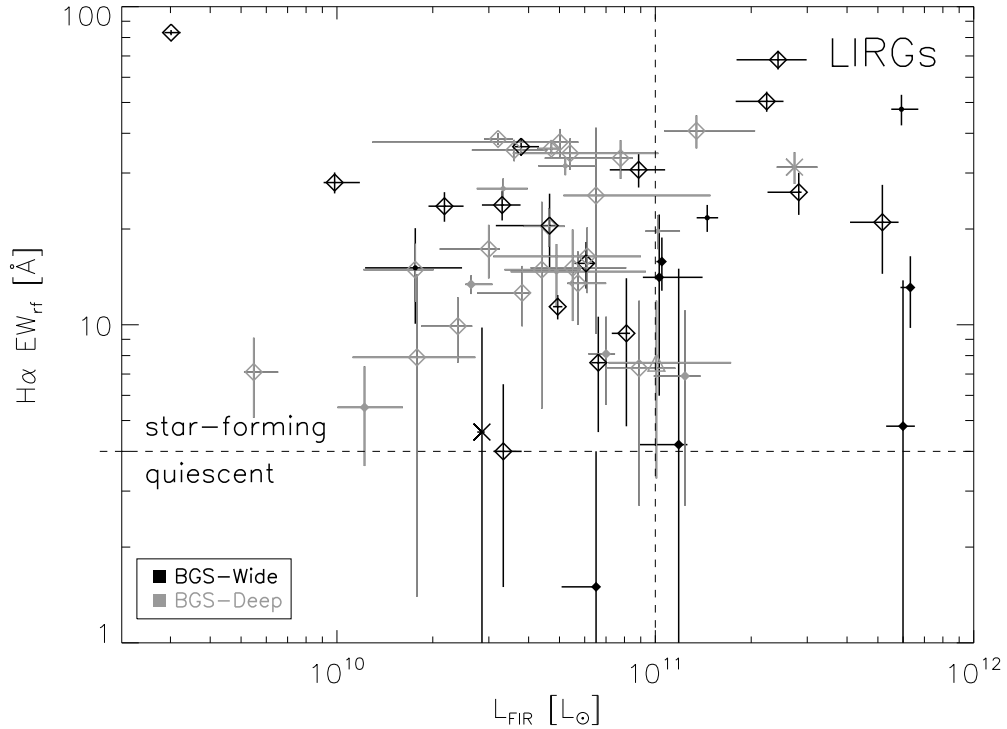


Fig. 2.10 $H\alpha$ rest-frame equivalent widths (EW_{rf}) as a function of the FIR luminosity for the subset of 56 $z \lesssim 0.33$ sources described in Section 2.2.2. Note that we applied a 1 \AA correction to the $H\alpha$ EW_{rf} for underlying stellar absorption (Hopkins et al. 2003). Sources lying in the BGS-Wide region are in black, sources in BGS-Deep are in gray. We also encode here the morphological information discussed in Section 2.7: spiral galaxies are indicated with empty diamonds; compact objects with empty squares; ellipticals with triangles; interacting systems with crosses; Seyfert galaxies with filled diamonds; and objects without morphological classification with filled circles. The horizontal dashed line at 4 \AA separates galaxies with ongoing star formation from quiescent ones (Balogh et al. 2004). Clearly all galaxies in our sample but one are compatible with being actively forming stars.

2.4 UV Luminosities and SFRs

2.4.1 UV fluxes and rest-frame luminosities

The amount of unobscured star formation ongoing in each galaxy of our sample can be estimated in the UV for the BLAST IDs with a *GALEX* counterpart.

The (AB) UV magnitudes are corrected for extinction A_λ due to dust in our Galaxy, and converted into observed flux densities $S_{\nu_{\text{obs}}}$.

Rest-frame UV luminosities are calculated as

$$L_{\text{UV}}^{\text{rf}} = 4\pi S_{\nu_{\text{obs}}} D_{\text{L}}^2(z) \nu_{\text{obs}}, \quad (2.2)$$

where $D_{\text{L}}(z)$ is the luminosity distance.

The extinction coefficients used in the analysis are estimated following the prescription of Wyder et al. (2007), and the color excesses $E(B - V)$ as measured from DIRBE/*IRAS* dust maps (Schlegel et al. 1998) are listed in Table C2.

2.4.2 UV star-formation rates

Star-formation rates in the UV are estimated following the approach of Iglesias-Páramo et al. (2006; and references therein). These are related to rest-frame luminosities in the FUV and NUV by using a synthetic spectrum obtained with *starburst99*¹⁰ (*sb99*; Leitherer et al. 1999) for a star-forming galaxy. In the wavelength range 1000–3000 Å, the shape of the spectrum (shown in Figure 2.11) is very weakly dependent on the underlying stellar populations (e.g., Kennicutt 1998), and has a λ^{-2} slope.

NUV SFRs are estimated using the equation

$$\log \text{SFR}_{\text{NUV}} \left[\frac{M_{\odot}}{\text{yr}} \right] = \log L_{\text{NUV}}^{\text{rf}} [L_{\odot}] - K_{\text{NUV}}(z), \quad (2.3)$$

where $L_{\text{NUV}}^{\text{rf}}$ is the rest-frame luminosity calculated from the observed near-UV magnitude using Equation (2.2). $K_{\text{NUV}}(z)$ is a redshift-dependent numerical factor which incorporates the K-correction, and

¹⁰ Under the same assumptions of Iglesias-Páramo et al. (2006): continuous star formation, recent star-formation timescale $\sim 10^8$ yr, solar metallicity and Salpeter (1955) initial mass function (IMF) from 0.1 to 100 M_{\odot} .

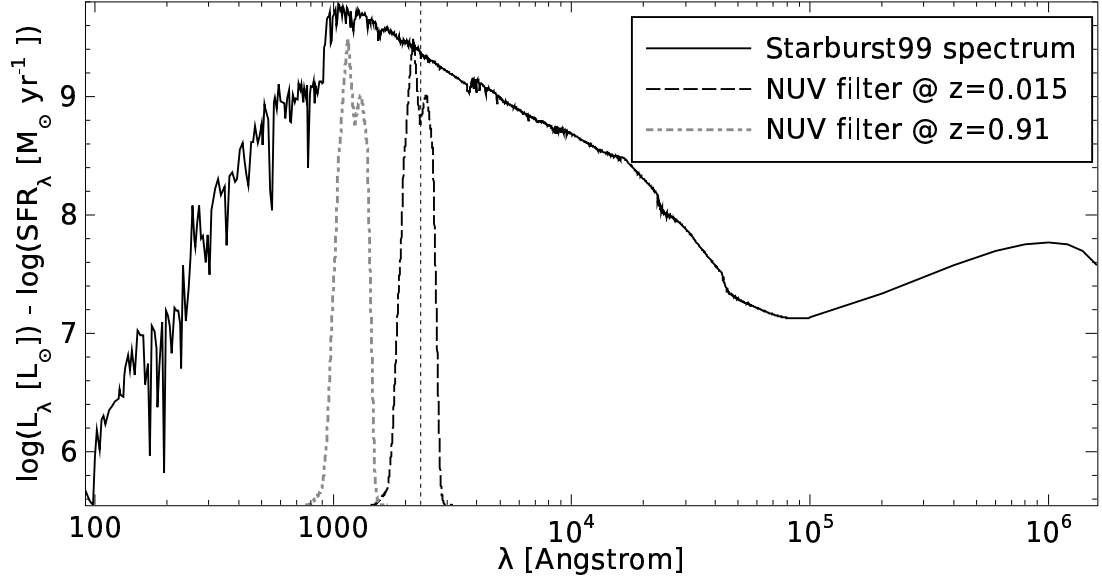


Fig. 2.11 Synthetic spectrum computed with *starburst99* (Leitherer et al. 1999), under the assumptions of solar metallicity and Salpeter (1955) IMF from 0.1 to 100 M_{\odot} . Following Equations (2.3) and (2.4), the K-correction factor for the NUV, $K_{\text{NUV}}(z)$, is computed by averaging the synthetic spectrum over the broad *GALEX* filter profile, also shown (in arbitrary units), blueshifted for reference in the rest frame of the nearest and farthest object in our UV subsample. The same can be done for the FUV filter (not shown here).

is derived from *sb99*, integrating over the *GALEX* filter profile f_{NUV} :

$$K_{\text{NUV}}(z) = \frac{\int (\log L_{\lambda}^{\text{sb99}} [L_{\odot}] - \log \text{SFR}_{\lambda}^{\text{sb99}} [\frac{M_{\odot}}{\text{yr}}]) f_{\text{NUV}} d\lambda^{\text{rf}}}{\int f_{\text{NUV}} d\lambda^{\text{rf}}}. \quad (2.4)$$

SFR_{FUV} and $K_{\text{FUV}}(z)$ are obtained in a totally analogous way. The values of $K_{\text{FUV}}(z = 0)$ and $K_{\text{NUV}}(z = 0)$ are the same as those used by Iglesias-Páramo et al. (2006) at $z = 0$. The photometric errors described in Section 2.2.3 are propagated in the estimate of the uncertainties on the UV SFRs.

A redshift limitation arises when the observed NUV and FUV sample the rest-frame Lyman continuum. This occurs at $z \sim 0.36$ in the FUV, and $z \sim 0.91$ in the NUV. Hereafter we exclude sources beyond these redshift limits, as their inferred SFRs would be unreliable. In order to have a more uniform and sufficiently large sample, in what

follows we only consider the NUV subset, which counts 89 sources (see Figure 2.5 for their redshift distribution). As anticipated, the UV luminosities/SFRs are not corrected for intrinsic dust extinction, and are combined in the following section with FIR luminosities to build an estimator of total SFR that is independent of extinction models.

2.5 *Total SFRs*

We now have two separate estimators for the SFRs in our galaxy sample, SFR_{dust} and SFR_{NUV} . Each of these is expected to have different biases and shortcomings. One can clearly do better at estimating the SFR by combining the two estimators in some way. The best way to do this is not obvious though, since it depends on how each of the estimators is calibrated, on the assumptions that go into them, on the range of galaxy SEDs being studied, and on how these relate to local galaxies that are used for calibration, including radiative transfer effects and other complications. Because of this, we choose to follow a prescription to estimate the total SFR in a galaxy which has already been used by several authors (Bell 2003, Hirashita et al. 2003, Iglesias-Páramo et al. 2006, Buat et al. 2007), so that we can at least compare our results to those of several related studies.

In order to estimate the total SFR (SFR_{tot}) in our sample, we combine the contribution from the obscured star formation with the unobscured star formation:

$$\text{SFR}_{\text{tot}} = \text{SFR}_{\text{NUV}} + (1 - \eta) \times \text{SFR}_{\text{dust}}. \quad (2.5)$$

A correction factor $(1 - \eta)$ is applied to the dust contribution to account for the IR emission from older stellar populations. Following Bell (2003) and Iglesias-Páramo et al. (2006), we use different values

of η depending on whether the object in question is more likely to be a starburst ($\eta \sim 0.09$ for $L_{\text{FIR}} > 10^{11} L_{\odot}$) or a normal star-forming galaxy ($\eta \sim 0.32$ for $L_{\text{FIR}} \leq 10^{11} L_{\odot}$). As anticipated in Section 2.3.3, this method can account for both the contrasting effects that come into play when we try to estimate the total SFR budget for an inhomogeneous sample of objects. Namely, η parameterizes the contribution to dust heating from older stellar populations as a function of the integrated FIR luminosity, whereas the contribution from the UV luminosity guarantees that all the UV photons that manage to escape the galaxy, due to the reduced optical depth of the dust, are actually taken into account.

We briefly recall here that the main selection effects of our sample are, on the one hand, that the rest-frame L_{FIR} increases steadily with redshift (see Figure 2.9 and D09), and on the other hand that the UV luminosity estimates are not reliable beyond $z \sim 0.9$. Moreover, we stress the importance of the blending effects reported in Section 2.3.1, which may lead to misidentifications, particularly in BGS-Deep (sources in gray).

The results of this analysis are shown in Figure 2.12. In the top panel, we plot the ratio of SFR_{NUV} to $(1-\eta)\text{SFR}_{\text{dust}}$ as a function of the FIR luminosity. With the exception of a few outliers,¹¹ there is a clear trend, namely the NUV contribution is more important at low L_{FIR} (low- z), whereas star formation is mainly obscured at $L_{\text{FIR}} \gtrsim 10^{11} L_{\odot}$, $z \gtrsim 0.5$. The same effect is evident in the bottom panel, where we plot SFR_{tot} as a function of redshift. The gray shaded area shows the 1σ confidence interval of a power-law fit $\text{SFR}_{\text{NUV}} \propto z^{1.6}$. Most sources with SFR_{tot} larger than a few $M_{\odot} \text{yr}^{-1}$ have negligible contribution from the UV. This is consistent with what Takeuchi et al. (2010b)

¹¹ In particular, ID#55 could be a misidentification because there is a secondary counterpart, see E09.

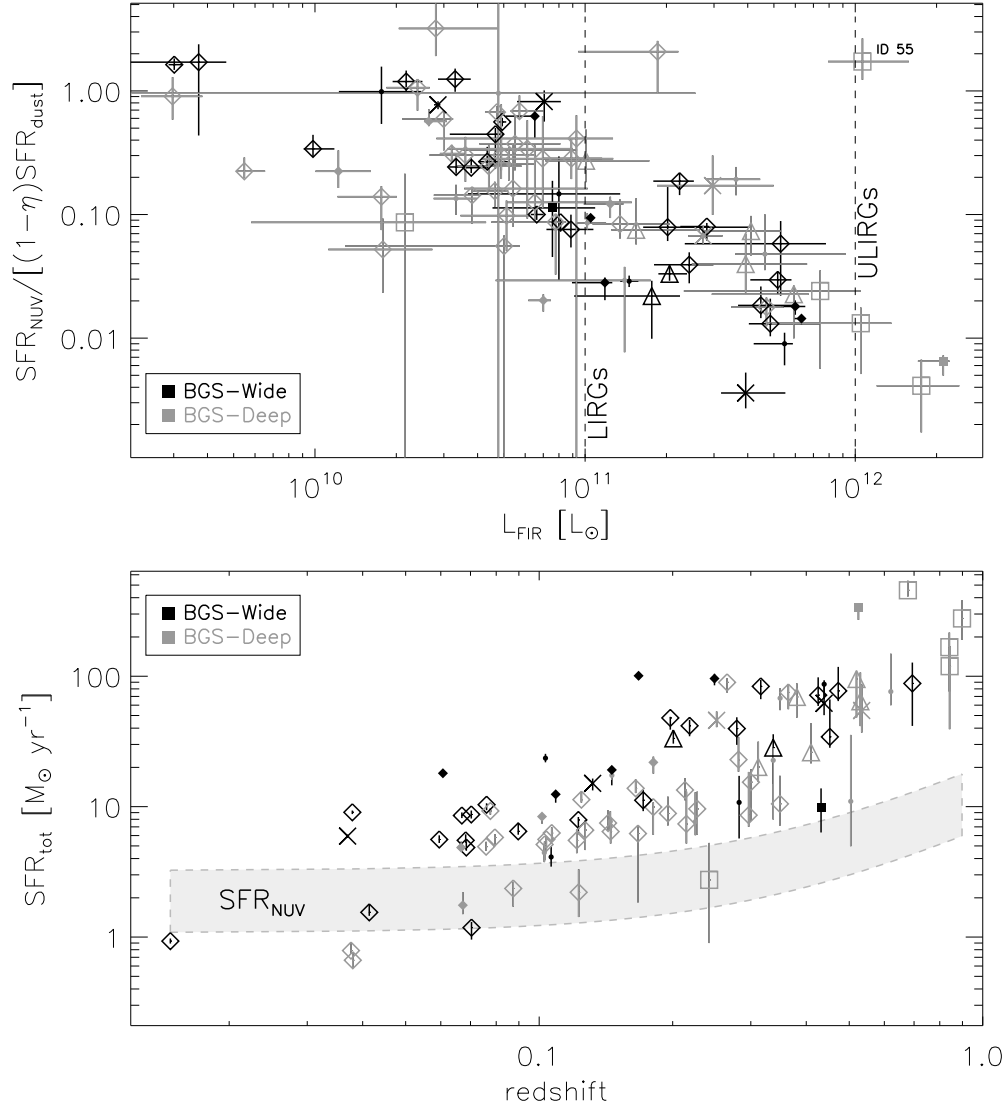


Fig. 2.12 Top panel: ratio of SFR estimated from the NUV only to SFR estimated from dust only, as a function of the FIR luminosity. Note that SFR_{dust} is corrected by a factor $(1 - \eta)$ to account for the IR emission from old stellar populations (see text). Bottom panel: total SFR (SFR_{tot} , see Equation 2.5) as a function of redshift. The gray shaded area shows the 1σ confidence interval of a power-law fit to $\text{SFR}_{\text{NUV}} \propto z^{1.6}$. Symbols are as in Figure 2.10. Filled squares indicate that the source is a quasar (see Section 2.6).

find in the local Universe for an FIR-selected sample: at $\text{SFR}_{\text{tot}} > 20 M_{\odot} \text{ yr}^{-1}$, the fraction of directly visible SFR (SFR_{NUV}) decreases. A very similar trend is also observed at higher redshifts by Buat et al. (2008), with a $24 \mu\text{m}$ -selected sample at $0 \leq z \leq 0.7$ that closely

resembles our sample at those redshifts, in terms of dynamic ranges and FIR-to-UV ratios.

Such a behavior in the individual BLAST IDs can be related to the greater evolution of the total FIR luminosity density with respect to the optical–UV one, as reported for instance by Pascale et al. (2009). On the other hand, we stress that at $L_{\text{FIR}} \lesssim 10^{11} L_{\odot}$, $z \lesssim 0.25$, FIR-only observations would lead to underestimates of the total SFR of at least a factor of two.

By comparing our sample in Figure 2.12 with the *IRAS*/FIR-selected local sample of Iglesias-Páramo et al. (2006), we notice that the overlap is quite modest and limited to $L_{\text{FIR}} \lesssim 10^{10} L_{\odot}$, $z \lesssim 0.1$ sources. We point out that this conclusion should not be diminished by considerations on the extent of the local volume sampled by the BLAST survey.

At the very high luminosity end, only two objects (one of which is flagged as quasar, see Section 2.6) with $z \leq 0.91$ have a UV counterpart. We thus investigate the 30 galaxies with $L_{\text{FIR}} \geq 10^{12} L_{\odot}$ in the full set of BLAST IDs, finding that 16 are flagged as quasars, most of which are optically bright. At $z > 1$, the optical *U* and *g* bands probe the rest-frame UV, and we calculate that these objects would virtually populate the top right corner of the upper panel of Figure 2.12. However, the UV emission from quasars is strongly contaminated by the active nucleus, and cannot be directly associated with recent star formation. Of the remaining 14 ULIRGs with no AGN signatures, only four have optical magnitudes, and would occupy the bottom right corner, indicating severe dust attenuation. We can therefore argue that, even if our subset of objects lacks the abundance of most luminous IR galaxies detected in the SHADES survey (see Coppin et al. 2008, Serjeant et al. 2008), SCUBA-like sources will likely lie in the bot-

tom right corner and beyond, following the same trend of increasing dust attenuation at higher FIR luminosities. This is a first hint that our analysis begins to detect SCUBA galaxies, which are known to overlap considerably with the fainter BLAST galaxy population, following joint studies of LABOCA $870\ \mu\text{m}$ and BLAST data (Dunlop et al. 2010, Chapin et al. 2011). We will discuss this in more detail in Section 2.8.

The $24\ \mu\text{m}$ -selected sample described by Le Floc’h et al. (2005) most resembles our $z \leq 0.9$ sample in terms of $L_{\text{FIR}}-z$ parameter space, although our objects are in general more massive, as we will see in Section 2.8. This, in combination with Figure 2.10, points to the conclusion that the BLAST counterparts detected in this survey at $z \lesssim 1$ are mostly run-of-the-mill star-forming galaxies. Finally, given the steep number counts at the BLAST wavelengths (Patanchon et al. 2009) and the smaller beam sizes of *Herschel*, we expect SPIRE to detect roughly a factor of 10 more sources than BLAST, probing fainter fluxes and therefore higher redshifts. Figure 2.12 suggests that SPIRE will likely fill the $10^{11} \lesssim L_{\text{FIR}} \lesssim 2 \times 10^{12} L_{\odot}$ region (see e.g., Chapin et al. 2011), but probably will not be dominated by SCUBA-like sources.

2.6 AGN Fraction and Quasars

In this section, we describe the AGN and quasar content of our sample and investigate whether the submm emission that we see with BLAST is mainly due to the host galaxy or to the active nucleus.

AGNs are identified using spectroscopic and photometric methods, and the information is listed in Table C1. Of the 82 sources in our sample with optical spectra, 56 have a measurement of the line ratio

$[\text{N II}]/\text{H}\alpha$; 14 of these have $[\text{N II}]/\text{H}\alpha \gtrsim 0.6$, and we flag them as AGNs (Kauffmann et al. 2003, Miller et al. 2003; and references therein). Broad emission lines, such as $\text{C III}] 190.9$ and $\text{C IV } 154.9$, which appear in the accessible waveband at $z > 1$, are used to identify five additional sources as quasars. A search on NED yields that 10 more sources in our sample are classified as AGNs by other authors.

Active galaxies can also be identified using a number of photometric empirical methods. Quasars occupy a distinct region in the IRAC color space by virtue of their strong, red continua in the MIR (Lacy et al. 2004). IRAC fluxes are available for 205 sources, and we use the three color–color cut prescriptions of Hatziminaoglou et al. (2005), Stern et al. (2005), and Marsden et al. (2009). Optical magnitudes and postage-stamp images are also available for 114 sources, along with radio fluxes for 107 sources from D09. A source is considered a quasar when it is compact¹² and satisfies the three aforementioned color–color cut prescriptions. If only two color–color cuts prescriptions are satisfied, we also require the source to be either radio-loud ($L_{1.4\text{GHz}} \gtrsim 10^{39}$ W), optically bright ($L_{U/g} \gtrsim 10^{11} L_{\odot}$), or one of the 10 NED AGNs.

Using these empirical methods, we find 24 quasars plus 10 additional sources showing weaker yet significant quasar activity, when the above conditions are near the threshold. The five quasars identified spectroscopically are all contained in this photometric list. Of the 14 spectroscopically identified AGNs, 10 are definitely not compact, but rather spiral in shape (see the following section on morphology), and mostly radio-quiet. We believe that these objects are Seyfert galaxies (e.g., Cid Fernandes et al. 2010).

In conclusion, we have assessed that about 15% of the galaxies in

¹² By “compact” we mean objects unresolved in the optical and MIR, with linear sizes $\lesssim 3$ kpc at $z \gtrsim 1$.

our sample show strong indication of having an active nucleus and an additional 6% have weaker yet significant evidence. Chapin et al. (2011) found a comparable proportion¹³ of sources with excess radio and/or MIR that can be interpreted as an AGN signature. Several recent observations find close association of AGN activity and young star formation (Silverman et al. 2009), consistent with a scenario in which the FIR/submm emission is mainly due to star formation ongoing in the host galaxy, rather than to emission from a dusty torus obscuring the inner regions of the active nucleus (Wiebe et al. 2009, Coppin et al. 2010, Muzzin et al. 2010, Hatziminaoglou et al. 2010, Shao et al. 2010, Elbaz et al. 2010). In addition, our AGN selection criteria, which use optical and MIR data, tend to favor type-1 AGNs, i.e., unobscured Seyfert galaxies and quasars. This is definitely the case for the IRAC color–color selection methods, as reported by Hatziminaoglou et al. (2005) and Stern et al. (2005), but it is also corroborated by the fact that most of the quasars we identify are optically bright. We aim to address this issue in greater detail in a future paper.

2.7 *Morphology*

We assign a broad morphological classification to 137 (60%) of the BLAST IDs presented in this work, based upon visual inspection of UV, optical and MIR postage-stamp images (see Section 2.2.5) centered at $[\alpha_{\text{BLAST}}, \delta_{\text{BLAST}}]$. A selection of cutouts is shown in Figure B1.

In addition to the visual examination of the multi-wavelength images, we corroborated our choice with ancillary information (when available), such as: (1) location on the color–magnitude diagram, typically $(U - r)$ versus M_r ; (2) spectral features; (3) UV detection; (4) FIR luminosity. Our findings are listed in the “morphology” column

¹³ Only sources with a redshift estimate.

Table 2.2. Broad Morphological Classification of BLAST IDs

| Type | Sub-type | Number | Frequency |
|--------------------|--------------|--------|-----------|
| Spiral | | 69 | 50% |
| | Seyfert | 8 | 6% |
| Compact | | 52 | 38% |
| | Quasar | 31 | 23% |
| | Blue compact | 5 | 4% |
| | Red compact | 3 | 2% |
| Elliptical | | 8 | 6% |
| Interacting system | | 7 | 5% |
| Irregular | | 1 | < 1% |

Note. — Morphological classification available for 137 out of 227 BLAST IDs (60%), based upon visual inspection of UV, optical and mid-IR (MIR) postage-stamp images (see Section 2.2.5). By “compact” here we mean objects unresolved in the optical and MIR, with linear sizes $\lesssim 3$ kpc. By “interacting system” we mean a visually obvious physical association of two or more objects.

in Table C1 and summarized in Table 2.2.

At low redshift, we find predominantly spirals, whereas most of the BLAST sources identified at high redshift are compact and show AGN signatures. This is probably a selection bias, as the fraction of submm sources identified at other wavelengths is known to gradually decrease with z (see D09), and the most distant sources are often identified only thanks to their extreme radio and/or optical emission, due to the AGN. In fact, the study by Dunlop et al. (2010) shows that a deep survey at $250 \mu\text{m}$ not only reveals low- z spirals, but also extreme dust-enshrouded starburst galaxies at $z \sim 2$. The latter tend to be missed in our selection, because they are typically extremely faint in the optical/UV, unless they also host an AGN.

We point out here that this broad morphological scheme should not be regarded as meaningful on a source-by-source basis, but rather be considered as guidance for interpreting the other results of this work. For this purpose, we encoded the morphological information in Figures 2.10, 2.12, 2.13, 2.14, and 2.15.

2.8 Stellar Masses

Stellar masses (M_*) are computed by Dye et al. (2010b) for a subset of 92 sources in our sample with counterparts in a minimum of five bands, from the optical to NIR. The distribution has median of $10^{10.9} M_\odot$, and interquartile range of $10^{10.6}$ – $10^{11.2} M_\odot$.

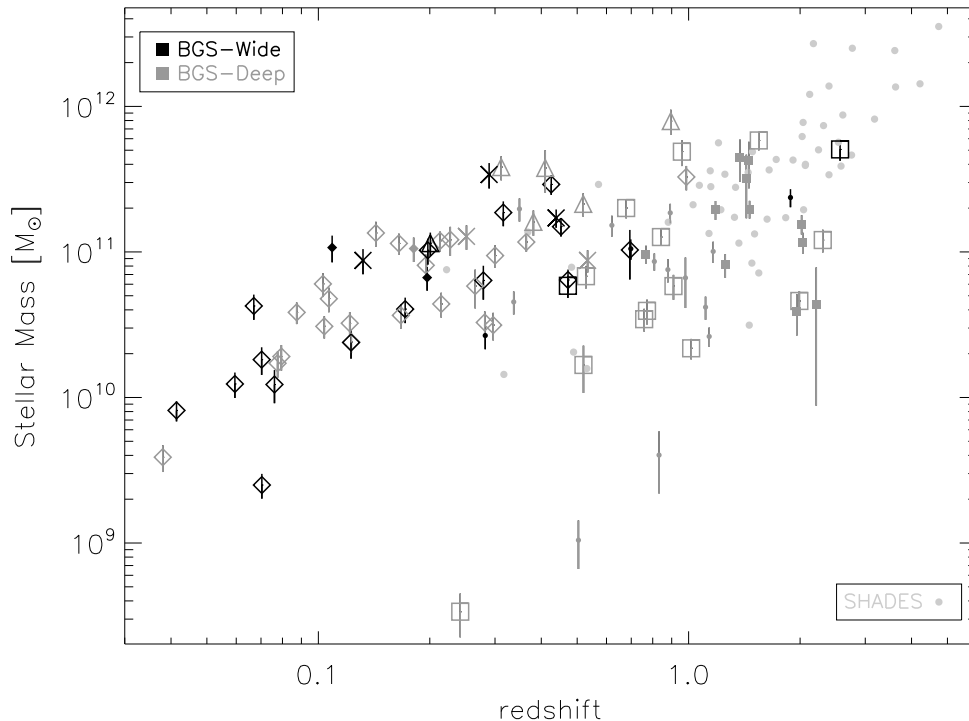


Fig. 2.13 Stellar mass as a function of redshift for the whole subset of 92 sources described in Section 2.8. Symbols are as in Figure 2.10. Filled squares indicate that the source is a quasar. We overplot SHADES sources (Dye et al. 2008) as light gray filled circles.

These stellar masses are plotted versus redshift in Figure 2.13; we

also show for comparison the stellar masses of SCUBA sources in SHADES, computed by Dye et al. (2008) using a methodology and photometry almost identical to ours.

Except for three outliers (that may well be misidentifications as they all lie in BGS-Deep), the monotonic trend of increasing stellar masses is the result of multiple selection effects; sources at a given redshift are not detected with arbitrarily low, or arbitrarily high stellar masses. As we discuss later in this section, there is an approximately constant relation between L_{FIR} and stellar masses in our sample. Low-luminosity sources (with low stellar masses) are excluded at a given redshift because of sensitivity. On the other hand, sources with L_{FIR} (and stellar masses) above a certain threshold are excluded from our sample despite the well-documented strongly evolving FIR luminosity function (E09, Dye et al. 2010a, Eales et al. 2010b); our present study simply does not go deep enough to start detecting the bulk of high- z (and higher volume density) K-corrected sources. In particular, sources with $M_{\star} \gtrsim 10^{12} M_{\odot}$, which are present in the SHADES sample, are absent from ours. Indeed, these very massive sources are not detected among $24 \mu\text{m}$ -selected samples, down to a flux density level of $\sim 20 \mu\text{Jy}$ (GOODS survey; see e.g., Le Floch et al. 2005, Pérez-González et al. 2005, Caputi et al. 2006, Elbaz et al. 2007, Santini et al. 2009)¹⁴. The $24 \mu\text{m}$ catalog used by D09 to find counterparts to the BLAST sources goes down to the same depth; therefore, we are only left with the radio catalogs. It is indeed possible that our analysis is missing very massive galaxies that, though having a radio ID, do not have an estimate of

¹⁴ All the authors cited above adopt a Salpeter (1955) IMF. Caputi et al. (2006), Santini et al. (2009), and Dye et al. (2008, 2010b) estimate the stellar masses by means of an optical-to-NIR SED fit of each galaxy at the determined redshift. Le Floch et al. (2005) and Pérez-González et al. (2005) simply convert, respectively, V - and K -band luminosities into stellar masses. Finally, Elbaz et al. (2007) compute stellar masses by modeling the stellar populations of each galaxy using stellar absorption-line indices.

stellar mass because measurements are not available in a minimum of 5 optical/NIR bands. An accurate account of the selection effects at work for $M_{\star} \gtrsim 10^{12} M_{\odot}$, which is beyond the scope of this work, would not invalidate the results of the rest of this chapter.

Our subsample is composed of relatively massive objects, with a significant fraction of sources (45%) with stellar masses greater than $10^{11} M_{\odot}$. This fraction soars to 84% in the SHADES survey, whereas the majority of sources detected at $24 \mu\text{m}$ in deep surveys of the CDFS (down to a flux density level of $\sim 20 \mu\text{Jy}$) have $M_{\star} \leq 10^{11} M_{\odot}$ (e.g., Le Floc'h et al. 2005, Pérez-González et al. 2005, Caputi et al. 2006, Elbaz et al. 2007, Santini et al. 2009). However, a direct comparison of the detection rates of massive galaxies among these surveys is very difficult because of the dissimilar comoving volumes probed; in fact, BLAST samples a volume roughly 14 (57) times larger than SHADES (GOODS)¹⁵. Furthermore, it would be necessary to quantify the numerous selection effects and the different shape of the stellar mass function at the wavelengths in question.

Nevertheless, BLAST observes a significant number of large, massive and actively star-forming galaxies (typically spirals, see Section 2.7), which qualitatively appear to link the $24 \mu\text{m}$ and SCUBA populations at $0 < z < 2$. With the deep $24 \mu\text{m}$ GOODS survey, other authors seem to be already detecting this linking population (in particular Caputi et al. 2006 and Elbaz et al. 2007), but their most massive sources at $0 < z < 1$ all have long ($\geq 4 \text{ Gyr}$) star-formation timescales (defined as the ratio of already assembled stellar mass over the recent SFR, see later in this section), indicating prolonged star formation histories. In contrast, about 60% of our galaxies in the same $M_{\star}-z$ range

¹⁵ Based on the following redshift depth and sky area covered by, respectively, the GOODS survey, the SHADES survey and the present BLAST study: $\sim 140 \text{ arcmin}^2$ out to $z \sim 3$; $\sim 320 \text{ arcmin}^2$ out to $z \sim 5$; and $\sim 4.15 \text{ deg}^2$ out to $z \sim 2$.

have star-formation timescales shorter than 4 Gyr, consistent with the findings that submm-selected $M_{\star} \gtrsim 10^{11} M_{\odot}$ systems at $z \geq 0.5$ form their stellar mass predominantly at late and at early times, but less so when the galaxies are middle-aged (Dye et al. 2010b, 2008). These figures indicate that the moderately massive population detected at $0 < z < 1$ by BLAST is more actively forming stars than the equally massive $24 \mu\text{m}$ -selected galaxies in the same redshift range. One might wonder whether this observation arises just as a consequence of a selection effect in the shallower BLAST sample; although our data do not allow us to investigate the stellar masses of fainter BLAST galaxies, a thorough examination of the M_{\star} distribution at $0 < z < 1$ in the GOODS survey (e.g., Figure 7 of Caputi et al. 2006) does not suggest that the exclusion of the fainter $24 \mu\text{m}$ sources (below e.g., $83 \mu\text{Jy}$, the 80% completeness limit in the CDFS) would dramatically alter the proportions of galaxies with stellar mass above and below $10^{11} M_{\odot}$. It is certainly possible that a cut at a brighter $24 \mu\text{m}$ flux density would bias high the detection rate of massive galaxies; however, the massive BLAST galaxies at $z \leq 1$ have a median SFR of $\sim 70 M_{\odot} \text{ yr}^{-1}$ that equals the maximum SFR among the likewise massive and aged galaxies in GOODS. This would still be true if the $24 \mu\text{m}$ sample were shallower.

Moreover, Figure 2.13 exhibits, in the range $1 < z < 2$, a substantial overlap between BLAST and SCUBA sources. Therefore, assuming that the BGS is a representative field, our data suggest that the BLAST galaxies seem to connect the $24 \mu\text{m}$ and SCUBA populations, in terms of both stellar mass and star-formation activity. Figures 2.14 and 2.15 further corroborate this conclusion. It is worth reminding the reader that the M_{\star} estimates are based on the optical/NIR fluxes of BLAST IDs and do not employ any BLAST-specific photometric

data.

Figure 2.14 plots stellar masses (top panel) and SSFR_{tot} (bottom panel) versus L_{FIR} for the subset of 55 sources at $z \leq 0.9$ that have an estimate of both these quantities. There are 37 additional sources in our catalog with $L_{\text{FIR}} \gtrsim 10^{11} L_{\odot}$ and stellar mass estimates, but no reliable SFR_{NUV} . These are included in Figure 2.14, because in this case $\text{SFR}_{\text{tot}} \simeq (1 - \eta) \text{SFR}_{\text{dust}}$ (see Section 2.5). SHADES sources are also shown in this figure. S. Dye (2010, private communication) estimates their FIR luminosities using a two-component SED fit from Dunne & Eales (2001) that has cold/hot ratio of 186, with $T_{\text{hot}} = 44 \text{ K}$ and $T_{\text{cold}} = 20 \text{ K}$. SFRs are estimated using Equation (2.1) and corrected by $(1 - \eta)$. Finally, star-formation timescales, defined as $\tau_{\text{SF}} = \text{SSFR}^{-1}$, are shown as the secondary y -axis.

BLAST IDs selected in BGS-Wide show a positive correlation between their stellar masses and L_{FIR} , but there is no strong evidence for a correlation between SSFR_{tot} and FIR luminosities. Although BLAST IDs selected in BGS-Deep appear to have different trends, one should be cautious as they are, in general, less reliable than the IDs in BGS-Wide. However, BGS-Deep sources can be used to study bulk properties under appropriate caveats. The emerging picture appears to confirm Figure 2.13, in which there is a non-negligible overlap between the BLAST and SCUBA populations in the range $1 < z < 2$. In particular, the high luminosity tail of the BLAST sample appears to encroach on the SHADES sources in terms of both L_{FIR} and M_{\star} , bridging the gap with the lower-redshift Universe populated by $24 \mu\text{m}$ sources and by run-of-the-mill star-forming BLAST galaxies, with τ_{SF} spanning the interval 1–10 Gyr. A considerable overlap between fainter BLAST sources and $870 \mu\text{m}$ -selected galaxies has already been established by Dunlop et al. (2010) and Chapin et al. (2011), but

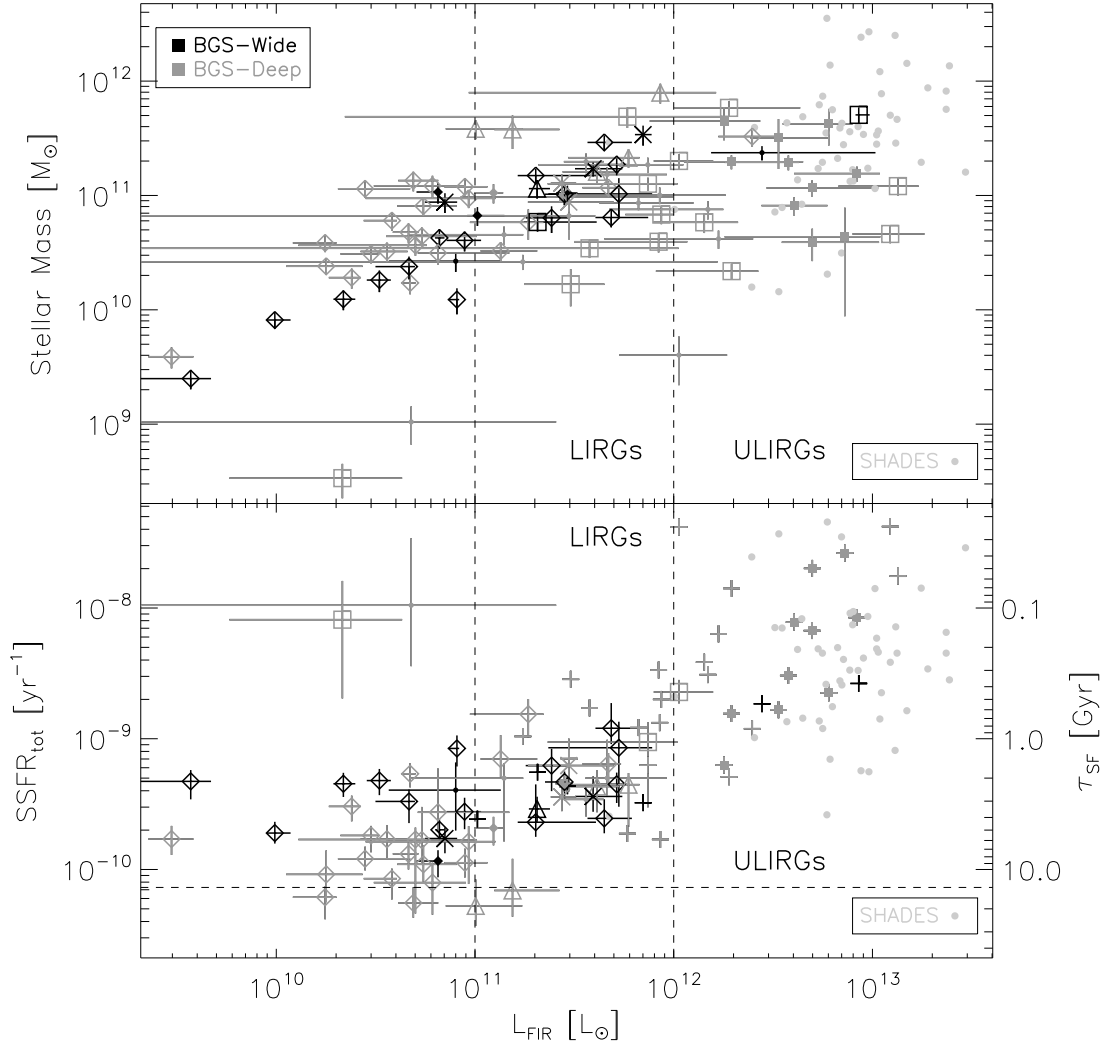


Fig. 2.14 Top panel: stellar mass as a function of FIR luminosity for the whole subset of 92 sources described in Section 2.8. Bottom panel: specific total SFR (SSFR_{tot}) as a function of FIR luminosity for the subset of 55 sources at $z \leq 0.9$ that have an estimate of SFR_{tot} . Symbols are as in Figure 2.10. For the remaining 37 sources, we assume $\text{SFR}_{\text{tot}} = (1 - \eta) \text{SFR}_{\text{dust}}$ as they all have $L_{\text{FIR}} \gtrsim 10^{11} L_{\odot}$; these are shown as crosses without error bars. The right-hand ordinate shows the corresponding star-formation timescales, defined as $\tau_{\text{SF}} = \text{SSFR}^{-1}$. Filled squares indicate that the source is a quasar. The horizontal dashed line shows the inverse of the age of the Universe. We overplot in both panels SHADES sources (Dye et al. 2008) as light gray filled circles.

it is important to have confirmed an additional, less direct, connection with our shallower BLAST sample, by means of a comparable analysis to that of SHADES.

We investigate if a temporal connection between the two populations is allowed by the data, in a scenario where the BLAST sources are SCUBA sources fading at the end of their late star-formation burst (Borys et al. 2005, Dye et al. 2008). However, Dye et al. (2010b) seem to rule out this possibility, because the higher- z , more massive BLAST IDs are observed during a star-formation burst lasting too briefly in redshift to allow this connection. This disconnection is consistent with the phenomenon of downsizing observed in optically-selected samples of galaxies (e.g., Heavens et al. 2004).

The approximately flat trend between SSFR_{tot} with FIR luminosity of Figure 2.14 evidenced by the BLAST IDs selected in BGS-Wide is consistent with Serjeant et al. (2008). The inclusion of BGS-Deep sources at high FIR luminosities seems to suggest a different, mild trend of increasing SSFR_{tot} , also reported by Santini et al. (2009) and Rodighiero et al. (2010). The data available to us do not manifest enough evidence to support either scenario. Larger samples now accessible with *Herschel* will shed more light on the evolution of the specific SFR.

In Figure 2.15, we plot SSFR_{tot} versus stellar mass, for BLAST and SHADES sources. The dotted isolines correspond to constant SFRs, under the assumption that M_* is the galaxy's total stellar mass. We do not find any clear correlation between specific total SFR and stellar mass, which is not surprising as we are sampling a population of young, active, star-forming galaxies (see also Santini et al. 2009). Expectedly, the bulk of SHADES sources occupies a well-defined region of the plane, around the isoline of $\text{SFR} = 1000 M_{\odot} \text{yr}^{-1}$, whereas practically

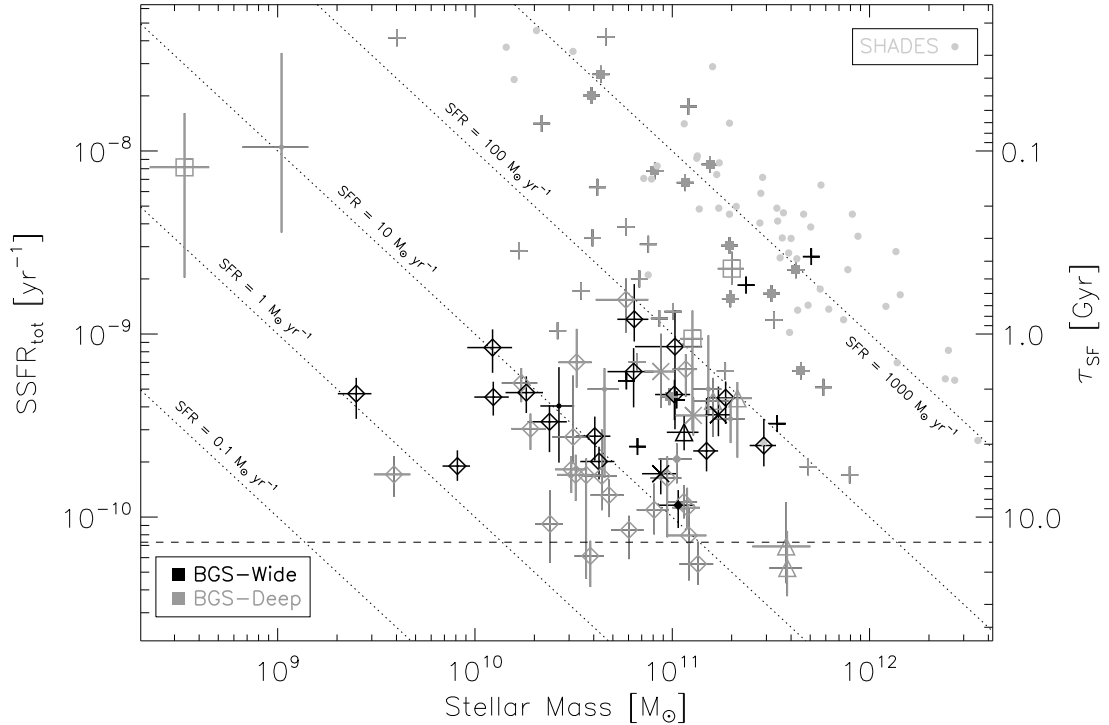


Fig. 2.15 Specific total SFR (SSFR_{tot}) as a function of stellar mass for the subset of 55 sources at $z \leq 0.9$ that have an estimate of SFR_{tot} . Symbols are as in Figure 2.10. For the remaining 37 sources, we assume $\text{SFR}_{\text{tot}} = (1 - \eta) \text{SFR}_{\text{dust}}$ as they all have $L_{\text{FIR}} \gtrsim 10^{11} L_{\odot}$; these are shown as crosses without error bars. The right-hand ordinate shows the corresponding star-formation timescales, defined as $\tau_{\text{SF}} = \text{SSFR}^{-1}$. Dotted isolines correspond to constant SFRs, under the assumption that M_{\star} is the galaxy’s total stellar mass. The horizontal dashed line shows the inverse of the age of the Universe. We overplot SHADES sources (Dye et al. 2008) as light gray filled circles.

all the BLAST counterparts at $z \leq 0.9$ lie below the isoline of $\text{SFR} = 100 M_{\odot} \text{yr}^{-1}$. The gap is again filled by the BLAST IDs at higher redshift.

We can compare our results in Figure 2.15 with Buat et al. (2008), who derive mean relationships between observed SSFR and stellar mass at $z = 0$ and $z = 0.7$, and confront these with models based on a progressive infall of gas into the galactic disk, starting at high z . Both their data and models exhibit a flat distribution of SSFR for galaxies with masses between 10^{10} and $10^{11} M_{\odot}$. Our $z \leq 0.9$ subset of

star-forming galaxies shares a similar behavior, as well as the dynamic ranges. On the other hand, we can also compare the high- z tail of the BLAST IDs with the $z > 0.85$ sample of Rodighiero et al. (2010): although the scatter is quite large in both subsets, we observe the same negative trend of SSFR with M_* , again consistent with downsizing.

The in-depth analysis of the bright BLAST counterparts reveals a population with an intrinsic dichotomy in terms of SFR, stellar mass, and morphology. The bulk of BLAST counterparts at $z \lesssim 1$ appears to be run-of-the-mill star-forming spiral galaxies, with intermediate stellar masses (median $M_* \sim 7 \times 10^{10} M_\odot$) and approximately constant specific SFR (τ_{SF} in the range 1–10 Gyr); in addition, they form stars more actively than the equally massive and aged $24 \mu\text{m}$ sources. On the other hand, the high- z BLAST counterparts significantly overlap with the SCUBA population, and the observed trends of SSFR, albeit inconclusive, suggest stronger evolution and downsizing. In conclusion, our study suggests that the BLAST galaxies may act as linking population between the star-forming $24 \mu\text{m}$ sources and the more extreme SCUBA starbursts.

2.9 *Concluding Remarks*

We have carried out a panchromatic study of individual bright BLAST galaxies identified at other wavelengths, extending the analysis of previous BLAST works. Our basic results are as follows.

1. The flux densities of BLAST sources are boosted due to a combination of Eddington bias, source confusion and blending. We have developed a Monte Carlo method to quantify these biases, both in confusion-limited maps and in maps dominated by instrumental noise. The boosting effects are more pronounced in

the confusion-limited regime, and become more important as the wavelength increases. In addition, flux densities are heavily correlated among the BLAST bands, again more prominently in BGS-Deep. We have accounted for all these effects coherently while calculating the FIR luminosities of BLAST galaxies. We have also shown how crucial the BLAST/SPIRE photometry is to estimate without bias the FIR luminosity of a galaxy, especially at high redshift.

2. We have measured that star formation is predominantly obscured at $L_{\text{FIR}} \gtrsim 10^{11} L_{\odot}$, $z \gtrsim 0.5$. On the other hand, unobscured star formation is important at $L_{\text{FIR}} \lesssim 10^{11} L_{\odot}$, $z \lesssim 0.25$ and FIR-only evaluations of SFR would lead to underestimates up to a factor of two. This is probably a direct consequence of the well documented stronger evolution of the FIR luminosity density with respect to the optical–UV one.
3. We have compared, in terms of $L_{\text{FIR}}-z$ parameter space, the BLAST counterparts to the *IRAS*/FIR-selected sample of local galaxies, to the $24\ \mu\text{m}$ -selected sample observed by *Spitzer*, and to the SCUBA $850\ \mu\text{m}$ -selected sample. The overlap with the local *IRAS* sample is minimal and this conclusion should not be belittled by the extent of local volume surveyed by BLAST. Similarly, our sample lacks the abundance of most luminous IR galaxies detected in the SHADES survey, but the high- L_{FIR} , high- z tail of the BLAST counterparts seems to overlap with the SCUBA population. The $24\ \mu\text{m}$ -selected sample most resembles the bulk of BLAST IDs in terms of L_{FIR} and redshift distribution.
4. We have assessed that 15% of the galaxies in our sample show strong indication of an active nucleus and an additional 6% have weaker yet significant evidence. In particular, these are pre-

dominantly type-1 AGNs, i.e., unobscured Seyfert galaxies and quasars. The AGN fraction and the SFRs inferred for these objects are comparable to recent observations at similar wavelengths and point to a scenario in which the submillimeter emission detected by BLAST is mainly due to star formation ongoing in the host galaxy, rather than to emission from a dusty torus obscuring the inner regions of the active nucleus.

5. We have computed stellar masses for a subset of 92 BLAST counterparts. These appear to be relatively massive objects, with a median mass of $10^{10.9} M_{\odot}$, and an interquartile range of $10^{10.6}$ – $10^{11.2} M_{\odot}$. In particular, a significant fraction of them fill the region of $M_{\star} \sim 10^{11} M_{\odot}$ at $z \lesssim 1$ that is practically vacant in the SCUBA surveys, and sparsely populated by $24 \mu\text{m}$ -selected samples. Although the dissimilar volumes sampled by these surveys discourage a direct comparison of the detection rates of massive galaxies, our study suggests that the BLAST counterparts seem to link the $24 \mu\text{m}$ and SCUBA populations, in terms of both stellar mass and star-formation activity.
6. We have highlighted a dichotomy in the BLAST population in terms of star-formation rate, stellar mass and morphology. The bulk of BLAST counterparts at $z \lesssim 1$ comprises run-of-the-mill star-forming galaxies, typically spiral in shape, with intermediate stellar masses and nearly constant specific SFR. On the other hand, the higher redshift BLAST counterparts significantly overlap with the SCUBA population, and the observed trends of SSFR, albeit inconclusive, suggest stronger evolution. Other BLAST studies have already described the significant overlap existing between fainter BLAST sources and $870 \mu\text{m}$ -selected galaxies, but here we have established an additional link with a shal-

- lower BLAST sample, via an analysis equivalent to that of SHADES.
7. We rule out a temporal connection between the BLAST and SCUBA populations, in a scenario where BLAST sources would correspond to SCUBA galaxies whose burst of star formation is ceasing. This disconnection is consistent with the downsizing observed in optical samples.

The findings described in this work represent a taste of what should be possible with a significantly larger sample of sources. The increased sensitivity and resolution of the *Herschel Space Observatory*, which recently started operation, will soon provide vastly increased numbers of sources. This will enable significantly reduced uncertainties and therefore much improved constraints on models of galaxy evolution and formation. Nevertheless, the BLAST data have provided a very valuable benchmark for the *Herschel* data and the various analyses that will emerge for some time to come. Furthermore, the results in this work probably will not immediately become obsolete, as even the much more sensitive SPIRE surveys will have to face the lack of deeper ancillary data, especially in the optical/NIR and in the radio. Identifying the precise location of the submm sources will require either deep and very wide-area VLA data, or a combination of MIPS 24 μm and PACS, or ultimately ALMA and the *Space Infra-Red Telescope for Cosmology and Astrophysics* (SPICA; Swinyard & Nakagawa 2009). Finally, in order to study the rest-frame optical/NIR of the $z > 2$ submm galaxies in much more detail than BLAST or SCUBA, future studies will really require instruments like the Wide Field Camera 3 (WFC3; Kimble et al. 2008) or the *James Webb Space Telescope* (JWST; Gardner et al. 2006).

3. MEASURING STAR FORMATION IN MASSIVE HIGH- z GALAXIES

3.1 *Introduction*

The observed structural properties of massive galaxies ($M_{\star} \gtrsim 10^{11} M_{\odot}$) at high redshift ($z \gtrsim 1$) are difficult to reconcile with those of galaxies that populate the local Universe. Most strikingly, they are much more compact in size than local galaxies of similar mass (Daddi et al. 2005, Trujillo et al. 2006). For the spheroid-like galaxy population, the size evolution has been particularly dramatic (a factor of 4–5 since $z \sim 2$, see e.g., Trujillo et al. 2007, Buitrago et al. 2008, Damjanov et al. 2009), with subsequent observations confirming these findings (e.g., Muzzin et al. 2009, Trujillo et al. 2011). Only a tiny fraction of massive galaxies in the local Universe have sizes comparable to those found at high redshift (Trujillo et al. 2009). The absence of similar mass counterparts in the local Universe (Trujillo et al. 2009) implies that some mechanism is acting on those high-redshift galaxies to make them grow in size (Hopkins et al. 2009, Bezanson et al. 2009).

In order to understand the mechanism responsible for this galaxy growth, a crucial point that needs to be addressed is the level of star formation (or star-formation rate [SFR]) in this population. From an observational point of view, evidence for star formation in massive galaxies at high redshift is unclear, especially for the spheroid-like population. For example, small samples of high-quality spectroscopy (Kriek et al. 2006, 2009a) find little or no star formation in this pop-

ulation; whereas, about 50% of these galaxies appear to have $24\ \mu\text{m}$ counterparts (Pérez-González et al. 2008), indicating an elevated level of star formation. This discrepancy may be due to biases inherent to their respective SFR estimators, which are either susceptible to errors in extinction correction and require deep spectroscopic observations, or probe emission from polycyclic aromatic hydrocarbons (PAHs), and thus provide a poor constraint on the thermal spectral energy distribution (SED).

An alternative probe of star formation is to observe in the far-infrared/submillimeter bands (FIR/submm), where emission is primarily from heated dust. It is known that in the local Universe the dust luminosity in star-forming regions is correlated with SFR (e.g., Kennicutt 1998, Chary & Elbaz 2001, Buat et al. 2007), with the most actively star-forming galaxies often the most dust obscured or even optically thick in the optical/UV (Genzel et al. 1998). Therefore, it is reasonable to expect that if high-redshift, compact, massive galaxies are vigorously forming stars, then they should be observable in the rest-frame FIR/submm.

However, due to the large beams of current submm telescopes, source confusion and flux boosting present significant obstacles to studying the star formation properties of anything other than the most luminous galaxies at high redshift (see Chapter 2). For example, the $1\ \sigma$ noise limit in the $250\ \mu\text{m}$ band of *Herschel*/SPIRE is 5.8 mJy (Nguyen et al. 2010), which corresponds to the flux from galaxies at $z \sim 2$ with bolometric FIR luminosities of $L_{\text{FIR}} \sim 2 \times 10^{12} L_{\odot}$, i.e., ultra-luminous infrared galaxies (ULIRGs). As a result, a catalog of galaxies at $z > 2$ robustly detected above the confusion noise ($5\ \sigma$) in the submm can only probe the bright end of the luminosity distribution. Stacking provides a mechanism to examine the full distribution,

provided a reliable external catalog extending to faint fluxes is available (see e.g., Marsden et al. 2009, Pascale et al. 2009).

In this work we perform a stacking analysis using a catalog of distant massive galaxies from the GOODS NICMOS Survey (GNS; Conselice et al. 2011) — which we select to have stellar masses $M_{\star} \geq 10^{11} M_{\odot}$ and redshifts $1.7 < z < 2.9$ — on maps from: *Spitzer*/MIPS (Rieke et al. 2004) at $24 \mu\text{m}$; *Herschel*/PACS (Poglitsch et al. 2010) at 70, 100, and $160 \mu\text{m}$; the Balloon-borne Large Aperture Submillimeter Telescope (BLAST; Devlin et al. 2004, Pascale et al. 2008) at 250, 350, and $500 \mu\text{m}$; and the Large APEX Bolometer Camera (LABOCA; Weiß et al. 2009) at $870 \mu\text{m}$. Our objective is to estimate the average SFRs of high-redshift massive galaxies, and to look for differences between the disk-like and spheroid-like galaxies.

An alternative approach, based on counterpart identification of similar GNS catalog sources, is carried out by Cava et al. (2010); we discuss how their results compare to ours in Section 3.5.3.

3.2 Data

We perform our analysis on the Great Observatories Origins Deep Survey South field (GOODS-South), also known as the Extended Chandra Deep Field South (E-CDFS), which has field center coordinates $3^{\text{h}}32^{\text{m}}30^{\text{s}}, -27^{\circ}48'20''$. Here we briefly describe the catalog and maps.

3.2.1 Mass-selected catalog

Our catalog is the Buitrago et al. (2008) subset of the publicly available GOODS NICMOS Survey¹ (Conselice et al. 2011). Here we summarize its main features; for a more detailed description see Buitrago et al.

¹ <http://www.nottingham.ac.uk/astronomy/gns/index.html>

| | N | z_{median} | z_{iqr} | M_{\star} (M_{\odot}) | R_e (kpc) | n | SFR ($M_{\odot} \text{ yr}^{-1}$) |
|------------|----|---------------------|------------------|--------------------------------|----------------|------|--|
| All | 36 | 2.285 | 1.980–2.500 | 1.85×10^{11} | 2.00 | 2.03 | 63_{-11}^{+11} [48, 81] |
| $n \leq 2$ | 20 | 2.285 | 2.085–2.500 | 1.93×10^{11} | 2.43 | 1.05 | 122_{-15}^{+15} [100, 150] |
| $n > 2$ | 16 | 2.270 | 1.865–2.625 | 1.74×10^{11} | 1.49 | 3.25 | 14_{-8}^{+2} [9, 20] |

Tab. 3.1 Average properties of stacked samples. R_e is the effective radius. SFR are corrected to a Chabrier (2003) IMF, and are shown with the corresponding upper and lower Gaussian uncertainties, and interquartile ranges in square brackets.

(2008), Bluck et al. (2009) and Conselice et al. (2011). The GNS is a large *HST* NICMOS-3 camera program of 60 H -band pointings (180 orbits), with limiting magnitudes of $H \sim 26.8$ (5σ), optimized to collect data for as many massive ($M_{\star} \gtrsim 10^{11} M_{\odot}$) galaxies as possible at high redshift ($1.7 < z < 2.9$), making it the largest sample of such galaxies to date. Of these, 36 are in the southern field for which we have infrared and submm maps.

Redshifts and stellar masses of these objects are calculated using the BVRIzJHK filters. Photometric redshifts are found using standard techniques (e.g., Conselice et al. 2007), while spectroscopic redshifts for 7 objects are compiled from the literature. Stellar masses of these objects are estimated by fitting the multi-color photometry to model SEDs — produced with stellar population synthesis models — resulting in uncertainties of ~ 0.2 dex (e.g., Bundy et al. 2006).

Additionally, due to the excellent depth and resolution of the NICMOS images (pixel scale after resampling of $0.1'' \text{ pixel}^{-1}$, and a point-spread function [PSF] of $0.3''$ full width half maximum [FWHM]), we are able to estimate the Sérsic (1968) indices and sizes of the objects using the GALFIT code (Peng et al. 2002). Average properties of the sources used in our analysis are listed in Table 3.1.

Besides being optically-selected, these galaxies are not chosen by any other criteria than mass and redshift, and therefore consist of a mix of different galaxy types, including: distant red galaxies (DRGs) from

Papovich et al. (2006), IRAC-selected extremely red objects (IEROs) from Yan et al. (2004), and BzK galaxies from Daddi et al. (2007). Furthermore, the deep limiting H -band magnitude greatly exceeds that of the expected upper bound for dusty submm galaxies (~ 23.3 mag, Frayer et al. 2004), so that we are confident that we are not missing the dustiest galaxies due to attenuation. Lastly, it is expected that this selection of galaxies closely approximates the true ratio of red to blue galaxies in these mass and redshift ranges.

3.2.2 *Spitzer*

We use the publicly available *Spitzer*/MIPS map at $24\ \mu\text{m}$ from the Far Infrared Deep Extragalactic Legacy Survey (FIDEL; Dickinson & FIDEL team 2007), data release 2² (DR2). The $5\ \sigma$ point source sensitivity of this map is 0.03 mJy.

3.2.3 *PACS*

We use publicly available *Herschel*/PACS (Poglitsch et al. 2010) observations of the GOODS-South field from the PACS Evolutionary Probe (PEP³; Lutz et al. 2011) survey. The data is re-processed with the *Herschel* Processing Environment (HIPE, continuous integration build number 6.0.2110; see Ott 2010). The PEP survey is designed to provide data in all three PACS bands; since PACS can only observe in two bands simultaneously — at $160\ \mu\text{m}$ (red) and either 70 (blue) or $100\ \mu\text{m}$ (green) — we use two sets of observations to produce maps at all three wavelengths. We combine the available deep observations using the standard PACS pipeline, choosing a high-pass filter parameter of 20 for the blue and green bands, and 30 for the red

² http://data.spitzer.caltech.edu/popular/fidel/20070917_enhanced/docs/fidel_dr2.html

³ <http://www.mpe.mpg.de/ir/Research/PEP/>

band (corresponding to suppression of scales larger than 40 and 60'' on the sky, respectively; see Müller et al. 2011a). In order to prevent ringing effects around bright sources caused by the high-pass filter, the pipeline performs an initial crude reduction and automatically masks out the brightest sources in the subsequent iterations of de-glitching and filtering. The rms depths of the final maps are 0.31, 0.44, and 1.5 mJy at 70, 100, and 160 μm , respectively.

As reported by Müller et al. (2011a), the relatively strong high-pass filter adopted along with the masking of the bright sources may attenuate the final photometry of faint sources. To test and account for the combination of these effects in our specific case, we produce maps of a few, isolated, unmasked, faint point sources of different flux density, using the same parameters employed in the reduction of the GOODS-South maps; we then mask these sources out, and create new maps. We use the average ratio of the flux densities of the same sources in the two maps as our estimate of the attenuation factor due to the high-pass filter. We find that the magnitude of the attenuation mildly increases for increasing wavelengths, as expected given the shape of the $1/f$ noise over the relevant frequency range ($\propto f^{-0.5}$; Lutz et al. 2011). The estimated attenuation factors are 0.80, 0.78, and 0.75 at 70, 100, and 160 μm , respectively. Note that a slightly different approach is followed by Lutz et al. (2011), who perform tests on the red band by adding simulated sources to the timelines before masking and high-pass filtering; they find that the filtering modifies the fluxes by 16% for very faint unmasked point sources. Despite the slight disagreement with our finding at 160 μm , and because of the lack of an estimate for the blue and green bands from the PEP team, we choose to adopt our three estimated factors for consistency. The above attenuation factors are therefore used in our subsequent analysis to correct the

measured PACS flux densities and their uncertainties for attenuation due to filtering and source masking.

3.2.4 BLAST

We refer to Section 2.2.1 of this thesis for a description of the BLAST dataset. Figure 3.1 depicts how the BGS-Deep region completely encompasses the southern sources in the Buitrago et al. (2008) catalog.

3.2.5 LABOCA

The LABOCA E-CDFS Submm Survey (LESS; Weiß et al. 2009) provides deep $870\ \mu\text{m}$ data, with an rms depth to better than 1.2 mJy across the full $30' \times 30'$ field, with an effective resolution of $27''$ FWHM. For a detailed description of the instrument see Siringo et al. (2009).

3.3 Method

3.3.1 Stacking formalism

Stacking is a well established technique for finding the average properties of objects which individually are undetectable by using external knowledge of their positions in a map (e.g., Dole et al. 2006, Wang et al. 2006, Marsden et al. 2009, Pascale et al. 2009). We follow the formalism of Marsden et al. (2009; hereafter M09), which we review and expand in Appendix A. Here we summarize the salient features of the technique.

M09 show that the mean flux density of an external catalog is simply the covariance of the mean-subtracted map with the catalog, divided by the variance of the catalog density. If the catalog is Poisson-distributed, then a powerful diagnostic is that the variance of the source density should equal the mean, and the average flux density

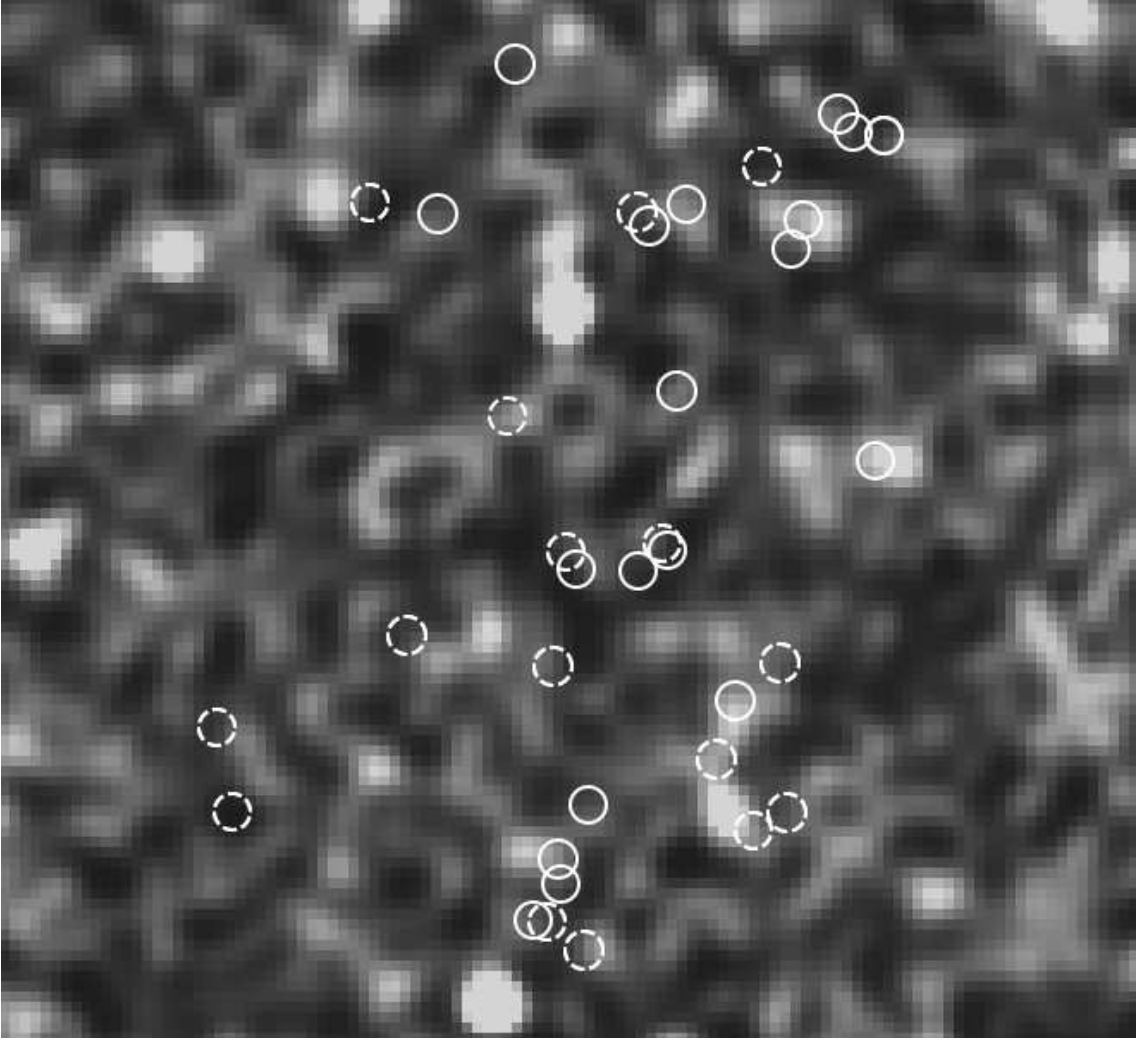


Fig. 3.1 GNS catalog positions (white circles, $36''$ in diameter, solid are $n \leq 2$; dashed are $n > 2$) overlaid on a $20' \times 20'$ region of the BLAST $250 \mu\text{m}$ map in GOODS-South. The map is convolved with a matched-filter (see Chapin et al. 2011) to help enhance the regions of submm emission. Most of the sources in our catalog lie along regions of faint emission. Note that the BLAST beam is many (~ 18 – 30) times larger than a resolved galaxy, necessitating the stack. Furthermore, since the angular resolution of *Herschel*/SPIRE images will only improve by a factor of two, stacking will still be required to understand the FIR/submm properties of the faint population.

can be re-written as the mean map value at the position of each catalog source (see Appendix A). This is true no matter what the size of the beam or surface density of sources in the map, so long as the sources are uncorrelated at the scale of the beam. The algorithm is extensively tested with Monte Carlo simulations on mock random maps

with increasing source densities, and is shown to consistently recover the correct mean flux density, with no dependence on the number of sources per beam (Figure 3.2). If however the catalog *is* clustered on the beam scale, the stacked flux will be biased high, compared to the properly normalized covariance, by a factor equal to the catalog variance at the beam scale divided by the mean source density. In the following section we show that this factor is consistent with unity for our data.

Uncertainties and possible biases of our measurement are estimated by generating random catalogs and stacking them on the actual maps themselves. We find that the uncertainties are Gaussian-distributed and scale as the map rms (including confusion noise) divided by the square root of the number of catalog entries (see Appendix A).

3.3.2 *Testing the Poisson hypothesis*

Stacking provides an unbiased estimate of the mean flux only when the sources in the sky are uncorrelated. While massive galaxies have been shown to cluster quite strongly (e.g., Foucaud et al. 2010), we find that on scales relevant for this analysis they are essentially Poisson-distributed, as we show with the following tests:

1) In the presence of clustering, the FWHM of the postage-stamp of stacked sources would be larger than the nominal instrumental PSF. We compare our measured stacked $24\ \mu\text{m}$ PSF to that measured from stacking the sources used in M09 (Magnelli et al. 2009), which are shown to be Poisson-distributed (see Figure 3 of M09), and find that they are identical to within $\sim 0.6''$ (one tenth of the PSF FWHM).

2) If the sources are Poisson-distributed over a given scale, then by definition the average number of sources in a cell of that size should equal the variance. We test that by dividing the field into equal sized

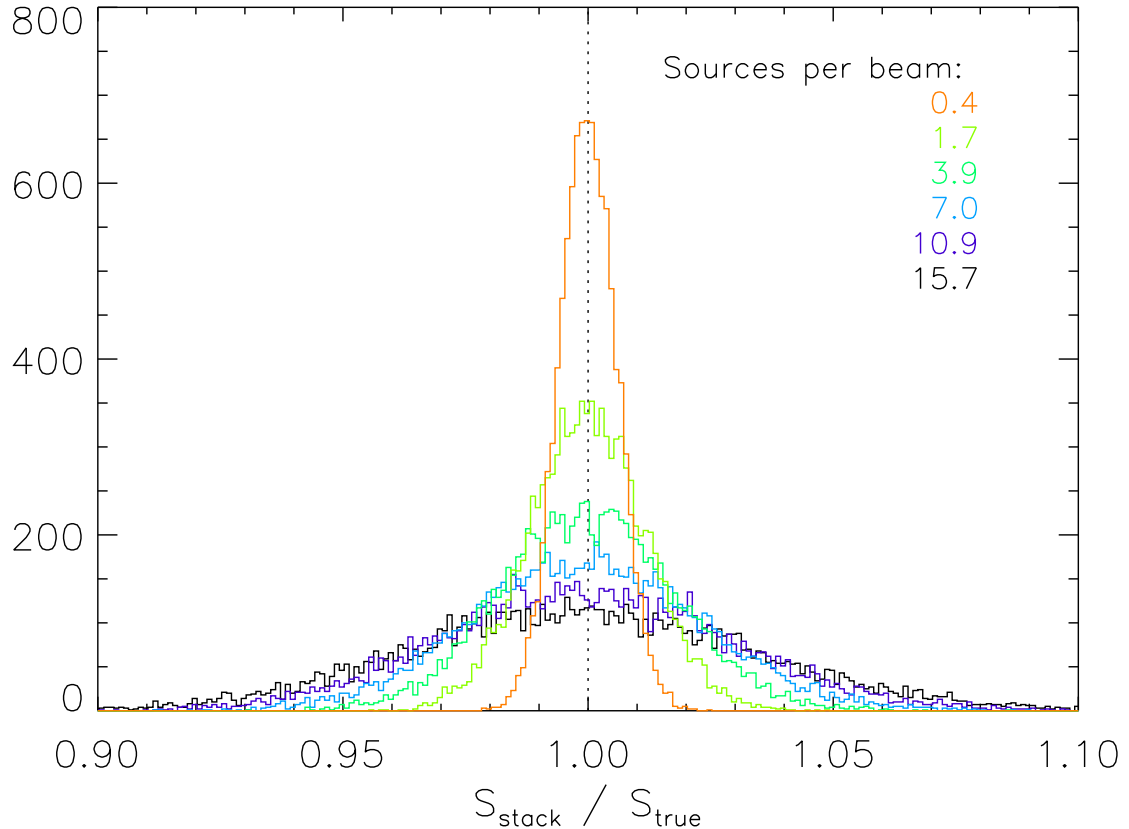


Fig. 3.2 Histograms showing the ratio of recovered stacked fluxes to true flux for 10,000 simulations. The stacks are performed on simulated 0.25 deg^2 maps based on a random catalog of 12,500 sources, with size and source densities typical for deep $24 \mu\text{m}$ MIPS catalogs. We repeat the test for six beam sizes in the range $10\text{--}60''$, which probe the effects of stacking at source densities ranging from 0.4 to 16 sources per beam. As described in Section 3.3.1 and in M09, larger beams lead to larger uncertainties, but in all cases, the stacked values are consistent with the true catalog flux, showing that there is no bias when stacking on uncorrelated catalogs.

cells, from 2.7 to $0.225'$ on a side, and find that the ratio of the variance to the mean is consistent with unity at all scales.

3) In the presence of strong clustering around massive galaxies we would expect to find more sources per beam surrounding the galaxies than would be found at random. We calculate the number of sources inside a BLAST beam radius at the locations of each massive galaxy and compare that to what we would expect at random. From 1,000 Monte Carlo simulations we find 1.10 ± 0.13 , 1.16 ± 0.17 , and 1.28 ± 0.21

sources per beam at 250, 350, and 500 μm , compared to the measured 1.04, 1.13, and 1.17, respectively. We extend this test to galaxies with $\log(M_*/M_\odot) > 9$ (catalog provided by Kevin Bundy, private communication), to account for the possibility of less massive galaxies clustering around our more massive ones. We find there are 2.85 ± 0.40 , 3.83 ± 0.51 , and 5.97 ± 0.73 sources per beam at 250, 350, and 500 μm , compared to the measured 2.53, 4.04, and 5.87, respectively. Thus, while there are multiple sources per beam at all wavelengths, because their distribution is consistent with a Poissonian, they do not bias the result.

There still remains the possibility, however, that even fainter, undetected sources (with flux densities $< 13 \mu\text{Jy}$ at 24 μm) may cluster around detected ones. We can estimate their potential contribution in the following way. If clustered, faint sources contribute significantly to the stacked flux density for large beams, then after convolving the 24 μm map (whose beam FWHM is 6'') with a much larger beam, we would expect the stacked flux density to increase. On the other hand, as described in the previous section, if the faint sources are Poisson-distributed, then we would expect only the noise to increase. We find that after convolving the 24 μm map with a 60'' beam, the stacked flux density per source is $0.08 \pm 0.11 \text{ mJy}$, compared to the original $0.081 \pm 0.005 \text{ mJy}$ (see Table 3.3). Thus, the stacked signal does not change, but the errors increase substantially, which is consistent with what we would expect from additional, Poisson-distributed sources in the beam. We therefore conclude that the contribution from faint clustered sources is negligible.

3.3.3 SED fitting, IR luminosities, and star-formation rates

We model the thermal dust emission as a modified blackbody with an SED of the form:

$$S_\nu = A \nu^\beta B(\nu, T), \quad (3.1)$$

where $B(\nu, T)$ is the blackbody spectrum, of amplitude A , and β is the emissivity index, which we fix to 1.5 (Hildebrand 1983). Furthermore, we replace the mid-infrared exponential on the Wien side of the spectrum with a power-law of the form $f_\nu \propto \nu^{-\alpha}$ (with $\alpha = 2$, following Blain 1999, Blain et al. 2003) to account for the variability of dust temperatures within a single galaxy (see also Section 2.3.2 of this thesis). Our SED fitting procedure estimates the amplitude and temperature of the above template, keeping α and β fixed.

For the BLAST points, the SED fitting procedure (described in detail in Chapin et al. 2008) takes the width and shape of the photometric bands into account, as well as the absolute photometric calibration uncertainty in each band (see Truch et al. 2009). Correlations due to instrumental noise are estimated and accounted for with a Monte Carlo procedure. Because we do not possess similar detailed data for *Spitzer*/MIPS and LABOCA, these photometric points are not color-corrected, whereas we do apply a color-correction to the PACS points, following the standard procedure described in Müller et al. (2011b; see their Table 4.2, for a power law ν^{-2}); the color-correction factors are 1.016, 1.012, 1.017 at 70, 100, and 160 μm , respectively, and have a negligible impact on the final results. The PACS points are assumed to have completely uncorrelated instrumental noise among bands.

The portion of noise arising from source confusion may be highly correlated among bands; if that is in fact the case, correlated confusion noise must be accounted for in the fit, as these correlations reduce the

Table 3.2. Correlations among all bands under analysis

| Band [μm] | Pearson Correlation Matrix | | | | | | | |
|---------------------------|----------------------------|------------------|-------------------|-------------------|-------------------|-------------------|-------------------|-------------------|
| | 24 μm | 70 μm | 100 μm | 160 μm | 250 μm | 350 μm | 500 μm | 870 μm |
| 24 | 1 | 0.11 | 0.13 | 0.23 | 0.35 | 0.28 | 0.22 | 0.05 |
| 70 | | 1 | 0.92 | 0.77 | 0.22 | 0.15 | 0.08 | 0.006 |
| 100 | | | 1 | 0.86 | 0.27 | 0.19 | 0.11 | 0.007 |
| 160 | | | | 1 | 0.44 | 0.33 | 0.20 | 0.04 |
| 250 | | | | | 1 | 0.70 | 0.62 | 0.11 |
| 350 | | | | | | 1 | 0.70 | 0.14 |
| 500 | | | | | | | 1 | 0.13 |
| 870 | | | | | | | | 1 |

significance of a combination of single band detections. We estimate the Pearson coefficients of the correlation matrix for all bands (see Table 3.2) from the beam-convolved maps, within a region of 0.064 deg^2 that encompasses all the sources in the GOODS-South NICMOS catalog. We find that correlation effects are indeed important, especially among PACS and BLAST bands (see also Section 2.3.2⁴), and thus include them in the SED fitting algorithm.

SEDs are corrected for redshift by assuming the median redshift for each subset (see column 3, Table 3.1). Interquartile errors reflecting the uncertainty in dimming due to the width of the redshift bin are estimated with a Monte Carlo, where 1000 mock redshifts with the same distribution as the chosen subset (i.e., all, disk-like, and spheroid-like) are drawn, and the dimming factor for each redshift is calculated.

The resulting infrared luminosity, L_{FIR} , is conventionally the integral of the rest-frame SED between 8 and $1000 \mu\text{m}$, and the SFR is estimated using Equation (2.1) of this thesis, which assumes Salpeter (1955) initial mass function (IMF). In order to compare our results to

⁴ The slight discrepancy with the BLAST numbers as reported Table 2.1 for the whole BGS-Deep can be explained by the particular sky coverage under analysis.

| Band (μm) | All (mJy/source) | $n \leq 2$ (disk-like) (mJy/source) | $n > 2$ (spheroid-like) (mJy/source) |
|---------------------------|---------------------|--|---|
| 24 | 0.081 ± 0.005 | 0.130 ± 0.007 | 0.020 ± 0.007 |
| 70 | 0.16 ± 0.07 | 0.36 ± 0.09 | -0.05 ± 0.10 |
| 100 | 0.39 ± 0.09 | 0.84 ± 0.13 | -0.17 ± 0.14 |
| 160 | 1.2 ± 0.3 | 2.9 ± 0.5 | -0.66 ± 0.50 |
| 250 | 5.0 ± 2.9 | 9.3 ± 3.9 | -0.3 ± 4.4 |
| 350 | 7.9 ± 2.3 | 10.7 ± 3.1 | 4.5 ± 3.5 |
| 500 | 5.3 ± 1.9 | 6.2 ± 2.6 | 4.2 ± 2.9 |
| 870 | 0.97 ± 0.26 | 1.03 ± 0.35 | 0.9 ± 0.4 |

Tab. 3.3 The mean flux densities of massive galaxies in the GNS catalog from stacking. Reported are the results for all of the sources, as well as those identified as disk-like and spheroid-like, based on their Sérsic indices, n .

those of other relevant studies in the literature, we convert the SFRs to a Chabrier (2003) IMF by lowering $\log(\text{SFR})$ by a factor 0.23 dex (e.g., Kriek et al. 2009a, van Dokkum et al. 2010).

3.4 Results

3.4.1 Stacking results

Stacking results and 1σ uncertainties are reported in the second column of Table 3.3. We find statistically significant, non-zero signals in all the submm bands, with 2, 3, 3, and 4 σ detections at 250, 350, 500, and 870 μm , respectively, as well as robust 16, 3, 4, and 4 σ detections at 24, 70, 100, and 160 μm , respectively.

Next, we divide the catalog by Sérsic index into: those with $n > 2$, which are spheroid-like and thus more likely to have suppressed star formation; and those with $n \leq 2$, which are disk-like and thus more likely to be actively forming stars (Ravindranath et al. 2004). The results are listed in the third and fourth columns of Table 3.3. At 24 μm , we measure a distinct signal from both populations, with 19 σ and 3 σ detections from the disk-like and spheroid-like sources, respectively.

At longer wavelengths, for the disk-like population we detect signals with greater significance than that of the combined catalog, between 2.5 and 6.5σ in each FIR/submm band; whereas for the spheroid-like population we find a much weaker signal, with four bands consistent with zero.

While the error on the stacks is Gaussian, the uncertainty associated with the average rest-frame L_{FIR} is dominated by the width of the redshift distribution, which is not Gaussian. Hence, as anticipated in the previous section, we choose to adopt for T , L_{FIR} , and SFR the median value as our best estimate and the interquartile range as the associated error, because these best reflect the asymmetric shape of the redshift distribution, which ultimately determines the uncertainty of our measurement. However, we also quote the Gaussian uncertainties. We anticipate that the lower Gaussian errors on T , L_{FIR} , and SFR for the spheroid-like subset exceed the lower bound of the interquartile range, and reflect the elevated level of uncertainty in our measurement.

3.4.2 *Contribution of stellar emission*

At $z \sim 2.3$ the observed $24\mu\text{m}$ band probes rest-frame wavelengths of $6\text{--}8\mu\text{m}$, which in addition to PAH emission, is where the Rayleigh-Jeans tail of stellar emission lies. Thus it is possible that stellar emission could contaminate our measurement, considering the nature and stellar masses of our sample. To investigate this potential bias in our analysis, we calculate the predicted $24\mu\text{m}$ observed flux densities due to stellar emission using the redshifts and stellar masses as per our catalog (see Section 3.2.1). We opt to use a galaxy template with solar metallicity and an exponentially declining SFR with an e-folding time of 500 Myr , generated with the stellar population synthesis code PEGASE.2 (Fioc & Rocca-Volmerange 1997). Output from non-stellar

emission or evolving main-sequence stars is not included, as the source of non-stellar emission at $7\ \mu\text{m}$ is assumed to be the same as that of the FIR emission. Assuming a formation redshift of $z = 9$, the galaxy ages range from 1.5 to 3 Gyr and the predicted $24\ \mu\text{m}$ flux densities due to stellar emission range from 1.3 to $8.8\ \mu\text{Jy}$, depending primarily on the galaxy's redshift. For each stacked sample, we find the predicted contamination per galaxy from stellar emission to be at most $\sim 50\%$ of our error on the stacks (Table 3.3), with amounts of 3.0, 2.9, and $3.9\ \mu\text{Jy}$ for the entire sample, the disk-like and spheroid-like populations, respectively. Therefore, the $24\ \mu\text{m}$ flux densities included in our analysis are primarily dominated by non-stellar emission (dust and PAH), and we choose not to apply any correction to them.

3.4.3 Best-fit SEDs and star-formation rates

The best-fit SED and interquartile range to the stacked values of the complete catalog are shown in the left panel of Figure 3.3 (which we choose to display full-page and rotated for visual clarity), corresponding to a median (plus/minus Gaussian) [interquartile] temperature of $T = 29.4^{+1.4}_{-0.8}$ [27.3, 31.6] K, luminosity of $L_{\text{FIR}} = 6.2^{+1.1}_{-1.0}$ [4.7, 8.0] $\times 10^{11} L_{\odot}$, and SFR = 63^{+11}_{-11} [48, 81] $M_{\odot} \text{yr}^{-1}$.

We check the validity of our modified blackbody approximation by comparing to the templates of Chary & Elbaz (2001; hereafter CE01). For each of the 101 templates, we approximate the stacked SED by taking the average of templates shifted to the redshift of each galaxy in the catalog; this acts to smear out the otherwise highly-variable PAH region of the rest-frame SED probed by the $24\ \mu\text{m}$ band. We fit the resulting template to our photometric points without accounting for calibration uncertainties, color corrections, or correlations among bands. The best-fit template is shown as a 3-dot-dashed line in Fig-

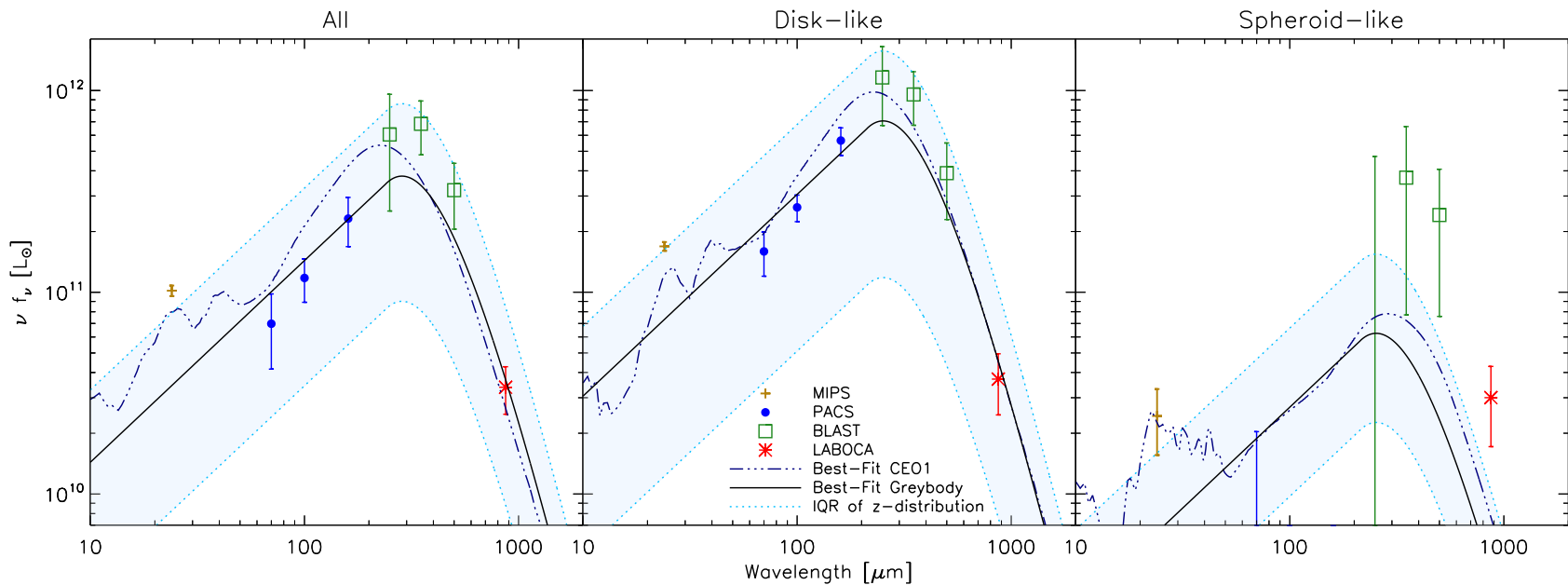


Fig. 3.3 SED fits to the stacked flux densities of all (left), disk-like (center), and spheroid-like (right) sources. The median value of the redshift distribution, $z \sim 2.3$, is used here to convert flux densities into rest-frame luminosity. The brown crosses are from *Spitzer* ($24 \mu\text{m}$); the blue dots are from PACS (70 , 100 , and $160 \mu\text{m}$); the green squares are from BLAST (250 , 350 , and $500 \mu\text{m}$); and the red asterisks are from LABOCA ($870 \mu\text{m}$). The error bars represent the 1σ Gaussian uncertainties from the stacks as listed in Table 3.3. The SED is modeled as a modified blackbody with a fixed emissivity index $\beta = 1.5$, and a power-law approximation on the Wien side with slope $\alpha = 2$. The solid black lines are the best-fit SEDs, while the dotted light-blue lines enclosing the shaded regions show the uncertainties due to the width of the redshift distribution (interquartile range), which clearly dominate over the Gaussian errors on the stacks (see Section 3.4.1). The navy 3-dot-dashed lines are the best-fit, redshift-averaged templates from Chary & Elbaz (2001).

ure 3.3, and falls well inside our error region. However, the SFR of the best-fit template is $\text{SFR} = 87 M_{\odot} \text{yr}^{-1}$, which is $\sim 38\%$ larger than our modified blackbody estimate, and lies outside the interquartile range. This overestimate arises because the fit with the CE01 template does not include the substantial correlations among bands (see Section 3.3.3), which reduce the significance of the combination of individual photometric points.

We then separately fit the stacked flux densities measured for disk-like and spheroid-like galaxies. The best-fit modified blackbody SED for the disk-like population is shown in the center panel of Figure 3.3, and results in a median (plus/minus Gaussian) [interquartile] temperature of $T = 32.6_{-0.4}^{+1.0}$ [30.8, 34.6] K, luminosity of $L_{\text{FIR}} = 12.0_{-1.5}^{+1.4}$ [9.8, 14.8] $\times 10^{11} L_{\odot}$, and $\text{SFR} = 122_{-15}^{+15}$ [100, 150] $M_{\odot} \text{yr}^{-1}$. The best-fit CE01 template is also shown, and corresponds to a $\text{SFR} = 142 M_{\odot} \text{yr}^{-1}$.

Likewise, the best-fit modified blackbody SED for the spheroid-like population is shown in the right panel of Figure 3.3, and results in a median (plus/minus Gaussian) [interquartile] temperature of $T = 27.6_{-7.6}^{+0.3}$ [24.2, 30.8] K, luminosity of $L_{\text{FIR}} = 1.4_{-0.8}^{+0.2}$ [0.9, 2.0] $\times 10^{11} L_{\odot}$, and $\text{SFR} = 14_{-8}^{+2}$ [9, 20] $M_{\odot} \text{yr}^{-1}$. Note that the lower Gaussian errors exceed the lower bound of the interquartile range, thus reflecting the elevated level of uncertainty in our measurement. Once again, the best-fit CE01 template is shown, which corresponds to a $\text{SFR} = 16 M_{\odot} \text{yr}^{-1}$.

Thus, although the best-fit SED to the combined stack returns a robust, 4σ detection, it is clear that the signal is dominated by the disk-like, $n \leq 2$ galaxies, which are detected at 5σ . The best-fit to the spheroid-like, $n > 2$ galaxies, on the other hand, returns a marginal 2σ result, which suggests, but does not formally detect, a low level of star formation taking place in the spheroid-like population.

3.5 Discussion

3.5.1 Consequences for galaxy growth

There are indications that massive galaxies at high redshift are the cores of present-day massive ellipticals (Hopkins et al. 2009, Bezanson et al. 2009), and that the growth of these galaxies takes place mostly in the outskirts via star formation and minor mergers (Hopkins et al. 2009, van Dokkum et al. 2010) — a process sometimes referred to as “inside-out” growth, which has also been observed in hydrodynamical cosmological simulations (Naab et al. 2009, Johansson et al. 2009, Oser et al. 2010). Furthermore, van Dokkum et al. (2010) find that a SFR of $55 \pm 13 M_{\odot} \text{ yr}^{-1}$ at $z \sim 2$ is necessary to account for the mass growth they observe in massive galaxies selected by number density, from $z = 2$ to the present day, and that for $z \gtrsim 1.5$ the mechanism for growth is primarily star formation. At first glance, the level of star formation we measure in galaxies with $n > 2$ appears too low to quantitatively endorse this scenario; however, we note that nearly half of their $z \sim 2$ subsample of massive galaxies has $n < 2$ (see right panel of their Figure 7) — a fraction similar to our own. While it is difficult for us to quantify the magnitude of this contamination to the quoted SFR, our measurement of $63 [48, 81] M_{\odot} \text{ yr}^{-1}$ for the entire sample may be a fairer term of comparison⁵. Though this agrees well with their finding, and hence is qualitatively consistent with a picture of gradual growth in the outer regions due to star formation, it may be more an indication of how sensitive the signal is to contamination from disk-like galaxies. We conclude that the our data do not manifest convincing

⁵ We verify that the quoted SFR can be compared to our measurements without a significant correction due to different assumed IMF. In fact, van Dokkum et al. (2010) use a Kroupa (2001) IMF, which yields SFRs and stellar masses that are a factor 1.6 smaller (Marchesini et al. 2009) than those obtained with a Salpeter (1955) IMF; our correction factor of 0.23 dex to a Chabrier (2003) IMF is only 6% different.

enough evidence to envision star formation as the mechanism driving the expansion in spheroid-like galaxies.

3.5.2 Potential contribution from other sources of dust heating

Star formation may not be the only explanation for infrared emission in our sample, which consists of very massive, yet relatively young systems. The age of the universe by $z = 3$ –1.8, is just ~ 1.5 –3 Gyr, providing a strict upper limit on the ages of the stellar populations. If these galaxies formed the bulk of their stellar mass, as their colors suggest, early on, then it is likely that they contain a large population of stars undergoing post-main-sequence phases in which carbonaceous dusty material is being produced and heated by very luminous stars. While it is generally accepted in the current versions of stellar population synthesis models (Maraston 2005, Bruzual 2010, Conroy & Gunn 2010) that thermally-pulsating asymptotic giant branch (TP-AGB) stars can contribute up to 70% of the emission seen in the near-infrared bands at ages of 1-2 Gyr, there has been little work calibrating the global contribution of this population to a galaxy’s infrared luminosity. By extension, given the masses and ages of our galaxies, we cannot rule out the possibility that the infrared emission we detect in our analysis is partially due to dust heated and created by post-main-sequence stars.

3.5.3 Red and dead?

Our best-fit SED to stacked data does not correspond to a formal detection of star formation in the spheroid-like ($n > 2$) galaxies, however, the high $24\mu\text{m}$ flux might indicate a non-zero star formation rate. Though we have stated that $24\mu\text{m}$ emission alone is insufficient for accurately estimating the overall *level* of star formation in a galaxy,

locally, $24\ \mu\text{m}$ emission is typically well correlated with star-forming regions (Calzetti et al. 2007, Kennicutt et al. 2009). Additionally, emission from evolved stars seems unable to account for the level of $24\ \mu\text{m}$ emission observed (Section 3.4.2). Therefore, it seems plausible that star formation may be occurring in these galaxies at some level. Furthermore, if a low level of star formation does indeed exist, given the noise properties of our maps, the only bands which would permit a significant detection are the 24 and $870\ \mu\text{m}$ bands — those in which our measurements have signal-to-noise greater than 2.5.

If star formation is occurring in the spheroid-like galaxies, even at a low level, and if they are fair analogs of the apparently red-and-dead compact spheroids seen by e.g., Kriek et al. (2009b), then why is it that star formation is not significant in ultra-deep spectroscopy? One possibility is that the star formation is localized in very dust-obscured, clumpy regions. The standard hierarchical picture of galaxy growth is currently being contested by new galaxy growth models where at high redshift massive galaxies are mainly built up through diffuse gas accreting along cold flows (Dekel et al. 2009, Kereš et al. 2009). An observational signature of this is highly clumpy star formation (Bournaud & Elmegreen 2009), whereby the majority of the star formation would be dust obscured and emitted in the infrared.

In fact, although Kriek et al. (2009b) detect a faint $\text{H}\alpha$ line, concluding that SFRs are at most $1\text{--}3\ M_{\odot}\ \text{yr}^{-1}$, that is after correcting for a very moderate amount of extinction ($A_v = 0\text{--}0.3\ \text{mag}$). For this galaxy to actually be forming around $14\ M_{\odot}\ \text{yr}^{-1}$, $L_{\text{H}\alpha}$ would need to have been underestimated by a factor of $\sim 3.5\text{--}7$, which corresponds to $1.4\text{--}2.1\ \text{mag}$ of extinction. Considering that resolved observations of nearby galaxies showing extinction values of $A_{\text{H}\alpha} > 3$ are common in H II regions (Prescott et al. 2007) and regions of high star forma-

tion (Mentuch et al. 2010), this amount of extinction is not unrealistic. However, this does not mean that we expect star formation to be ubiquitous across these galaxies. Had star formation been more widespread, and ongoing over 10–500 Myr, then it would have been detected in optical images, but the rest-frame UV and optical colors do not support that scenario. Rather, we interpret the signal as galaxies having clumpy regions of star formation, on timescales of ~ 10 Myr, which lead to the low observed $H\alpha$ line emission, but stronger infrared emission. Overall, these galaxies are red and evolved, with most of their stellar mass set in place long ago. This picture is consistent with the recent findings of Bauer et al. (2011).

Lastly, we report that our results are in slight disagreement with Cava et al. (2010), who (after correcting by 0.23 dex due to differences in assumed IMF) find average SFRs of $147\text{--}178 M_{\odot} \text{ yr}^{-1}$ for disk-like galaxies and $30\text{--}60 M_{\odot} \text{ yr}^{-1}$ for spheroid-like galaxies. Note that their average SFRs are based on photometry of individual galaxies at $24 \mu\text{m}$, and at 250, 350, and $500 \mu\text{m}$ from *Herschel*/SPIRE; however, we point out that their mean detection fraction for the spheroid-like population is ~ 0.4 at $24 \mu\text{m}$ and ~ 0.15 at $250 \mu\text{m}$. Furthermore, their SED fitting routine does not account for correlations among bands due to source confusion, which, albeit certainly smaller for SPIRE than for BLAST, undoubtedly reduce the significance of the combined detection.

3.6 *Concluding Remarks*

Our goal was to search for evidence of star formation in high-redshift massive galaxies, with the hope of leading to a better understanding of the mechanisms responsible for their growth. We found that on average the full catalog of sources are forming stars with a median

(plus/minus Gaussian) [interquartile] SFR = 63_{-11}^{+11} [48, 81] $M_{\odot} \text{yr}^{-1}$, which can be decomposed into a relatively strong signal for the disk-like galaxies, with a median [interquartile] SFR = 122_{-15}^{+15} [100, 150] $M_{\odot} \text{yr}^{-1}$, and a marginal signal for the spheroid-like population, with a median [interquartile] SFR = 14_{-8}^{+2} [9, 20] $M_{\odot} \text{yr}^{-1}$.

The level of star-formation detected for the full catalog is in good agreement with other measurements of galaxy growth (e.g., van Dokkum et al. 2010), which show that star formation can account for most of the growth at these redshifts. However, despite having detected stacked emission at 24 and 870 μm , we are unable to say convincingly that star formation is responsible for the dramatic size evolution of the spheroid-like population.

Lastly, though a red sequence appears to already be in place by $z \sim 2$ (Kriek et al. 2009a), we found hints that perhaps the red, compact, spheroid-like galaxies may not be completely dead. Future stacking work with larger catalogs and better maps will go a long way to further understanding this question. Deeper and higher resolution data bracketing the peak with *Herschel*/SPIRE (Griffin et al. 2010), will make more robust estimates of the SED possible, and will greatly increase our understanding of star formation in high-redshift massive galaxies.

Part Two

4. THE BLAST-POL INSTRUMENT

4.1 Introduction

BLAST-Pol, the Balloon-borne Large Aperture Submillimeter Telescope for Polarimetry, is a stratospheric 1.8 m telescope which maps linearly polarized submillimeter (submm) emission with bolometric detectors operating in three 30% wide bands at 250, 350, and 500 μm . BLAST-Pol's diffraction-limited optics are designed to provide a resolution of 36", 42", and 60" at the three wavebands, respectively. The detectors and cold optics are adapted from those of the SPIRE instrument (Griffin et al. 2010) on *Herschel* (Pilbratt et al. 2010).

BLAST-Pol is a rebuilt and enhanced version of the BLAST telescope (Pascale et al. 2008), with added linear polarization capability. As described elsewhere in this thesis (see Chapters 2 and 3), BLAST was designed to conduct confusion-limited, wide-area extragalactic and Galactic surveys at submm wavelengths from a balloon platform.

BLAST had two Long Duration Balloon (LDB) flights. The first was a 4-day flight from Kiruna, Sweden in June 2005 (BLAST05). Unfortunately the telescope was found to be out of focus, due to a possible damage of the primary mirror during the launch or ascent, so the telescope was restricted to observing bright Galactic targets. BLAST was repaired and flown again over Antarctica in December 2006 for 11 days (BLAST06). In a rather eventful landing, the telescope was largely destroyed, but the pressure vessel containing the hard drives, which stored all of the experiment data, was recovered. During the

very successful BLAST06 flight, multiple deep, large-area maps were obtained for Galactic and extragalactic fields. The BLAST06 campaign has left a legacy of fantastic science results, some of which we have first-handedly derived in the first part of this thesis. In addition to the hard drives, the mirrors, detectors and receiver were all recovered, and have been used in the construction of BLAST-Pol.

With the addition of a polarimeter, BLAST has now been transformed into BLAST-Pol, a uniquely sensitive instrument for probing linearly polarized Galactic dust emission. In January 2011, BLAST-Pol successfully completed its first 9.5-day flight over Antarctica. Ten science targets were mapped with unprecedented combined mapping speed and resolution; the data are currently being analyzed. These observations comprise an exciting dataset for studying the role played by magnetic fields in star formation (see Chapter 1).

BLAST-Pol will ultimately yield maps of the inferred magnetic fields across entire Giant Molecular Clouds (GMCs), with sufficient resolution to probe fields in dense filamentary sub-structures and molecular cores. The experiment provides a crucial bridge between the large-area but coarse-resolution polarimetry provided by experiments such as *Planck* (5' resolution; Planck Collaboration 2011) and the high-resolution but limited field-of-view (FOV) maps of the Atacama Large Millimeter/submillimeter Array (ALMA; Wootten & Thompson 2009). Finally, the BLAST-Pol observations are complementary to those planned with the SCUBA-2 polarimeter (Bastien et al. 2005) at $850\ \mu\text{m}$, as the disadvantage in mapping speed due to the smaller pixel count of BLAST-Pol is almost completely compensated by the increasing flux density at shorter wavelengths.

4.2 Optical Design

BLAST-Pol is equipped with a Cassegrain (Ritchey–Chrétien) telescope consisting of a 1.8 m hyperbolic primary mirror (M1) and a 40 cm correcting secondary (M2). The field of view of the telescope at $250\ \mu\text{m}$ is $13.5' \times 6.5'$ at the Cassegrain focus. This system redirects the light to a series of cryogenically cooled (1.5 K) re-imaging optics (M3, M4, M5) arranged in an Offner-relay configuration, where M4 is a Lyot stop (a cold image of the primary mirror) that blocks stray radiation due to scattering and diffraction. Figure 4.1 shows a schematic of the optical path of the telescope; Figure 4.2 is a close-up picture of the cold optics box taken just before the cooldown in November 2010. The BLAST-Pol telescope and receiver parameters are listed in Table 4.1.

| | | |
|------------|---|---|
| Telescope: | temperature | ambient |
| | primary diameter | 1.8 m |
| | effective focal length | 9 m |
| | $f_{\#}$ | 5 |
| | antenna efficiency | $\geq 80\%$ |
| | emissivity | 0.06 |
| Detectors: | bolometer optical NEP | $3.0 \times 10^{-17}\ \text{W Hz}^{-\frac{1}{2}}$ |
| | bolometer quantum efficiency | 0.8 |
| | bolometer feed-horn efficiency | 0.7 |
| | throughput for each pixel | $A\Omega = \lambda^2$ ($2f\lambda$ feed-horns) |
| Bands: | central wavelengths | 250 350 500 μm |
| | number of pixels | 149 88 43 |
| | nominal beam FWHM | 36 42 60 arcseconds |
| | field of view for each array | 6.5×13.5 arcminutes |
| | overall instrument transmission | 30% |
| | filter widths ($\lambda/\Delta\lambda$) | 3 |
| | observing efficiency | 90% |

Tab. 4.1 Nominal or measured parameters of the BLAST-Pol telescope and receiver.

Radiation from the telescope undergoes many stages of optical filtering before it reaches the detectors. The first stage of low-pass filters

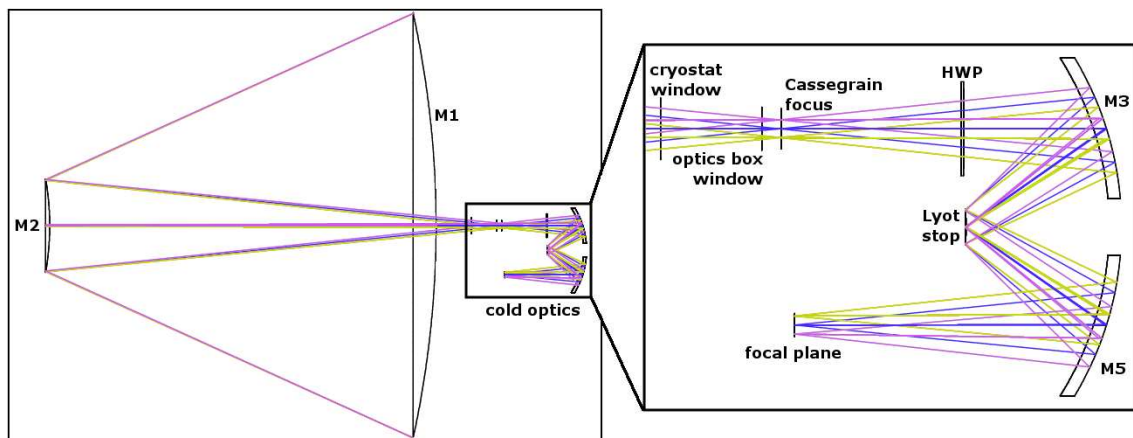


Fig. 4.1 Schematic of the optical layout for the BLAST-Pol telescope and receiver is shown on the left, with the 1.5 K optics, located within the cryostat, shown in an expanded view on the right. The image of the sky formed at the input aperture is re-imaged onto the bolometer detector arrays at the focal plane. The M4 mirror serves as a Lyot stop, which defines the illumination of the primary mirror for each element of the bolometer detector arrays. The three wavelength bands are separated by a pair of dichroic beam-splitters (not shown here, but clearly visible in Figure 4.2). The sapphire half-wave plate (HWP; see Section 4.5) is also shown, mounted 19.174 cm from the Cassegrain focus of the telescope.

rejects high-frequency thermal emission, which more precisely defines the band passes and minimizes the thermal loading within the cryostat. A series of metal-mesh filters reject short wavelength radiation at each of the 4 thermal stages of the cryostat. Once inside the optics box, radiation emerging from M5 is split into three frequency bands by low-pass edge dichroic filters, which allow us to image the sky simultaneously at 250, 350 and, 500 μm . The first dichroic filter reflects wavelengths shorter than 300 μm and transmits longer wavelengths. This reflected light is directed onto a filter directly in front of the 250 μm array, which reflects wavelengths shorter than 215 μm , and is further defined by the waveguide frequency cut-off at the exit of each of the feed-horns coupled to the detector array. For the 350 and 500 μm arrays, the band is defined at the short-wavelength end by the transmission of the dichroic filter and at the long-wavelength



Fig. 4.2 Close-up photograph of the cold optics box taken during the BLAST-Pol flight campaign, just before the cryostat cooldown in November 2010. Clearly visible are: on the left side, the spherical mirrors M3 and M5; the two dichroic beam splitters, which separate the three wavelength bands; the three bolometer detector array (BDA) assemblies with the polarizing grids installed (see Section 4.5). Less visible, right in the center of the optics box, is the circular Lyot stop (M4), whose optical surface faces M3 and M5. Most of the optically-inactive surfaces are blackened to prevent unwanted reflections from stray light. Photo credits: Matthew Truch.

end by the waveguide cut-off. Each band has a 30% width. For a review of the metal-mesh filter technology, see Ade et al. (2006). The combined frequency performance of the stack of filters is measured via Fourier transform spectroscopy during the integration campaign at the Columbia Scientific Balloon Facility (CSBF), Palestine (TX), in June 2010. We find that the relative spectral response of the three BLAST-Pol channels is identical to that of BLAST06 (see bottom panel of Figure 2 in Pascale et al. 2008), as expected given that the specifications of the whole filter chain have not changed. We also verify that having the dichroic filters tilted by an angle with respect to the optical path (see Figure 4.2) produces negligible amounts of unwanted instru-

mental polarization. To this end, we measure with a polarizing Fourier transform spectrometer (pFTS; briefly described in Section 5.2.5.1) the spectral performance of the dichroic filters tilted by 45° , and find that to first order they do not induce significant spurious polarization in a polarization-sensitive receiver.

Although the primary mirror was recovered after the destruction of BLAST06, we decided that a new primary mirror was needed. The surface of the new mirror has an rms of $\sim 1.0 \mu\text{m}$, with the overall shape of the mirror good to $\sim 10 \mu\text{m}$. The secondary mirror was also recovered after BLAST06, and has been reused for BLAST-Pol (after resurfacing to remove some scratches). The estimated antenna efficiency of the telescope is $> 80\%$, with losses caused by both the roughness of the primary and the quality of the re-imaging optics. More information about the optical design and performance of the BLAST telescope can be found in Olmi (2002) and Pascale et al. (2008).

Temperatures of the primary and secondary mirrors do not remain constant throughout the flight. Diurnal temperature variations of $\sim 10^\circ \text{C}$ have been observed in previous BLAST flights (Pascale et al. 2008). These thermal variations result in changes to the radii of curvature of various optical surfaces. To compensate, the position of the secondary mirror with respect to the primary can be changed in flight by three stepper motor actuators. These actuators are also used to set the original tip/tilt alignment of the secondary (see Rex 2007). Analysis of the BLAST optical system indicates that the distance between the primary and secondary mirrors must be kept to within $100 \mu\text{m}$ to avoid significant image degradation at the shortest wavelength band.

Because of the insertion of a $\sim 2.5 \text{ mm}$ -thick sapphire half-wave plate (HWP; see Section 4.5 and Chapter 5) in the optical path, we have to compensate for the fact that submm light propagates for

~ 2.5 mm in a medium with refractive index of ~ 3.2 (Loewenstein et al. 1973, Cook & Perkowski 1985). We find that, in order to account for this effect, the distance between the back of the primary mirror and the window of the cryostat must be increased by 1.62 mm with respect to the BLAST06 optical configuration (see Figure 4.1).

4.3 Detectors

The BLAST-Pol focal plane consists of 149, 88, and 43 detectors at 250, 350, and 500 μm respectively. The bolometer detector array design is based on that of the *Herschel* SPIRE instrument (Bock et al. 1998, Rownd et al. 2003, Chattopadhyay et al. 2003). The three detector assemblies consist of silicon-nitride micromesh (“spider-web”) bolometers coupled with arrays of smooth-walled conical $f/5$ feed-horns. The feed-horns are designed for maximum aperture efficiency, requiring an entrance aperture of $2f\lambda$, where λ is the wavelength and f is the final optics focal number (see Griffin et al. 2002 for details on the optimization of the detector architecture). Detector sensitivity is limited by photon shot-noise from the telescope, a regime usually referred to as background-limited photometry (BLIP). The total emissivity for the warm optics of $\sim 6\%$ is dominated by blockage from the secondary mirror and supports. The estimated detector loading, noise equivalent flux densities (NEFDs) and sensitivities are shown in Table 4.2; preliminary analyses of the flight data in both the timeline and map domains indicate nominal sensitivity for BLAST-Pol at 500 μm .

The detectors are read out with an AC-biased differential circuit. The data acquisition electronics demodulate the detector signals to provide noise stability to low frequencies (< 30 mHz), which allows the sky to be observed in a slowly-scanned mode. Slow scanning is

Table 4.2. BLAST-Pol loading, BLIP noise, and nominal sensitivities

| Band [μm] | | 250 | 350 | 500 |
|--|---|---------|---------|---------|
| background power | [pW] | 27 | 20 | 15 |
| background NEP | $[\times 10^{-17} \text{ W Hz}^{-1/2}]$ | 10 | 7 | 5 |
| NEFD | $[\text{mJy s}^{1/2}]$ | 250–300 | 250–300 | 250–300 |
| depth (1σ , 5 hr, 1 deg ²) | $[\text{MJy sr}^{-1}]$ | 0.50 | 0.41 | 0.20 |
| depth (1σ , 50 hr, 1 deg ²) | $[\text{MJy sr}^{-1}]$ | 0.16 | 0.13 | 0.06 |
| $S_{Q,U}$ ($\sigma_p = 0.005$, 5 hr, 1 deg ²) | $[\text{MJy sr}^{-1}]$ | 282 | 231 | 113 |
| $S_{Q,U}$ ($\sigma_p = 0.005$, 50 hr, 1 deg ²) | $[\text{MJy sr}^{-1}]$ | 89 | 73 | 36 |
| A_v (5 hr, 1 deg ² , 10 K dust) | [mag] | 81 | 68 | 56 |
| A_v (50 hr, 1 deg ² , 10 K dust) | [mag] | 26 | 22 | 18 |
| A_v (5 hr, 1 deg ² , 20 K dust) | [mag] | 4.3 | 7.8 | 11 |
| A_v (50 hr, 1 deg ² , 20 K dust) | [mag] | 1.4 | 2.5 | 3.4 |

Note. — The noise equivalent flux densities (NEFDs) are from Pascale et al. (2008); the background power and noise equivalent power (NEP) are opportunely scaled to account for the fact that the loading on the detectors is reduced by a factor of two due to the polarizing grids (see Section 4.5). The nominal sensitivities $S_{Q,U}$ are computed as the threshold fluxes of a source needed for BLAST-Pol to obtain 0.5% polarization error bar. Although the detectors operate in near-BLIP conditions (compare the bolometer optical NEP in Table 4.1 with the background NEP in this table), in the sensitivity calculations we assume conservatively that detector noise is larger than the noise due to fluctuations in the background loading. If instead we were to consider the regime whereby the background radiation dominates over the detector noise and is fully unpolarized, the sensitivities would improve by a factor $\sqrt{2}$ due to the reduced loading. In the previous BLAST flights, the noise was always dominated by the background loading from the telescope struts and warm optics; in BLAST-Pol however, because each polarizing grid rejects half of the incoming radiation, the contribution of detector noise may no longer be negligible in the total noise budget, especially at 500 μm . We therefore choose to quote the more conservative sensitivity estimates. Finally, we convert the nominal BLAST-Pol sensitivities (for 0.5% polarization error bars) to optical extinctions A_v , following the prescription of Bianchi et al. (2003) and assuming a dust emissivity with spectral index $\beta = 2$. These values of optical extinctions are halved if one relaxes the requirement on the polarization error bars to 1%.

preferable to a mechanical chopper for mapping large regions of sky. The data are collected using a high-speed, flexible, 22-bit data acquisition system developed at the University of Toronto. The system can synchronously sample up to 600 channels at any rate up to 4 kHz. Each channel consists of a buffered input and an analog to digital converter. The output from 24 channels are then processed by an Altera programmable logic device, which digitally anti-alias filters and demodulates each input. The results then are stored to disk.

4.4 *Cryogenics*

The receiver consists of an optical cavity inside a long hold-time liquid-nitrogen and liquid-helium cryostat. Both the nitrogen and helium are maintained at slightly more than the standard atmospheric pressure during the flight to minimize loss due to pressure drop at altitude. A ^3He refrigerator maintains the detectors at 280 mK during flight. The self-contained, recycling refrigerator can maintain a base temperature of 280 mK with $30\ \mu\text{W}$ of cooling power for 4 days. It can be recycled within 2 hr. The ^3He refrigerator uses a pumped ^4He pot at $\sim 1\ \text{K}$ for cycling and to increase the hold time of the system. The pumped pot maintains 1 K with 20 mW of cooling power with outside pressure of $\sim 2000\ \text{Pa}$ or less. The entire optics box containing the re-imaging optics is also cooled to 1 K.

4.5 *Polarimetry*

Chapter 5 of this thesis is entirely dedicated to the description of BLAST-Pol's polarizing components and their pre-flight performance. However, here we give a brief overview for completeness and outline the strategy we adopt for optimal polarization recovery.

4.5.1 Polarization recovery strategy

In a complex balloon-borne instrument such as BLAST, there are potentially several sources of polarization systematics that need to be accounted for in the design of a polarimetric upgrade (e.g., pointing errors, detector/electronics response and noise, observation and scan strategy). In order to test for these effects, we perform “jackknife” simulations using BLAST06 observations of an unpolarized source (VY Canis Majoris [VY CMa]; Fissel 2008, private communication). We produce two maps of the same source using odd and even detectors, so to simulate the presence of polarizers with alternate (horizontal and vertical) grid orientation in front of adjacent detectors. In the case of an ideal polarimeter, a map obtained as the difference between the two sets of detectors should be null, because adjacent detectors sample perpendicular polarization angles. In reality, the detectors have different gains (optical efficiencies¹, η), which are difficult to intercalibrate at the required accuracy of 0.05% (for 1% error bars on a 5% polarized source) or less, and are affected by drifts on long timescales (low-frequency [1/f] noise). These systematics degrade our ability to unbiasedly recover the Stokes parameters Q, U in the sky.

We establish that further polarization modulation is needed to compensate for the differences in detector gains and for the presence of 1/f noise in the timelines. In particular, a half-wave plate (HWP; see Section 5.2.2) is an optical element that produces a polarization rotation of 180° . By continuously rotating or stepping the HWP, polarization modulation of the Stokes Q and U is thus achieved (at four times the rotation angle; see Equations 6.1 and 6.2). The use of a rotating HWP as a linear polarization modulator is a widespread technique

¹ Here we refer to gain or optical efficiency, η , as a combination of numerical factors, such as the bolometer responsivity, the feed-horn efficiency, and the pixel throughput.

at millimeter and submillimeter wavelengths (see, e.g., Hanany et al. 2005, Pisano et al. 2006, Savini et al. 2006, 2009, Johnson et al. 2007, Matsumura et al. 2009, Bryan et al. 2010b).

A simple argument can help us see how the presence of a HWP may compensate for the above effects. A bolometric (polarization insensitive) detector measures an intensity I ; by placing a vertical (horizontal) polarizing grid in front of it, the detector will now be only sensitive to light polarized perpendicularly to the grid wires, i.e. I_x (I_y), and $I = I_x + I_y$. The Stokes parameters *in the sky* are defined as $q_{\text{sky}} = (I_y - I_x) / I$ and $u_{\text{sky}} = (I_{y'} - I_{x'}) / I$, where the primes indicate that x', y' are defined in a reference frame that is rotated by 45° counterclockwise (CCW) with respect to x, y . Following the astronomers' convention, $\pm q_{\text{sky}}$ is oriented along the N-S (E-W) direction on the celestial sphere, while $\pm u_{\text{sky}}$ is oriented along NE-SW (SE-NW). Let us now assume that the HWP is ideal (we will tackle the HWP non-idealities in Chapter 5): a HWP rotation of $\theta = 45^\circ$ simply transforms $I_x \leftrightarrow I_y$ and $I_{x'} \leftrightarrow I_{y'}$. One can immediately see that the recovery of $\pm q_{\text{sky}}$ through a straight difference between two adjacent detectors would require very accurate knowledge of their optical efficiencies:

$$q_{\text{sky}} = \frac{d_1(\theta = 0^\circ) - d_2(\theta = 0^\circ)}{d_1(\theta = 0^\circ) + d_2(\theta = 0^\circ)} = \frac{\eta_1 I_y - \eta_2 I_x}{\eta_1 I_y + \eta_2 I_x}. \quad (4.1)$$

On the other hand, the presence of a HWP allows to unbiasedly recover the Stokes parameters in the sky by taking differences of adjacent detectors, at two HWP positions that are 45° apart, as follows:

$$\begin{aligned} q_{\text{sky}} &= \frac{[d_1(\theta = 0^\circ) - d_2(\theta = 0^\circ)] - [d_1(\theta = 45^\circ) - d_2(\theta = 45^\circ)]}{[d_1(\theta = 0^\circ) + d_2(\theta = 0^\circ)] + [d_1(\theta = 45^\circ) + d_2(\theta = 45^\circ)]} = \\ &= \frac{\eta_1 (I_y - I_x) + \eta_2 (I_y - I_x)}{\eta_1 (I_y + I_x) + \eta_2 (I_y + I_x)} = \frac{(I_y - I_x)}{(I_y + I_x)}. \end{aligned} \quad (4.2)$$

A similar expression can be derived for u_{sky} with $\theta = [22.5^\circ, 67.5^\circ]$.

An additional bonus of this strategy is that the differences between pairs of adjacent detectors indicated in Equation (4.2) effectively cancel out the portion of the noise that is correlated among detectors (in the assumption that two pixels observe the same patch of sky within a time much shorter than the typical timescale of noise correlation; this is in fact the case for BLAST-Pol as explained in the next section). As detailed in Chapter 6, this simplification, along with the assumption that the noise in each detector is white on timescales relevant to BLAST-Pol’s scan strategy, allows us to implement a “naive binning” solution for the complex problem of map-making.

Furthermore, the use of a HWP greatly simplifies the design of the polarizing grid array. Had we not included an additional polarization modulator, the polarizing grids would have needed to be oriented *also* at 45° and 135° for the recovery of u_{sky} , much like the design of Balloon Observations Of Millimetric Extragalactic Radiation and Geophysics (BOOMERanG; Masi et al. 2006). In that case, however, two bolometers, which are sensitive to orthogonal polarization directions (Polarization Sensitive Bolometer [PSB; Jones et al. 2003]), observe the sky through the same feed structure. Therefore, the inter-calibration of the optical efficiencies can be achieved with much higher accuracy than it would be possible with BLAST-Pol.

4.5.2 Polarimeter design

Photolithographed polarizing grids are mounted in front of each of the three feed-horn arrays (see photograph on the left side of Figure 4.3). The grids are patterned to alternate the polarization angle sampled by 90° from horn-to-horn and thus bolometer-to-bolometer along the scan direction (see scheme on the right side of Figure 4.3). BLAST-Pol

scans so that a source on the sky passes along a row of detectors, and thus the time required to measure one Stokes parameter (either Q or U ; see Equation 4.1) is just equal to the separation between bolometers divided by the scan speed. For the $250\ \mu\text{m}$ detector array where the bolometers are separated by $45''$, and assuming a typical scan speed of $0.1^\circ\ \text{s}^{-1}$, this time would be 0.125 s. This timescale is short compared to the characteristic low-frequency ($1/f$) noise knee for the detectors at 35 mHz (Pascale et al. 2008).

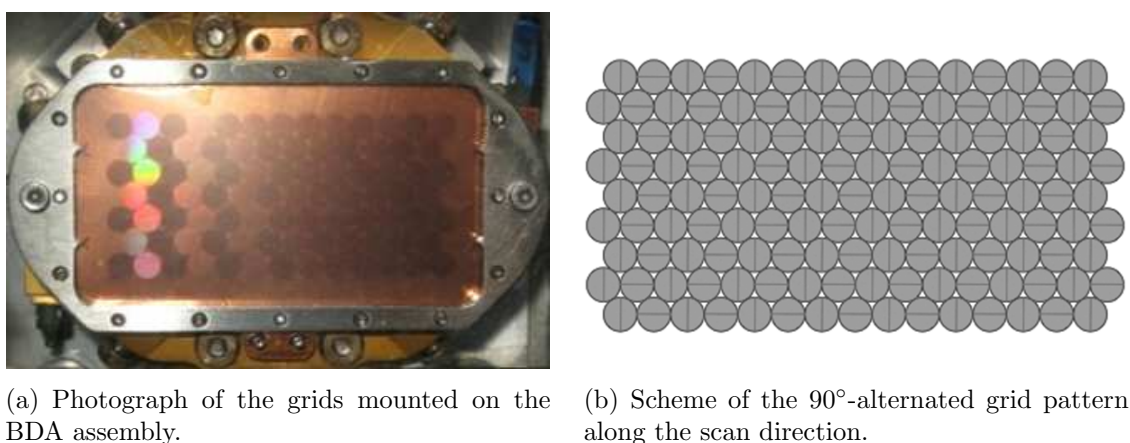


Fig. 4.3 BLAST-Pol photo-lithographed polarizing grids.

As discussed in the previous section, the additional polarization modulation required to unbiasedly measure the Stokes parameters is provided by a cryogenic achromatic HWP (see Chapter 5), which is incorporated into the optical design as shown in Figure 4.4. The HWP is mounted on the 4 K stage inside the optics box, 19.174 cm from the Cassegrain focus of the telescope; at this distance, the beam is wide enough to uniformly illuminate the optically-active area of the HWP (88 mm; see Section 5.2.3), without being vignetted, thus minimizing the modulation of any potential local defects of the plate.

The BLAST-Pol HWP is 10 cm in diameter and is constructed from 5 layers of birefringent sapphire, each $500\ \mu\text{m}$ in thickness. The layers are interspersed with one $6\ \mu\text{m}$ layer of polyethylene and glued together

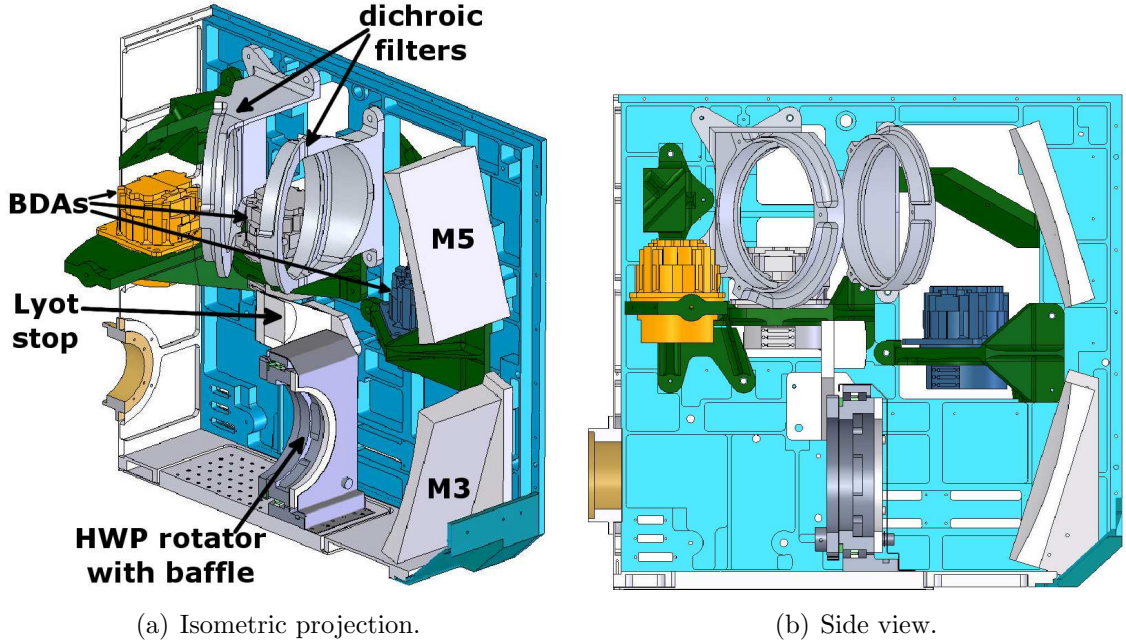


Fig. 4.4 Two cutaway views of the BLAST-Pol optics box. The light enters from the lower left and is re-imaged onto the bolometer detector arrays (BDAs). Dichroic filters split the beam into each of the BDAs for simultaneous imaging of the sky at 250, 350, and 500 μm . A modulating half-wave plate (HWP) is placed between the entrance to the optics box and M3, and polarizing grids are mounted directly in front of each of the BDAs. The HWP rotator, equipped with a protective blackened baffle, is mounted on the 4 K stage at 19.174 cm from the Cassegrain focus. The stepper motor that rotates the HWP is located outside the optics box.

with a hot-pressing technique (Ade et al. 2006). A broadband anti-reflection coating (ARC; employing metal-mesh filter technology, see Section 5.2.4.2) is glued to each surface of the HWP to match the impedance of sapphire to that of free space.

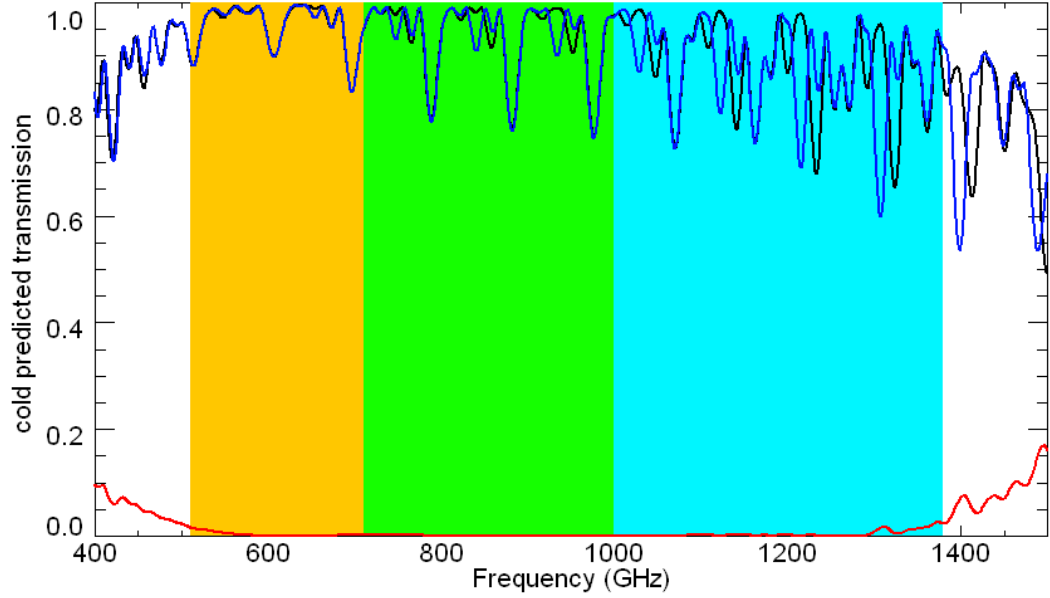
The HWP modulation efficiency is defined as $(T_{\text{cp}}^{0^\circ} - T_{\text{xp}}^{0^\circ}) / (T_{\text{cp}}^{0^\circ} + T_{\text{xp}}^{0^\circ})$, where the “co-pol” and “cross-pol” transmissions, $T_{\text{cp}}^{0^\circ}$ and $T_{\text{xp}}^{0^\circ}$, are the spectral transmission response of the HWP, with its axis at 0° , between parallel and perpendicular polarizers, respectively (as depicted in Figure 5.9). Figure 4.5 shows, as a function of frequency, the predicted co-pol/cross-pol transmissions and modulation efficiency of the BLAST-Pol HWP at 4 K. These are based on a comprehensive set of data taken with the HWP cooled at ~ 120 K (see Section 5.2.5.3),

which we extrapolate to 4 K.

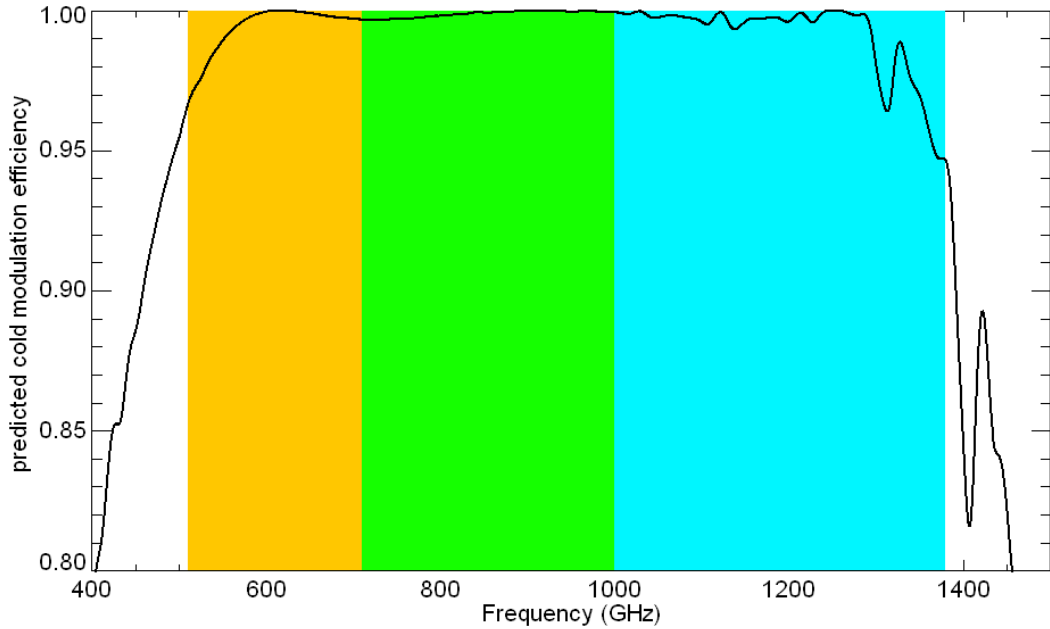
The band-integrated transmission of the HWP at its maxima is ~ 0.87 , ~ 0.91 , and ~ 0.95 at 250, 350, and 500 μm , respectively; whereas the band-integrated HWP cross-pol is $\lesssim 0.5\%$, $\lesssim 0.2\%$, and $\lesssim 0.5\%$, respectively. The band-integrated HWP modulation efficiency is $\sim 98.8\%$, $\sim 99.5\%$, and $\sim 99.0\%$ at 250, 350, and 500 μm , respectively. As anticipated, more details on the HWP and its ARC are given in Chapter 5.

We operate the HWP in a stepped mode, rather than a continuously rotating mode. The rotator employs a pair of thin-section steel ball bearings to a link stator and rotor (both made out of stainless steel), and is driven via a gear train and a G-10 shaft leading to a stepper motor outside the cryostat. A ferrofluidic vacuum seal is used for the drive shaft. The angle sensing at liquid Helium temperatures is accomplished by a potentiometer element making light contact with phosphor bronze leaf springs. During operation, we carry out spatial scans at four HWP angles spanning 90 degrees of rotation (22.5° steps). The rotator and encoder are based on the successful design of the Submillimeter Polarimeter for Antarctic Remote Observations (SPARO; Novak et al. 2003, Renbarger et al. 2004), and are shown in Figure 4.6.

The exposed metallic surfaces of the rotator assembly are blackened with a combination of silicon carbide (SiC), carbon black and epoxy to prevent unwanted reflections from stray light. Finally, in order to avoid spurious signals from light scattered off the moving parts of the rotator, the side of the rotator that faces the detectors is equipped with a protective blackened baffle (shown in Figures 4.4 and 4.6b), which has a circular aperture slightly larger than the optically-active area of the HWP (~ 90 mm in diameter).

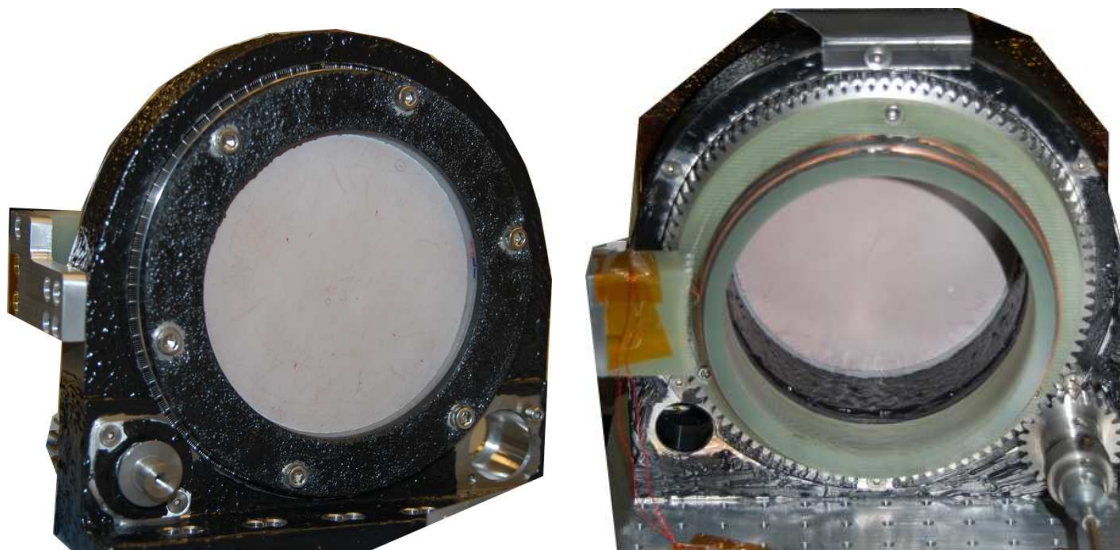


(a) The predicted transmissions through the cold HWP as a function of frequency. The black line shows the HWP transmission, $T_{\text{cp}}^{0^\circ}$, between two parallel polarizers ($Q = 1 \rightarrow Q = 1$) with the HWP axis at 0° . The blue line shows $Q = -1 \rightarrow Q = -1$ in the same reference frame (or equivalently $Q = 1 \rightarrow Q = 1$ with the HWP axis at 90°). The red line shows the transmission, $T_{\text{xp}}^{0^\circ}$, with the HWP axis at 0° between two perpendicular polarizers. The approximate extent of the BLAST-Pol bands is also indicated.



(b) Predicted modulation efficiency of the cold HWP as a function of frequency, obtained as $(T_{\text{cp}}^{0^\circ} - T_{\text{xp}}^{0^\circ}) / (T_{\text{cp}}^{0^\circ} + T_{\text{xp}}^{0^\circ})$. Note that the y -axis scale ranges from 0.8 to 1.

Fig. 4.5 Predicted performance of the BLAST-Pol HWP at 4 K, extrapolated from a set of spectral data collected with the HWP cooled at ~ 120 K (see Section 5.2.5.3). “Co-pol” and “cross-pol” transmissions, T_{cp} and T_{xp} , are defined as per Figure 5.9.



(a) This side of the rotator faces the M3 mirror inside the optics box. Any light scattered off the moving parts on this side of the rotator could potentially represent a source of spurious signal on the detectors, synchronous with the HWP rotation. To prevent this, we build a protective blackened baffle (not shown here) that has a circular aperture slightly larger than the optically-active area of the HWP (~ 90 mm).

(b) This side of the rotator faces the window of the optics box, about 19.1 cm away on the optical path. Visible in the photograph are the potentiometer, the gear train with the pinion assembly, and the back side of the blackened baffle, which is secured by one screw at the top of the stator, and two more on the 4K stage. On the left side is visible the encoder readout assembly with the leaf springs.

Fig. 4.6 BLAST-Pol rotator assembly with installed HWP.

4.6 Gondola

The BLAST-Pol gondola provides a pointing platform for the telescope and attaches to the balloon flight train. The gondola consists of two parts: an outer aluminum frame, which can be pointed in azimuth; and an inner aluminum frame, which points in elevation. Figure 4.7 shows a schematic layout of the gondola with several features labeled.

The outer frame is suspended from a $1.1 \times 10^6 \text{ m}^3$ helium balloon, provided by NASA's CSBF, through a steel cable ladder and parachute. Control systems, including flight computers and telemetry systems are mounted on the outer frame. Data are stored on solid state disks on the computers. Some portion of the data can be transmitted to a ground station by satellite links. The inner frame houses the

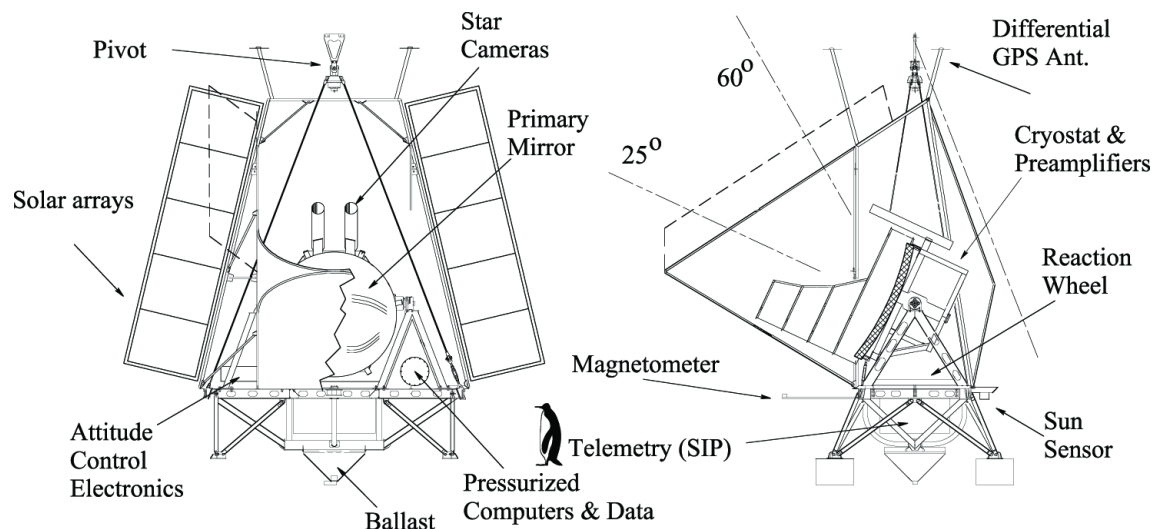


Fig. 4.7 Front and side schematic drawings of the BLAST gondola (from Pascale et al. 2008). A 1-m tall Emperor penguin is shown for scale. The inner frame, which can be pointed in elevation, consists of the two star cameras, the telescope and its light baffle, the receiver cryostat, and associated electronics. The telescope baffles and sunshields have been updated for BLAST-Pol, and are shown in Figure 4.8.

mirrors, the receiver, the receiver read-out electronics and the primary pointing sensors. These are all rigidly mounted with respect to each other on the inner frame in order to ensure that mechanical alignment is maintained throughout the flight.

To avoid large thermal changes in the optics both the inner and outer frames have attached sunshield structures. Figure 4.8 shows the BLAST-Pol sunshields. Shields on the outer frame are constructed from aluminized mylar and mounted on an aluminum frame, and are similar to those used in previous BLAST flights. In addition, for BLAST-Pol we design and build new shields, which are attached to a carbon fiber frame and are mounted to the inner frame. This 4-m shield allows us to point the telescope to within 45° of the Sun, in order to observe targets close to the Galactic Center (e.g., Lupus).

Telescope pointing is controlled by three motors. The azimuth pointing is controlled by a brushless, direct drive servo motor attached

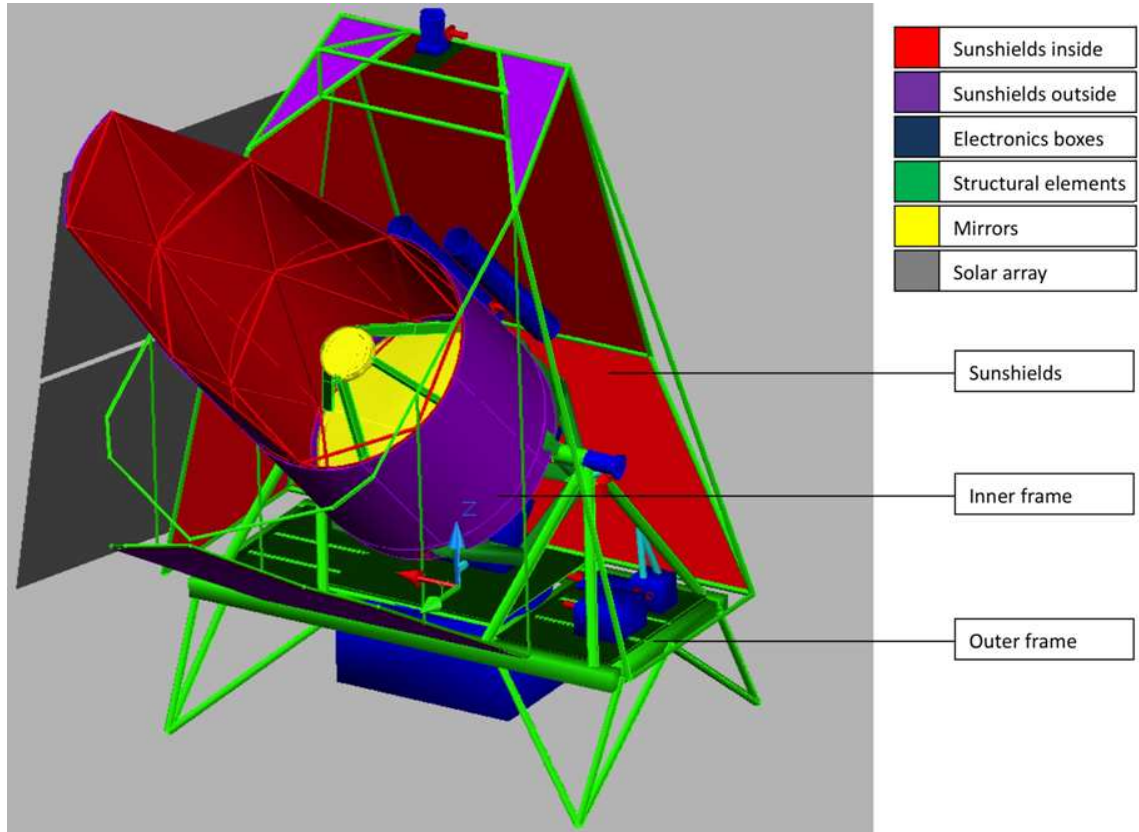


Fig. 4.8 A drawing of the BLAST-Pol gondola showing the inner and outer frame gondola structures, including the new inner frame sunshields that allow the telescope to point to a minimum azimuth distance of 45° from the Sun. Drawing credits: Juan Diego Soler.

to a high moment of inertia reaction wheel, and an active pivot motor which connects the cable-suspended gondola to the balloon flight train. The reaction wheel consists of a 1.5-m disk made of 7.6 cm thick aluminum honeycomb, with 48 0.9 kg brass disks mounted around the perimeter. The reaction wheel is mounted at the center of mass of the telescope, directly beneath the active pivot. By spinning the reaction wheel, angular momentum can be transferred to and from the gondola, allowing precise control over the azimuth velocity of the telescope with minimal latency. The active pivot motor provides additional azimuthal torque by twisting the flight train, and can also be used over long time

scales to transfer angular momentum to the balloon.

The elevation of the inner frame is controlled by a servo motor mounted on one side of the inner frame at the attachment point to the outer frame. A free bearing provides the connection point between the inner and outer frames, on the other side.

In-flight pointing is measured to an accuracy of $\sim 30''$ by a number of fine and coarse pointing sensors. These include fiber optic gyroscopes, two optical star cameras, a differential GPS, an elevation encoder, inclinometers, a magnetometer and a Sun sensor (a description of these devices can be found in Pascale et al. 2008). The star cameras are the primary pointing sensor for BLAST-Pol; LM was responsible for the hardware/software testing and deployment of both of them, as well as for the flight operations and post-flight pointing reconstruction. In the following section we briefly describe the components of the star-camera assembly, the principles of operation, and the in-flight performance. Incidentally, we mention that LM has participated in the software deployment and performance characterization of one star camera for the E and B Experiment (EBEX; Reichborn-Kjennerud et al. 2010).

4.7 *Star Cameras*

4.7.1 *Overview*

The BLAST-Pol star cameras are closely based on the successful BLAST design, and therefore we refer elsewhere for a thorough description of the theory, principles of operation and pattern-matching algorithms of these sensors (Pascale et al. 2008), their hardware implementation and overall performance (Rex et al. 2006, Rex 2007). Nevertheless, it is useful to review here the design requirements and the basic equations that allow an optimization of the optics.

Four primary factors drive the design of the star cameras:

1. an absolute pointing accuracy of $\sim 5''$ is required to over-sample the diffraction-limited size of the $250 \mu\text{m}$ beam;
2. integration times have to be short enough to avoid significant smearing of stars in each frame taken at the typical scan angular velocity of the gondola (0.1° s^{-1});
3. the system must always detect stars to calibrate gyroscope drifts;
4. the frequency of the solutions must be high enough to control the $1/f$ random walk noise in the integrated gyroscopes ($4'' \text{ s}^{-0.5}$; Pascale et al. 2008).

We incorporate two star cameras for redundancy, and to enable increased positional accuracy in the post-flight processing. In order to meet the above requirements, each star camera is designed to detect in each frame several stars² with significance $\geq 5\sigma$. The signal-to-noise ratio (SNR) of a star detection depends upon its effective temperature (color), the brightness of the sky background at balloon float altitude, and the optical properties of the camera itself.

The flux of a star of visual magnitude m_v can be written as $I_{\text{tot}} = I_0 10^{-0.4m_v} [\text{W m}^{-2}]$, where I_0 is the reference zero-magnitude flux. Assuming that stars radiate with a blackbody spectrum at temperature T_{eff} , the flux density reads:

$$\begin{aligned} I_\lambda &= I_{\text{tot}} \frac{B(T_{\text{eff}}, \lambda)}{\int B(T_{\text{eff}}, \lambda) d\lambda} \\ &= I_0 \pi 10^{-0.4m_v} \frac{B(T_{\text{eff}}, \lambda)}{\sigma_{\text{SB}} T_{\text{eff}}^4} \left[\frac{\text{W}}{\text{m}^2 \text{ nm}} \right], \end{aligned} \quad (4.3)$$

² At the very least 1–2 stars per frame are necessary for the post-flight pointing reconstruction.

where $B(T_{\text{eff}}, \lambda)$ is the Planck function, and σ_{SB} is the Stefan–Boltzmann constant.

The actual signal from a star received by a CCD pixel on the star camera depends upon several parameters, as follows:

$$S_{\text{star}} = \frac{\pi d_l^2}{4P} \eta t \int Q_e T_\lambda I_\lambda \frac{\lambda}{hc} d\lambda \quad [\text{e}^- \text{pix}^{-1}] \quad (4.4)$$

where: d_l is the diameter of the lens coupled to the CCD; P is the size of the lens PSF in number of pixels (the lens is not diffraction-limited and typically $P = 2\text{--}4$); η is the total optical transmission of the optics (we estimate $\eta \sim 0.95$ using Equation 4.4, by performing aperture photometry on star-camera frames of a bright star of known T_{eff} , after having measured all the other unknown parameters independently); t is the exposure time in seconds; Q_e is the quantum efficiency of the device, expressed as electrons generated per incident photon, where 1 represents 100% efficiency (see Table 4.3 for its wavelength dependence); and T_λ is the optical filter response (see Table 4.3).

The star cameras are operated during the daytime; even at balloon float altitudes, the noise in each star-camera frame is dominated by the background flux from the sky (see also Section 4.7.3). The background signal from the sky in one pixel can be written as:

$$S_{\text{sky}} = \frac{\pi d_l^2}{4} \eta \Omega_p t \int Q_e T_\lambda B_\lambda^{\text{sky}} \frac{\lambda}{hc} d\lambda \quad [\text{e}^- \text{pix}^{-1}] \quad (4.5)$$

where Ω_p is the solid angle of one pixel projected onto the sky, and B_λ^{sky} is the sky brightness, which at balloon altitudes approaches a few tens of $\text{nW sr}^{-1} \text{cm}^{-2} \text{nm}^{-1}$ (Rex 2007). In this photon-noise limited regime (see Section 4.7.3), the noise from S_{sky} is Poissonian in nature,

Table 4.3. Specifications of the two BLAST-Pol star cameras

| feature | spec |
|-------------------------------------|---|
| Camera | QImaging Retiga-EXL ^a |
| CCD sensor | Sony ICX285 ^b |
| Light sensitive pixels | 1392 × 1040 |
| Pixel size | 6.45 μm × 6.45 μm |
| Quantum efficiency at peak response | 60% |
| Range of maximum spectral response | 400–800 nm |
| Digital output | 14 bit |
| Well depth | 18,000 e ⁻ |
| Readout noise | 6.5 e ⁻ |
| Dark current | 0.15 e ⁻ pix ⁻¹ s ⁻¹ |
| Lens diameter | 100 mm |
| Focal length | 200 mm |
| Lens f _# | 2 |
| Nominal plate-scale | 6.652'' pix ⁻¹ |
| Camera FOV | 2.57° × 1.92° |
| Filter cut-off | 600 nm (Nikon R60 ^c) |
| Computer model | PC/104-Plus MSM800SEV ^d |

Note. — The numbers quoted are for a readout frequency of 10 MHz, and with the “high sensitivity” mode enabled^a. A plot of the quantum efficiency as a function of wavelength is given on the second page of the camera datasheet^a. The CCDs can be cooled to 0° C during normal operations by means of a thermoelectric Peltier cooler.

^awww.qimaging.com/products/datasheets/retiga-exl.pdf

^bwww.ccd.com/pdf/ccd_285.pdf

^cThe filter spectral response is shown in Figure 4.6 of Rex (2007)

^dwww.qscomp.cz/Pdf/msm800sev.pdf

and the total SNR from a star reads:

$$\text{SNR}_{\text{star}} \simeq \frac{S_{\text{star}}}{\sqrt{S_{\text{sky}}}} \propto d_l \sqrt{\frac{t}{\Omega_p}} \propto d_l f \sqrt{t} \quad (4.6)$$

where f is focal length of the star-camera lens and $\Omega_p \propto f^{-2}$.

We require each star to be detected at least with a 5σ significance, $\text{SNR}_{\text{star}} \gtrsim 5$. We also require that the CCD does not saturate, i.e. $W_{e^-} > S_{\text{sky}} \propto (d_l/f)^2 t$, where W_{e^-} is the electron well depth of each pixel (Table 4.3).

The two inequalities above allow us to optimize the optical parameters of the device; in particular, the most effective way to fulfill both conditions is to maximize f , and hence minimize the pixel FOV, with the caution of keeping P in the range 2–4 pix, in order to avoid dilution of the signal on an overly sampled PSF. The SNR is also improved by choosing an optical filter that selects a wavelength region where the sky brightness is relatively low, and the average star brightness is relatively high; Alexander et al. (1999) find that a red filter with cut-off at 600 nm enhances the average star signal over the background. In addition, a 1.2 m long cylindrical baffle is attached to the front of each camera to reduce stray-light contamination beyond 10° from the optical axis. The star cameras use a Nikon lens with a 200 mm focal length and a 100 mm aperture to produce a $2.57^\circ \times 1.92^\circ$ FOV with $\sim 6.65''$ pixels. With this lens, coupled with a red Nikon R60 filter, the devices can detect $m_v = 9$ stars at a 5σ level in ~ 100 ms of integration time. Figure 4.9 shows an exploded view of the star-camera assembly, while Figure 4.10 is a collage of the BLAST-Pol star-camera hardware.

Each camera is controlled by its own PC/104-Plus, 500 MHz AMD computer, which commands the CCDs via FireWire, controls the focus and aperture size using stepper motors via a serial port, and regulates

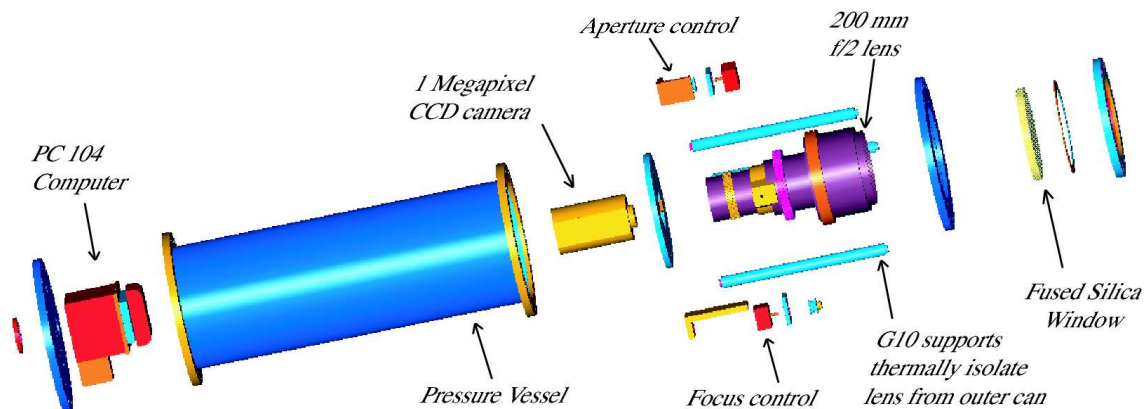


Fig. 4.9 Mechanical drawing of star-camera assembly. The device comprises a CCD camera coupled to 200 mm f/2 lens with a $2.57^\circ \times 1.92^\circ$ FOV. The camera, along with the aperture/focus adjustment mechanisms and the temperature/pressure sensors (not shown here) are controlled by a PC/104-Plus computer. The entire system is contained in a pressure vessel to maintain atmospheric pressure for the mechanical hard drive, provide a stable thermal environment and protect the system mechanically. (from Rex et al. 2006).

the temperature of the camera using a small USB DAQ module. The entire system is contained in a pressure vessel to allow the operation of the mechanical hard drive, control the thermal environment, and maintain mechanical rigidity; a sensor continuously monitors the pressure inside the vessel. Control of the thermal environment is crucial as the focus position is very sensitive to changes in the lens temperature.

The fully-autonomous software controlling the camera in flight provides real-time pointing information, at a rate of ~ 1 Hz, by analyzing the star patterns in the CCD frames. The pointing algorithm locates blobs with $\text{SNR} > 5$ in the current camera image, rejecting the known bad pixels (see Section 4.7.2). The best-fit positions of star candidates are then used by a pattern recognition algorithm to identify a unique constellation matching the observed angular separations in a star catalog (Guide Star Catalog 1.1; Lasker et al. 1987). The magnitude limit of the catalog is chosen manually (9 mag achieves sufficient completeness), and no brightness information for the stars is otherwise used.

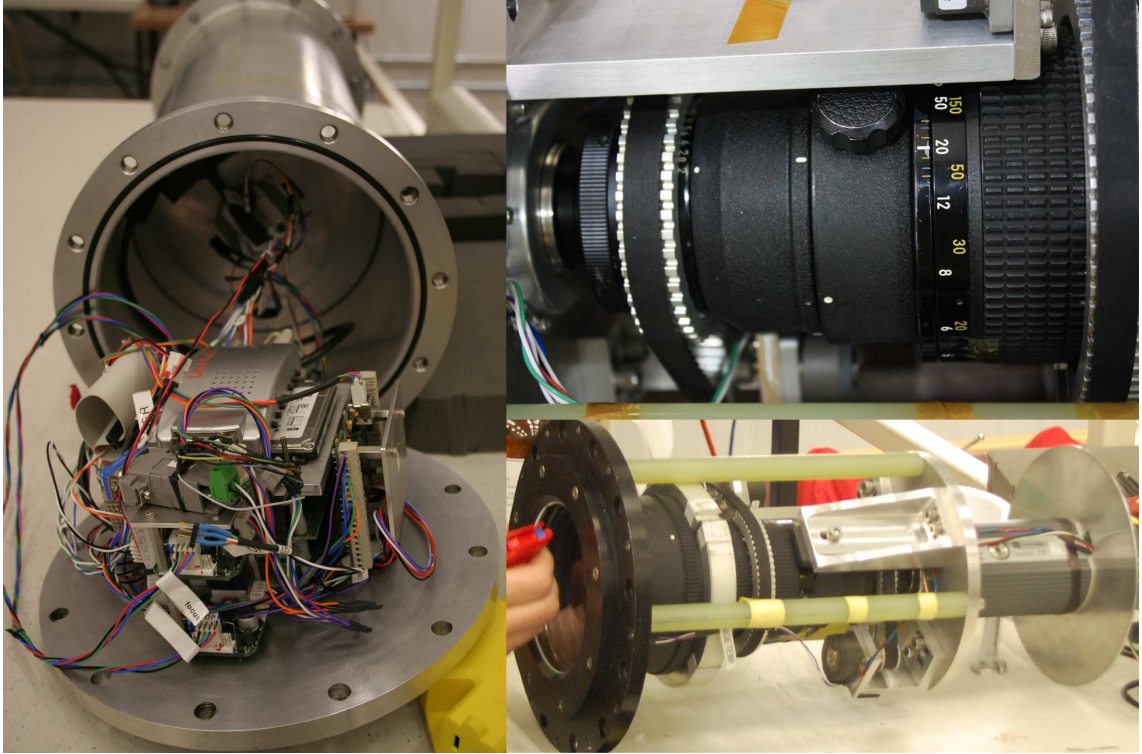


Fig. 4.10 A collage of photographs of the BLAST-Pol star-camera hardware. *Left*: view from behind of the pressure vessel, with back flange open to show the PC/104-Plus computer assembly. *Top right*: a closeup view of the Nikon lens, with retrofitted belts and gears for the focus and aperture adjustment mechanisms. *Bottom right*: side view of the star-camera body, whose exploded mechanical drawing is shown in Figure 4.9. Photo credits: Steve Benton.

The algorithm is aided by an approximate “guess” pointing solution from the flight computer (a combination of the pointing information registered by the several coarse sensors on board, see Section 4.6), required to be accurate to about 5° in order to reduce the number of candidate star identifications. A “Lost in Space” algorithm based on the Pyramid technique (Mortari et al. 2004) is also implemented to be used if the guess solution is found to be unreliable; however, such an instance never occurred during the three BLAST flights.

Once the CCD blob centroids are matched to i stars with known coordinates $[\alpha_i, \delta_i]$, the pointing solution is calculated in terms of the celestial coordinates of the center pixel $[\alpha_0, \delta_0]$, and the roll of the

camera, ϕ_0 . A star-camera frame is modeled to be a perfect gnomonic tangent-plane projection, with the tangent point at $[\alpha_0, \delta_0]$, and rotation ϕ_0 with respect to the local meridian; the coordinates of each matched star, $[\alpha_i, \delta_i]$, are projected into the plane of the CCD. The rms distance between the CCD and model star coordinates is then minimized using an iterative Newton solver with respect to the three model parameters, $[\alpha_0, \delta_0, \phi_0]$. This procedure produces pointing solutions with uncertainties of $\sim 3.5''$ and $\sim 200''$ for the position of the tangent point and of the roll, respectively. A post-flight comparison of simultaneous pointing solutions from both cameras will result in an rms uncertainty of $\lesssim 2''$ (see Section 4.7.4).

4.7.2 Bad/hot pixels

As with every CCD, we need to exclude some bad (or, more appropriately, “hot”) pixels, whose brightness increases steadily with integration time on dark frames. In general, this is true for all active pixels, because of dark currents (see next section); however, the brightness of hot pixels increases with time much more rapidly than that of other pixels. An overdensity of a few adjacent hot pixels in a star-camera frame could lead to a spurious star detection.

Hot pixels are individual sensors on the CCD with higher than normal rates of charge leakage. They can appear as small pixel-sized bright points of light on longer exposures. Because the rate of charge leakage is the same for a given pixel over time, the longer the exposure, the brighter they appear, even on dark frames. This charge leakage is worse at higher temperatures, even a 10°C difference can cause a noticeable increase in the number of hot pixels (on frames taken with the same exposure time).

It is worth making here a clear distinction between hot, stuck, and

dead pixels. Stuck pixels always read high (maximum) on all exposures, whereas dead pixels read zero on all exposures. The BLAST-Pol star-camera CCDs appear to have neither stuck nor dead pixels, only hot pixels. Here we describe our methodology to isolate them.

We take several dark frame, with exposure times ranging from 100 ms to 10 s. We then create a synthetic image which is the weighted mean of all the dark frames taken, where the weights are the inverse of the exposure time. We normalize such a synthetic image with the image with shortest integration time (100 ms). This image should now contain information on the relative rate of charge leakage in every pixel, averaged over several frames. We perform a weighted mean because otherwise only the long-exposure frames would dominate. We can now make a histogram of such image (see Figure 4.11) and isolate the pixels with counts $\geq 5\sigma$, where σ is the standard deviation calculated across all the synthetic image. 5σ is a somewhat arbitrary but very conservative choice. We find about ~ 70 hot pixels per camera, which is a mere 0.005% of the whole frame and is expected in every CCD. This method is found to be in extremely good agreement with a visual inspection of a long-exposure dark frame.

4.7.3 Noise model

In a CCD image sensor, the noise consists of undesirable signal components arising in the electronic system, and inherent natural variation of the incident photon flux. The three primary sources of noise in a CCD imaging system are photon noise, dark-current noise, and read-out noise.

Photon noise (sometimes referred to as shot noise) results from the intrinsic statistical variation in the arrival rate of photons incident on the CCD. Photoelectrons generated within the semiconductor device

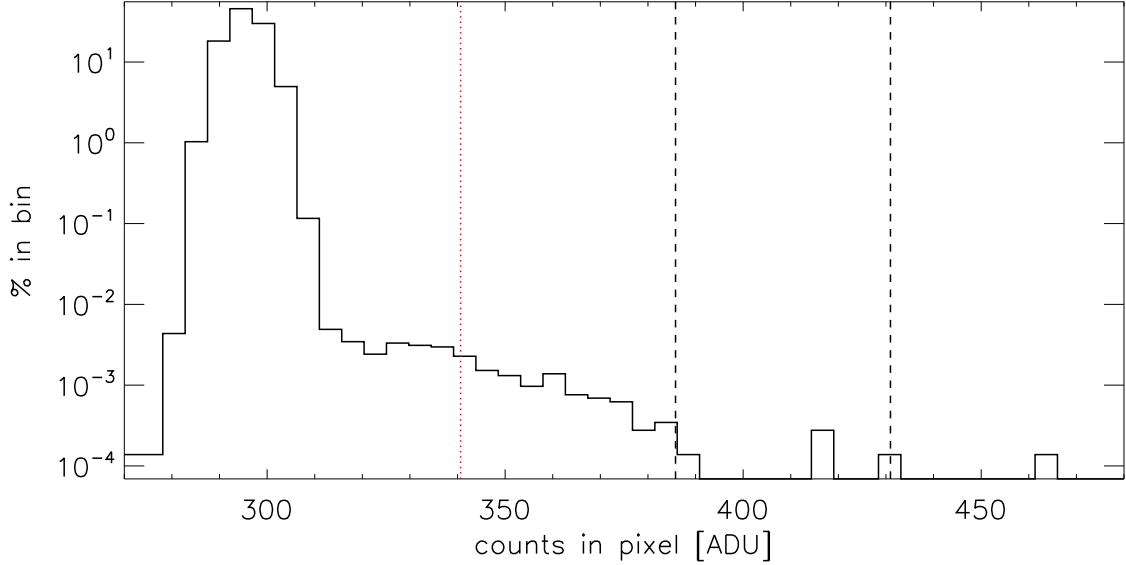


Fig. 4.11 Histogram of the synthetic frame obtained as the weighted mean of dark frames taken at different exposure times. The dotted red vertical line indicates the 5σ threshold chosen to discriminate bad/hot pixels. We also show for reference the 10σ and 15σ levels (dashed black lines).

constitute the signal, the magnitude of which is perturbed by fluctuations that follow the Poisson statistical distribution of photons incident on the CCD at a given location. The photon noise is therefore equal to the square-root of the signal.

Dark-current noise arises from statistical variation in the number of electrons thermally generated within the silicon structure of the CCD, which is independent of photon-induced signal, but highly dependent on device temperature. The rate of generation of thermal electrons at a given CCD temperature is termed dark current. Similarly to photon noise, dark-current noise follows a Poisson distribution, and is equivalent to the square-root of the number of thermal electrons generated within the image exposure time. Cooling the CCD reduces the dark current dramatically, and in practice, high-performance cameras are usually cooled to a temperature at which dark current is negligible over a typical exposure interval. The BLAST-Pol star cameras have a

nominal dark current, D_c , of $0.15 \text{ e}^- \text{ pix}^{-1} \text{ s}^{-1}$ at 0° C . Their operating temperature is typically around 20° C in flight. Although the CCDs may be cooled to 0° C via a thermoelectric Peltier cooler, we do not make use of this feature because at 20° C dark currents are negligible compared to the sky background, as explained later in this section.

Readout noise is a combination of electronic noise components inherent to the process of converting CCD charge carriers into a voltage signal for quantification, and the subsequent processing and analog-to-digital conversion. The major contribution to readout noise is usually due to the on-chip preamplifier, and this noise is added uniformly to every image pixel. High-performance camera systems utilize design enhancements that greatly reduce the level of readout noise. The BLAST-Pol star cameras have nominal readout noise, R , of $6.5 \text{ e}^- \text{ pix}^{-1}$ (rms) when using a readout frequency of 10 MHz (see Table 4.3).

The photon noise contribution to the total noise budget is a function of the signal level. The measured signal, S , depends upon several parameters, as described in Section 4.7.1. In a CCD imaging system, the number of photoelectrons generated per pixel, $N_{e^-} = S_{\text{star}} + S_{\text{sky}}$ (as given by Equations 4.4 and 4.5), is converted in analog-to-digital units (ADUs) per pixel as follows:

$$S = \mathfrak{R} \times N_{e^-}, \quad (4.7)$$

where \mathfrak{R} is the intrinsic responsivity (or gain) of the camera, which is nominally the ratio between the analog-to-digital converter (ADC) output resolution (the ADC has a maximum resolution of 14-bit, thus 2^{14} ADU) and the electron well depth of each pixel ($W_{e^-} = 18,000 \text{ e}^-$, see Table 4.3), and therefore is expressed in ADU/e^- .

We can now write the total noise budget, σ_S , in ADUs per pixel as:

$$\sigma_S = \mathfrak{R} \times \sqrt{N_{e^-} + D_c t + R^2}, \quad (4.8)$$

and therefore the variance reads:

$$\sigma_S^2 = \mathfrak{R} S + \mathfrak{R}^2 D_c t + \mathfrak{R}^2 R^2. \quad (4.9)$$

Because photon noise is an inherent property of CCD signal detection, which cannot be reduced by camera design factors, it represents a noise floor that is the minimum achievable noise level. Consequently, it is desirable to operate an imaging system under conditions that are limited by photon noise, with other noise components being reduced to negligible (very much like the background-limited photometry, BLIP, of infrared and submm detectors; see Section 4.3). The integration time can be increased to collect more photons and increase the SNR, until a point is reached at which photon noise exceeds both the read-out noise and dark-current noise. Above this exposure time, the image is said to be photon-noise limited. As discussed in Section 4.7.1, star cameras operating at balloon float altitudes with the exposure times required to detect $m_v = 9$ stars at a 5σ (~ 100 ms) are always photon-noise limited because of the high background flux from the sky.

We see from Equation (4.7) that the signal measured by the camera is directly related to the number of photoelectrons generated per pixel, N_{e^-} , via the intrinsic gain of the camera, \mathfrak{R} . It is therefore of utter importance to pinpoint experimentally the actual value of \mathfrak{R} , primarily to have full control over the filling level of the electron well and thus avoid saturating the sensor. Furthermore, we see from Equation (4.8) that the noise level also depends directly upon \mathfrak{R} ; the knowledge of \mathfrak{R} enables a prompt estimate of the noise corresponding to a signal S .

In the photon-noise limited regime, the terms $D_c t$ and R^2 in Equation (4.9) are negligible, and the variance has a linear relationship with the signal. When the camera observes a uniform background, our best estimate of the signal S is the mean value of a frame, μ_f , in ADUs, once the bad/hot pixels have been masked away (see Section 4.7.2). Similarly, our best estimate of σ_S^2 is the variance of a frame with masked bad pixels, which we will refer to as σ_f^2 . In practice, we will see that for our purposes it is convenient to introduce an additional offset, O_f , such that $\sigma_f^2 = \mathfrak{R} \times (\mu_f - O_f)$. The error bars on the mean are given by Poisson statistics, $\sigma_P = \sqrt{2^{14} \mu_f / W_{e^-}}$. By taking a series of frames at different exposures times (within the photon-noise limited regime), we can therefore make a plot of frame variance versus mean and perform a linear fit: the slope will be the measured gain, which can be compared to the nominal one.

Here we describe our operational strategy to measure the intrinsic gain of the BLAST-Pol star cameras before flight. We point the camera at a background intrinsically as uniform as possible in brightness. This is either a white background in the laboratory (with diffuse, not direct, light reflected on it), or a patch of clear sky, during the daytime. We take exposures at different integration times, making sure that we sufficiently sample the regime in which μ_f falls within the range 20–60% of the saturation value (2^{14} ADU), i.e. not readout/dark-current noise dominated and not saturated.

Often the frames have a large-scale gradient due to non-uniform illumination of the CCD, or to aberrations in the optics. To prevent our results to be biased by such gradient, we select a region of interest (ROI) of 200 by 200 pixel at the center of the frames, namely where the optics-generated gradient is minimized. We check that the frame is uniform within the ROI to a 1–2% level, and we calculate μ_f and

σ_f^2 within this ROI for each frame. We now make a diagnostic plot of μ_f versus exposure time, as shown in Figure 4.12, that allows us to quantitatively identify the linear regime of operation of the camera.

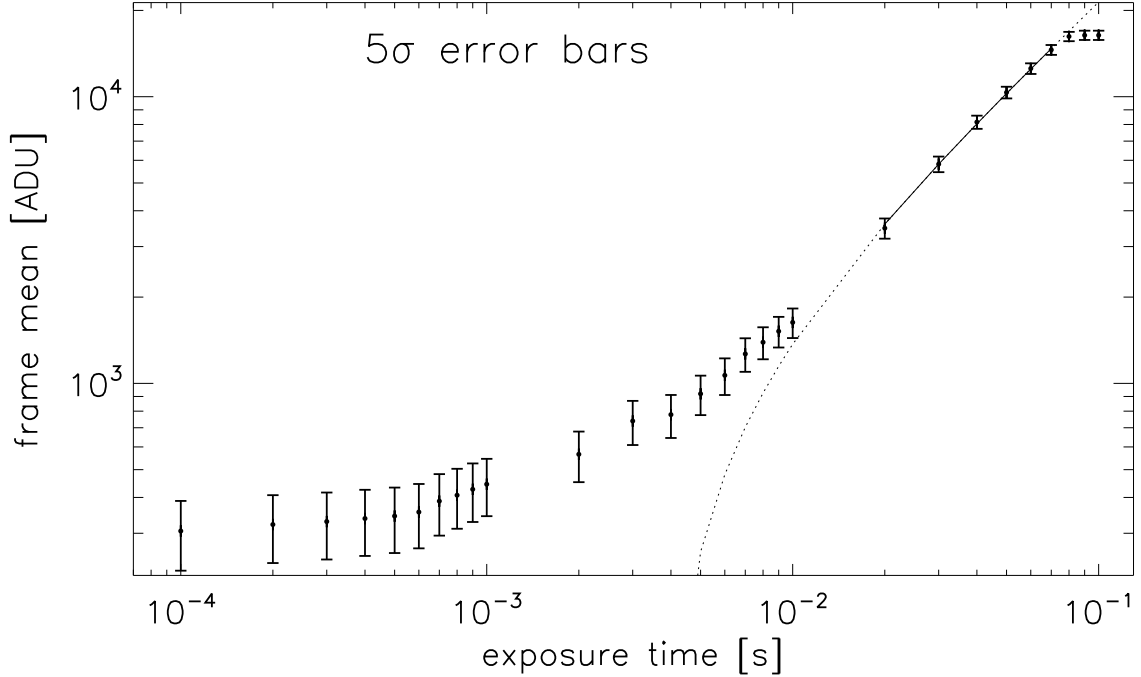


Fig. 4.12 Plot of frame mean, μ_f , as a function of exposure time, t . The error bars are given by Poisson statistics, $\sigma_P = \sqrt{2^{14} \mu_f / W_{e^-}}$, and are drawn as 5σ for better visualization. A linear fit (dotted line) is performed only in the photon-noise limited regime (between 20 and 70 ms; solid line), where the illumination level of the CCD scales linearly with t . At the long exposure time end, we can clearly recognize the saturation point of the camera at about $\sim 2^{14}$, whereas below 0.01 s the frame starts to be dominated by readout noise, reaching a plateau at about 300 ADU.

In Figure 4.13, we show the plot of σ_f^2 versus μ_f , with a linear fit performed in the photon-noise limited regime (in this case between 20 and 70 ms, as measured in Figure 4.12). For both star cameras, the measured intrinsic gain is in very good agreement with the nominal one, which is $2^{14} \text{ ADU} / 18,000 e^- = 0.91$. We find $\mathfrak{R} = (0.91 \pm 0.02) \text{ ADU}/e^-$ for one star camera, and $\mathfrak{R} = (0.90 \pm 0.02) \text{ ADU}/e^-$ for the other one, where the uncertainty is obtained following Section 15.3 of Press et al. (1992). We also find that the offset O_f is always compatible with zero, confirming that in the photon-noise limited regime the contributions of

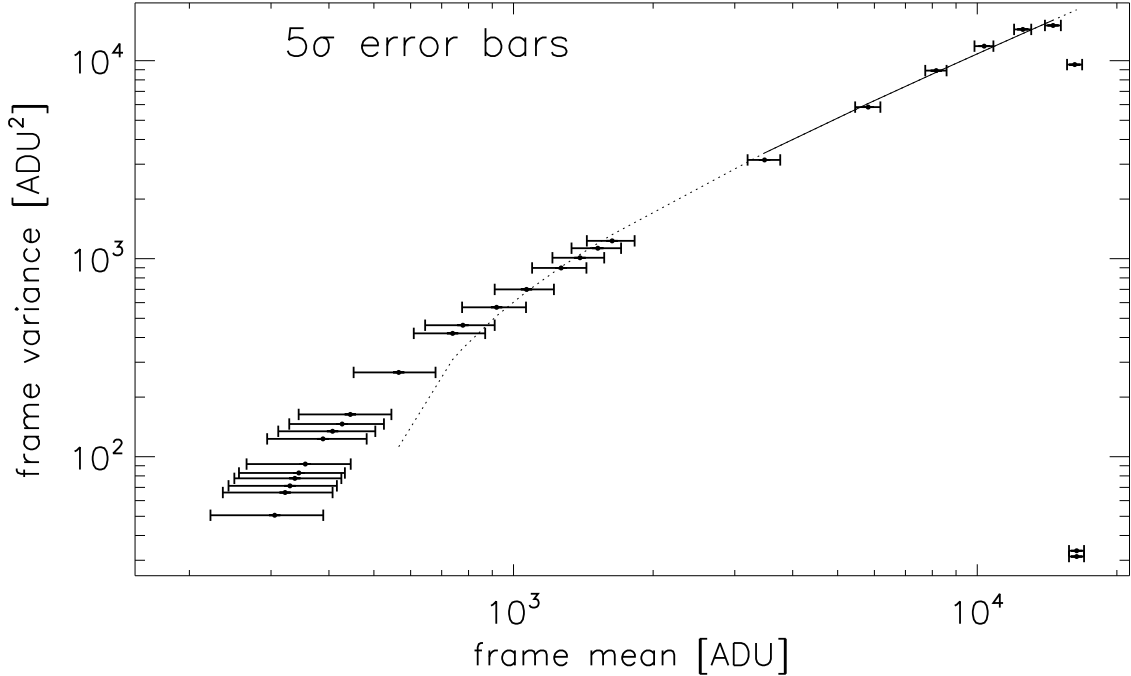


Fig. 4.13 Plot of frame variance, σ_f^2 , as a function of frame mean, μ_f . The x -error bars are given by Poisson statistics, $\sigma_P = \sqrt{2^{14} \mu_f / W_{e^-}}$, and are drawn as 5σ for better visualization. The y -error bars are not drawn for visual clarity. A linear fit (dotted line) is performed only in the photon-noise limited regime (between 20 and 70 ms; solid line), where the illumination level of the CCD scales linearly with the exposure time. The slope of such fit gives the intrinsic gain of the camera. The sharp drop in variance for $\mu_f \sim 2^{14}$ indicates the camera saturation point. On the other hand, for small values of μ_f , we clearly see how the readout and dark-current contributions to the total noise budget (as defined in Equation 4.9) become more important than the photon noise.

readout and dark-current noise to the total noise budget are negligible.

4.7.4 Post-flight pointing reconstruction

The post-flight pointing reconstruction is needed to estimate, at each detector sample, the rotation (attitude) of the gondola with respect to the celestial sphere as a function of time, providing right ascension (α), declination (δ), and rotation angle (ϕ or “roll”). The post-flight pointing reconstruction only makes use of the fiber optic gyroscopes and the star cameras. The star cameras provide absolute attitude on

an unevenly sampled time grid (~ 1 Hz), with an accuracy of $< 2''$ rms, while the gyroscopes are sampled at the same rate as the bolometers (100 Hz; “fast channels”). The gyroscopes are used to optimally interpolate the pointing information between two consecutive star camera solutions.

Each star camera solution is sampled at a known phase with respect to the detectors, whereas the bolometer and gyroscope sampling is synchronized. The integration of the angular velocities as measured by the gyroscopes gives an estimate of the gondola attitude; the star camera is used to correct the random walk drift induced by the integrated gyroscope noise ($4'' \text{ s}^{-0.5}$; Pascale et al. 2008) and to give an estimate of the integration constant.

As extensively described in Pascale et al. (2008), the pointing reconstruction algorithm is based on the multiplicative extended Kalman filter (Markley 2003) technique used by the Wilkinson Microwave Anisotropy Probe (WMAP; Harman 2005). The Kalman filter allows to incorporate the correlated uncertainties on the three model parameters for Ra, Dec, and roll, $[\alpha_0, \delta_0, \phi_0]$, which are returned as solutions by the star camera pointing code (see Section 4.7.1). The filter thus provides an optimally-weighted attitude reconstruction, which simultaneously accounts for both the integrated gyroscope noise and the uncertainty on the star camera solutions.

Using just one star camera and the digital gyroscopes, the final attitude reconstruction for the BLAST06 campaign is found to be $\lesssim 4''$ rms (Pascale et al. 2008). The achieved precision is more than sufficient to over-sample the diffraction-limited size of the $250 \mu\text{m}$ beam. Using stacking analysis, we independently estimate the absolute pointing accuracy for BLAST06 to be $< 2''$, with random pointing errors $< 3''$ rms (see Section A.6 in Appendix A).

We are currently carrying out a similar post-flight pointing reconstruction for the BLAST-Pol 2010 flight. Figure 4.14 shows preliminary results of the pointing reconstruction for about 300 s of observations of Centaurus A, obtained by integrating the gyroscopes between consecutive solutions from one star camera. The accuracy of the process can be assessed by estimating the residuals between the integrated pointing solution and the star camera positions³. Histograms of the yaw ($\simeq \alpha \cos \delta$) and pitch ($\simeq \delta$) residuals (shown in Figure 4.15) suggest that the overall pointing performance will reach that of BLAST06.

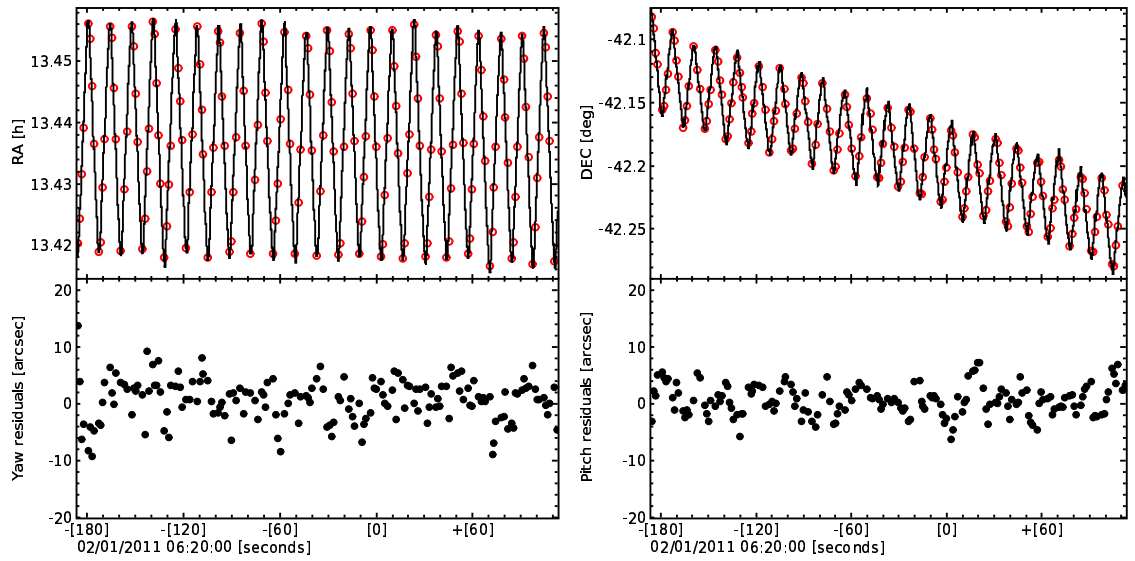


Fig. 4.14 An example of pointing reconstruction for 300 s during a scan of Centaurus A (NGC 5128) from the BLAST-Pol 2010 flight. In the top panels, the solid black lines represent the reconstructed pointing solution obtained by integrating the gyroscopes between consecutive solutions from one star camera (red empty circles). In the bottom panels, we show the residuals as yaw ($\simeq \alpha \cos \delta$) and pitch ($\simeq \delta$).

The post-flight pointing reconstruction is an iterative process. Firstly, the star camera pointing code (see Section 4.7.1) is run again on the whole flight length, using the same star candidates as those found in

³ A better metric to quantify the absolute accuracy of the pointing reconstruction is to compare the pointing solution reconstructed by integrating the gyroscopes onto one of the two star cameras, with the positions reported by the other star camera. However, this procedure requires the precise knowledge of the rotation angle between the boresight directions of the two star cameras, which we are still striving to pinpoint at this stage of the analysis.

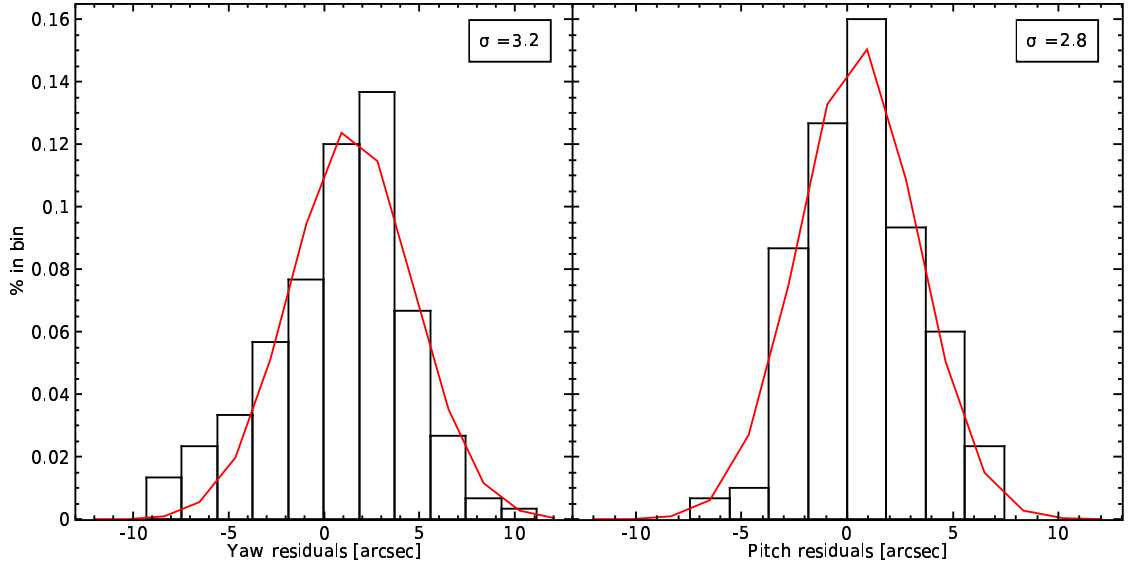


Fig. 4.15 Histograms of the yaw and pitch residuals from Figure 4.14. The red lines show Gaussian fits whose standard deviations are reported in the top right corners.

flight and the pointing solution calculated by the flight computer as “guess” solution. This first run requires a minimum of 3 star candidates per camera frame to calculate a robust solution, which is found for about half of the usable frames. The Kalman filter is then applied to integrate the gyroscopes onto the set of discrete camera solutions. The continuous Kalman-integrated attitude reconstruction can now be used as the guess solution for the star camera pointing code. An improved guess solution helps the star camera pointing code identify solutions for frames containing two stars, or even only one. Therefore, this process is iterated until the number of usable *and* solved frames converges. As of this thesis’ submission date, a pointing solution has been successfully assigned to 93.1% and 90.3% of the frames with at least one star detected by the star camera named “ISC” and “OSC”, respectively. We are currently working to find a solution to the remaining 7% and 10% of the frames, which all contain one star only.

The pointing solution is calculated in the star camera reference frame and needs to be rotated into the submm array coordinate frame.

This rotation is evaluated by observing bright optical and submm point sources (calibrators) simultaneously and repeatedly throughout the flight. For all the BLAST flights, the relative pointing between the star cameras and telescope is found to vary as a function of the inner frame elevation and temperatures, requiring corrections to yaw and pitch of $\sim 20''$ and $\sim 125''$, respectively.

Both star cameras performed well during the BLAST-Pol 2010 flight, being able to detect $m_v = 9$ stars with ~ 100 ms integration times. Figure 4.16 shows histograms of the magnitude of the stars observed by each of the two star cameras during the whole flight. In Figure 4.17 we show histograms of the total number of stars detected in one frame by each star camera, throughout the whole flight. Two to five stars were observed on average, with less than 10% of the frames having no candidate stars. We investigate how frequently it occurs that both star cameras simultaneously detect no stars; we find that zero-star frames usually result as sporadic episodes of desynchronization between one star camera computer and the flight computer, and do not affect both cameras together.

4.8 Concluding Remarks

In this chapter, we have given an overview of the BLAST-Pol instrument, collecting and updating all the information available as of the 2010 Antarctic flight campaign. In particular, we have delved into the strategy adopted for optimal polarization recovery, as well as the hardware and software characteristics of the primary pointing sensors, the star cameras. Finally, we have given an outline of the post-flight pointing reconstruction process; albeit preliminary, the results presented here suggest that BLAST-Pol's absolute pointing accuracy will

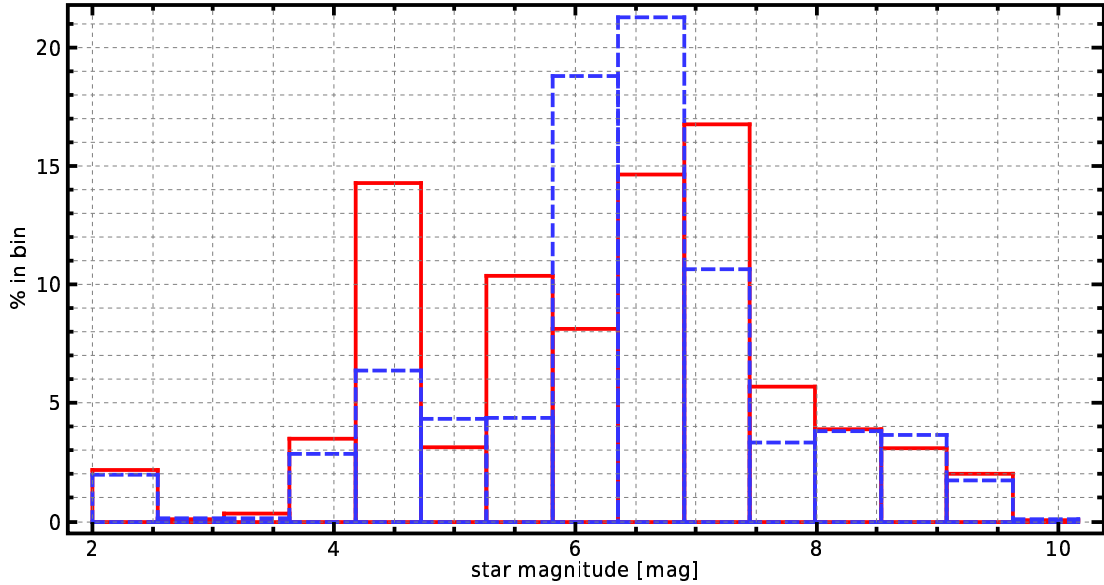


Fig. 4.16 Histograms of the star magnitudes observed by the two star cameras during the whole BLAST-Pol 2010 flight. The blue dashed histogram corresponds to the “ISC” and the red solid histogram to the “OSC”.

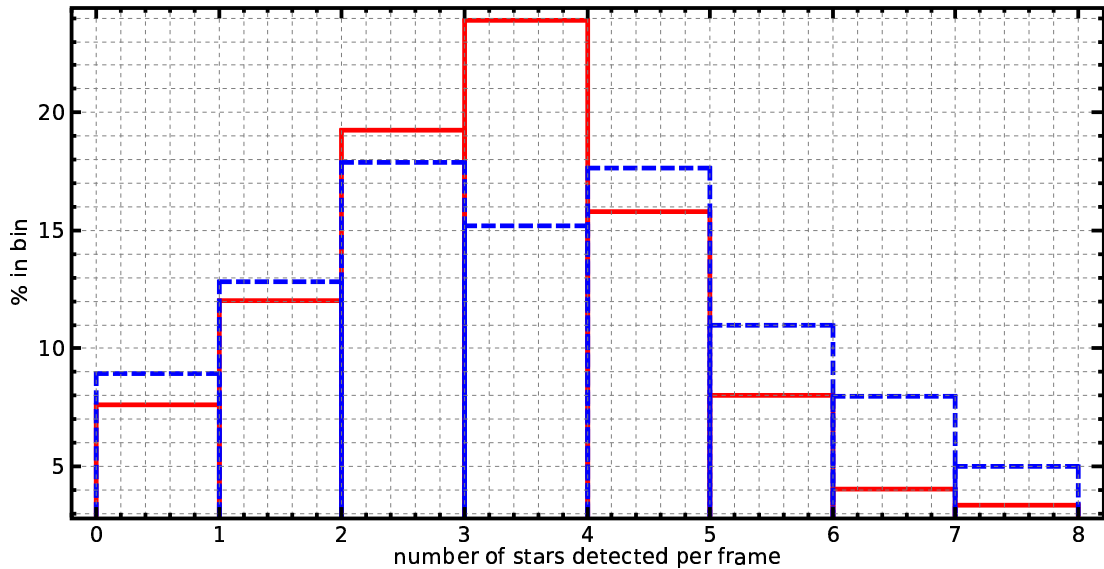


Fig. 4.17 Histograms of the number of stars detected in one frame by each of the two star cameras during the whole BLAST-Pol 2010 flight. The color-code and line style are preserved from Figure 4.16.

equal that of BLAST06 ($\lesssim 3''$ rms). In addition, the next chapter is completely dedicated to the description of the optical components of the BLAST-Pol polarimeter and their pre-flight performance.

As of this thesis' submission date, the analysis of the data collected by BLAST-Pol during the 9.5-day flight over Antarctica (see Section 1.2.5) is still ongoing. With a few exceptions, we have not included in this work the in-flight performance and calibrations, as they have not been finalized yet.

Nevertheless, in Chapter 6 we show a sample of preliminary polarization maps, which result as the culmination of the whole data analysis process and qualitatively demonstrate the overall success of the mission. A thorough assessment of the in-flight performance and calibrations of the instrument will be published by the BLAST-Pol team along with the first scientific results.

5. HALF WAVE PLATE AND POLARIMETRY

5.1 Introduction

In this chapter we describe in detail the components of the BLAST-Pol polarimeter, a cryogenic achromatic half-wave plate (HWP) and photolithographed polarizing grids acting as analyzers. The use of a continuously rotating or stepped HWP as a polarization modulator is a widespread technique at millimeter (mm) and submillimeter (submm) wavelengths (e.g., Renbarger et al. 2004, Hanany et al. 2005, Pisano et al. 2006, Savini et al. 2006, 2009, Johnson et al. 2007, Li et al. 2008, Matsumura et al. 2009, Bryan et al. 2010a,b, Dowell et al. 2010).

In Section 4.5 we have given an overview of the BLAST-Pol polarization modulation scheme and outlined our strategy for optimal polarization recovery. The final goal of this chapter is to provide a set of usable parameters that completely characterize the optical properties and efficiency of the HWP (see Section 5.2.6) and the polarizing grids (see Section 5.3), as measured in the laboratory.

We delve into the theoretical framework, principles of operation, and manufacturing process of a five-plate sapphire HWP, which is, to our knowledge, the most achromatic ever built at mm and submm wavelengths. We include a brief account of the various solutions considered for the anti-reflection coating (ARC), and highlight the technical challenges of a broadband design at submm wavelengths. We discuss how the ARC applied to the BLAST-Pol HWP represents the first successful application of a novel artificial dielectric metamaterial.

Using a polarizing Fourier transform spectrometer, we fully characterize the spectral response of the coated BLAST-Pol HWP at room temperature and at 120 K. We present the pre-flight performance of the HWP in terms of its measured Mueller matrix and phase shift as a function of frequency and extrapolated at 4 K. We show that most of the HWP non-idealities can be more easily modeled by quantifying one wavelength-dependent parameter, which is then readily implemented in the map-making algorithm described in Chapter 6. We also derive this parameter for a range of spectral signatures of an input astronomical source, including that of a blackbody and of dust emission; we discuss the possible implications for BLAST-Pol.

In the following, we adopt the Stokes (1852) formalism to represent the time-averaged polarization state of electromagnetic radiation; for a review of polarization basics we refer the reader to Appendix A of Moncelsi (2007), which in turn follows the notation of Collett (1993).

5.2 *The BLAST-Pol Half-Wave Plate*

5.2.1 *Birefringent wave plates*

Wave plates (or retarders), are optical elements used to change the polarization state of an incident wave, by inducing a predetermined phase difference between two perpendicular polarization components. A (monochromatic) wave plate can be simply obtained with a single slab of uniaxial birefringent crystal of specific thickness, which depends upon the wavelength and the index of refraction of the crystal.

Birefringence results from the anisotropy in the binding forces between the atoms forming a crystal. Such anisotropy originates from an asymmetric spatial distribution of the atoms in some crystals. An anisotropy in the binding forces in the lattice will manifest itself as an

anisotropy in the refractive index. Crystals belonging to the trigonal (e.g., calcite, quartz, sapphire) or tetragonal (e.g., rutile) systems are uniaxial, in that they possess a unique optic axis, most often coincident with the crystallographic axis.

Light propagating through a uniaxial birefringent material experiences different refraction indices depending on its propagation direction and polarization orientation inside the crystal: light propagating along the birefringent optic axis (extraordinary axis) will see an ordinary refraction index regardless of the polarization orientation. Light propagating orthogonally to the optic axis will see extraordinary or ordinary refraction indices depending on whether the polarization is, respectively, aligned or perpendicular to the optic axis.

In wave plates, the crystal is cut so that the extraordinary axis is parallel to the surfaces of the plate; light polarized along this axis travels through the crystal at a different speed than light with the perpendicular polarization, creating a phase difference. When the extraordinary index is larger than the ordinary index, as in (cold) sapphire, the extraordinary axis is called the “slow axis” and the perpendicular direction in the plane of the surfaces is called the “fast axis”.

A birefringent crystal is characterized by four parameters, n_e , n_o , α_e , α_o , the real part of the indices of refraction and the absorption coefficient (in cm^{-1}) for the extraordinary and ordinary axes of the crystal. At a specific wavelength λ_0 , the phase shift induced by a slab is determined uniquely by its thickness d , and reads:

$$\Delta\varphi(\lambda_0) = \frac{2\pi d}{\lambda_0} (n_e - n_o) \quad (5.1)$$

Given the operating wavelength λ_0 , the required phase shift for the wave plate is achieved by tuning the thickness d .

5.2.2 Achromatic half-wave plate design

While monochromatic wave plates have been (and are still being) used in mm and submm astronomical polarimeters (see e.g.,¹ Renbarger et al. 2004, Li et al. 2008, Bryan et al. 2010a,b, Dowell et al. 2010), the inherent dependence of the phase shift with wavelength expressed in Equation (5.1) constitutes an intrinsic limit in designing a polarization modulator that operates in a broad spectral range (i.e., achromatic).

Achromaticity is necessary for wave plates that are designed for use with multi-band bolometric receivers, such as BLAST-Pol (see Chapter 4 of this thesis), PILOT (Bernard et al. 2007), or SCUBA-2 (Bastien et al. 2005, Savini et al. 2009). To achieve a broadband performance, multiple-plate solutions have been conceived in the past (Pancharatnam 1955, Title & Rosenberg 1981) to compensate and to keep the phase shift approximately constant across the bandwidth, by stacking an odd number (usually 3 or 5) of birefringent plates of the same material, which are rotated with respect to each other about their optical² axes by a frequency-dependent set of angles.

Achromatic wave plates have been designed and built for astronomical polarimeters at mm and submm wavelengths by many authors in the last decade (Hanany et al. 2005, Pisano et al. 2006, Savini et al. 2006, 2009, Matsumura et al. 2009), following the Poincaré sphere (PS) method first introduced by Pancharatnam (1955). We briefly recall it here for completeness (see also Appendix A of Moncelsi 2007). The polarization state of a monochromatic wave in a given reference frame can

¹ The references listed here describe instruments with wave plates optimized to operate in a single photometric waveband, centered at λ_0 and typically 10–30% wide; hence, these are not strictly monochromatic. However, these wave plates are referred to as monochromatic in astronomical jargon, because they cover a single waveband, within which Equation (5.1) is a good approximation.

² We distinguish between “optic” axis of a crystal, that is the direction in which a ray of transmitted light experiences no birefringence, and “optical” axis, that is the imaginary line along which there is some degree of rotational symmetry in the optical system described.

be represented by a set of coordinates, latitude and longitude, on the PS that quantify, respectively, the ellipticity angle ($\sin 2\chi \propto \sin \Delta\varphi$) and the orientation angle of its major axis ($\tan 2\psi \propto \cos \Delta\varphi$). A linearly polarized state appears only on the equator (with $\pm Q$ and $\pm U$ at the four antipodes), while the left and right circularly polarized states ($\pm V$) lie at the north and south poles, respectively (see Figure 5.1).

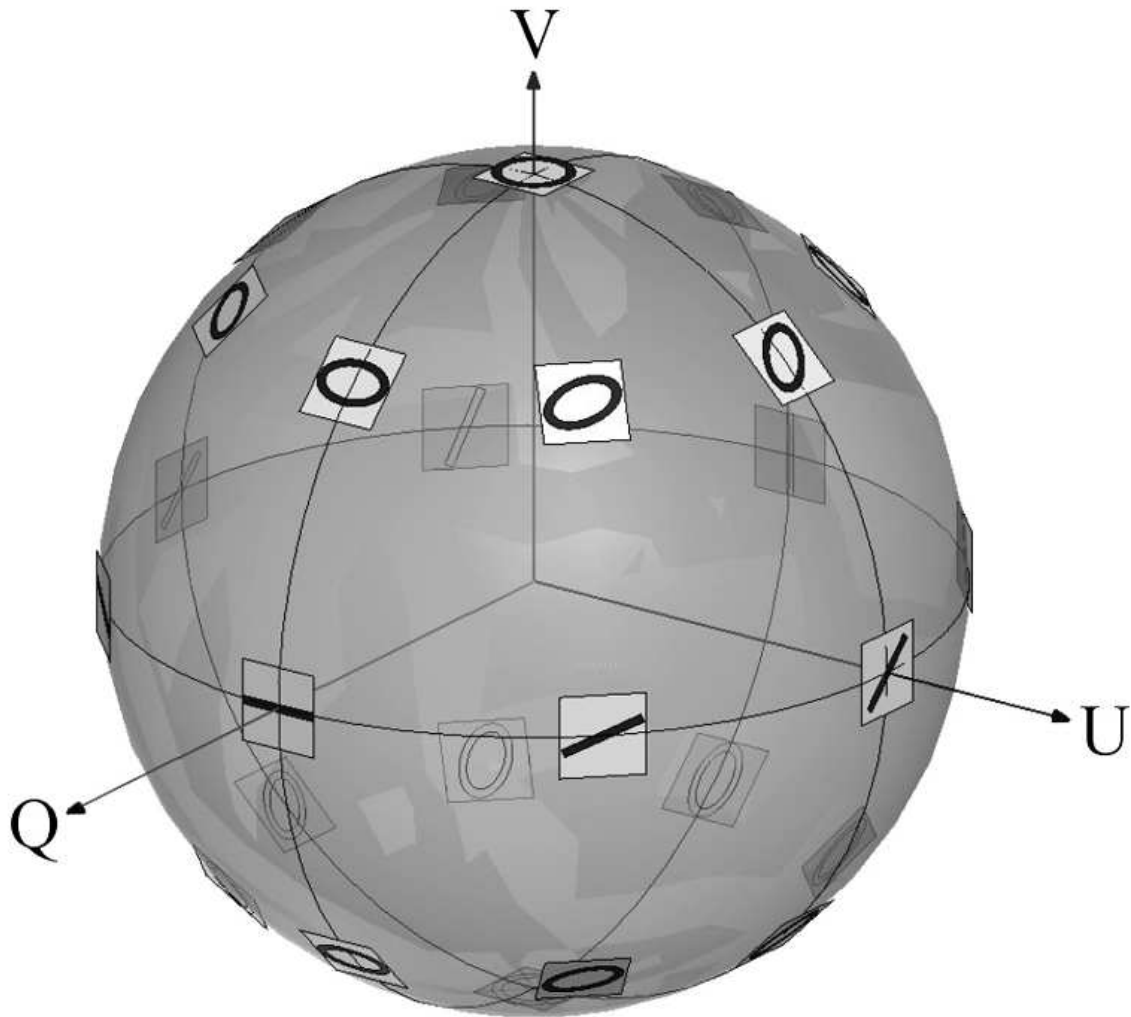


Fig. 5.1 Polarization states on the Poincaré sphere. Note that in physics $\pm Q$ is taken to be horizontal (vertical) polarization rather than N-S (E-W) polarization as per the astronomers' convention (see Section 4.5.1). (from Savini et al. 2006).

Propagation of a wave through a single birefringent slab will rotate its polarization state on the PS by an amount dependent on the

relation between wavelength and thickness (Equation 5.1), about an axis whose orientation depends upon the position of the optic axis of the wave plate with respect to the reference frame of the incoming polarization state. Specifically, an ideal monochromatic half-wave plate produces one PS rotation of 180° , changing a linear polarization state to another one on the equator.

When a polychromatic wave packet enters a multiple-plate HWP, the input polarized states of all wavelengths overlap in a single point on the PS (see point 1 in Figure 5.2). After the rotation due to the first plate, the polarization states of different wavelengths will be scattered along an arc on the PS (point 2 in Figure 5.2), with separations that depend on the bandwidth $\Delta\lambda$ of the wave packet. As anticipated, this effect can be compensated for by stacking together an odd number of birefringent slabs, rotated with respect to each other by a symmetric pattern of angles ($\alpha, \beta, \gamma, \beta$, and α for 5 slabs) about their optical axes (as derived by e.g., Pancharatnam 1955, Title & Rosenberg 1981). Figure 5.2 visually illustrates how the various polarization states regroup in a small area of the PS surface, thus achieving a nearly frequency-independent output polarization state, within a certain $\Delta\lambda$.

We note that, strictly speaking, all the four parameters that characterize a crystal, $n_e, n_o, \alpha_e, \alpha_o$, depend upon wavelength (as we will illustrate in detail for sapphire); in particular, the different frequency-dependence of the ordinary and extraordinary refraction indices enters Equation (5.1) in a non-trivial way, thus rendering the design of an achromatic HWP increasingly difficult as $\Delta\lambda$ broadens.

Using the above PS method, we design and manufacture a HWP for the BLAST-Pol instrument, which is successfully used as a polarization modulator to study the role of magnetic fields in the earliest, highly obscured stages of star formation, via the polarized submm

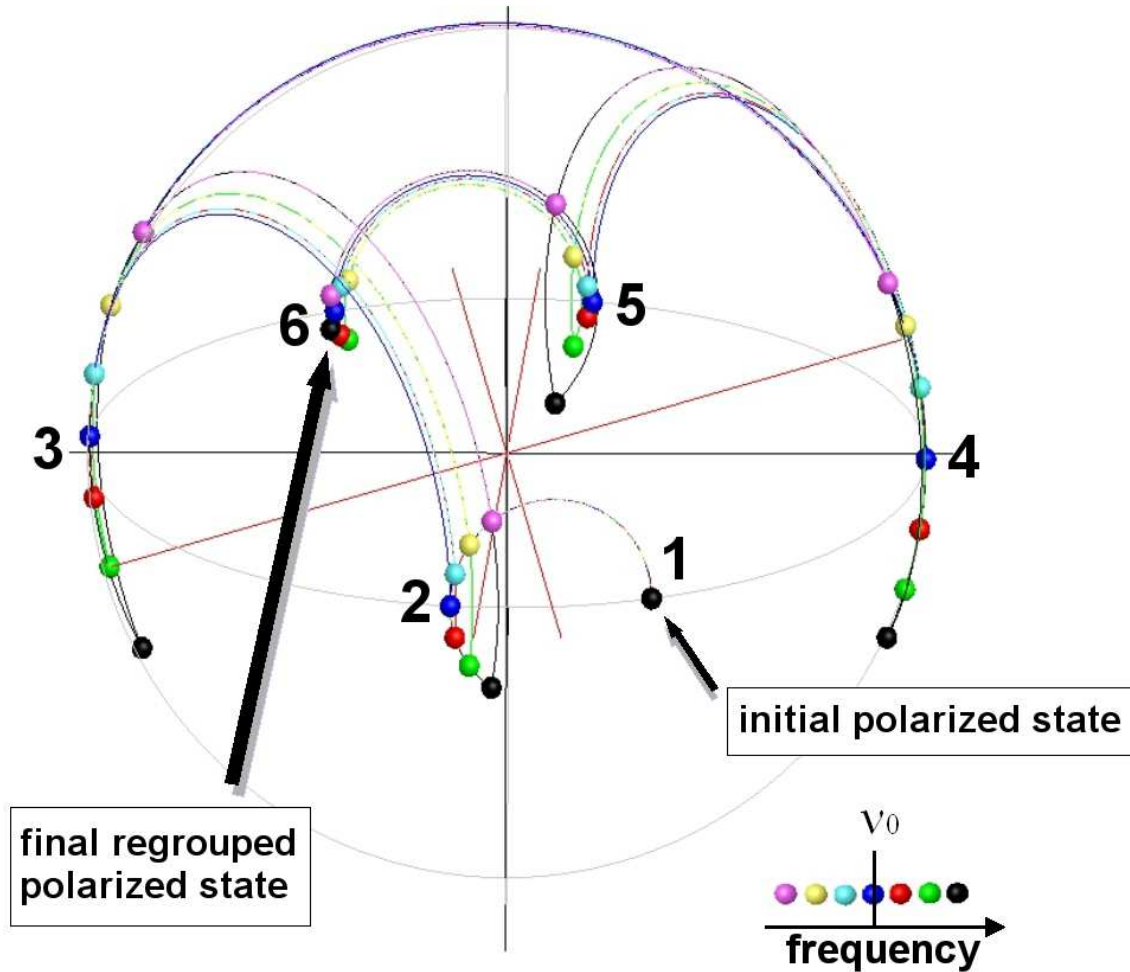


Fig. 5.2 Rotations on the Poincaré sphere for a five-plate HWP. We note that the regrouping of polarized states at different frequencies is independent of the initial position on the PS equator. (modified from Savini et al. 2006).

emission from aligned elongated dust grains (see Chapter 1). BLAST-Pol requires an extended frequency range to cover three adjacent 30% wide spectral bands at 250, 350, and 500 μm . A Pancharatnam (1955) five-plate design is chosen with axis orientations of $\alpha = 0^\circ$, $\beta = 26^\circ$, $\gamma = 90.3^\circ$, $\beta = 26^\circ$, and $\alpha = 0^\circ$; these angles are optimized using the physical and analytical model developed by Savini et al. (2006) for an achromatic HWP, which in turn is based on the work of Title & Rosenberg (1981). In Figure 5.3 we show an exploded view of the BLAST-Pol HWP assembly; to our knowledge, this is the most achro-

matic half-wave plate ever produced at mm and submm wavelengths.

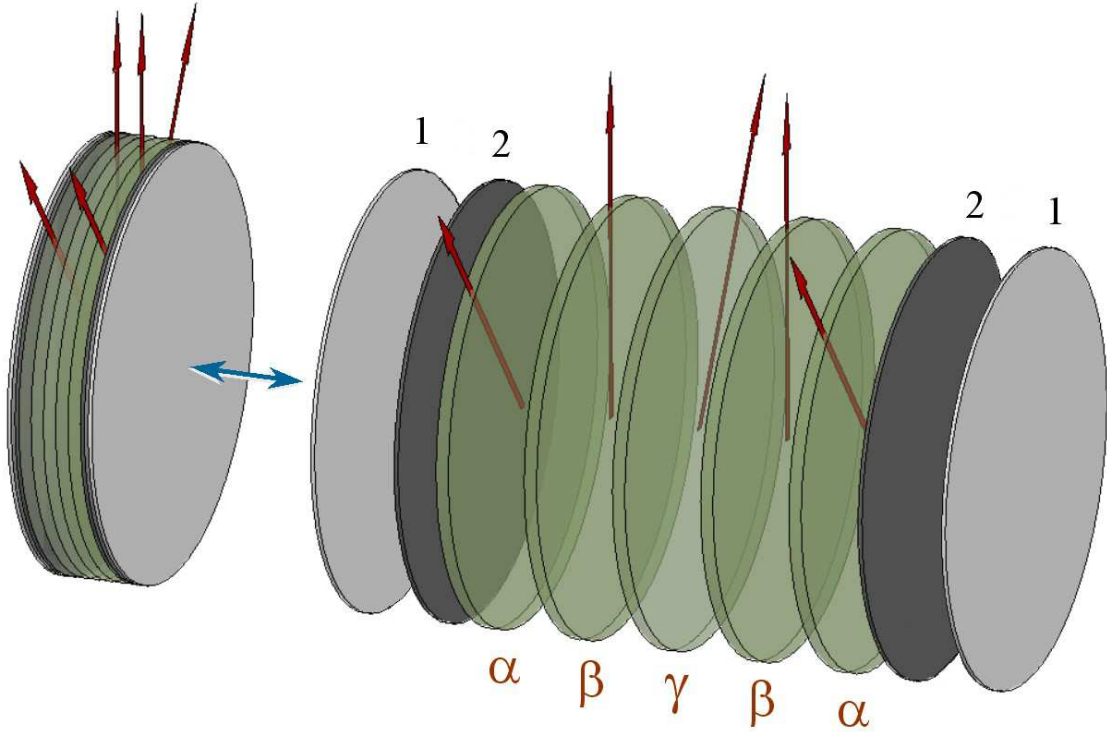


Fig. 5.3 Exploded view of the BLAST-Pol HWP. We also show the two-layer anti-reflection coating described in Section 5.2.4. (modified from Savini et al. 2006).

5.2.3 HWP manufacture

In addition to the broad spectral range of operation, the BLAST-Pol HWP is required to function at cryogenic temperatures (4 K, see Section 4.5) for two main reasons: (1) reduce the thermal emission from a warm optical element placed in the optical path, which would constitute a significant background load on the bolometric detectors (see Section 4.3); and (2) reduce the losses in transmission due to absorption from the stack of five crystal plates, which drops dramatically with temperature. The absorption in a crystal at FIR wavelengths is the result of the interactive coupling between the motions of thermally induced vibrations of the constituent atoms of the substrate crystal

lattice (which propagate as waves called phonons) and the incident radiation. Because the phonon population is much reduced at low temperatures, cooling the crystal effectively reduces the absorption.

The two obvious candidates (uniaxial birefringent) crystals are sapphire and quartz, because of their favorable optical properties in the FIR/submm (Loewenstein et al. 1973). Sapphire is chosen over quartz due to its larger difference between ordinary and extraordinary refraction index ($\Delta n_{e-o} \approx 0.34$ for sapphire, and ≈ 0.13 for quartz Loewenstein et al. 1973; see also Figures 5.4, 5.5), which implies a smaller thickness for the plates (see Equation 5.1). Since quartz and sapphire have a comparable level of absorption at cryogenic temperatures in the wavelength range of 200–600 μm (Loewenstein et al. 1973), thinner substrates are desirable to minimize absorption losses ($\propto 1 - e^{-\alpha d}$).

Nonetheless, the thin sapphire substrates chosen for the BLAST-Pol HWP do indeed show appreciable absorption, especially at the shortest wavelengths (250 μm band; see Section 5.2.5). We have highlighted how the frequency dependence of both the refractive index and absorption coefficient for the chosen birefringent crystal is crucial to the overall performance of the HWP. Therefore, in Figures 5.4, 5.5, 5.6, and 5.7 we graphically report a collection of spectral measurements³ and analytical expressions from the literature of the indices of refraction and the absorption coefficient at the wavelengths relevant to BLAST-Pol, for the extraordinary and ordinary axes of sapphire, both at room and cryogenic temperatures. The details and relevant references are given in the captions. Albeit not necessarily complete, to our knowledge this collection represents the most comprehensive

³ Throughout this Chapter we make use of the wavenumber, k , as a unit of frequency, expressed in cm^{-1} as customary in spectroscopy, with $k [\text{cm}^{-1}] = \frac{\nu [\text{Hz}]}{100 c [\text{m s}^{-1}]} = \frac{0.01}{\lambda [\text{m}]}$, or $k [\text{cm}^{-1}] = \frac{10^7 \nu [\text{GHz}]}{c [\text{m s}^{-1}]} = \frac{10^4}{\lambda [\mu\text{m}]}$, where c is the speed of light in vacuum. Furthermore, we adopt a color code in the plots whereby curves referring to the three BLAST-Pol bands, 250, 350, and 500 μm are drawn in blue, green, and red, respectively.

characterization of the optical properties of sapphire at submm wavelengths, both at room and cryogenic temperatures. We capitalize on this information in the analysis that follows in this chapter, though we anticipate that, from the data shown in Figure 5.7, we would expect a residual absorption from sapphire of at least 2.5% at $250\ \mu\text{m}$ (for a total thickness of $\sim 2.5\ \text{mm}$; see later on in this section), even at 4 K.

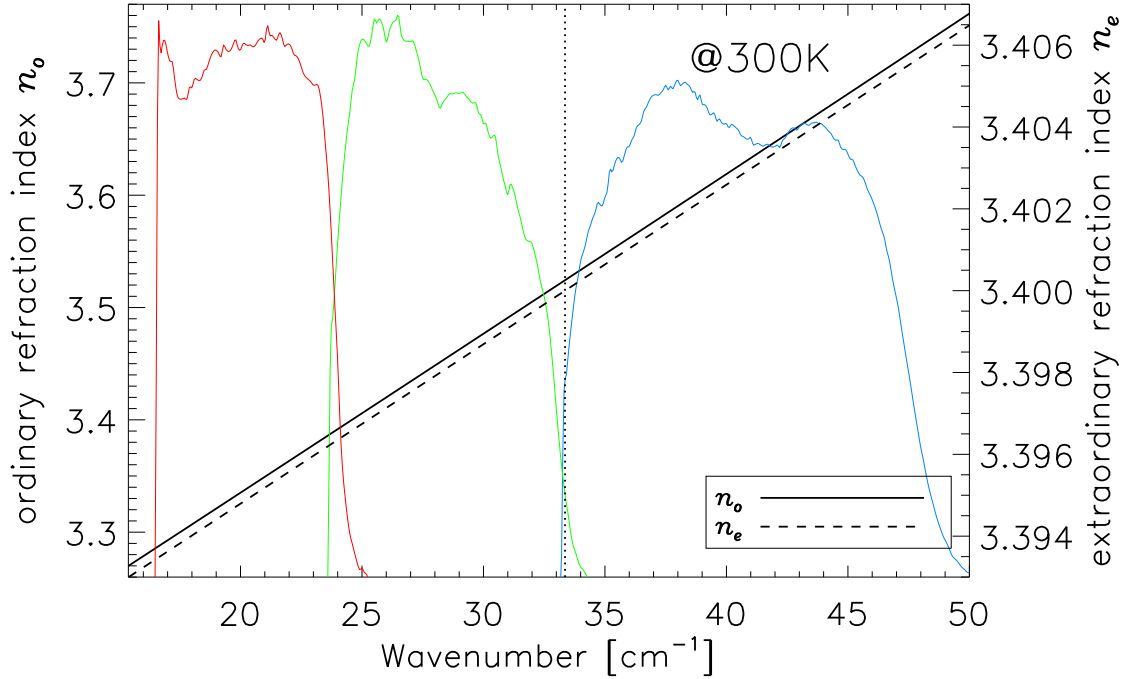


Fig. 5.4 Sapphire ordinary (solid line, relative to the primary y -axis) and extraordinary (dashed line, relative to the secondary y -axis) real part of the refractive indices as a function of wavenumber, at room temperature. The analytical relations are given by Savini et al. (2006), and, strictly speaking, only apply for frequencies $\lesssim 1\ \text{THz}$ (dotted vertical line). Also shown is the relative spectral response of the three BLAST-Pol channels, in arbitrary units (see Section 4.2).

The five plates of the Pancharatnam (1955) design all have the same thickness. To cover the broad wavelength range of $200\text{--}600\ \mu\text{m}$, a plate thickness is chosen to produce a HWP at the central wavelength of the central band, $350\ \mu\text{m}$. By using the spectral measurement of the refractive indices for cold sapphire presented in Figure 5.5 ($\Delta n_{e-o}^{350\ \mu\text{m}} \approx 0.33$), and imposing the required phase shift of 180° between the two

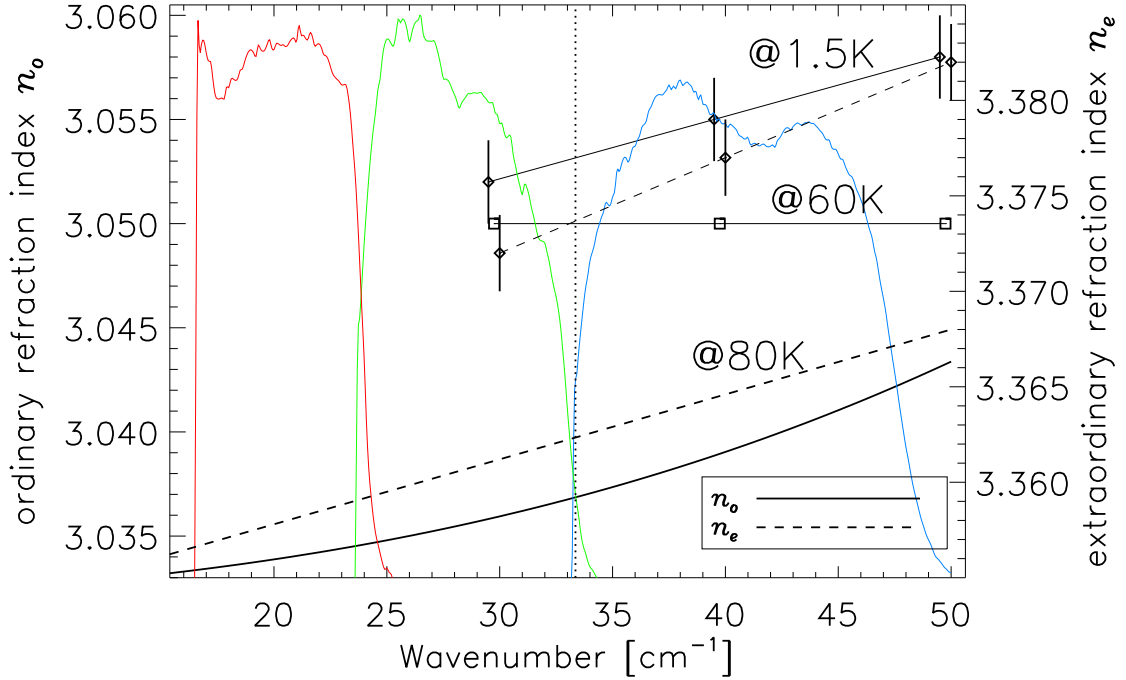


Fig. 5.5 Sapphire ordinary (solid lines, relative to the primary y -axis) and extraordinary (dashed lines, relative to the secondary y -axis) real part of the refraction indices as a function of wavenumber, at cryogenic temperatures. The two analytical relations covering the whole frequency range are derived by Savini (2010, private communication) from a set of spectral measurements of a sapphire sample at 80 K, and, strictly speaking, only apply for frequencies $\lesssim 1$ THz (dotted vertical line). We also plot measurements from Loewenstein et al. (1973; diamonds) at 1.5 K and Cook & Perkowitz (1985; squares) at 60 K, displaced in x by 0.25 cm^{-1} for visual clarity; the lines connecting these data points follow the convention shown in the legend.

orthogonal polarizations traveling through the plate, Equation (5.1) yields for the thickness of a single plate a value $\sim 0.53 \text{ mm}$. The nearest available thickness on the market is 0.5 mm . A deviation of $\sim 0.3 \text{ mm}$ from the desired thickness translates in a departure of $\sim 10^\circ$ from the ideal phase shift of 180° at $350 \mu\text{m}$, which is approximately what we measure (see Figure 5.27). We briefly discuss the implications of this systematic at the end of Section 5.2.6.

The orientation of the optic axis on each sapphire plate is determined with a polarizing Fourier transform spectrometer (pFTS hereafter), which is briefly described in Section 5.2.5.1. Each plate is ro-

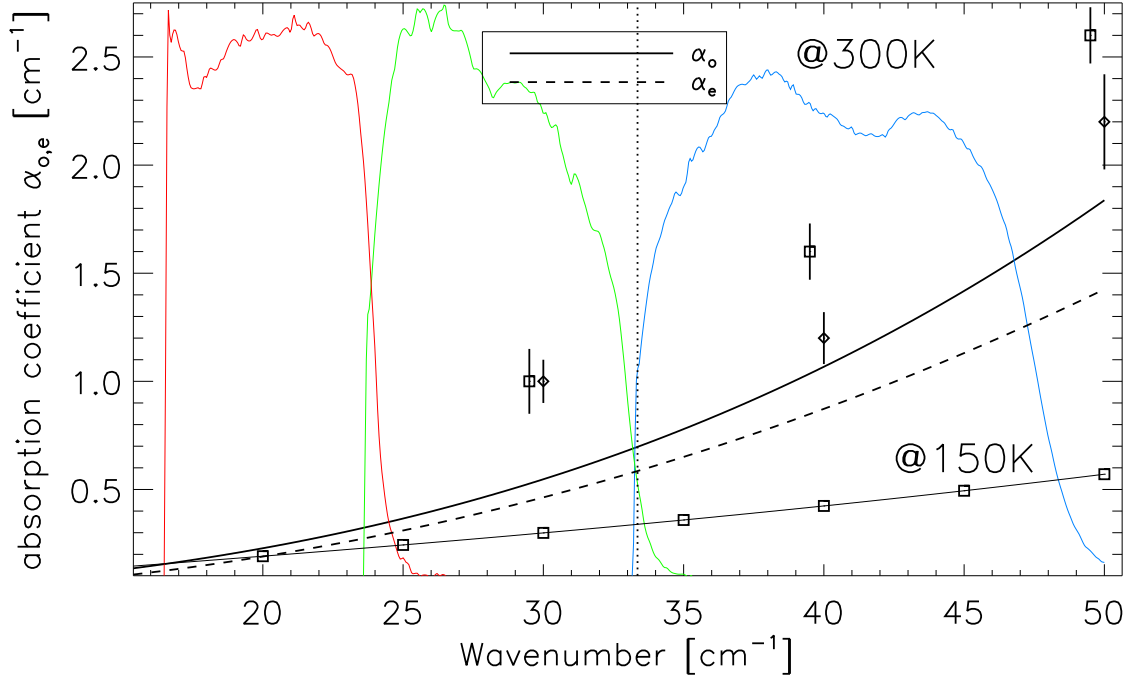


Fig. 5.6 Ordinary (solid lines) and extraordinary (dashed line) sapphire absorption coefficient as a function of wavenumber, at room temperature and at 150 K. The upper two analytical relations are given by Savini et al. (2006) at room temperature, and, strictly speaking, only apply for frequencies $\lesssim 1$ THz (dotted vertical line). We also plot for reference room temperature measurements from Loewenstein et al. (1973; diamonds) and Cook & Perkowitz (1985; squares without connecting line), displaced in x by 0.5 cm^{-1} for visual clarity. Also shown is the relative spectral response of the three BLAST-Pol channels, in arbitrary units (see Section 4.2). Finally, we include the analytical dependence of α_o at 150 K, as published by Cook & Perkowitz (1985; squares with connecting solid line).

tated between two aligned polarizers at the pFTS output until a maximum signal is achieved. The use of two polarizers avoids any complication from a partially polarized detecting system and any cross polarization incurred from the pFTS output mirrors. The HWP is assembled by marking the side of each plate with its reference optic axis and rotating each element according to the Pancharatnam design described in the previous section. The stack of five carefully-oriented sapphire substrates, interspersed with one $6 \mu\text{m}$ layer of polyethylene, are fused together with a hot-pressing technique used in standard filter production (Ade et al. 2006). The polyethylene has negligible effects on the

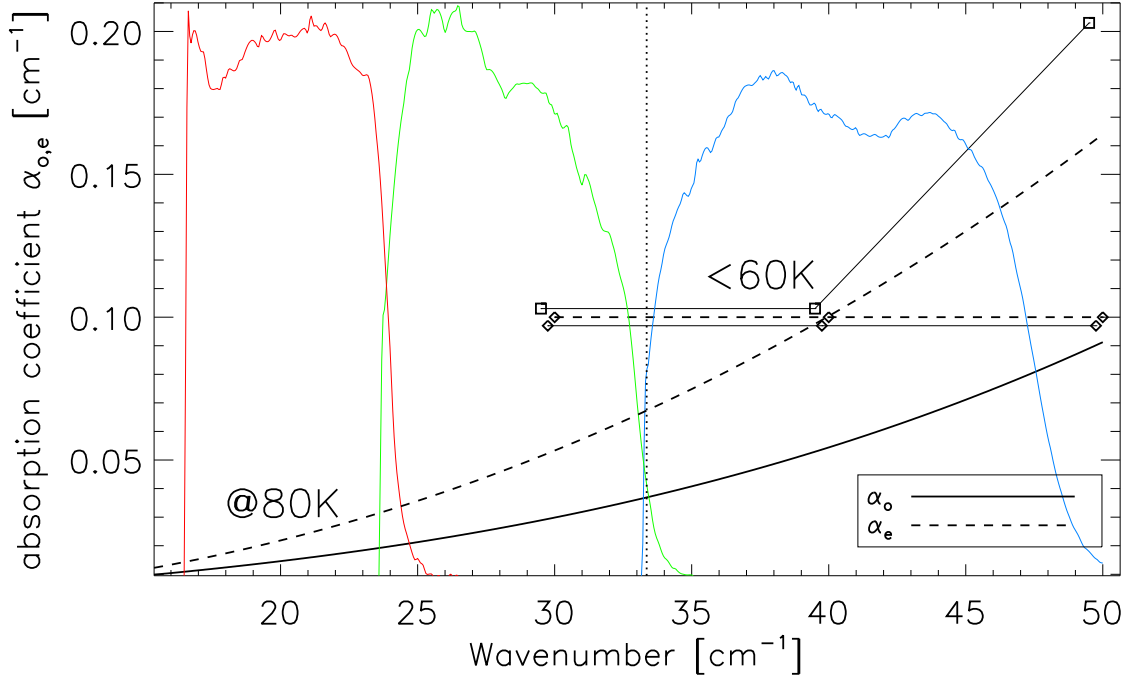


Fig. 5.7 Ordinary (solid lines) and extraordinary (dashed lines) sapphire absorption coefficient as a function of wavenumber, at cryogenic temperatures. The two analytical relations covering the whole frequency range are derived by Savini (2010, private communication) from a set of spectral measurements of a sapphire sample at 80 K, and, strictly speaking, only apply for frequencies $\lesssim 1$ THz (dotted vertical line). We also plot for reference measurements from Loewenstein et al. (1973; diamonds) at 1.5 K and Cook & Perkowitz (1985; squares) at 60 K, displaced in x by 0.25 cm^{-1} and in y by 0.003 cm^{-1} for visual clarity; the lines connecting these data points follow the convention shown in the legend.

final optical performance of the HWP, because when heated it seeps into the roughened⁴ surfaces of the adjacent plates. The thickness of the resulting stack (uncoated HWP) is $2.55 \pm 0.01 \text{ mm}$; its diameter is $100.0 \pm 0.1 \text{ mm}$. A two-layer anti-reflection coating (ARC), necessary to maximize the in-band transmission of the HWP (see Section 5.2.4), is also hot-pressed to the front and back surfaces of the assembled plate, again using $6 \mu\text{m}$ layers of polyethylene; the layer adjacent to

⁴ In order to improve the robustness of the bond, the individual substrates are sandblasted with aluminium oxide (Al_2O_3) prior to fusion; this procedure dramatically improves the grip of the polyethylene between adjacent crystal surfaces. Careful cleansing and degreasing of all the crystal surfaces is required after sandblasting; in particular, we use trichloroethylene, which we found to be most effective to remove the traces of oily substances due to the sandblasting process.

the sapphire is an artificial dielectric metamaterial composed of metal mesh patterned onto polypropylene sheets (Zhang et al. 2009), while the outer layer is a thin film of polytetrafluoroethylene (PTFE). The thickness of the final stack (coated HWP) is 2.80 ± 0.01 mm. The diameter of the ARC is set to 88.0 ± 0.1 mm, slightly smaller than that of the HWP to avoid any contact between the coating and the HWP mount (see Section 4.5); the ARC is bonded concentrically to the HWP and thus its diameter defines the optically-active area of the HWP. A photograph of the coated HWP is shown in Figure 5.8.

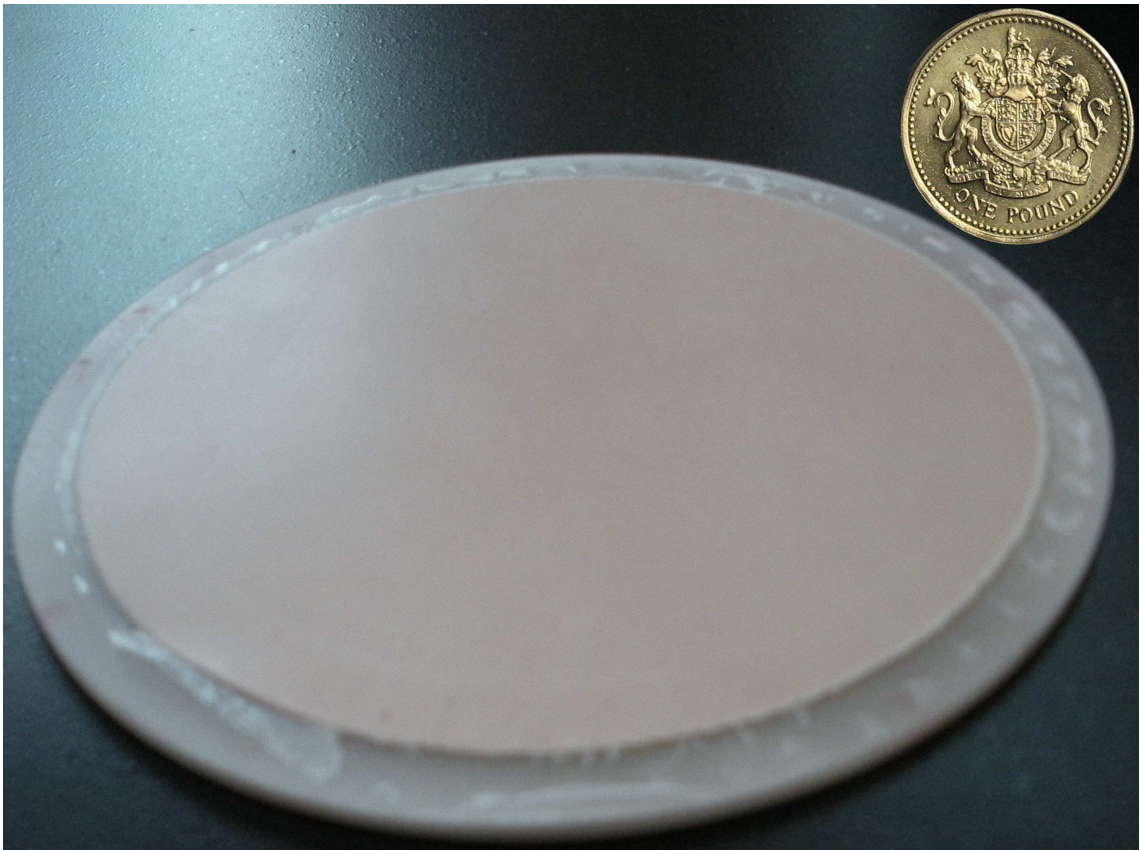


Fig. 5.8 Photograph of the anti-reflection coated BLAST-Pol HWP.

Because of the thermal expansion mismatch between the sapphire and the polypropylene, the HWP assembly has undergone countless cryogenic cycles prior to the flight to test the robustness of the bond at liquid helium temperatures. We point out that the HWP has been

successfully installed in the BLAST-Pol cryogenic receiver and flown from balloon platform for about ten days, without delamination of the ARC or damage to the assembly.

5.2.4 Anti-reflection coating

The presence of an anti-reflection coating (ARC) on both sides of the HWP is required to minimize the reflections due to the impedance mismatch between the high- n birefringent crystal and free space, which would substantially degrade the overall optical efficiency of the system. As a consequence of the inclusion of an ARC, the in-band transmission is maximized and very little radiation is reflected off the HWP, which would otherwise be scattered inside the optics box and could eventually end up on the detectors. The large bandwidth of BLAST-Pol dictates the need for an ARC solution that is at least as achromatic as the HWP. Furthermore, the materials employed must be suitable for use at liquid helium temperatures.

Before describing the particular solution adopted for the BLAST-Pol HWP, we briefly review here the principles of operation of an ARC. In propagating from one medium (air) with refractive index n_1 into another one with refractive index n_2 (sapphire), a fraction $R = \left(\frac{n_2-n_1}{n_2+n_1}\right)^2$ of the light will be reflected off the boundary surface between the two media. By applying a coating, with refractive index n_3 and thickness t , on the sapphire plate, the light is reflected twice at the two boundary surfaces; if the optical path difference between the two reflections is a half-integer number of wavelengths, the two reflections interfere destructively and the reflection is minimized. This condition is satisfied when

$$t = \frac{\lambda}{4n_3} \quad (5.2)$$

For fully destructive interference the amplitudes of the two reflections should be equal; this is achieved by choosing $n_3 = \sqrt{n_1 n_2}$. It is clear from Equation (5.2) that a single layer of ARC is effective only at one wavelength. Broadband performance can be achieved by stacking multiple layers of materials with progressively higher refractive indices, which create a smoother impedance match between n_1 and n_2 .

5.2.4.1 Old recipes: high- n powders and loaded ceramics

ARC solutions at mm wavelengths use multiple layers of either specially prepared polypropylene layers loaded with high refractive index powders (TiO_2 ; Pisano et al. 2006, Savini et al. 2006) or ceramic-based materials (e.g., Rogers TMM material⁵; Savini et al. 2009) to create a particular refractive index. These ARC recipes need usually three layers to achieve a flat response across the band. Each layer requires hot-pressing onto the HWP stack, and subsequent grinding to the required thickness. There are several disadvantages to both these approaches: the loaded powder layers are slow to manufacture because the powder needs to be uniformly mixed in the polypropylene, and then the layers have to be hot-pressed to the appropriate thickness; the ceramics are brittle and can only be thinned with a grinding technique, which is time-consuming and unreliable for thicknesses below $\sim 100 \mu\text{m}$. Among all the drawbacks listed, this latter point is the one that engages us to design a new ARC solution (described in the next section), as at submm wavelengths the required thicknesses of high refractive index materials ($n \approx 1.2\text{--}2.75$) are of the order of tens of microns (see Equation 5.2).

⁵ Rogers Corporation supply TMM high-frequency laminate materials: www.rogerscorp.com.

5.2.4.2 *New recipes: artificial dielectric metamaterials*

As anticipated in the previous sections, the technical difficulties in the manufacture of conventional ARC solutions at submm wavelengths led us to develop a novel artificial dielectric metamaterial (ADM), which is thoroughly described in Zhang et al. (2009); we briefly review here its salient features.

The material is manufactured from layers of photolithographed metal mesh (copper; Tucker & Ade 2007) patterned onto thin polypropylene sheets, which act as embedding dielectric. Specifically, two metal-mesh layers (periodic structures of square grids patterns) are immersed in the polypropylene substrate at a distance of $8\ \mu\text{m}$ from the top and bottom surfaces and with a spacing of $24\ \mu\text{m}$ between the two layers. The $40\ \mu\text{m}$ multi-layer structure is assembled and then hot-pressed at temperatures close to the polypropylene melting point (160°C).

The artificial material thus created has the consistency of a solid plastic film that can be easily handled, cut to the desired size, and reliably cycled to liquid helium temperatures. The refractive index of this metamaterial can be tuned by adjusting the geometry and spacing of the metal-mesh layers. The particular ADM prototype that Zhang et al. (2009) describe and fully characterize is applied as an ARC to a quartz substrate; subsequently, the recipe has been optimized for sapphire substrates in the wavelength range $200\text{--}600\ \mu\text{m}$.

As anticipated, a second layer of coating is necessary to achieve the required broadband performance. We use a $54\ \mu\text{m}$ layer of porous PTFE⁶, which has refractive index $n = 1.375$; its thermal expansion coefficient is closely matched to that of polypropylene, so it represents an ideal solution for our application at cryogenic temperatures.

Finally, the two ARC layers are interspersed by $6\ \mu\text{m}$ layers of

⁶ <http://www.porex.com/porous.cfm>

polyethylene and hot-pressed concentrically to the top and bottom surfaces of the HWP stack (the two layers can in fact be bonded in one single press cycle). The final ARC assembly has a thickness of $125 \pm 15 \mu\text{m}$ and an outer diameter of 88 mm.

Such a metal-mesh ADM design has complete control over the thickness of the coating layer and the embedding material is not brittle, hence it has better performance in thermal cycling. The BLAST-Pol coated HWP represents the first successful application of the new-concept THz coating. Incidentally, we mention that the design and manufacture of the HWP for the PILOT experiment (with similar photometric bands to those of BLAST-Pol; Bernard et al. 2007) has gone hand in hand with that of BLAST-Pol; LM has participated in its fabrication, spectral characterization and cryogenic testing.

Because of the thermal expansion mismatch between polypropylene and sapphire (or quartz), the application of this metal-mesh ADM as an ARC is challenging for large-aperture cryogenic HWPs. Extending previous work by Pisano et al. (2008), we have recently designed and realized a prototype polypropylene-embedded metal-mesh broadband achromatic HWP for millimeter wavelengths (Zhang et al. 2011); this will allow next generation experiments with large-aperture detector arrays to be equipped with large-format ($\gtrsim 20$ cm in diameter) HWPs for broadband polarization modulation.

5.2.5 Spectral characterization

5.2.5.1 Introduction

We fully characterize the spectral performance of the BLAST-Pol HWP by using a pFTS of the Martin–Puplett (1970) type. The source is an incoherent mercury arc lamp with an aperture of 10 mm,

whose emission is well approximated by a blackbody spectrum at $T_{\text{eff}} \approx 2000 \text{ K}$; a low-pass filter blocks radiation from the source at wavelengths shorter than $\sim 3.4 \mu\text{m}$. The interferometer is equipped with a P1⁷ beam divider, a P2 input polarizer (at the source), and a P10 output polarizer. The pFTS has a (horizontally) polarized output focused beam with $f_{\#} = 3.5$ or, in other words, a converging beam with angles $\theta \lesssim 8^\circ$.

As we will show in the next sections, the pFTS allows us to measure the HWP performance as a function of frequency and incoming polarization state. Furthermore, because of the strong dependence of the sapphire absorption coefficient on temperature (see Section 5.2.3), we measure the spectral response of the HWP both at room temperature (Section 5.2.5.2) and at cryogenic temperatures ($\sim 120 \text{ K}$; Section 5.2.5.3). Ultimately, we want to retrieve the frequency-dependent HWP Mueller matrix and phase shift, which, in turn, determine the spectral response and modulation efficiency we measure.

5.2.5.2 Room-temperature measurements

The schematic drawing of the room-temperature measurement configuration is shown in Figure 5.9, while a photograph of the optical bench is shown in Figure 5.30, albeit with a different rotating sample. In the following, we describe each element in sequential order from the polarized pFTS output to the detector system.

In order to measure the HWP performance at near-normal incidence, we use a planar convex polyethylene lens (with focus at the position of the output pFTS image) to generate a quasi-parallel beam section; a second lens refocuses the beam onto the horn aperture of

⁷ We denote with P# [μm] the period of a photolithographed wire grid polarizer, which has $\# / 2$ copper strips with $\# / 2$ gaps on a $1.5 \mu\text{m}$ mylar substrate.

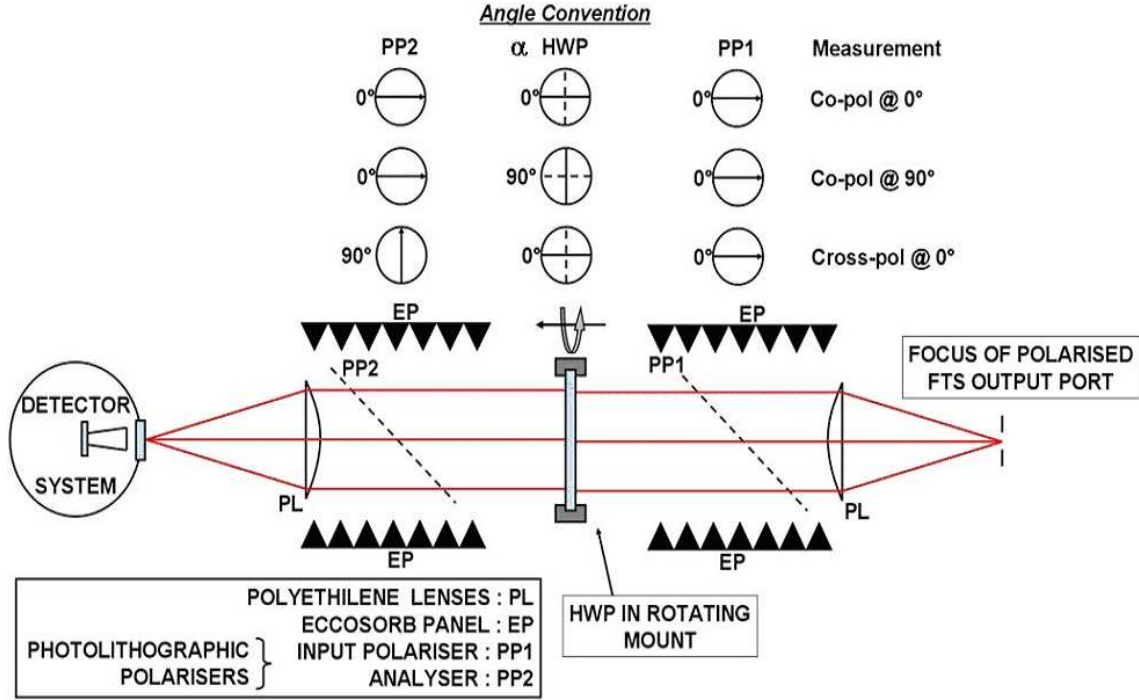


Fig. 5.9 Schematic drawing of the room-temperature spectral measurements setup. The horizontally polarized output of a pFTS feeds into a polyethylene lens that creates a quasi-parallel beam and is then refocused onto the horn aperture of the bolometric detector. Two polarizers alternatively parallel and perpendicular create the necessary polarization selection for the “co-pol” and “cross-pol” sets of measurements. The arrows for PP1 and PP2 indicate the selected polarization, so that the wire grid orientations are perpendicular to the arrows. (from Zhang et al. 2011).

the detector system. The maximum range of incident angles is thus limited by the input source aperture (10 mm), a beam spread of only 1.6° . This allows to evenly illuminate the entire optically-active area of the HWP, as if it would be inside the BLAST-Pol optics box (see Section 4.5.2).

The HWP is placed centrally in the collimated beam section between two P10 polarizers (the output polarizer is usually referred to as “analyzer”), which are tilted by 45° with respect to the optical axis to avoid standing waves between the optical elements. This tilt introduces four ports that are optically terminated with a close to ideal

blackbody, Eccosorb AN72 absorber⁸. The efficiency of these polarizers is separately determined to exceed 99.8% over the range of frequencies of interest, with a cross-polarization of less than 0.1%. The polarizers are initially aligned with respect to each other with the grid wires vertical (thus selecting horizontal polarization) with respect to the optical bench, in order to avoid any projection effect when tilted.

Following the convention depicted in Figure 5.9, measurements with aligned polarizers are referred to as “co-pol” transmission, T_{cp} . As shown in the next section, the HWP has a complementary response when the output polarizer (analyzer) is rotated by 90° about the optical axis of the system (i.e., horizontal wires, selecting vertical polarization); data taken with this configuration are also necessary to completely characterize the HWP, and are referred to as “cross-pol” transmission⁹, T_{xp} .

Common to both the warm and cold measurements is the requirement to position and rotate the HWP accurately with respect to its optical axis. When at room temperature, the HWP is held and rotated by a motorized rotating mount positioned centrally between the two tilted polarizers. The mount has a fixed orientation with respect to the optical axis of the system; we position it so that the collimated beam has normal incidence on the HWP (within 1°), and evenly illuminates its surface. The electronically-controlled rotating mount can rotate the HWP about its optical axis to obtain the polarization modulation; the resolution of the digital angular encoder on the rotation angle is 0.001° . Besides Figures 5.9 and 5.30, a CAD drawing of the optical bench setup, including the motorized rotating mount, can be found in Figure 1 of Pisano et al. (2006).

⁸ Emerson and Cuming, Microwave Products, <http://www.eccosorb.com/>.

⁹ We note that this definition of cross-pol may differ from other conventions adopted in the literature (e.g., that of Masi et al. 2006, who operate without a HWP).

Finally, the detecting system used is a 4.2 K liquid helium cooled indium antimonide (InSb) detector, which is cryogenically filtered to minimize photon noise. The spectral coverage of the data is thus defined by the cut-off frequency of the light collector waveguide (5 cm^{-1}) and by two low-pass filters in the cryostat housing the bolometric detector (60 cm^{-1}). We pay particular attention to ensure the absorption of any diffracted or reflected stray radiation. Besides terminating all unused optical ports as described above, additional Eccosorb AN72 covers all the exposed metallic surfaces close to the optical path.

The rapid scan system records interferograms with a $8\text{ }\mu\text{m}$ sampling interval over a 10 cm optical path difference, at a scan speed of 1 cm s^{-1} ; this results in a Nyquist frequency of 625 cm^{-1} and a spectral resolution of 0.05 cm^{-1} .

A first dataset is obtained in co-pol configuration by scanning the spectrometer in the absence of the HWP, which we refer to as the background spectrum. This dataset defines the pFTS reference spectral envelope, and it is the set against which all the following spectra are divided in order to account for the spectral features of the source, pFTS optics, detector system, and laboratory environment (i.e., water vapor). Subsequently, the HWP is inserted in between the tilted polarizers in co-pol configuration, and spectra are acquired at many different HWP rotation angles (resulting in a data cube). To enhance the spectral signal-to-noise ratio, each dataset at a given angle consists of an average of two spectra, each obtained by computing the Fourier transform of an (apodized and phase-corrected) average of 30 interferograms¹⁰ with the mirror scanned in both the forward and backward directions. As anticipated, the resulting spectra are divided by the background dataset, which in turn is the average of three spectra, to

¹⁰ This is to all intents and purposes equivalent to averaging 60 interferograms together. However, we proceed as described in the text for operative convenience.

obtain the transmission of the coated HWP alone as a function of frequency.

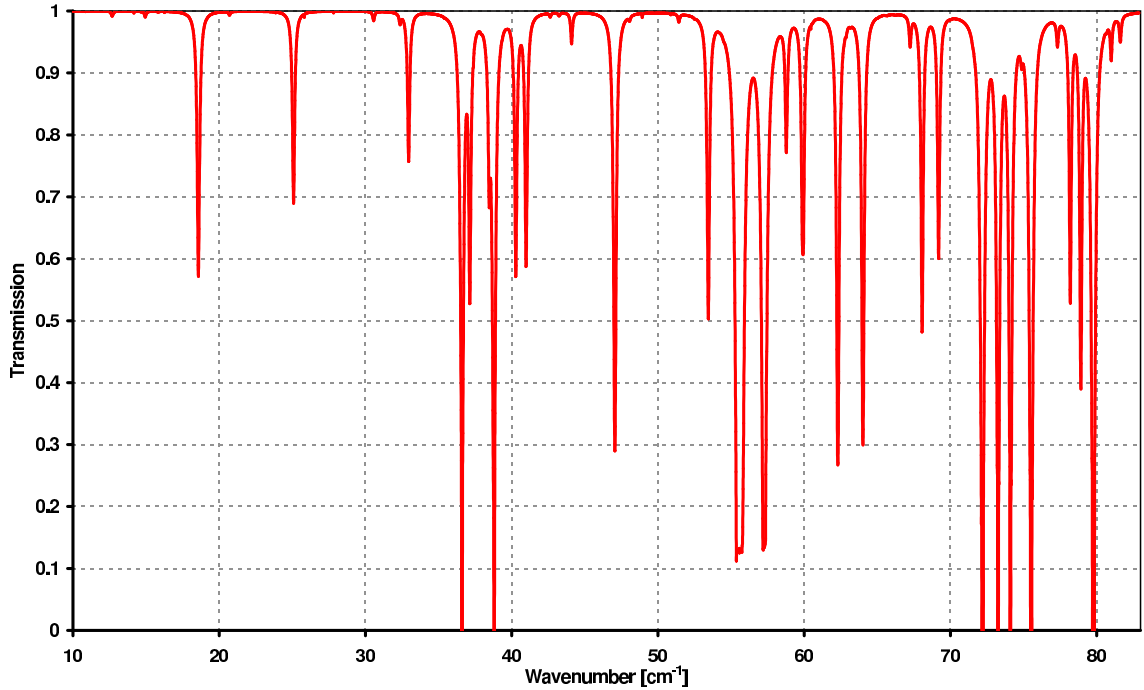


Fig. 5.10 Synthetic transmission spectrum from an atmospheric model, in arbitrary units. Provided by Ade (2009, private communication).

Because these data are collected over several hours, the amount of water vapor in the room is likely to slightly change with time; we account for this by taking background spectra approximately every hour and dividing the HWP spectra taken within that hour only by the corresponding background dataset. Nevertheless, discernible residuals from atmospheric features can still be appreciated in the final HWP spectra, especially at wavenumbers $k \gtrsim 30 \text{ cm}^{-1}$ (the BLAST-Pol $250 \mu\text{m}$ band). We use a synthetic atmospheric transmission spectrum (provided by Ade 2009, private communication; shown in Figure 5.10) to correct the original spectra by concurrently scaling the amplitude of the most prominent features, which are due to water vapor. We find that while some of the spectra do not need any correction at all, others need to be corrected by as much as $\sim 15\%$; the corrected spectra

are shown in Figure 5.11, where each line is a spectrum at a different rotation angle of the HWP (in the range $\theta = 0^\circ\text{--}332^\circ$).

An ideal HWP modulates the polarization at 4θ , therefore in a complete revolution there are four maxima (and minima), two for each of the birefringent axes. The zero angle in this case coincides with the HWP maximum, which is the HWP angle at which we measure maximum total power on the detector; this of course includes signal outside of the HWP bands (in the range $5\text{--}60\text{ cm}^{-1}$). As we will see later on in this chapter, the position of the equivalent axes of the sapphire plate stack (and hence the position of the HWP maxima/minima) depends upon the wavelength. Therefore the HWP maxima (and minima) we assign while taking spectra are just a rough approximation. Although we do increase the angle sampling rate in the vicinities of a maximum or minimum, in order to fully characterize the HWP it is not necessary to take spectra *exactly* at its maxima or minima.

Due to polarization symmetry, no appreciable change should be observed in pairs of datasets taken at angles that are 180° apart. We verify that the experimental setup is symmetric with respect to the HWP rotation by comparing spectra taken, for instance, near the two maxima, at $\theta_1^{\text{max}} = [0^\circ, 180^\circ]$ and at $\theta_2^{\text{max}} = [88^\circ, 268^\circ]$. The fact that the curves are superimposed confirms that there are no artifacts arising from misalignments in the optical setup.

Although we do correct for the residual contaminations due to atmospheric features, which mainly affect the shorter BLAST-Pol wavelengths, we cannot rule out the possibility that some of the spectral fringes may still be altered. Furthermore, and more importantly, these spectra show significant in-band transmission loss due to the absorption from sapphire at room temperature (recall Figures 5.6 and 5.7), which becomes more prominent with increasing frequency. Because

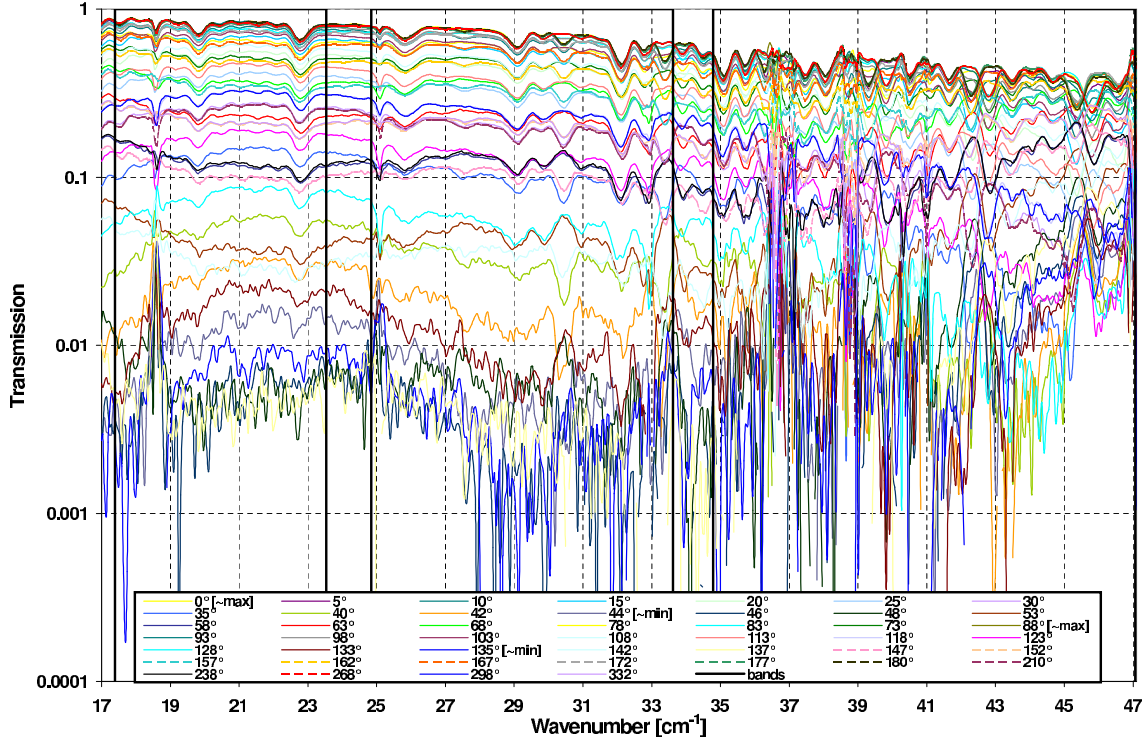


Fig. 5.11 Measured co-pol transmission spectra of the coated BLAST-Pol HWP at room temperature. Each line is obtained at a different HWP rotation angle and is the average of two spectra, each obtained by computing the Fourier transform of an (apodized and phase-corrected) average of 30 interferograms. The resulting spectra are corrected for residual contaminations due to atmospheric features by using the synthetic spectrum shown in Figure 5.10. The solid black lines show the approximate extent of the three BLAST-Pol bands.

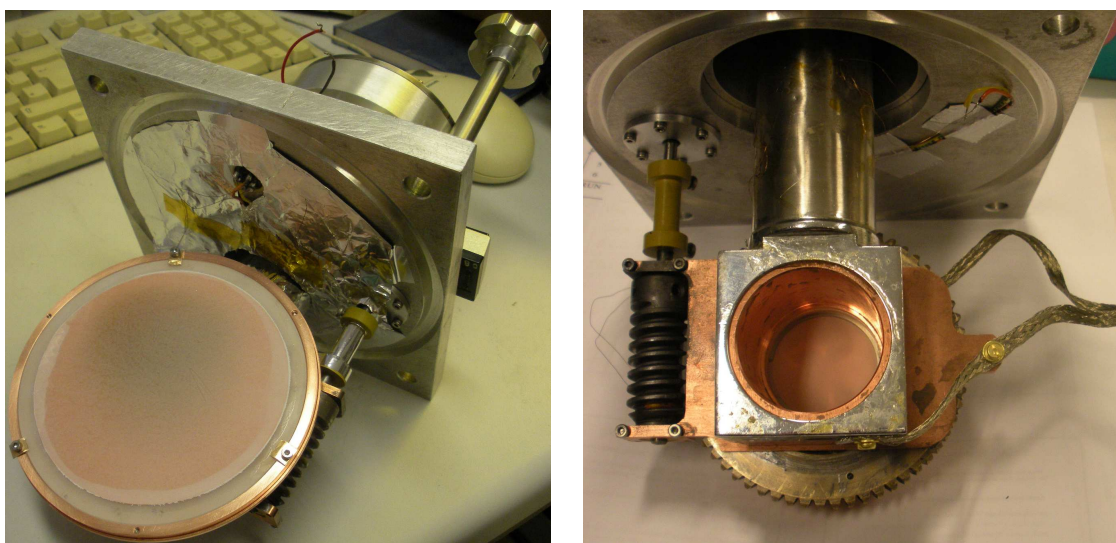
of these two reasons, we decide not to take cross-pol spectra at room temperature and repeat our measurements with the HWP in a vacuum cavity, at temperatures as low as currently possible with the experimental apparatus at our disposal.

5.2.5.3 Cold measurements

The experimental setup for spectral measurements of the cold HWP is substantially different than that described in the previous section, except for the radiation source and the main pFTS module.

We position the HWP in a removable module of the pFTS, which we refer to as “cold finger”. Two photographs and a brief description

of the module are given in Figure 5.12; it fits in the vacuum cavity at the output port of the pFTS, as indicated in Figure 5.30.



(a) Front view.

(b) Rear view.

Fig. 5.12 Photographs of the “cold finger” module of the pFTS, which fits in the vacuum cavity indicated in Figure 5.30. The central cylinder is hollow and must be continuously replenished with liquid nitrogen to maintain the temperature of the HWP at ~ 120 K. Aluminium insulation and a thick copper strap improve the thermal performance of the module. Two thermometers monitor the temperature at the bottom of the cylinder (base plate) at the edge of the copper HWP holder. The rotator is manually driven via a gear train and a vacuum-seal shaft leading to a manual knob outside the module. The resolution of the analog encoder on the rotation angle is 0.06° . The presence of a thermometer on the rotating element prevents rotations greater than $\sim 180^\circ$.

While the base plate reaches temperatures close to the boiling point of liquid nitrogen (77 K), the HWP holder thermalizes at about 120 K despite the improved insulation and thermal link to the base plate. Other cryogenic tests conducted by bonding a thermometer at the center of a single slab of sapphire ensure that the temperature measured at the edge of an aluminium or copper holder closely matches that of the sapphire substrate at its center.

After the roughly two hours needed for the cold finger to thermalize (while continuously filling it with liquid nitrogen), we can character-

ize the spectral response of the cold HWP, by rotating it inside the vacuum cavity with a resolution of 0.06° on the rotation angle. In this configuration, the P10 output polarizer of the pFTS acts as PP1 in the room temperature setup (see Figure 5.9), while a second P10 polarizer (analyzer, acting as PP2) is installed at the exit port of the vacuum cavity. On the outside of the cavity, the cryostat housing the bolometric detector is connected with no air gaps to the exit port. This time we use a composite bolometer cooled at 1.5 K by pumping on the liquid helium bath; this detector is again cryogenically low-pass filtered at 60 cm^{-1} to minimize photon noise.

Over two days of measurements, we acquire data cubes for co-pol (Figures 5.13 and 5.15) and cross-pol (Figures 5.14 and 5.16) transmissions using exactly the same parameters as quoted in the previous section, except for the scan speed, which we increase to 2 cm s^{-1} to quicken the measurement process at no expense of the quality of the spectra. The background dataset is obtained in co-pol configuration by scanning the spectrometer in the absence of the whole cold finger. Because of the controlled environment in the vacuum cavity, our measurements are now much less susceptible to the external environment; however, we repeat background scans at the very end of our measurement session to monitor drifts in the bolometer responsivity and other potential systematic effects. Next, prior to inserting the cold finger in the cavity, we characterize the instrumental cross-pol of this setup by rotating PP2 by 90° in cross-pol configuration and acquiring three spectra. By averaging these cross-pol spectra and dividing by the co-pol background, we measure a cross-pol level of 0.2% or less across the entire spectral range of interest ($5\text{--}60\text{ cm}^{-1}$); we include the resulting cross-pol spectrum in Figures 5.13 and 5.14 (dark pink line).

In the surfaces depicted in Figures 5.15 and 5.16, slices of the data

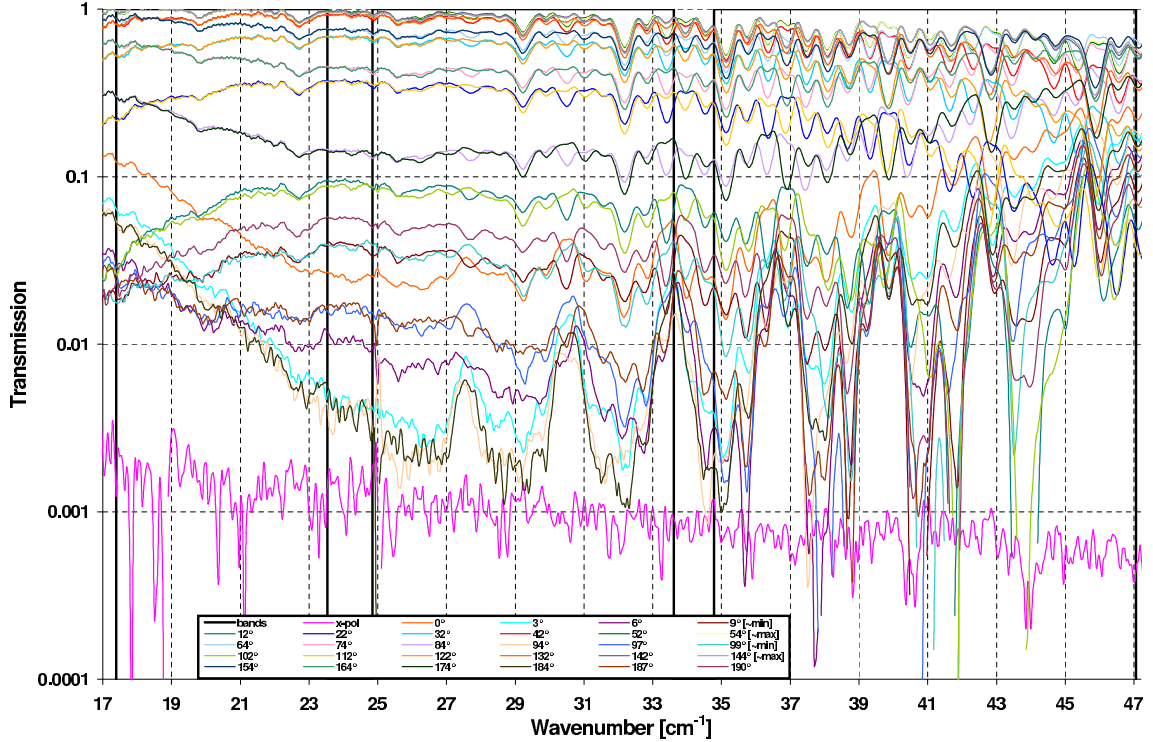


Fig. 5.13 Measured co-pol transmission spectra of the coated BLAST-Pol HWP at ~ 120 K. Each line is obtained at a different HWP rotation angle and is the average of two spectra, each obtained by computing the Fourier transform of an (apodized and phase-corrected) average of 30 interferograms. The solid black lines show the approximate extent of the three BLAST-Pol bands.

cube along the wavenumber axis constitute the measured spectra for different angles of the HWP, while slices along the angle axis represent the modulation function of the wave plate at a given frequency or, more precisely, within a narrow band of frequencies defined by a combination of spectral resolution and the spectrometer's instrument function.

The features visible in all spectra (including those shown previously in Figure 5.11) are spectral fringes due to standing waves generated inside the stack of dielectric plates (even with a quasi-perfect impedance matching coating on the outer surfaces); the presence of several interspersed layers of polyethylene enhances the amplitude of the fringes by introducing small amounts of absorption at every internal reflection.

We note that both the co-pol and cross-pol transmission near the

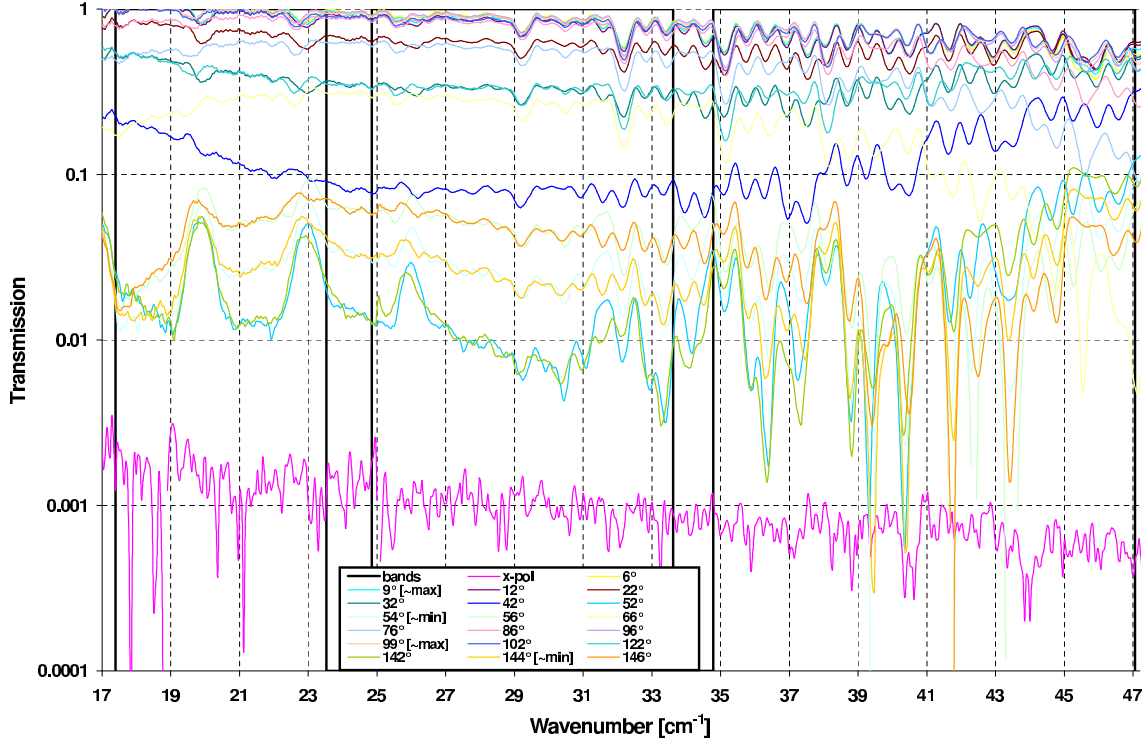


Fig. 5.14 Measured spectra equivalent to those shown in Figure 5.13 but for cross-pol transmission.

maxima occasionally exceed unity by 1–2% at low frequencies, which is theoretically not possible. While the band integration of the transmission curves still yields a transmission ≤ 1 (see later on, Equation 5.3 and Figures 5.18, 5.19), we discuss here possible issues in the experimental setup that may cause some of the spectral fringes to slightly exceed unitary transmission at the longest wavelengths. First, we recall that for the room-temperature measurements we place the HWP in a quasi-parallel beam by using two polyethylene lenses; this is not the case here, where the HWP is positioned roughly at the focus of the polarized pFTS output. As mentioned in Section 4.2, an optical path is slightly stretched by the insertion of a ~ 2.5 mm-thick sapphire HWP. In the case of a collimated beam this effect is usually harmless, whereas it could constitute a problem in a converging beam. In our case, the optical coupling between the converging pFTS output and

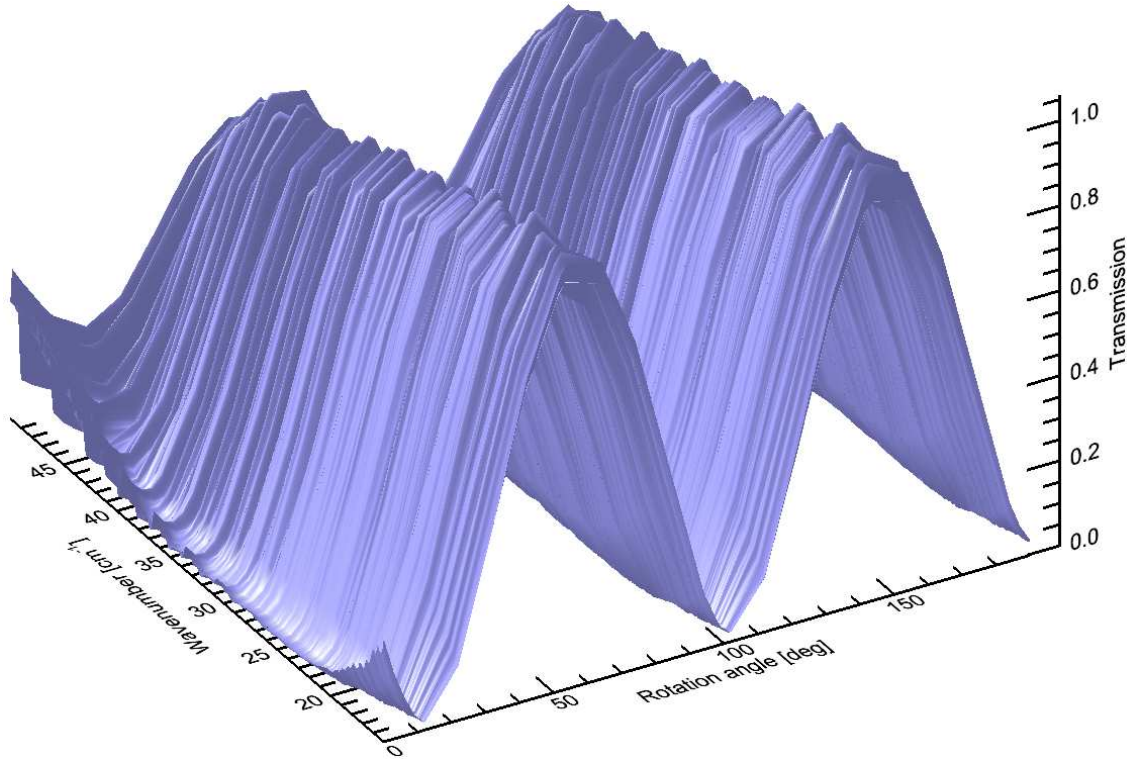


Fig. 5.15 Data cube represented by a surface obtained by stacking a set of spectral co-pol transmissions of the HWP at different angles. Each measured spectra (as shown in Figure 5.13) is a slice of the surface perpendicular to the angle axis.

the bolometer feed-horn may be altered with respect to the background configuration by the stretch in optical path due to the insertion of the HWP in the vacuum cavity. In addition, the insertion of the cold HWP in the vacuum cavity effectively decreases the thermal background load on the bolometer, thus increasing its responsivity. A combination of both these limitations in the experimental setup is likely to produce a misestimation of the background level at low frequencies, thus causing an excess transmission. Correcting for these effects is beyond the scope of this thesis and may be treated in a future work.

On the other hand, characterizing the uncertainty on the measured spectra is certainly very relevant to the discussion that follows in the next sections. Because we average a consistent number of interferograms (30×2) to obtain the final spectra, the statistical uncertainty

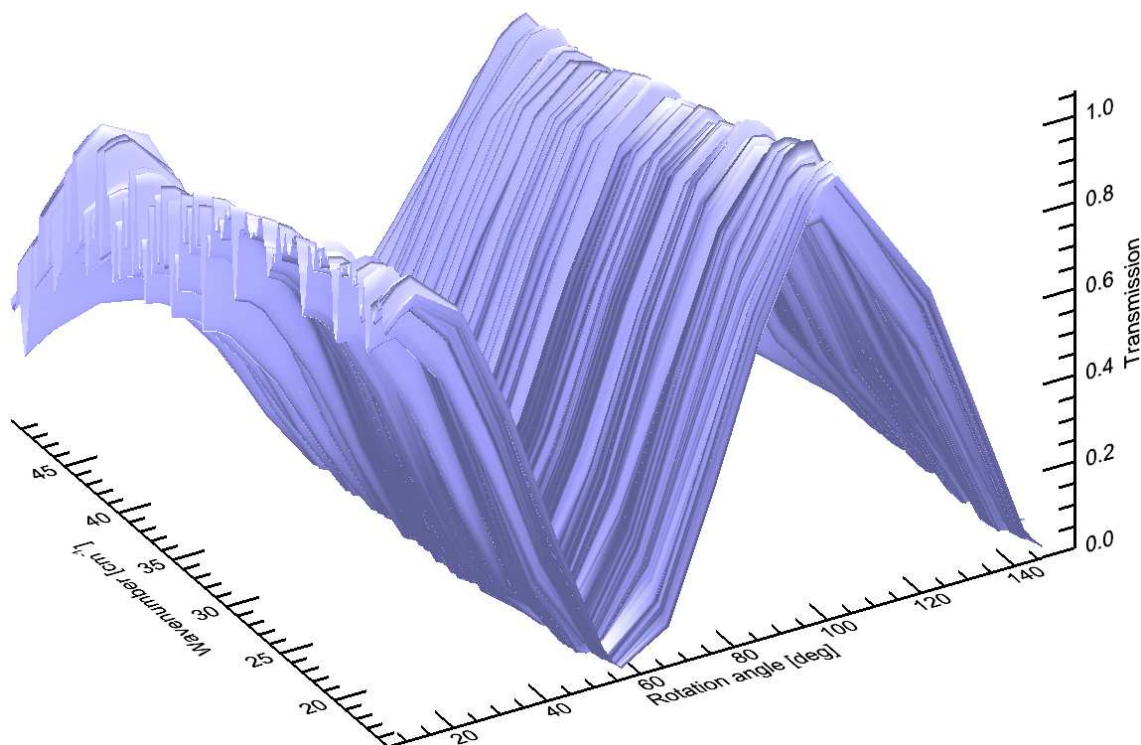


Fig. 5.16 Equivalent data cube to that shown in Figure 5.15 but for cross-pol transmission. Note how the two surfaces are complementarily in counterphase to each other. Each measured spectra (as shown in Figure 5.14) is a slice of the surface perpendicular to the angle axis.

associated with the average on a single dataset is found to be negligible, as expected. Rather, we average together all the available background interferograms that are collected over one day of measurements, and take the statistical dispersion as our estimate of the uncertainty associated with all the spectra collected on that day. Because the thermodynamic conditions in the cavity under vacuum are not susceptible to changes in the external environment, this procedure allows us to account for drifts in the bolometer responsivity and other potential systematic effects. We show in Figure 5.17 the mean background spectra and the associated error for the co-pol and cross-pol measurement sessions. These errors are used in the following section to estimate the uncertainties on the HWP Mueller matrix coefficients.

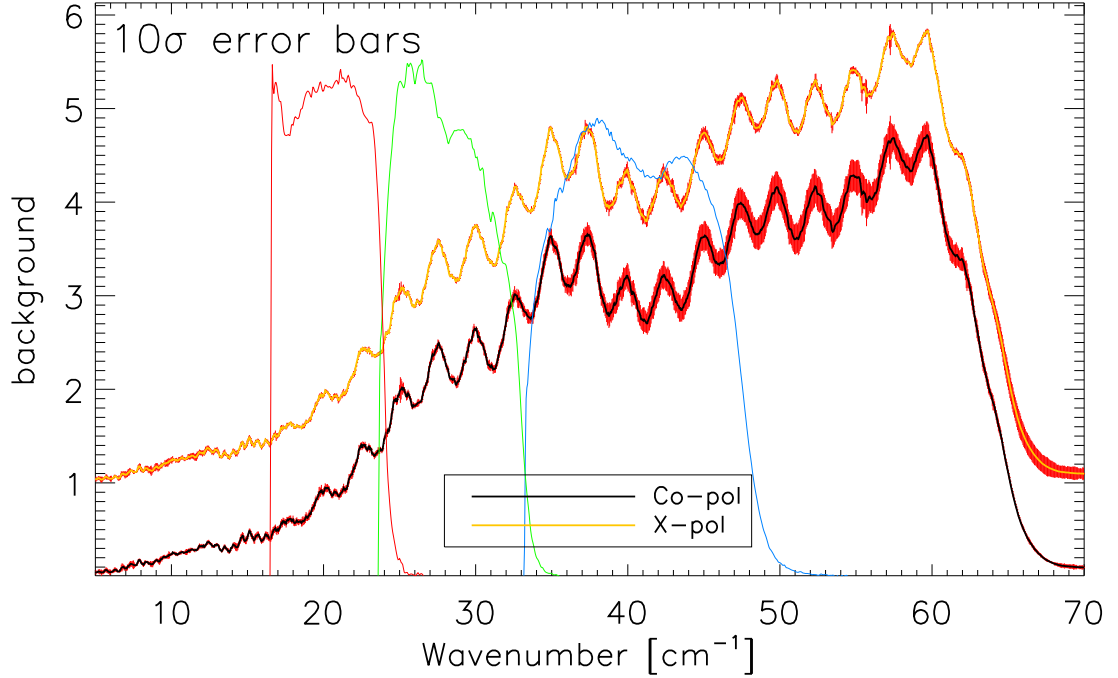


Fig. 5.17 Noise estimation for the spectra shown in Figures 5.13 and 5.14. We plot the mean background spectra (in arbitrary units) for the co-pol (black solid line) and cross-pol (yellow solid line, shifted by 1 in the positive y direction for visual clarity) as a function of wavenumber. The (10σ) error bars (in red) are quantified as the statistical error on the mean. Also shown for reference is the relative spectral response of the three BLAST-Pol channels, in arbitrary units (see Section 4.2).

We can now reduce the dependence on frequency of our data cubes by integrating over the spectral bands of BLAST-Pol, as follows:

$$\bar{T}_{\text{cp}}^{\text{ch}}(\theta) = \frac{\int_0^\infty \Sigma^{\text{ch}}(\nu) T_{\text{cp}}(\theta, \nu) d\nu}{\int_0^\infty \Sigma^{\text{ch}}(\nu) d\nu}, \quad (5.3)$$

where the superscript “ch” refers to one among 250, 350, and 500 μm ; $\Sigma^{\text{ch}}(\nu)$ is the spectral response of each BLAST-Pol band (see Section 4.2); and $T_{\text{cp}}(\theta, \nu)$ are points on the co-pol surface depicted in Figure 5.15. A similar expression can be written for the cross-pol band-integrated transmission. By performing this integration at every angle for which spectral data has been obtained, the interpolation of these data points will result in the modulation functions of the HWP

at ~ 120 K for each of the BLAST-Pol spectral bands; these curves are shown in Figure 5.18 for co-pol and in Figure 5.19 for cross-pol.

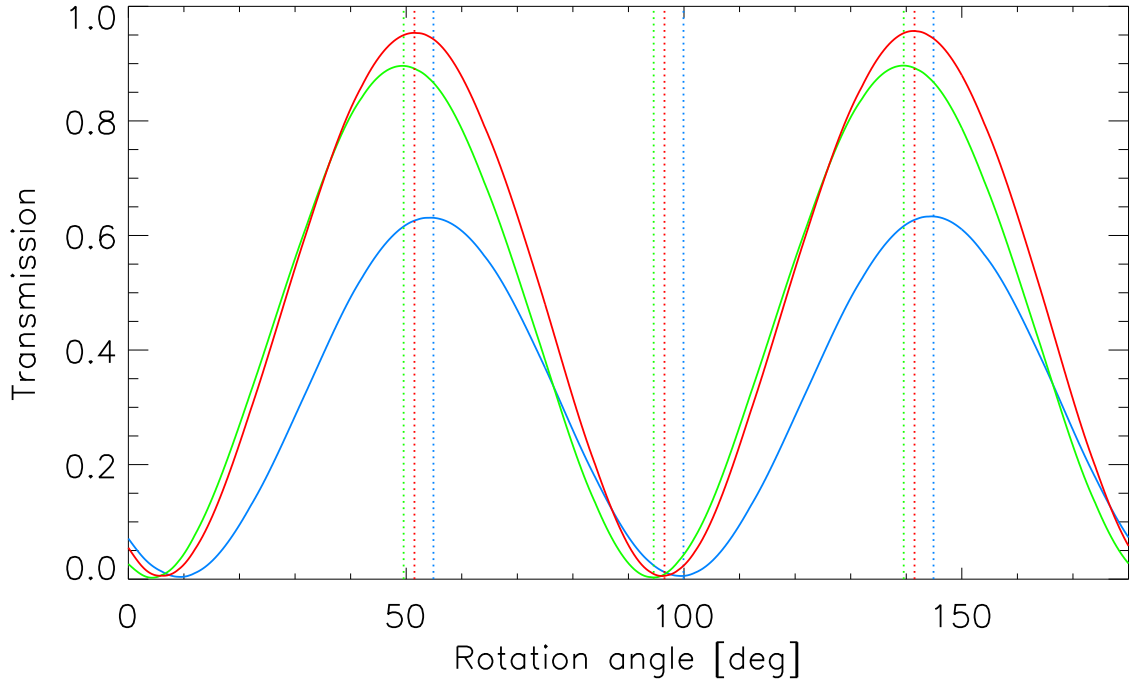


Fig. 5.18 Band-integrated co-pol modulation functions of the BLAST-Pol HWP at ~ 120 K. The curves show the HWP polarization modulation functions for a fully polarized source (with a flat spectrum) parallel to the analyzer in the three spectral bands. Note how the position of the maxima (and minima) depend on the wavelength, even when considering a flat-spectrum polarized input source; the dotted vertical lines show the band-integrated positions of the HWP minima (shown in Figure 5.24), which result from the fitting routine described in the next sections.

The modulation curves presented here assume that the incoming polarized radiation has no dependence on frequency, or in other words that the input source has a flat spectrum. Equation (5.3) can be generalized to include the known (or assumed) spectral signature of a given astronomical or calibration source. More generally, all the band-averaged quantities that we have defined here and will be defined in the following are potentially affected by the spectral shape of the input source. However, we will see how the HWP transmission and modulation efficiency are very weakly dependent on the spectral index of the input source, whereas the position of the equivalent axes of the

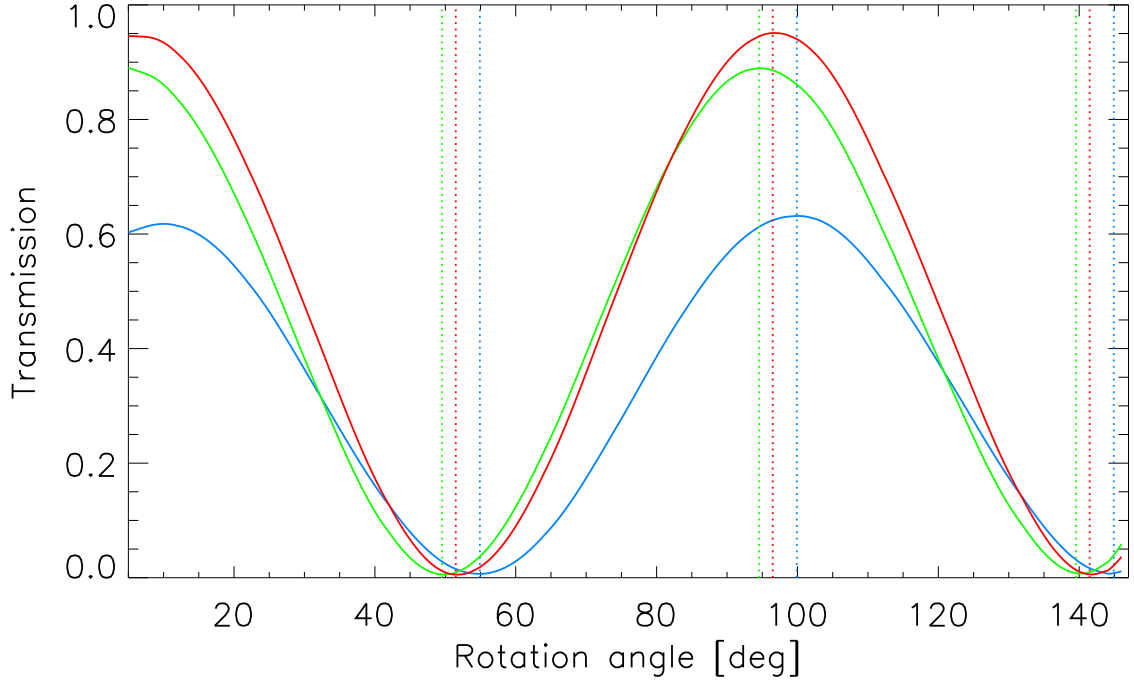


Fig. 5.19 Band-integrated modulation functions equivalent to those shown in Figure 5.18 but for cross-pol transmission.

sapphire plate stack is more significantly affected (see also the analysis carried out by Savini et al. 2009), especially at 250 and 500 μm .

Figures 5.18 and 5.19 clearly show that there is a significant dependence of the position of the HWP maxima and minima upon frequency, even when considering a flat-spectrum polarized input source. These effects are particularly important for a “HWP step and integrate” experiment such as BLAST-Pol (see Section 4.5), and a careful post-flight polarization calibration must be performed by using all the information available from the pre-flight characterization of the HWP. We begin to tackle this problem in the next section, where we outline a relatively simple solution to account for most of the HWP non-idealities in the data analysis pipeline, and in particular in the in map-making algorithm (see Chapter 6).

The spectral transmission datasets of the HWP cooled at ~ 120 K, when compared to those taken with the HWP at room temperature

(Figure 5.11), show a definite abatement of the in-band losses due to absorption from sapphire, as expected. However the effect is still appreciable, especially above $\sim 25 \text{ cm}^{-1}$. We have independent evidence that the residual absorption nearly vanishes when the sapphire is further cooled to 4 K, as it is when the HWP is installed in the BLAST-Pol cryostat. While it is not currently feasible for us to measure the spectral response of the HWP cooled at 4 K, the unique quality and completeness of our dataset allow us to fully characterize the performance of the BLAST-Pol HWP, as we will show in the following.

As anticipated in the previous chapter, we extrapolate our “cold” dataset to 4 K, using the data shown in Figure 5.7¹¹. The inferred co-pol/cross-pol transmissions and modulation efficiency of the BLAST-Pol HWP (with its axis at 0°) at 4 K are shown in Figure 4.5¹². For a flat-spectrum input source, here we quote the band-averaged specifications of the HWP. The transmission at the maxima is ~ 0.87 , ~ 0.91 , and ~ 0.95 at 250, 350, and 500 μm , respectively; whereas the cross-pol is $\lesssim 0.5\%$, $\lesssim 0.2\%$, and $\lesssim 0.5\%$, respectively. Finally, the modulation efficiency, defined as $(T_{\text{cp}}^{0^\circ} - T_{\text{xp}}^{0^\circ}) / (T_{\text{cp}}^{0^\circ} + T_{\text{xp}}^{0^\circ})$, is $\sim 98.8\%$ $\sim 99.5\%$, and $\sim 99.0\%$, respectively.

5.2.6 Mueller matrix characterization

The final goal of this chapter is to provide a set of usable parameters that completely describe the performance of the HWP as measured in

¹¹ We use a combination of the analytical expression and the data points; the former, strictly speaking, applies at 80 K and for $k \lesssim 33 \text{ cm}^{-1}$, thus we complement it at higher frequencies with the data points, which apply at $< 60 \text{ K}$. It is evident from Figure 5.7 that the sapphire absorption coefficient has a very weak dependence on temperature below 80 K (see also Loewenstein et al. 1973, Cook & Perkowitz 1985), and in particular data points collected at 1.5 K are in good enough agreement (within 2% on the resulting absorption for $d = 2.5 \text{ mm}$) with those collected at higher temperatures (up to 80 K). Therefore we can safely claim that for our application a combination of the data shown in Figure 5.7 is a good representation of the sapphire absorption at 4 K.

¹² We have chosen to displace Figure 4.5 to Section 4.5.2 in order for Chapter 4 to be self-contained, since this figure depicts the overall performance of the HWP to the best of our knowledge.

the laboratory. This set of parameters consists of the 16 coefficients of the Mueller matrix of a generic HWP, and the actual phase shift. For an ideal HWP, the Mueller matrix at $\theta = 0^\circ$ reads

$$\mathcal{M}_{\text{HWP}} = \begin{pmatrix} 1 & 0 & 0 & 0 \\ 0 & 1 & 0 & 0 \\ 0 & 0 & -1 & 0 \\ 0 & 0 & 0 & -1 \end{pmatrix}, \quad (5.4)$$

and the phase shift is $\Delta\varphi = 180^\circ$.

For a real HWP, these parameters always depart from ideality to some extent, and by all means depend upon frequency. In the following we describe an empirical model that we develop specifically for the characterization of the BLAST-Pol HWP, though we note that it can be applied to any HWP to recover its frequency-dependent descriptive parameters. Such an empirical model is complementary to the physical and analytical one developed by Savini et al. (2006, 2009), which produces an analogous output by modeling the non-idealities of the building components and their optical parameters.

By recalling the Stokes formalism (see Appendix A of Moncelsi 2007), we can formalize the experimental apparatus described in Sections 5.2.5.2 and 5.2.5.3 as a series of matrix products as follows:

$$S_{\text{out}}^{\text{cp}} = \vec{D}^{\text{T}} \cdot \mathcal{M}_{\text{p}}^{\text{h}} \cdot \mathcal{R}(-\theta) \cdot \mathcal{M}_{\text{HWP}} \cdot \mathcal{R}(\theta) \cdot \vec{S}_{\text{in}}^{\text{h}} \quad (5.5)$$

$$S_{\text{out}}^{\text{xp}} = \vec{D}^{\text{T}} \cdot \mathcal{M}_{\text{p}}^{\text{v}} \cdot \mathcal{R}(-\theta) \cdot \mathcal{M}_{\text{HWP}} \cdot \mathcal{R}(\theta) \cdot \vec{S}_{\text{in}}^{\text{h}}, \quad (5.6)$$

where \vec{D} is the Stokes vector for a bolometric (polarization insensitive) intensity detector, $\mathcal{M}_{\text{p}}^{\text{h}}$ is the Mueller matrix of an ideal horizontal polarizer, $\mathcal{M}_{\text{p}}^{\text{v}}$ is that of an ideal vertical polarizer, $\mathcal{R}(\theta)$ is the generic Mueller rotation matrix, and $\vec{S}_{\text{in}}^{\text{h}}$ is the horizontally polarized input

beam from the pFTS. By expanding all the matrices in Equation 5.5

$$S_{\text{out}}^{\text{cp}} = \frac{1}{4} \begin{pmatrix} 1 & 0 & 0 & 0 \\ 0 & 0 & 0 & 0 \\ 0 & 0 & 0 & 0 \\ 0 & 0 & 0 & 0 \end{pmatrix} \cdot \begin{pmatrix} 1 & 1 & 0 & 0 \\ 1 & 1 & 0 & 0 \\ 0 & 0 & 0 & 0 \\ 0 & 0 & 0 & 0 \end{pmatrix} \cdot \begin{pmatrix} 1 & 0 & 0 & 0 \\ 0 & \cos(2\theta) & \sin(2\theta) & 0 \\ 0 & -\sin(2\theta) & \cos(2\theta) & 0 \\ 0 & 0 & 0 & 1 \end{pmatrix} \cdot \begin{pmatrix} a_{00} & a_{01} & a_{02} & a_{03} \\ a_{10} & a_{11} & a_{12} & a_{13} \\ a_{20} & a_{21} & a_{22} & a_{23} \\ a_{30} & a_{31} & a_{32} & a_{33} \end{pmatrix} \cdot \begin{pmatrix} 1 & 0 & 0 & 0 \\ 0 & \cos(2\theta) & -\sin(2\theta) & 0 \\ 0 & \sin(2\theta) & \cos(2\theta) & 0 \\ 0 & 0 & 0 & 1 \end{pmatrix} \cdot \begin{pmatrix} 1 \\ 1 \\ 0 \\ 0 \end{pmatrix},$$

and computing the products¹³, we obtain the following expression:

$$S_{\text{out}}^{\text{cp}} = \frac{1}{2} \left(\frac{a_{00}}{2} + \frac{a_{10}}{2} \cos 2\theta - \frac{a_{20}}{2} \sin 2\theta \right) + \quad (5.7)$$

$$+ \frac{1}{2} \left[\left(\frac{a_{01}}{2} + \frac{a_{11}}{2} \cos 2\theta - \frac{a_{21}}{2} \sin 2\theta \right) \cos 2\theta + \right.$$

$$\left. - \left(\frac{a_{02}}{2} + \frac{a_{12}}{2} \cos 2\theta - \frac{a_{22}}{2} \sin 2\theta \right) \sin 2\theta \right],$$

which can be rearranged as follows:

$$S_{\text{out}}^{\text{cp}} = \frac{1}{8} \left[2a_{00} + a_{11} + a_{22} + 2(a_{01} + a_{10}) \cos 2\theta + \quad (5.8)$$

$$+ (a_{11} - a_{22}) \cos 4\theta - 2(a_{02} + a_{20}) \sin 2\theta - (a_{12} + a_{21}) \sin 4\theta \right]$$

$$= A + B \sin 2\theta + C \cos 2\theta + D \sin 4\theta + E \cos 4\theta, \quad (5.9)$$

with

$$A \equiv \frac{1}{4} \left(a_{00} + \frac{a_{11}}{2} + \frac{a_{22}}{2} \right) \quad (5.10)$$

$$B \equiv -\frac{1}{4} (a_{02} + a_{20}), \quad C \equiv \frac{1}{4} (a_{01} + a_{10})$$

$$D \equiv -\frac{1}{8} (a_{12} + a_{21}), \quad E \equiv \frac{1}{8} (a_{11} - a_{22}).$$

¹³ We validate the results of all the matrix products in this thesis with the software *Mathematica*.

Similarly, we rearrange Equation (5.6) as follows:

$$S_{\text{out}}^{\text{xp}} = \frac{1}{4} \begin{pmatrix} 1 & 0 & 0 & 0 \\ 0 & 0 & 0 & 0 \\ 0 & 0 & 0 & 0 \\ 0 & 0 & 0 & 0 \end{pmatrix} \cdot \begin{pmatrix} 1 & -1 & 0 & 0 \\ -1 & 1 & 0 & 0 \\ 0 & 0 & 0 & 0 \\ 0 & 0 & 0 & 0 \end{pmatrix} \cdot \begin{pmatrix} 1 & 0 & 0 & 0 \\ 0 & \cos(2\theta) & \sin(2\theta) & 0 \\ 0 & -\sin(2\theta) & \cos(2\theta) & 0 \\ 0 & 0 & 0 & 1 \end{pmatrix} \cdot \begin{pmatrix} a_{00} & a_{01} & a_{02} & a_{03} \\ a_{10} & a_{11} & a_{12} & a_{13} \\ a_{20} & a_{21} & a_{22} & a_{23} \\ a_{30} & a_{31} & a_{32} & a_{33} \end{pmatrix} \cdot \begin{pmatrix} 1 & 0 & 0 & 0 \\ 0 & \cos(2\theta) & -\sin(2\theta) & 0 \\ 0 & \sin(2\theta) & \cos(2\theta) & 0 \\ 0 & 0 & 0 & 1 \end{pmatrix} \cdot \begin{pmatrix} 1 \\ 1 \\ 0 \\ 0 \end{pmatrix},$$

$$S_{\text{out}}^{\text{xp}} = \frac{1}{2} \left(\frac{a_{00}}{2} - \frac{a_{10}}{2} \cos 2\theta + \frac{a_{20}}{2} \sin 2\theta \right) + \quad (5.11)$$

$$+ \frac{1}{2} \left[\left(\frac{a_{01}}{2} - \frac{a_{11}}{2} \cos 2\theta + \frac{a_{21}}{2} \sin 2\theta \right) \cos 2\theta + \right.$$

$$\left. - \left(\frac{a_{02}}{2} - \frac{a_{12}}{2} \cos 2\theta + \frac{a_{22}}{2} \sin 2\theta \right) \sin 2\theta \right],$$

$$S_{\text{out}}^{\text{xp}} = \frac{1}{8} \left[2a_{00} - a_{11} - a_{22} + 2(a_{01} - a_{10}) \cos 2\theta + \quad (5.12)$$

$$+ (a_{22} - a_{11}) \cos 4\theta + 2(a_{20} - a_{02}) \sin 2\theta + (a_{12} + a_{21}) \sin 4\theta \right]$$

$$= A' + B' \sin 2\theta + C' \cos 2\theta + D' \sin 4\theta + E' \cos 4\theta, \quad (5.13)$$

with

$$A' \equiv \frac{1}{4} \left(a_{00} - \frac{a_{11}}{2} - \frac{a_{22}}{2} \right) \quad (5.14)$$

$$B' \equiv \frac{1}{4} (a_{20} - a_{02}), \quad C' \equiv \frac{1}{4} (a_{01} - a_{10})$$

$$D' \equiv \frac{1}{8} (a_{12} + a_{21}), \quad E' \equiv \frac{1}{8} (a_{22} - a_{11}).$$

Finally, by performing linear combinations of the quantities defined

in Equations (5.10) and (5.14), one can write the individual elements that compose the Mueller matrix of a generic HWP as follows:

$$\begin{aligned}
 a_{00} &= 2 (A + A'), & a_{01} &= 2 (C + C') \\
 a_{10} &= 2 (C - C'), & a_{11} &= 2 (A - A' + E - E') \\
 a_{02} &= -2 (B + B'), & a_{20} &= 2 (B' - B) \\
 a_{22} &= 2 (A - A' - E + E'), & a_{12} &= a_{21} = 2 (D' - D) ,
 \end{aligned} \tag{5.15}$$

where in the last equality we currently assume the symmetry of two coefficients, $a_{12} = a_{21}$. This degeneracy may be broken by imposing the conservation of energy, i.e. by requiring that the output Stokes vector resulting from a generic polarized input traveling through the recovered HWP Mueller matrix satisfies $I^2 = Q^2 + U^2$. This additional constrain may be included in a future work. Also, because our experimental setup is sensitive to linear but not circular polarization, this method only allows to constrain the 9 elements of the Mueller matrix associated with $[I, Q, U]$. The remaining 7 coefficients associated with V can only be measured with the use of a quarter-wave plate, which induces a phase shift of 90° between the two orthogonal polarizations traveling through the plate; this measurement is beyond the scope of this thesis and not pertinent to the needs of BLAST-Pol.

We want to estimate the 9 coefficients derived in Equation (5.15) from the co-pol and cross-pol data cubes described in Section 5.2.5.3. Equations (5.9) and (5.13) encode a simple dependence of $S_{\text{out}}^{\text{cp}}$ and $S_{\text{out}}^{\text{xp}}$ upon θ , the HWP rotation angle. Therefore, for a given frequency, a minimization routine can be applied to the measured transmission curves as a function of θ , to determine the parameter sets $[A, B, C, D, E]$ and $[A', B', C', D', E']$ for the co-pol and cross-pol configurations, respectively. By repeating the fit for every frequency, we

have an estimate of the 9 coefficients as a function of wavelength. However, this procedure does not allow us to associate any uncertainty to our estimates.

A better approach to this problem is to use a Monte Carlo simulation. We repeat the above fitting procedure an elevated number of times (1000 in our case); every time we add to every individual transmission curve a realization of white noise, scaled to the 1σ spectral uncertainty as estimated in Figure 5.17, and compute the fit using this newly generated transmission curve. In addition, for every frequency we introduce a random jitter on the rotation angle that has a 1σ amplitude of 1° . The dispersion in the fitted parameters due to the introduction of these two uncertainties, which are inherent to the measurement process, provides a realistic estimate of the uncertainty to be associated with each of the 9 coefficients. In particular, at each frequency, we produce 9 histograms of the 1000 fitted values. We use the mode of each distribution as our best estimate for the corresponding coefficient at that frequency, and the 68% confidence interval as the associated 1σ error.

In Figure 5.20 we show a graphical representation of the 9-element Mueller matrix of the BLAST-Pol HWP at a given angle ($\theta = 0^\circ$), as a function of wavenumber. In Figures 5.21, 5.22, and 5.23 we show the resulting histograms for the 9 coefficients at 20, 28.6, and 40 cm^{-1} , respectively (which are the center frequencies of the BLAST-Pol bands).

The behavior of the coefficients as a function of wavenumber shown in Figure 5.20 suggests that the position of the HWP equivalent axes, β_{ea} hereafter, may have an inherent frequency dependence, which we must investigate. β_{ea} can be readily retrieved at each frequency by locating the rotation angle that corresponds to the first minimum in the fitted transmission curve. Hence, β_{ea} is measured with respect to an

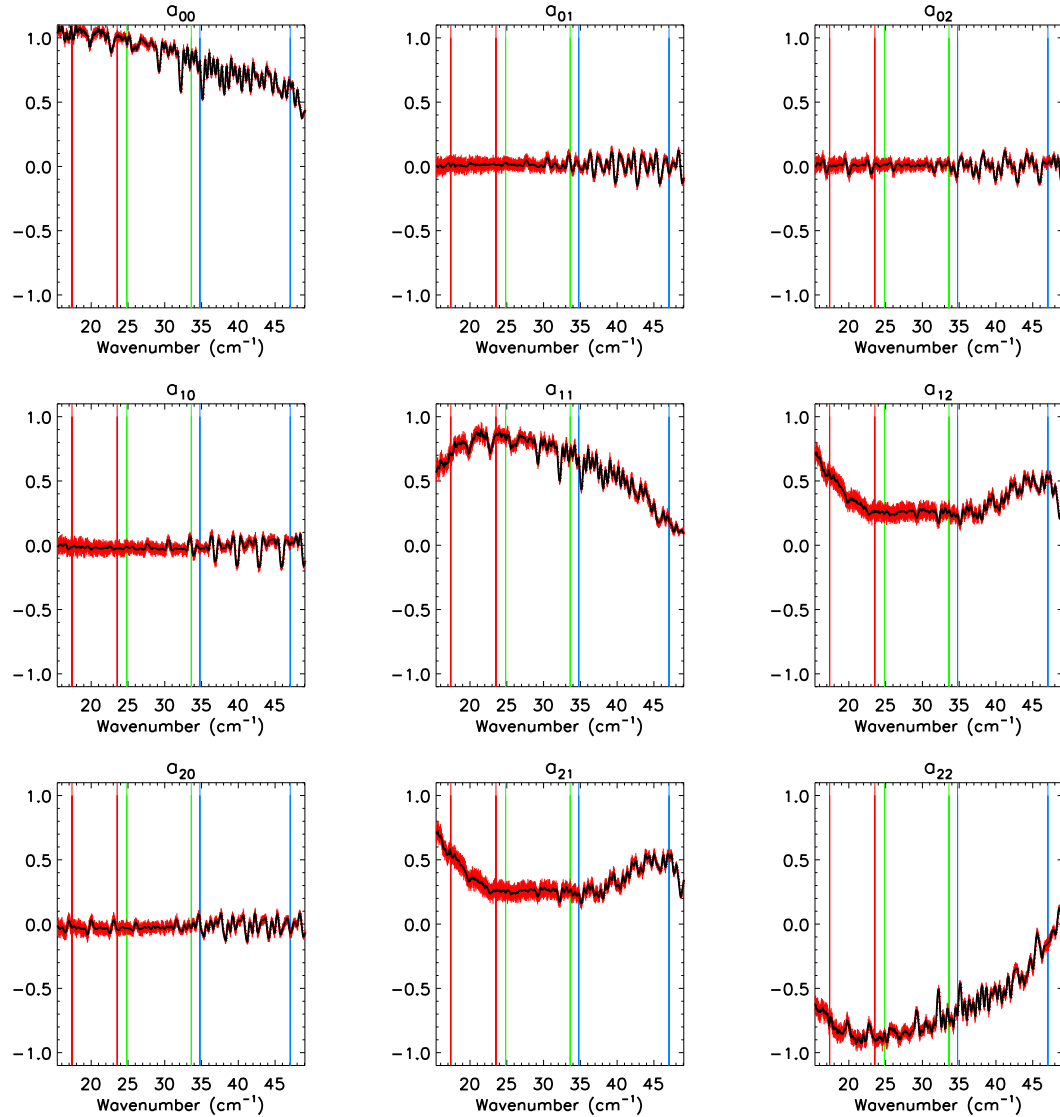


Fig. 5.20 Graphical representation of the Mueller matrix of the BLAST-Pol HWP at a given angle ($\theta = 0^\circ$), as a function of wavenumber. The (10σ) error bars (in red) are quantified via a Monte Carlo, which accounts for random errors in the spectra of amplitude as given in Figure 5.17, and random errors in the rotation angle of amplitude 1° .

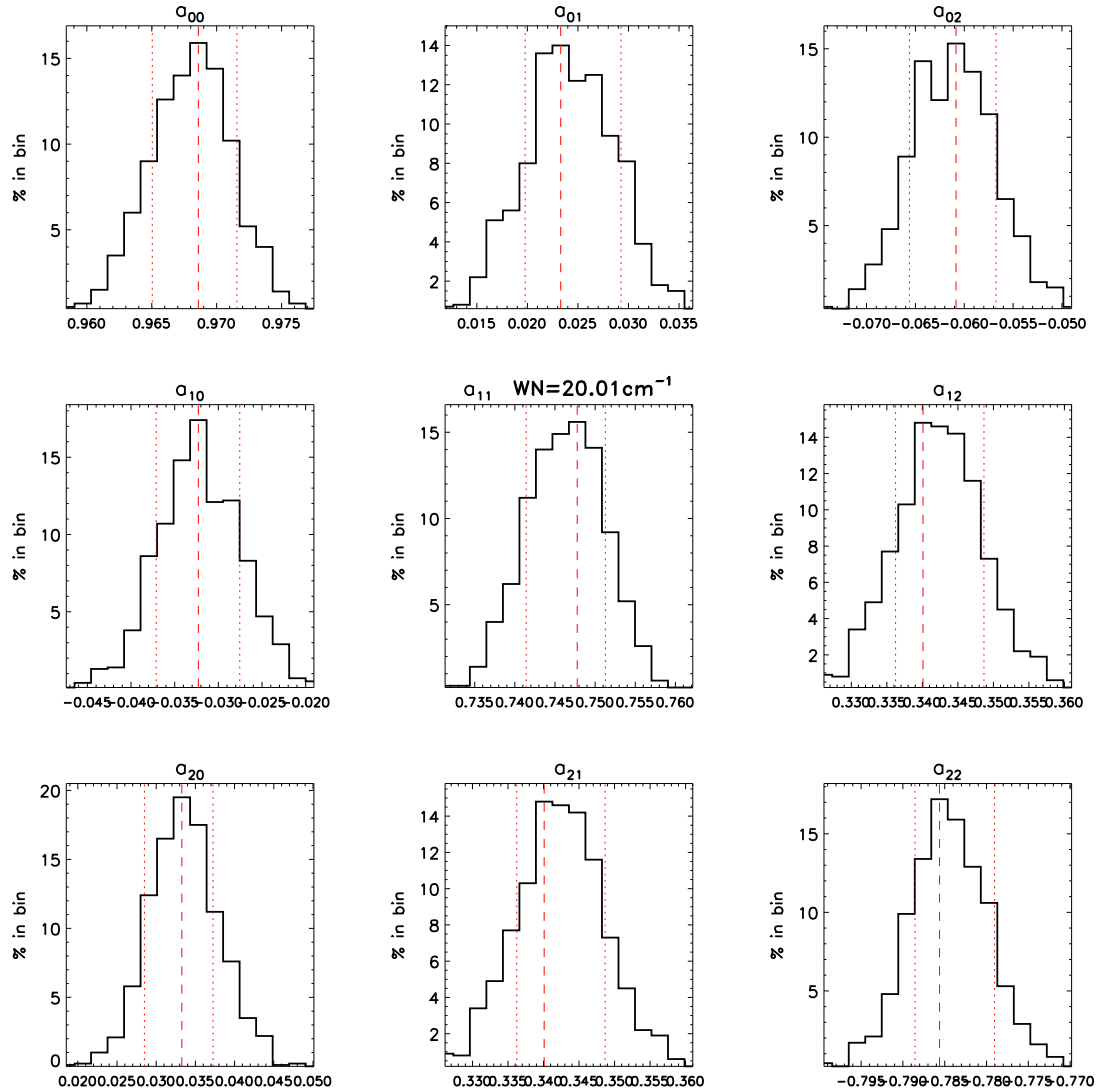


Fig. 5.21 Histograms at 20 cm^{-1} (central frequency of the $500 \mu\text{m}$ BLAST-Pol band) resulting from the Monte Carlo fit of the HWP parameters. For every histogram, the dashed red line indicates the mode of the distribution, which we adopt as our best estimate for the corresponding coefficient at that frequency, while the two dotted red lines indicate the 68% confidence interval, which we use as the uncertainty on the retrieved coefficient.

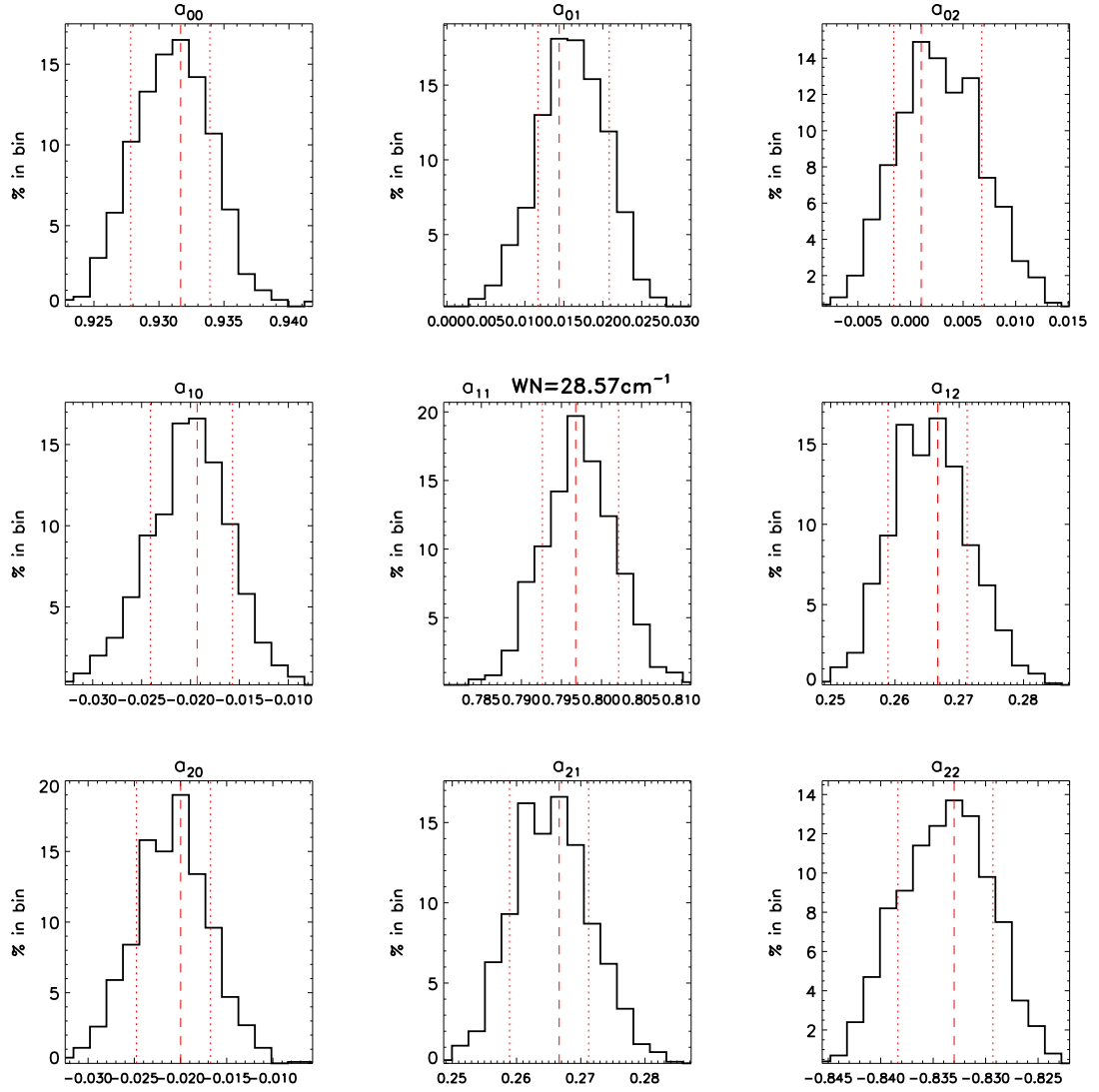


Fig. 5.22 Histograms at 28.57 cm^{-1} (central frequency of the $350 \mu\text{m}$ BLAST-Pol band) resulting from the Monte Carlo fit of the HWP parameters. For every histogram, the dashed red line indicates the mode of the distribution, which we adopt as our best estimate for the corresponding coefficient at that frequency, while the two dotted red lines indicate the 68% confidence interval, which we use as the uncertainty on the retrieved coefficient.

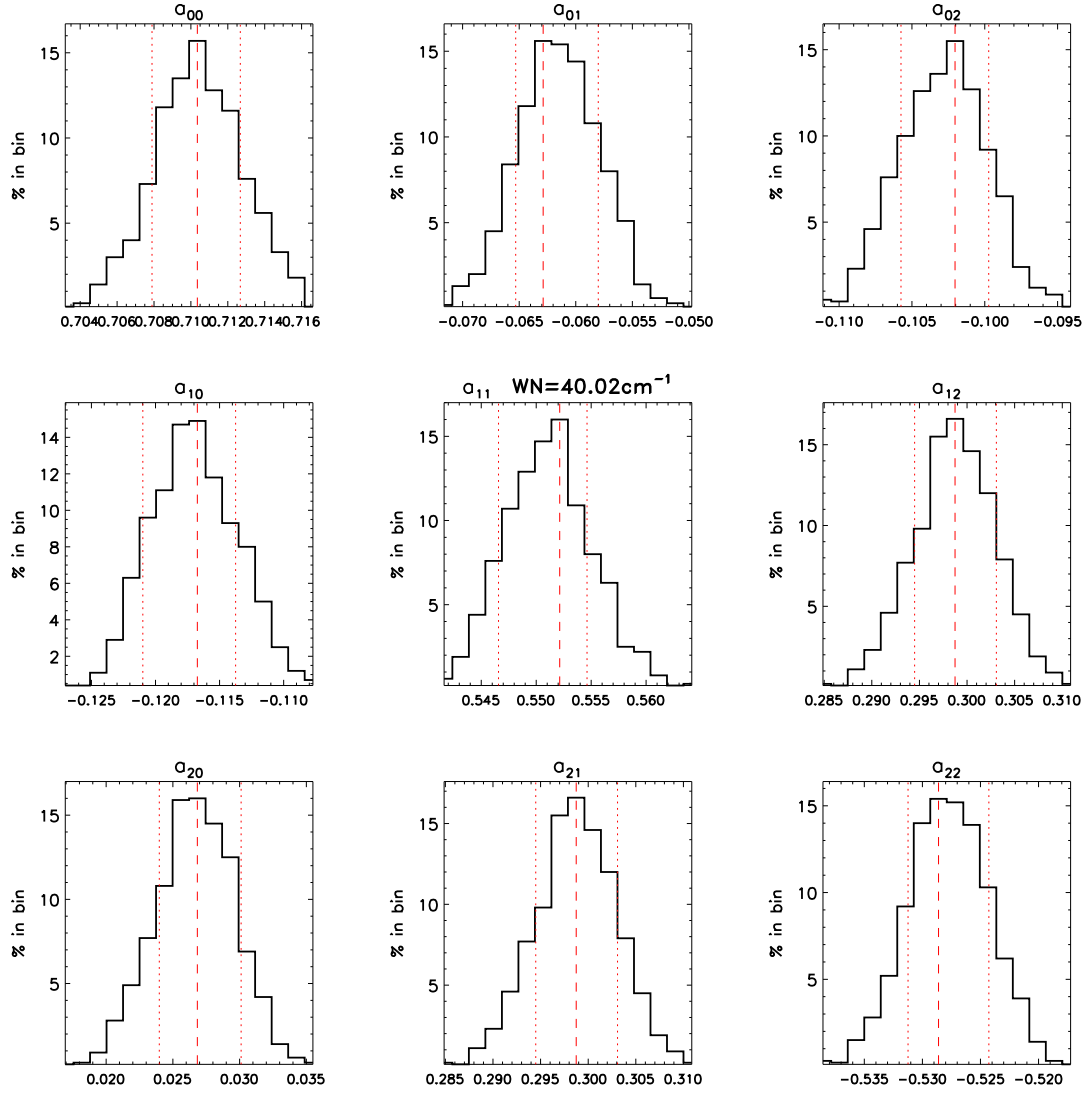


Fig. 5.23 Histograms at 40 cm^{-1} (central frequency of the $250 \mu\text{m}$ BLAST-Pol band) resulting from the Monte Carlo fit of the HWP parameters. For every histogram, the dashed red line indicates the mode of the distribution, which we adopt as our best estimate for the corresponding coefficient at that frequency, while the two dotted red lines indicate the 68% confidence interval, which we use as the uncertainty on the retrieved coefficient.

arbitrary constant offset that is inherent to the specific experimental setup; we set this offset to be zero at 25 cm^{-1} . Operatively, this means that the HWP zero angle in the instrument reference frame (β_0 ; see Equation 6.2) must be calibrated using the $350 \mu\text{m}$ band. A plot of β_{ea} as a function of wavenumber is given in Figure 5.24.

As anticipated, it is of crucial importance to derive the band-averaged value of β_{ea} for input sources with different spectral signature, as follows:

$$\bar{\beta}_{\text{ea}}^{\text{ch}} = \frac{\int_0^\infty \Sigma^{\text{ch}}(\nu) \beta_{\text{ea}}(\nu) \varsigma(\nu) d\nu}{\int_0^\infty \Sigma^{\text{ch}}(\nu) \varsigma(\nu) d\nu}, \quad (5.16)$$

where we adopt the same notation as in Equation (5.3) and the known (or assumed) spectrum of an astronomical or calibration source is modeled as $\varsigma(\nu) \propto \nu^\alpha$. We compute Equation (5.16) for a range of spectral indices of interest: $\alpha = 0$ for a flat spectrum; $\alpha = 2$ for the Rayleigh-Jeans tail of a blackbody; $\alpha = 4$ for interstellar dust, modeled as a modified blackbody with emissivity $\beta = 2$ (Hildebrand 1983); and finally $\alpha = -2$ as a replacement for the mid-infrared exponential on the Wien side of a blackbody to account for the variability of dust temperatures within a galaxy (Blain 1999, Blain et al. 2003; see also Sections 2.3.2 and 3.3.3). The results of this analysis are shown in Figure 5.24 and in Table 5.1.

Expectedly, the impact of different input spectral signatures is minimal at $350 \mu\text{m}$, where the HWP has been designed to function optimally (see Section 5.2.3); whereas the spectral dependence is more pronounced at 250 and $500 \mu\text{m}$, and, if neglected, it may lead to an arbitrary rotation of the retrieved polarization angle on the sky of magnitude $2\bar{\beta}_{\text{ea}} = 10\text{--}15^\circ$ ($3\text{--}5^\circ$) at 250 (500) μm (see Equation 6.2).

We have thus confirmed that the dependence of the HWP equivalent axes upon wavelength is inherent to the achromatic design. We

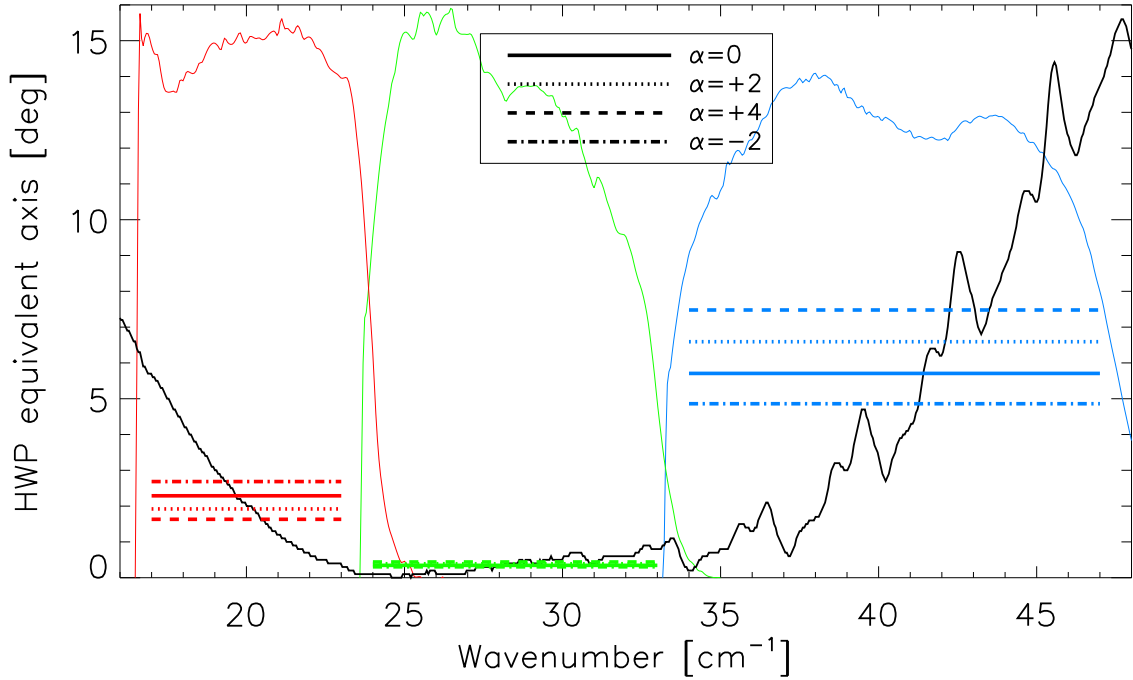


Fig. 5.24 Position of the HWP equivalent axis, β_{ea} , as a function of wavenumber (solid black line). Note that this quantity is defined with respect to an arbitrary constant offset that is inherent to the specific experimental setup; we set this offset to be zero at 25 cm^{-1} . The band-averaged values for input sources with different spectral index (α ; see legend) are drawn as thick horizontal lines. Also shown for reference is the relative spectral response of the three BLAST-Pol channels, in arbitrary units.

now postulate that most of the non-idealities we see in the measured HWP Mueller matrix (Figure 5.20) are primarily due to the wavelength dependence of β_{ea} , along with the residual absorption from sapphire at $\sim 120 \text{ K}$. This hypothesis naturally ensues from the discussion presented in Section 5.2.2 on the scatter in frequency that results from any polarization rotation on the PS sphere produced by a multiple-slab wave plate. The measurements of β_{ea} presented in Figure 5.24 effectively quantify the area of the PS surface in which the various polarization states regroup. One can imagine that the HWP performance would approach ideality once this effect is corrected for.

Therefore, we include $\beta_{ea}(\nu)$ in our Monte Carlo as a frequency-dependent offset in the array of rotation angles (so that $\theta \rightarrow \theta - \beta_{ea}$),

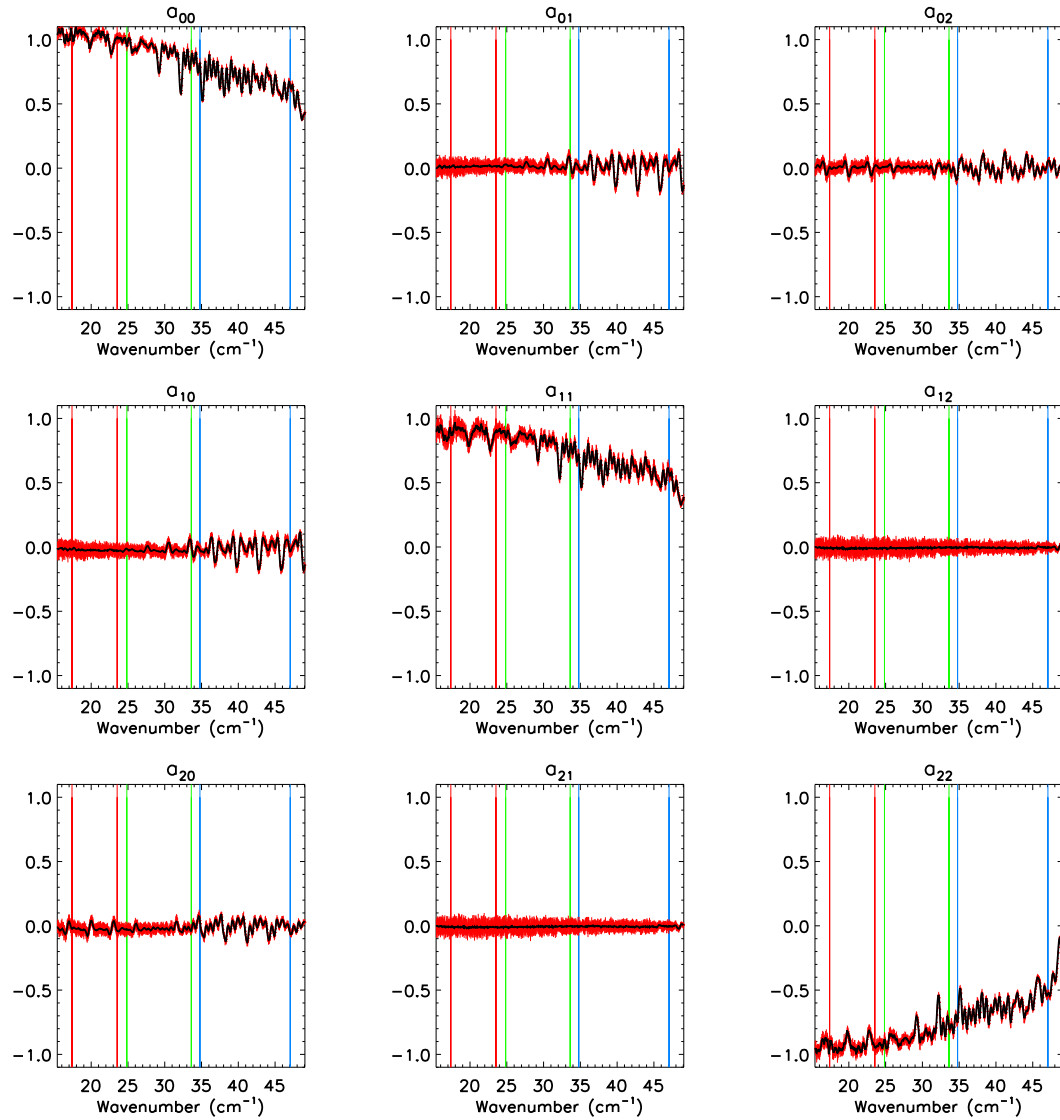


Fig. 5.25 Graphical representation of the Mueller matrix of the BLAST-Pol HWP at a given angle ($\theta = 0^\circ$), as a function of wavenumber. Note that here we include in the fit the frequency-dependent position of the HWP equivalent axis, as reported in Figure 5.24. The (10σ) error bars (in red) are quantified via a Monte Carlo, which accounts for random errors in the spectra of amplitude as given in Figure 5.17, and random errors in the rotation angle of amplitude 1° .

Table 5.1. Band-averaged position of the HWP equivalent axis for sources with different spectral index

| α | $\bar{\beta}_{\text{ea}}$ [deg] | | |
|----------|---------------------------------|-------------------|-------------------|
| | 250 μm | 350 μm | 500 μm |
| -2 | 4.9 | 0.30 | 2.7 |
| 0 | 5.7 | 0.35 | 2.3 |
| +2 | 6.6 | 0.39 | 1.9 |
| +4 | 7.5 | 0.44 | 1.6 |

Note. — The input source is assumed to have a spectrum $\zeta \propto \nu^\alpha$.

and repeat our simulations. The results, presented in Figure 5.25, can now be qualitatively compared to the Mueller matrix of an ideal HWP (Equation 5.4). The improvement is noticeable, especially in the off-diagonal elements, and the resemblance to an ideal HWP is remarkable across the entire spectral range of interest; this procedure effectively acts to diagonalize the HWP Mueller matrix. However, the transmission losses due to absorption from the sapphire at ~ 120 K still affect the diagonal elements of the matrix, as expected.

As a final improvement, we extrapolate the β_{ea} -corrected HWP Mueller matrix to 4 K by including in our Monte Carlo a correction for the residual sapphire absorption (as detailed in footnote # 11, using the data presented in Figure 5.7). The results are shown in Figure 5.26.

Although there still seems to be residual transmission losses due to sapphire absorption at 250 and 350 μm , the retrieved HWP Mueller matrix is nearly that of an ideal HWP. The band-averaged values of the matrix coefficients for a flat-spectrum input source are reported in Table 5.2, along with their propagated uncertainty; the off-diagonal elements are always consistent with zero within 2σ and the modulus

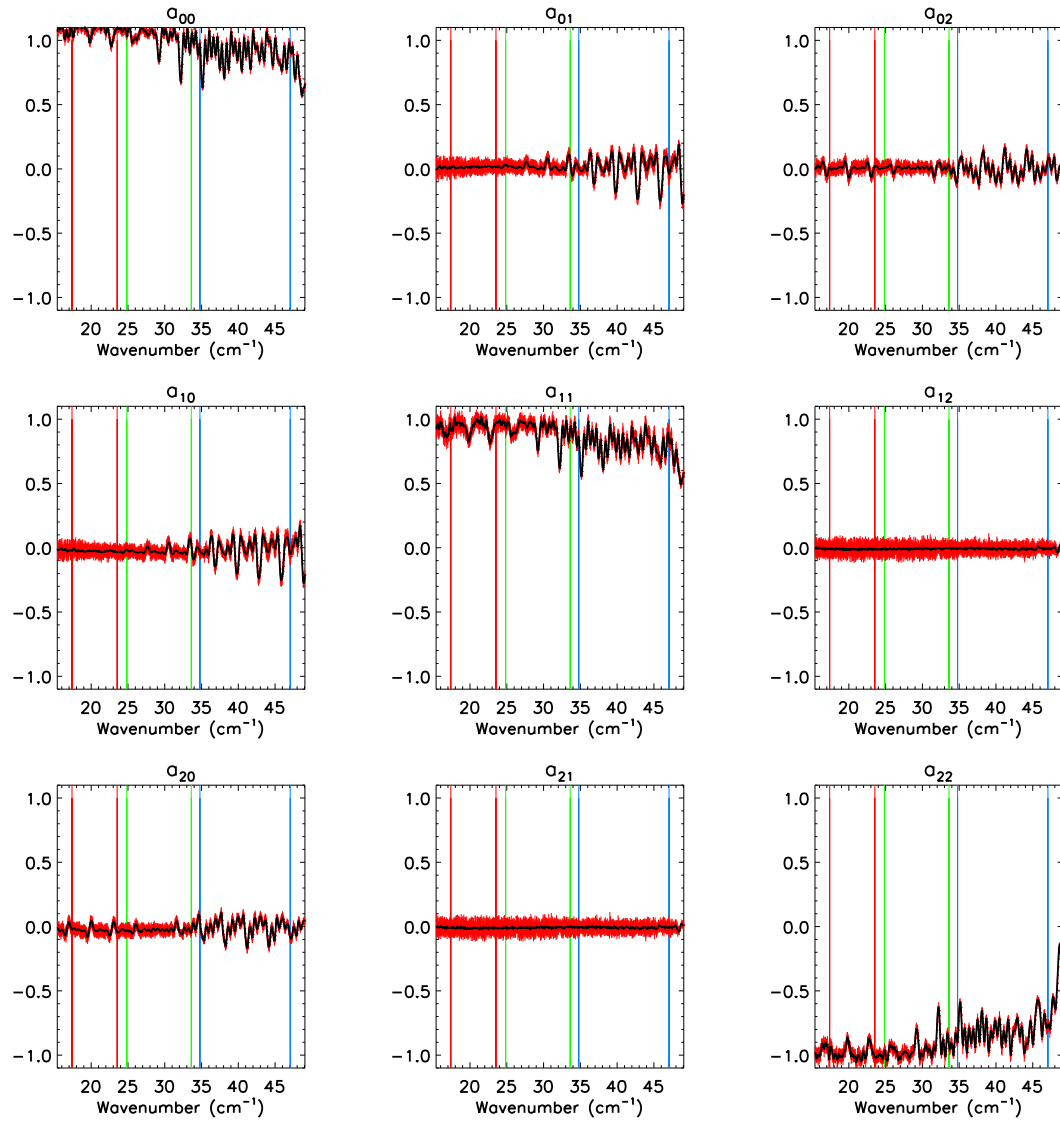


Fig. 5.26 Graphical representation of the Mueller matrix of the cold BLAST-Pol HWP at a given angle ($\theta = 0^\circ$), as a function of wavenumber. Note that here we correct for the temperature dependence of the sapphire absorption coefficient, as described in footnote # 11, using the data presented in Figure 5.7. The (10σ) error bars (in red) are quantified via a Monte Carlo, which accounts for random errors in the spectra of amplitude as given in Figure 5.17, and random errors in the rotation angle of amplitude 1° .

Table 5.2. Band-averaged Mueller matrix coefficients

| Band | 250 μm | 350 μm | 500 μm |
|----------------|--------------------|--------------------|--------------------|
| \bar{a}_{00} | 0.905 ± 0.006 | 1.001 ± 0.006 | 1.008 ± 0.007 |
| \bar{a}_{01} | 0.012 ± 0.010 | 0.017 ± 0.010 | 0.014 ± 0.011 |
| \bar{a}_{02} | -0.002 ± 0.008 | 0.006 ± 0.009 | 0.001 ± 0.009 |
| \bar{a}_{10} | -0.016 ± 0.010 | -0.021 ± 0.010 | -0.020 ± 0.011 |
| \bar{a}_{11} | 0.806 ± 0.011 | 0.928 ± 0.010 | 0.935 ± 0.012 |
| \bar{a}_{12} | -0.007 ± 0.011 | -0.009 ± 0.014 | -0.011 ± 0.014 |
| \bar{a}_{20} | -0.008 ± 0.008 | -0.022 ± 0.010 | -0.021 ± 0.010 |
| \bar{a}_{21} | -0.007 ± 0.011 | -0.009 ± 0.014 | -0.011 ± 0.014 |
| \bar{a}_{22} | -0.808 ± 0.008 | -0.960 ± 0.009 | -0.979 ± 0.010 |

Note. — These values are relative to Figure 5.26. The input source is assumed to have a flat spectrum.

of the three diagonal coefficients is always > 0.8 . The combination of these coefficients with the band-averaged values of β_{ea} given in Table 5.1 gives a complete account of the HWP non-idealities to the best of our ability.

We repeat the calculation of the band-averaged coefficients for the other spectral indices discussed in Figure 5.24; we find values that are always within 1–2% of those reported in Table 5.2, and thus we do not explicitly report them here. Because the three diagonal elements of the HWP Mueller matrix effectively determine the HWP co-pol/cross-pol transmission and modulation efficiency, this analysis confirms that these quantities are very weakly dependent on the spectral index of the input source; these findings are in very good agreement with those of Savini et al. (2009). We will see in the next Chapter how \bar{a}_{00} , \bar{a}_{11} , and \bar{a}_{22} can be incorporated in the map-making algorithm in terms of optical efficiency, η , and polarization efficiency, ε , of each detector.

Finally, we discuss a potential limitation to any linear polarization

modulator, i.e. the leakage between axes. In a HWP, the phase shift between the two axes should be as close to 180° as possible to avoid transforming linear polarization into elliptical, hence losing efficiency. The phase can not be directly measured in a pFTS, but it can be indirectly inferred from the HWP Mueller matrix.

In order to recover the wavelength-dependent phase shift of the HWP, we recall the Mueller matrix of a non-ideal impedance-matched single birefringent slab (Savini et al. 2009; at $\theta = 0^\circ$):

$$\mathcal{M}_{\text{slab}}(\theta = 0^\circ, \Delta\varphi) = \frac{1}{2} \times \begin{pmatrix} \alpha^2 + \beta^2 & \alpha^2 - \beta^2 & 0 & 0 \\ \alpha^2 - \beta^2 & \alpha^2 + \beta^2 & 0 & 0 \\ 0 & 0 & 2\alpha\beta \cos \Delta\varphi & 2\alpha\beta \sin \Delta\varphi \\ 0 & 0 & -2\alpha\beta \sin \Delta\varphi & 2\alpha\beta \cos \Delta\varphi \end{pmatrix} \quad (5.17)$$

By comparing the matrix in Equation (5.17) with that of a generic HWP, we can solve for the HWP phase shift as follows:

$$\cos \Delta\varphi = \frac{a_{22}}{2} \left(\frac{a_{00} + a_{01}}{2} \right)^{-\frac{1}{2}} \left(\frac{a_{00} - a_{01}}{2} \right)^{-\frac{1}{2}} \quad (5.18)$$

Equation (5.18) allows us to recover the phase shift from our knowledge of a_{00} , a_{01} and a_{22} . Figure 5.27 shows the estimated phase shift of the BLAST-Pol HWP as a function of wavenumber, before and after the introduction in our Monte Carlo routine of the wavelength-dependent position of the HWP equivalent axis depicted in Figure 5.24. The improvement is striking, and confirms the fact that most of the HWP non-idealities due to the achromatic design can be more easily modeled by estimating $\beta_{\text{ea}}(\nu)$. This finding further encourages us to implement $\bar{\beta}_{\text{ea}}$ in the map-making code (see Chapter 6).

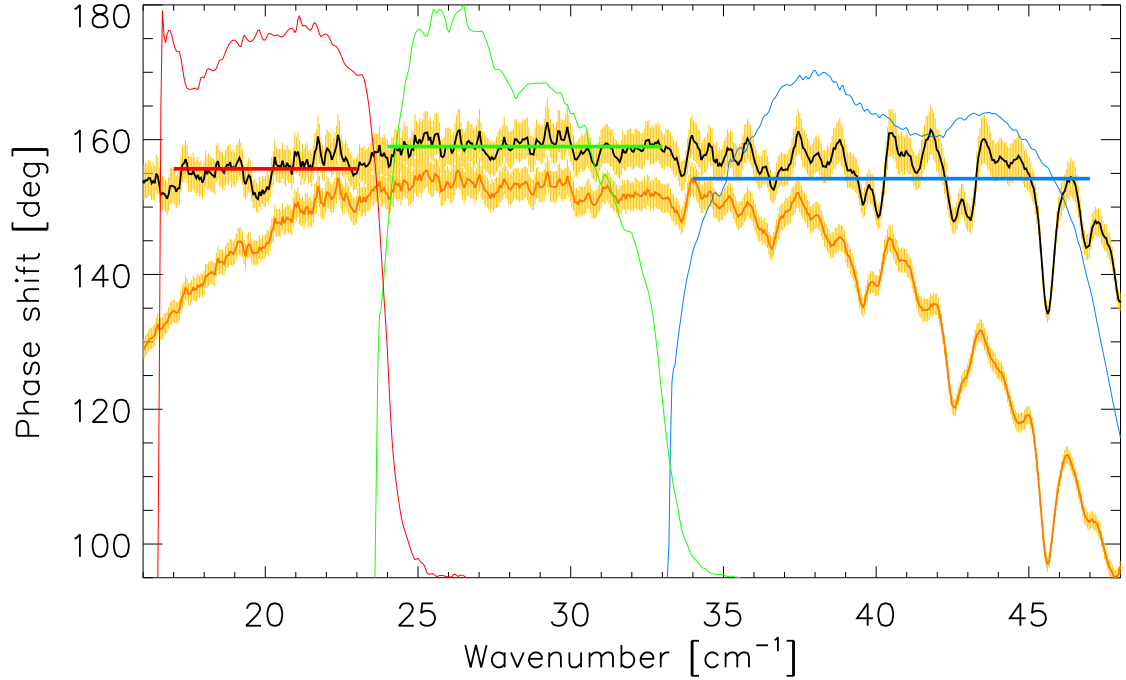


Fig. 5.27 HWP phase shift as a function of wavenumber, before (orange) and after (black) implementing in the Monte Carlo the wavelength-dependent position of the HWP equivalent axis (Figure 5.24). The (3σ) error bars (in yellow) are obtained by propagating the error on the Mueller matrix coefficients. The band-averaged values of the phase shift (for a flat-spectrum input source) are drawn as thick horizontal lines (only for the upper black line). Also shown for reference is the relative spectral response of the three BLAST-Pol channels, in arbitrary units (see Section 4.2).

Nonetheless, the β_{ea} -corrected phase shift appreciably departs from 180° . We have already highlighted that this deviation is primarily due to the ~ 0.3 mm difference between the desired thickness of the single sapphire substrates and that which was available on the market (see Section 5.2.3). However, we have indications that the modulation efficiency of the HWP at 4 K is only mildly affected by this departure from ideality. From Figure 4.5b we see that the extrapolated HWP modulation efficiency is always above 95% across the whole spectral range of interest, with band-integrated values exceeding 98%. Moreover, phase shift deviations of similar amplitude are measured in most mm and submm-wave achromatic half-wave plates manufactured to date (e.g., Savini et al. 2009, Zhang et al. 2011)

Finally, we verify that our methodology does not violate conservation of energy by ensuring that the output Stokes vector resulting from a generic polarized input traveling through the recovered HWP Mueller matrix satisfies $I^2 \leq Q^2 + U^2$ in every instance describe above.

5.3 Polarizing Grids

Wire-grids or photolithographed grids are commonly used as very efficient polarizers at submm–mm wavelengths. For incident wavelengths that are large with respect to the step of the grid, the component of the incoming electric field that is parallel to the metallic wires/strips induces a current in them, leading to an almost perfect reflection of this component. On the other had, the component of the electric field that is orthogonal to the wires/strips is almost perfectly transmitted.

In Section 4.5 we have introduced the BLAST-Pol polarimeter design, with photolithographed polarizing grids that are mounted in front of each of the three BLAST-Pol feed-horn arrays, acting as analyzers. The grids are patterned to alternate the polarization angle by 90° from horn-to-horn and thus bolometer-to-bolometer along the scan direction. P10 grids (see footnote # 7) have a performance close to that of an ideal polarizer in our frequency range of interest (200–600 μm); the BLAST-Pol polarizing grids are P10. In Figures 5.28 and 5.29 we show photographs of the photolithographed polarizing grids prior to the integration in the BLAST-Pol receiver.

In this section, we present the measured pre-flight global performance of the grids, and briefly describe the experimental procedure. We do not measure the performance of the individual polarizers composing each grid; rather, we characterize the global efficiency and cross polarization of the two families of polarizers, which we will refer to as

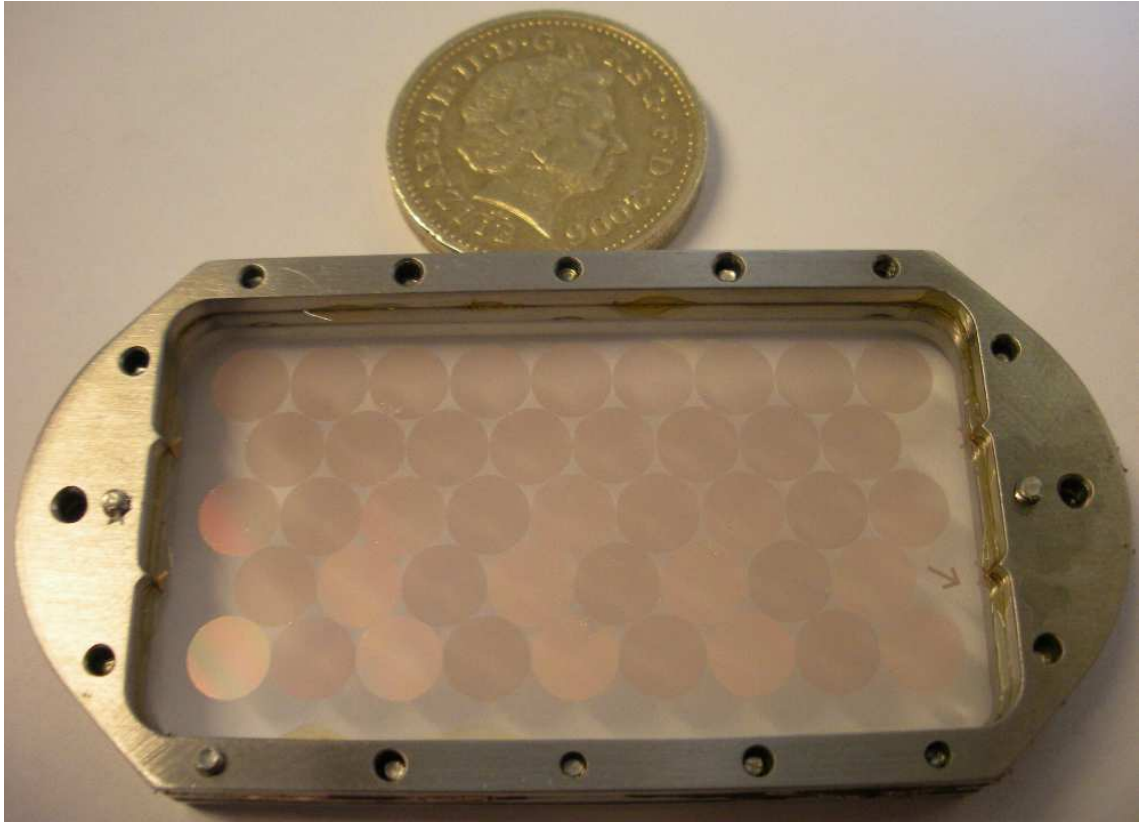


Fig. 5.28 Photolithographed polarizing grids for the $500\ \mu\text{m}$ feed-horn array.

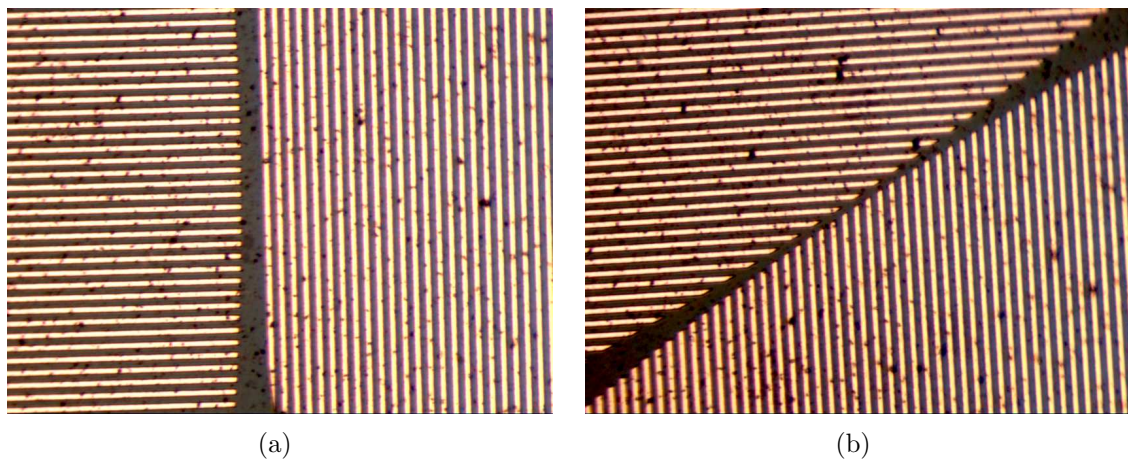


Fig. 5.29 Two high-resolution images of the P10 photolithographed polarizing grids for the $500\ \mu\text{m}$ channel, obtained with a digital microscope.

“Q mask” and “-Q mask” in direct reference to the vertical or horizontal orientation of the wires, respectively.

Although we do not record spectra, the experimental setup is very

similar to that described in Section 5.2.5.2 for the spectral measurements of the HWP at room temperature; a photograph of the apparatus is shown in Figure 5.30. We fix each grid to a manual rotator, which is positioned centrally between two tilted P10 polarizers, and with normal incidence with respect to the collimated beam section. We take measurements of the total transmitted power at different angles as we rotate the polarizing grid. In order to characterize the efficiency and cross polarization of the grid, we also need to measure the total transmitted power at the same angles *without* the grid. We repeat these measurements for the three grids at 250, 350, and 500 μm .

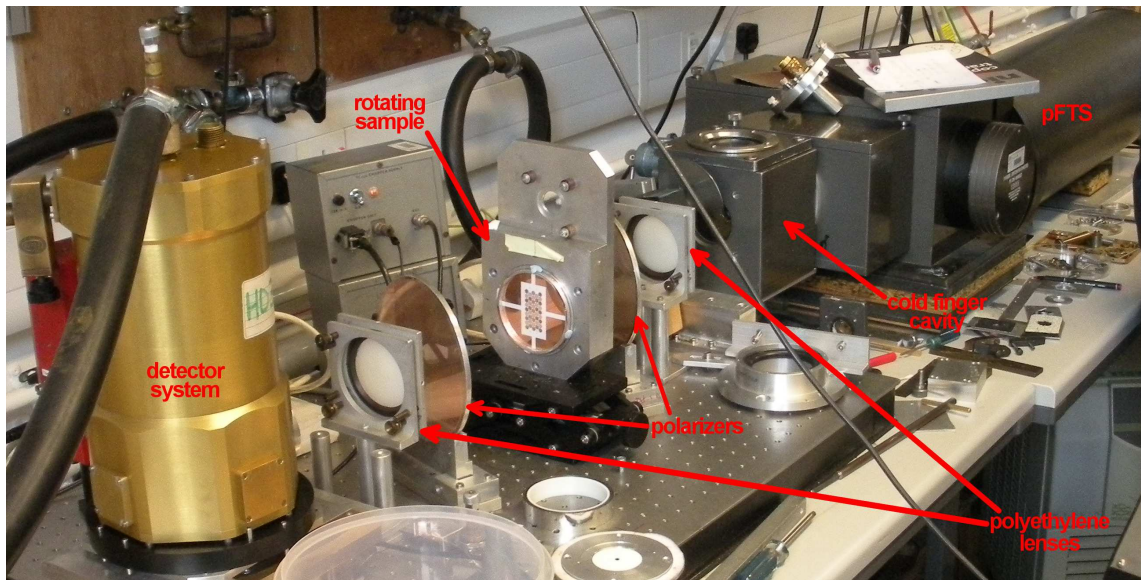


Fig. 5.30 Photograph of experimental setup for measurements of the global performance of the photolithographed polarizing grids. Although we do not record spectra, the experimental apparatus and procedure are very similar to those described in Section 5.2.5.2 for the spectral measurements of the HWP at room temperature.

Here we describe the mathematical formalism used to characterize the performance of the grids. A generic polarizer is a polarization active optical component that attenuates unequally the orthogonal components of an optical beam, with $0 \leq p_{x,y} \leq 1$ that are the transmissions of the two orthogonal components. The Mueller matrix of

a generic rotating polarizer reads (see for instance Equation A.38 in Appendix A of Moncelsi 2007):

$$\begin{aligned} \mathcal{M}_{\text{grid}}(\theta) &= \frac{1}{2} \times & (5.19) \\ & \begin{pmatrix} p_x^2 + p_y^2 & c(p_x^2 - p_y^2) & s(p_x^2 - p_y^2) & 0 \\ c(p_x^2 - p_y^2) & c^2(p_x^2 + p_y^2) + 2s^2 p_x p_y & s c(p_x^2 + p_y^2 - 2p_x p_y) & 0 \\ s(p_x^2 - p_y^2) & s c(p_x^2 + p_y^2 - 2p_x p_y) & s^2(p_x^2 + p_y^2) + 2c^2 p_x p_y & 0 \\ 0 & 0 & 0 & 2p_x p_y \end{pmatrix} \\ &= \frac{p^2}{2} \begin{pmatrix} 1 & c \cos 2\alpha & s \cos 2\alpha & 0 \\ c \cos 2\alpha & c^2 + s^2 \sin 2\alpha & s c(1 - \sin 2\alpha) & 0 \\ s \cos 2\alpha & s c(1 - \sin 2\alpha) & s^2 + c^2 \sin 2\alpha & 0 \\ 0 & 0 & 0 & \sin 2\alpha \end{pmatrix}, \end{aligned}$$

where $c \equiv \cos 2\theta$, $c_2 \equiv \cos^2 2\theta$, $s \equiv \sin 2\theta$, $s_2 \equiv \sin^2 2\theta$, and $p_x \equiv p \cos \alpha$, $p_y \equiv p \sin \alpha$.

By further defining the efficiency $\eta \equiv p_x^2 = p^2 \cos^2 \alpha$, the cross polarization $\epsilon \equiv p_y^2 = p^2 \sin^2 \alpha$, and $\Pi \equiv 2p_x p_y = p^2 \sin 2\alpha$, we can write Equation (5.19) as:

$$\begin{aligned} \mathcal{M}_{\text{grid}}(\theta) &= \frac{1}{2} \times & (5.20) \\ & \times \begin{pmatrix} \eta + \epsilon & c(\eta - \epsilon) & s(\eta - \epsilon) & 0 \\ c(\eta - \epsilon) & c^2(\eta + \epsilon) + 2s^2 \Pi & s c(\eta + \epsilon - 2\Pi) & 0 \\ s(\eta - \epsilon) & s c(\eta + \epsilon - 2\Pi) & s^2(\eta + \epsilon) + 2c^2 \Pi & 0 \\ 0 & 0 & 0 & 2\Pi \end{pmatrix}. \end{aligned}$$

The total normalized power transmitted through each grid is:

$$\begin{aligned}
 S_{\text{out}} &= \vec{D}^T \cdot \mathcal{M}_p^h \cdot \mathcal{M}_{\text{grid}}(\theta) \cdot \vec{S}_{\text{in}}^h \quad (5.21) \\
 &= \frac{1}{8} \begin{pmatrix} 1 & 0 & 0 & 0 \end{pmatrix} \cdot \begin{pmatrix} 1 & 1 & 0 & 0 \\ 1 & 1 & 0 & 0 \\ 0 & 0 & 0 & 0 \\ 0 & 0 & 0 & 0 \end{pmatrix} \cdot \mathcal{M}_{\text{grid}}(\theta) \cdot \begin{pmatrix} 1 \\ 1 \\ 0 \\ 0 \end{pmatrix},
 \end{aligned}$$

where we follow the same notation as in Section 5.2.6. Equation (5.21) can be further simplified, yielding:

$$\begin{aligned}
 S_{\text{out}} &= \frac{1}{8} [\eta + \epsilon + 2c(\eta - \epsilon) + c^2(\eta + \epsilon) + \Pi s^2] \quad (5.22) \\
 &= \frac{1}{8} [(\eta + \epsilon + \Pi) + 2c(\eta - \epsilon) + c^2(\eta + \epsilon - \Pi)] \\
 &= \frac{p^2}{8} [(1 + \sin 2\alpha) + 2c \cos 2\alpha + c^2(1 - \sin 2\alpha)]
 \end{aligned}$$

The dependency upon the rotation angle θ of the total normalized transmitted power S_{out} , expressed by Equation (5.22), can be used in a fitting routine to recover the efficiency η and cross polarization ϵ of both the Q and -Q masks for each of the three grids.

The results are presented in Figures 5.31, 5.32, and 5.33 for the polarizing grids at 250, 350, and 500 μm , respectively. The efficiency of the grids is 97% or better, while the cross polarization is estimated to be always less than 0.07%.

5.4 Concluding Remarks

The goal of this chapter was to identify and measure the parameters that characterize the optical properties and pre-flight efficiency of the polarizing components integrated in the BLAST-Pol instrument: a cryogenic achromatic half-wave plate, acting as linear po-

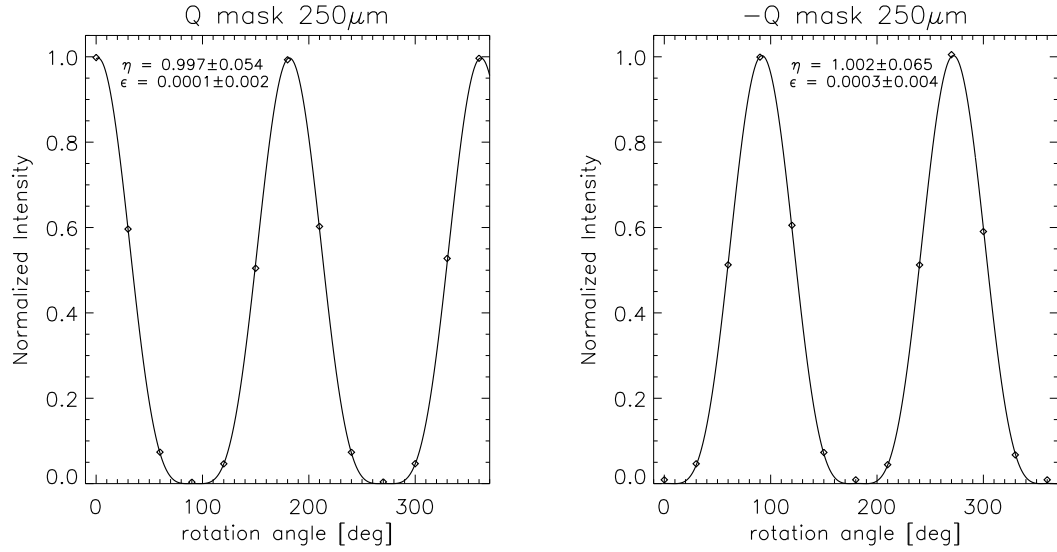


Fig. 5.31 Measurements of total normalized power transmitted through the 250 μm polarizing grid. The solid line is a fit to the data points obtained using the analytical expression given by Equation (5.22). The global values of efficiency η and cross polarization ϵ for each of the two families of polarizers are displayed, along with their propagated uncertainty.

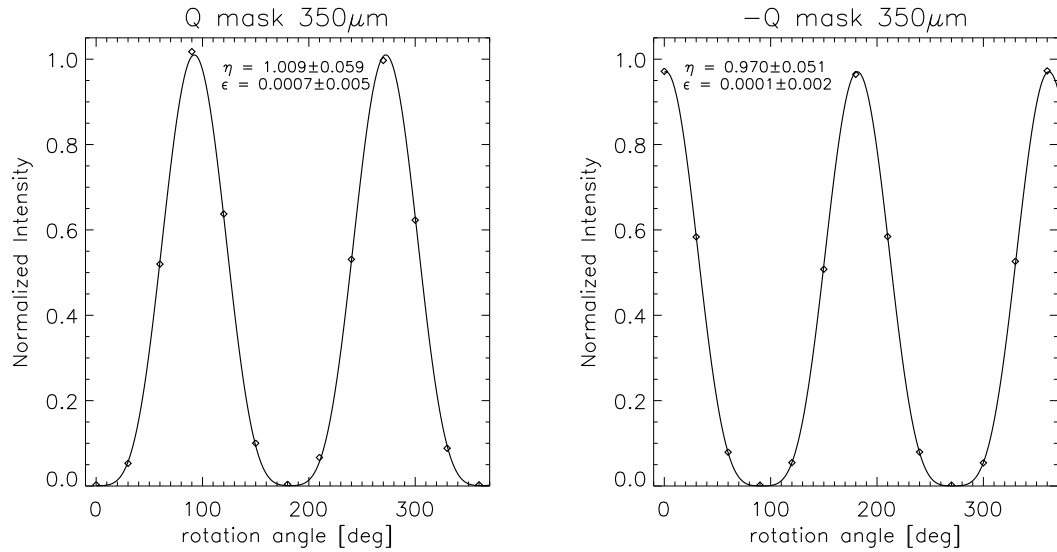


Fig. 5.32 Measurements of total normalized power transmitted through the 350 μm polarizing grid. More details are given in the caption of Figure 5.31.

larization modulator, and three sets of photolithographed polarizing grids mounted in front of the feed-horn arrays, acting as analyzers.

We have described in details the theoretical framework, principles

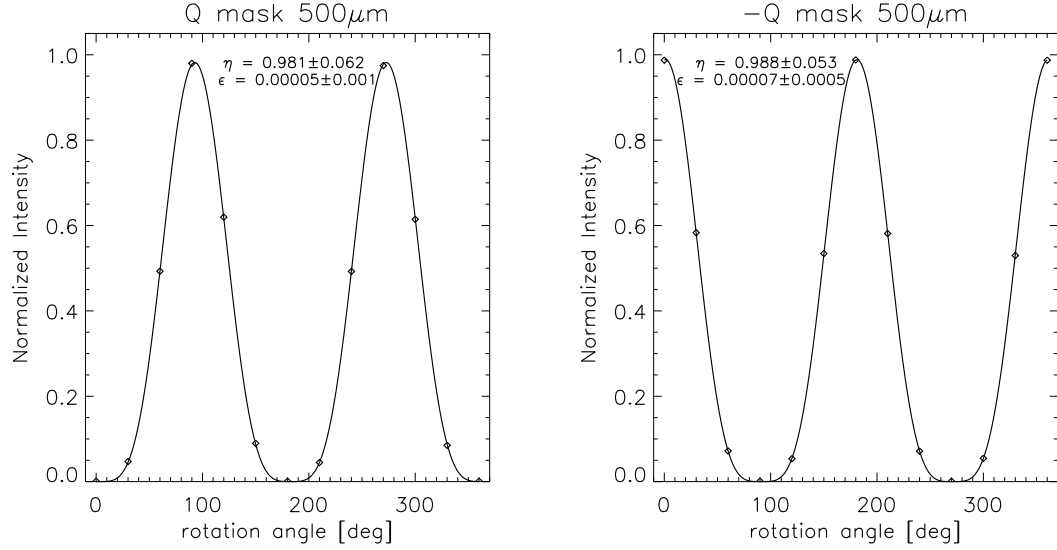


Fig. 5.33 Measurements of total normalized power transmitted through the 500 μm polarizing grid. More details are given in the caption of Figure 5.31.

of operation and manufacturing process of a five-plate sapphire HWP, which is, to our knowledge, the most achromatic ever built at mm and submm wavelengths. In the same context, we have provided a useful collection of spectral data from the literature for the sapphire refraction indices and absorption coefficients, both at room and at cryogenic temperatures.

We have briefly reviewed the past and present solutions adopted as anti-reflection coating, and highlighted the technical challenges for all the designs, which vary with the wavelengths of operation and the diameter of the HWP. The anti-reflection coating applied to the BLAST-Pol HWP represents the first successful application of a new-concept THz artificial dielectric metamaterial.

Using a polarizing FTS, we have fully characterized the spectral response of the coated BLAST-Pol HWP at room temperature and at 120 K; we have acquired data cubes by measuring spectra while rotating the HWP to produce the polarization modulation.

The cold dataset contains measurements in both co-pol and cross-

pol configurations; we have used these two data cubes to estimate 9 out of 16 elements of the Mueller matrix of the HWP as a function of frequency. We have developed an ad-hoc Monte Carlo algorithm that returns for every frequency the best estimate of each matrix element and the associated error, which is a combination of the uncertainty on the measured spectra and a random jitter on the rotation angle.

We have measured how the position of the equivalent axes of the HWP, β_{ea} , changes as a function of frequency, an effect that is inherent to any achromatic design. Once this dependence is accounted for in the Monte Carlo, and a correction is implemented for the residual absorption from sapphire, the Mueller matrix of the HWP approaches that of an ideal HWP, at all wavelengths of interest. In particular, the (band-averaged) off-diagonal elements are always consistent with zero within 2σ and the modulus of the three diagonal coefficients is always > 0.8 . Therefore, we have introduced in the BLAST-Pol mapping algorithm (Chapter 6) the band-integrated values of β_{ea} as an additional parameter in the evaluation of the polarization angle. To first order, this approach allows us to account for most of the non-idealities in the HWP.

We have investigated the impact of input sources with different spectral signatures on β_{ea} and on the HWP Mueller matrix coefficients. We find that the HWP transmission and modulation efficiency are very weakly dependent on the spectral index of the input source, whereas the position of the equivalent axes of the sapphire plate stack is more significantly affected. This latter dependence, if neglected, may lead to an arbitrary rotation of the retrieved polarization angle on the sky of magnitude $2\bar{\beta}_{\text{ea}} = 10\text{--}15^\circ$ ($3\text{--}5^\circ$) at 250 (500) μm . The 350 μm band, however, is minimally perturbed by this effect.

In principle, the measured Mueller matrix can be used to gener-

ate a synthetic time-ordered template of the polarization modulation produced by the HWP as if it were continuously rotated at $\theta = \omega t$. Continuous rotation of the HWP allows to reject all the noise components modulated at harmonics different than 4θ (synchronous demodulation) and is typically employed by experiments optimized to measure the polarization of the Cosmic Microwave Background (e.g., Johnson et al. 2007, Reichborn-Kjennerud et al. 2010). In such experiments, the HWP modulation curve leaves a definite synchronous imprint on the time-ordered bolometer data streams (timelines), hence it is of utter importance to characterize the template and remove it from the raw data. However, a time-ordered HWP template would be of no use to a step-and-integrate experiment such as BLAST-Pol, whose timelines are not dominated by the HWP synchronous signal.

We have measured the phase shift of the HWP across the wavelength range of interest to be $\sim 160^\circ$, which appreciably deviates from the ideal 180° ; this is primarily due to the unavailability on the market of sapphire substrates with the exact desired thickness. However, the modulation efficiency of the HWP is only mildly affected by this departure from ideality, being above 98% in all three BLAST-Pol bands. Moreover, departures of similar amplitude are not uncommon for HWPs at mm and submm wavelengths.

Finally, we have measured the efficiency the BLAST-Pol analyzers to be at least 97%, and their cross polarization to be at most 0.07%.

6. THE BLAST-POL MAP-MAKER

6.1 *Introduction*

Map-making is the operation that generates an astronomical map, which contains in every pixel an estimate of the sky emission, and is obtained by combining data from all detectors available at a given wavelength channel, their noise properties and the pointing information. The raw data consist of bolometer time-ordered streams (or timelines), which are cleaned and pre-processed before being fed into the map-maker: in order, cosmic rays are flagged and removed, the known electronics transfer function is deconvolved from the data streams, an elevation-dependent common-mode signal due to the residual atmosphere is removed concurrently with a polynomial fit to the data, and finally the timelines are high-pass filtered to suppress the low-frequency ($1/f$) noise. The details of the pre-processing of the BLAST timelines are extensively described elsewhere (Rex 2007, Truch 2007, Wiebe 2008, Pascale et al. 2008), and we refer to these works for a complete account of the low-level data reduction. Note that the process of cleaning and preparing the bolometer time-streams for map-making in BLAST-Pol has closely followed that of BLAST, exception made for the removal of discontinuities in the DC level of the bolometer, caused by the half-wave plate (HWP; see Section 4.5) being stepped approximately every 15 minutes (this operation is performed before the high-pass filtering); also, the subtraction of an elevation-dependent term from the timelines was not needed in BLAST.

In the following, we focus on the mathematical formalism of the map-making technique, and its algorithmic implementation in the specific case of BLAST-Pol. As a proof of concept, we produce preliminary intensity and polarization maps for a sample of the scientific targets observed by BLAST-Pol during its 9.5-day flight over Antarctica, completed in January 2011 (see Section 1.2.5). Although the reduction of this dataset has not yet been finalized, the maps presented here result as the culmination of the whole data analysis process and demonstrate the overall success of the mission.

6.2 Maximum Likelihood Map-making

For a non-ideal polarization experiment, by adopting the Stokes formalism¹ and assuming that no circular (V) polarization is present, we can model the data as follows:

$$d_t^i = \frac{\eta^i}{2} A_{tp}^i [I_p + \varepsilon^i (Q_p \cos 2\gamma_t^i + U_p \sin 2\gamma_t^i)] + n_t^i. \quad (6.1)$$

Here, i , t and p label detector index, time, and map pixel respectively; d_t^i are the time-ordered data for a given channel, related to the sky maps $[I_p, Q_p, U_p]$ by the pointing operator A_{tp}^i ; η^i is the optical efficiency of each detector; ε^i is the polarization efficiency of each detector with its polarizing grid (analyzer); and n_t^i represents a generic time-dependent noise term. Throughout this discussion it is assumed that the term within square brackets is the convolution of the sky emission with the telescope point-spread function (PSF). γ_t^i is the time-ordered vector of the observed polarization angle, defined as the angle between the polarization reference vector at the sky pixel p (in the chosen ce-

¹ We refer to Appendix A of Moncelsi (2007) for a review of polarization basics.

restrial frame) and the polarimeter transmission axis. γ_t^i is given by:

$$\gamma_t^i = \alpha_t^i + 2 [\beta_t - \beta_0 - \bar{\beta}_{\text{ea}}] + \delta_{\text{grid}}^i, \quad (6.2)$$

where α_t^i is the angle between the reference vector at pixel p and a vector pointing from p to the zenith along a great circle; β_t is the HWP orientation angle in the instrument frame; β_0 is the HWP zero angle in the instrument frame; $\bar{\beta}_{\text{ea}}$ is the band-averaged position of the equivalent axes of the HWP (dependent on the known or assumed spectral signature of the input source; see Section 5.2.6); and $\delta_{\text{grid}}^i = [0, \pi/2]$ accounts for the transmission axis of the polarizing grids (analyzers; see Section 4.5) being parallel/perpendicular to the zenith angle.

The notation outlined above can be connected to the Mueller formalism developed in Chapter 5 to determine under which circumstances Equation (6.1) is valid in the presence of a real (i.e., non-ideal) HWP. Because we have included in Equation (6.2) the band-averaged position of the equivalent axes of the HWP, $\bar{\beta}_{\text{ea}}$, the Mueller matrix of the BLAST-Pol HWP can be considered almost that of an ideal HWP, as discussed in Section 5.2.6. Nonetheless, we have shown that the band-averaged values of the three diagonal matrix coefficients are not identically unity (but always > 0.8 in modulus), probably as a result of residual absorption from sapphire, especially in the 250 and 350 μm bands, albeit we have corrected for it to the best of our knowledge.

In the light of these considerations, we now want to compare Equation (6.1) to Equation (5.9), which both represent the signal measured by a polarization insensitive intensity detector when illuminated by a polarized input that propagates through a rotating HWP and an analyzer. A term-by-term comparison yields that these two expressions are equivalent when the coefficients B and C (defined in Equation 5.10) are zero, i.e. when the HWP modulates the polarization

purely at four times the rotation angle, with no leakage in the second harmonic (twice the rotation angle) and thus no leakage of I into Q and U . These two coefficients are linear combinations of the HWP Mueller matrix elements $\bar{a}_{01}, \bar{a}_{10}, \bar{a}_{02}, \bar{a}_{20}$, which we have shown in Table 5.2 to be all compatible with zero within 2σ . In addition, their amplitude is at most $\sim 2\%$ of that of the diagonal matrix elements, and in the limit of elevated angle coverage, $\langle \cos 2\gamma \rangle^2 + \langle \sin 2\gamma \rangle^2 \approx 0$, these terms (in twice the rotation angle) effectively average out in the sums. Therefore, the coefficients B and C can be neglected to first order, and the two expressions can be considered equivalent. Nonetheless, these generally moderate levels of $I \rightarrow Q, U$ leakage can be readily accounted for by incorporating in the map-making algorithm a correction for the “instrumental polarization” (IP). We further this discussion in Section 6.7.

In addition, after some elementary algebra, it results that $\eta = a_{00} + \frac{a_{11}}{2} + \frac{a_{22}}{2}$, and that $\eta\varepsilon = \frac{a_{11}}{2} - \frac{a_{22}}{2}$. As anticipated in the previous chapter, the knowledge of the band-averaged values of the three diagonal matrix elements, $\bar{a}_{00}, \bar{a}_{11}, \bar{a}_{22}$ (which we have shown to depend weakly on the spectral index of the input source), can be readily incorporated in the map-making algorithm in terms of optical efficiency, η , and polarization efficiency, ε , of the HWP; these can be factored in the overall optical efficiency and polarization efficiency of each detector. From the values listed in Table 5.2, in our case we find $[\eta_{\text{hwp}}, \varepsilon_{\text{hwp}}] = [0.904, 0.893], [0.985, 0.958],$ and $[0.986, 0.971]$ at 250, 350, and 500 μm , respectively.

Finally, the comparison of Equations (6.1) and (5.9) also yields $\eta\varepsilon\chi = -a_{12} = -a_{21}$, where we have introduced a new parameter, χ , which quantifies the amplitude of the mixing of Q and U . From Table 5.2, we see that $\bar{a}_{12} = \bar{a}_{21}$ are always compatible with zero

within 1σ , and their amplitude is at most $\sim 1\%$ of that of the diagonal matrix elements. Nonetheless we quantify the amplitude of the $Q \leftrightarrow U$ mixing to be $\chi_{\text{hwp}} = 0.009, 0.010, \text{ and } 0.011$ at $250, 350, \text{ and } 500 \mu\text{m}$, respectively. While this correction is not currently included in our algorithm, we indicate that it can be implemented in a relatively straightforward way by modifying Equation (6.1) with a double change of variable, i.e. $Q \rightarrow Q + \chi U$ and $U \rightarrow U + \chi Q$. If χ is estimated to the required accuracy, the unmixed Q and U can be retrieved unbiasedly. This correction may be very relevant to Cosmic Microwave Background (CMB) polarization experiments, where any $Q \leftrightarrow U$ leakage leads to a spurious mixing of the EE and BB modes.

We remind the reader that the above factors have been computed directly from the band-averaged coefficients of the inferred HWP Mueller matrix extrapolated at 4 K, and offer a direct way to include the modeled HWP non-idealities in a map-making algorithm. On the other hand, the band-averaged HWP maximum transmission, polarization efficiency and cross-pol quoted at the end of Sections 4.5.2 and 5.2.5.3 are estimated directly from the spectra extrapolated at 4 K, and are only informative from an experimental point of view rather than for data analysis purposes.

Consider now one map pixel p that is observed in one band by k detectors ($i = 1, \dots, k$); let us define the generalised pointing matrix \mathbf{A}_{tp} , which includes the trigonometric functions and the efficiencies,

$$\mathbf{A}_{tp} \equiv \frac{1}{2} \begin{pmatrix} \eta^1 A_{tp}^1 & \eta^1 \varepsilon^1 A_{tp}^1 \cos 2\gamma_t^1 & \eta^1 \varepsilon^1 A_{tp}^1 \sin 2\gamma_t^1 \\ \vdots & \vdots & \vdots \\ \eta^i A_{tp}^i & \eta^i \varepsilon^i A_{tp}^i \cos 2\gamma_t^i & \eta^i \varepsilon^i A_{tp}^i \sin 2\gamma_t^i \\ \vdots & \vdots & \vdots \\ \eta^k A_{tp}^k & \eta^k \varepsilon^k A_{tp}^k \cos 2\gamma_t^k & \eta^k \varepsilon^k A_{tp}^k \sin 2\gamma_t^k \end{pmatrix}, \quad (6.3)$$

and the map triplet \mathbf{S}_p , along with the combined detector (\mathcal{D}_t) and noise (\mathbf{n}_t) timelines:

$$\mathbf{S}_p \equiv \begin{pmatrix} I_p \\ Q_p \\ U_p \end{pmatrix}, \quad \mathcal{D}_t \equiv \begin{pmatrix} d_t^1 \\ \vdots \\ d_t^i \\ \vdots \\ d_t^k \end{pmatrix}, \quad \mathbf{n}_t \equiv \begin{pmatrix} n_t^1 \\ \vdots \\ n_t^i \\ \vdots \\ n_t^k \end{pmatrix}. \quad (6.4)$$

Equation (6.1) can then be rewritten in a more compact form, as follows:

$$\mathcal{D}_t = \mathbf{A}_{tp} \mathbf{S}_p + \mathbf{n}_t. \quad (6.5)$$

Under the assumption that the noise is Gaussian and stationary, the likelihood of \mathbf{S}_p given the data can be maximized, thus yielding the well known generalised least squares (GLS) estimator for \mathbf{S}_p :

$$\tilde{\mathbf{S}}_p = (\mathbf{A}_{tp}^T \mathbf{N}^{-1} \mathbf{A}_{tp})^{-1} \mathbf{A}_{tp}^T \mathbf{N}^{-1} \mathcal{D}_t, \quad (6.6)$$

where \mathbf{N} is the noise covariance matrix of the data in the time domain:

$$\mathbf{N} \equiv \langle \mathbf{n}_t \mathbf{n}_{t'} \rangle = \begin{pmatrix} \langle n_t^1 n_{t'}^1 \rangle & \cdots & \langle n_t^1 n_{t'}^i \rangle & \cdots & \langle n_t^1 n_{t'}^k \rangle \\ \vdots & \ddots & \vdots & \ddots & \vdots \\ \langle n_t^i n_{t'}^1 \rangle & \cdots & \langle n_t^i n_{t'}^i \rangle & \cdots & \langle n_t^i n_{t'}^k \rangle \\ \vdots & \ddots & \vdots & \ddots & \vdots \\ \langle n_t^k n_{t'}^1 \rangle & \cdots & \langle n_t^k n_{t'}^i \rangle & \cdots & \langle n_t^k n_{t'}^k \rangle \end{pmatrix}, \quad (6.7)$$

where t, t' run over the detector time samples (typically $N_s \sim 10^6-10^7$).

Computation of the solution to Equation (6.6) is far from trivial in most astronomical applications, due to \mathbf{N} being a very large matrix, of size $kN_s \times kN_s$. Understandably, it is computationally challenging to invert this matrix, especially when there are correlations among

detectors, and a number of “optimal” map-making techniques have been developed in the literature to tackle this problem (e.g., Natoli et al. 2001, 2009, Masi et al. 2006, Johnson et al. 2007, Wu et al. 2007, Patanchon et al. 2008, Cantalupo et al. 2010).

6.3 Naive Binning

If, however, the noise is uncorrelated between different detectors, then the matrix in Equation (6.7) reduces to block diagonal:

$$\langle n_t^i n_{t'}^j \rangle = \langle n_t^j n_{t'}^i \rangle = 0 \quad (i \neq j) . \quad (6.8)$$

In addition, let us assume that there is no correlation between noise of different samples acquired by the same detector, or, in other words, that the noise in each detector is white. From Equations (6.7) and (6.8), we can see that each “block” of the noise covariance matrix collapses into one value, which is the timeline variance for each detector. Hence, \mathbf{N} becomes a $k \times k$ diagonal matrix where the diagonal elements are the sample variances of the detectors, σ_i^2 , and weights can thus be defined as the inverse of those variances, $w^i \equiv 1/\sigma_i^2$.

Therefore, in the assumption that the noise is white and uncorrelated among detectors, Equation (6.6) reduces to a simple, weighted binning (“naive” binning; see also Pascale et al. 2011) of the map:

$$\mathbf{S}_p = \begin{pmatrix} I_p \\ Q_p \\ U_p \end{pmatrix} = \frac{\sum_{i=1}^k \sum_{t=1}^{N_s} w^i \frac{(\mathbf{A}_{tp}^i)^T d_t^i}{(\mathbf{A}_{tp}^i)^T \mathbf{A}_{tp}^i}}{\sum_{i=1}^k w^i} . \quad (6.9)$$

In the light of these considerations, let us go back to Equation (6.1)

and model the generic time-dependent noise term n_t^i as:

$$n_t^i = u_t + \xi^i \rho, \quad (6.10)$$

where u_t represents a time-dependent noise term, completely uncorrelated among different detectors, while ρ describes the correlated noise (constant over timescales larger than the ratio of the size of the detector array to the scan speed), coupled to each detector via the ξ^i parameter, peculiar to each bolometer.

Let us define the following quantity for every pixel p in the map:

$$\mathbf{S}_p^e = \begin{pmatrix} I_p^e \\ Q_p^e \\ U_p^e \end{pmatrix} \equiv \begin{pmatrix} \sum_{i=1}^k \sum_{t=1}^{N_s} d_t^i \\ \sum_{i=1}^k \sum_{t=1}^{N_s} d_t^i \cos 2\gamma_t^i \\ \sum_{i=1}^k \sum_{t=1}^{N_s} d_t^i \sin 2\gamma_t^i \end{pmatrix}, \quad (6.11)$$

where N_s is now the number of samples in each detector timeline that fall within pixel p , and the superscript “e” stands for “estimated”. The above quantities can be computed directly from the detector timelines. Recalling Equations (6.1) and (6.10), we can outline the following linear system of 3 equations with 3 unknowns:

$$\begin{pmatrix} I_p^e \\ Q_p^e \\ U_p^e \end{pmatrix} = \frac{1}{2} \begin{pmatrix} \sum_{i,t} 1 & \sum_{i,t} \cos 2\gamma_t^i & \sum_{i,t} \sin 2\gamma_t^i \\ \sum_{i,t} \cos 2\gamma_t^i & \sum_{i,t} \cos^2 2\gamma_t^i & \sum_{i,t} \cos 2\gamma_t^i \sin 2\gamma_t^i \\ \sum_{i,t} \sin 2\gamma_t^i & \sum_{i,t} \cos 2\gamma_t^i \sin 2\gamma_t^i & \sum_{i,t} \sin^2 2\gamma_t^i \end{pmatrix} \cdot \begin{pmatrix} I_p \\ Q_p \\ U_p \end{pmatrix} + \begin{pmatrix} \sum_{i,t} (u_t + \xi^i \rho) \\ \sum_{i,t} (u_t + \xi^i \rho) \cos 2\gamma_t^i \\ \sum_{i,t} (u_t + \xi^i \rho) \sin 2\gamma_t^i \end{pmatrix}, \quad (6.12)$$

where we have temporarily assumed $\eta^i = \varepsilon^i = w^i = 1$ and combined the two sums in one, with the indices i and t running, respectively, over the bolometers and the samples in each detector timeline.

If we now define the following quantities,

$$\begin{aligned}
N_{\text{hit}} &\equiv \sum_{i,t} \frac{1}{2}, & c &\equiv \sum_{i,t} \frac{1}{2} \cos 2\gamma_t^i & c_2 &\equiv \sum_{i,t} \frac{1}{2} \cos^2 2\gamma_t^i \\
s &\equiv \sum_{i,t} \frac{1}{2} \sin 2\gamma_t^i & s_2 &\equiv \sum_{i,t} \frac{1}{2} \sin^2 2\gamma_t^i, & m &\equiv \sum_{i,t} \frac{1}{2} \cos 2\gamma_t^i \sin 2\gamma_t^i \\
\sum_{i,t} \sin^2 2\gamma_t^i &= N_{\text{hit}} - c_2, & U &\equiv \sum_{i,t} u_t, & C_2^u &\equiv \sum_{i,t} u_t \cos 2\gamma_t^i \\
S_2^u &\equiv \sum_{i,t} u_t \sin 2\gamma_t^i, & P &\equiv \sum_{i,t} \xi^i \rho, & C_2^\rho &\equiv \sum_{i,t} \xi^i \rho \cos 2\gamma_t^i \\
S_2^\rho &\equiv \sum_{i,t} \xi^i \rho \sin 2\gamma_t^i, & & & &
\end{aligned} \tag{6.13}$$

the system in Equation (6.12) can be rewritten in compact form as:

$$\begin{pmatrix} I_p^e \\ Q_p^e \\ U_p^e \end{pmatrix} = \begin{pmatrix} N_{\text{hit}} & c & s \\ c & c_2 & m \\ s & m & N_{\text{hit}} - c_2 \end{pmatrix} \cdot \begin{pmatrix} I_p \\ Q_p \\ U_p \end{pmatrix} - \begin{pmatrix} U + P \\ C_2^u + C_2^\rho \\ S_2^u + S_2^\rho \end{pmatrix}. \tag{6.14}$$

In order to retrieve an estimate of \mathbf{S}_p from the quantities computed in Equation (6.11), the above system has to be solved for every pixel p in the map. One can already see the computational advantage of inverting a 3×3 matrix $N_{\text{pix}} \times N_{\text{pix}}$ times, with respect the inversion of a generic $kN_s \times kN_s$ matrix (for detectors having uncorrelated 1/f noise as well as a common-mode 1/f noise; Patanchon et al. 2008), or k matrices of size $N_s \times N_s$ (for detectors having only uncorrelated 1/f noise; Cantalupo et al. 2010). The main difficulty is, of course, to estimate the noise terms $U, P, C_2^u, C_2^\rho, S_2^u, S_2^\rho$. However, recalling Equation (6.2) and the fact that adjacent detectors have orthogonal

polarizing grids ($\delta_{grid}^i = [0, \pi/2]$), we note that, in the sum over i , adjacent detectors have equal and opposite contributions to C_2^ρ and S_2^ρ (as anticipated in Section 4.5.1), under the following assumptions:

- the timescale over which the correlated noise is approximately constant is larger than the time elapsed while scanning the same patch of sky with two adjacent detectors;
- ξ^i is not too dissimilar between adjacent bolometers.

This means that the terms C_2^ρ and S_2^ρ can be neglected, under the above assumptions, while estimating the $[Q, U]$ maps. In particular, as a first step, we can solve for I only by high-pass filtering the timelines, in order to suppress the correlated noise term in I, P . Subsequently, I can be assumed known, and the $[Q, U]$ maps can be computed without filtering the timelines, so that polarized signal at large angular scales is not suppressed. In fact, we see from Equation (6.1) that in the limit of elevated angle coverage, the term in I , not being modulated at four times the HWP rotation angle, effectively averages out in the sums.

The other assumption required for the naive binning is that the noise is white, at least on the timescales relevant to BLAST-Pol's scan strategy (see Section 4.5). As a matter of fact, preliminary analysis of the bolometer timelines from the 2010 campaign shows that the knee of the $1/f$ noise in the difference between two adjacent detectors is typically located at frequencies $\lesssim 0.1$ Hz; assuming a typical scan speed of 0.1° s^{-1} , this corresponds to angular scales of $\gtrsim 1$ deg in the sky. The regions mapped by BLAST-Pol hardly exceed 1 deg in size (see Section 1.2.5), hence here we stipulate that the noise in the difference between pairs of adjacent detectors is white.

Therefore, under the assumptions above, we can solve the linear system outlined in Equation (6.14); by defining the following quanti-

ties:

$$\begin{aligned}
\Delta &\equiv c^2 (c_2 - N_h) - N_h (c_2^2 + m^2 - c_2 N_h) + 2 c s m - c_2 s^2 , \\
A &\equiv - (c_2^2 + m^2 - c_2 N_h) , \quad B \equiv c (c_2 - N_h) + s m , \\
C &\equiv c m - s c_2 , \quad D \equiv - [(c_2 - N_h) N_h + s^2] , \\
E &\equiv c s - m N_h , \quad F \equiv c_2 N_h - c^2 ,
\end{aligned} \tag{6.15}$$

the solution to the system can be written in compact form, as follows:

$$\mathbf{S}_p = \begin{pmatrix} I_p \\ Q_p \\ U_p \end{pmatrix} = \begin{pmatrix} \frac{A I_p^e + B Q_p^e + C U_p^e}{\Delta} \\ \frac{B I_p^e + D Q_p^e + E U_p^e}{\Delta} \\ \frac{C I_p^e + E Q_p^e + F U_p^e}{\Delta} \end{pmatrix} , \tag{6.16}$$

where we have renamed $N_{\text{hit}} \rightarrow N_h$ for brevity.

6.4 Weights and Uncertainties

The solution for \mathbf{S}_p given in Equation (6.16) is a simple, unweighed binning of the data into the map pixels. In reality, as anticipated in Equation (6.9), we want to perform a weighted binning, where the weight of each detector is given by the inverse of its timeline variance, which can be easily measured as the bolometer's white noise floor level. In our formalism, the weighted binning is simply achieved by defining $[I_p^e, Q_p^e, U_p^e]$ in Equation (6.11), as well as each of the quantities N_h , c , s , c_2 , s_2 , and m introduced in Equation (6.13), to include w^i in the sums. Similarly, the measured values of the optical efficiencies η^i and polarization efficiencies ε^i can readily be inserted in Equations (6.12) and (6.13) to account for the non-idealities of the optical system.

The introduction of the weights allows us to derive the expression for the statistical error on \mathbf{S}_p , in the continued assumption of uncorrelated noise, following the usual error propagation formula (e.g., Press

et al. 1992; here we omit the sum over t for simplicity):

$$\sigma_p^2 = \sum_i \frac{1}{w^i} \left(\frac{\partial \mathbf{S}_p}{\partial d^i} \right)^2. \quad (6.17)$$

After some tedious algebra, the expression for the statistical error is:

$$\begin{aligned} \sigma_p^2 &= \begin{pmatrix} \text{Var}_p^I \\ \text{Var}_p^Q \\ \text{Var}_p^U \end{pmatrix} = & (6.18) \\ &= \begin{pmatrix} \frac{2}{\Delta^2} (A^2 N_h + B^2 c_2 + C^2 s_2 + 2 A B c + 2 A C s + 2 B C m) \\ \frac{2}{\Delta^2} (B^2 N_h + D^2 c_2 + E^2 s_2 + 2 B D c + 2 B E s + 2 D E m) \\ \frac{2}{\Delta^2} (C^2 N_h + E^2 c_2 + F^2 s_2 + 2 C E c + 2 C F s + 2 E F m) \end{pmatrix}, \end{aligned}$$

where $s_2 \equiv N_h - c_2$, as noted in Equation (6.13). To first order, these expression can be used to quantify the uncertainty of $[I, Q, U]$ in each map pixel p . A more comprehensive account of the correlations in the noise, as well as a thorough validation of the assumptions made here, is beyond the scope of this thesis and will be treated in a future work. Finally, we note that a better approach to estimating the uncertainties on the $[I, Q, U]$ maps would be a Monte Carlo simulation, which more effectively accounts for the well known biases inherent to the direct error propagation method.

6.5 Preliminary Maps

Firstly, we want to test the ability of the algorithm to genuinely retrieve the correct polarization on the sky, i.e. without introducing artifacts. In order to do so, we produce simulated polarization maps using observations of VY Canis Majoris (VY CMa) from the BLAST06 dataset. The total intensity I map is shown in the top panel of Fig-

ure 6.1. We then simulate a $p_{\%} = 50$ polarized Q and U input, obtained from the BLAST06 timelines as $d_Q^{50\%} = d(1 + 0.5 \cos 2\gamma)$ and $d_U^{50\%} = d(1 + 0.5 \sin 2\gamma)$, respectively. These synthetic timelines, along with a simulated timeline containing the HWP angles, are then fed into the map-making code as if they had been observed by BLAST-Pol. The resulting polarization maps are shown in the four bottom panels of Figure 6.1. In the case of a simulated Q input, the Q map is retrieved correctly with a value at the source peak that is half of that in the corresponding pixel in the I map, while the U map is practically featureless, indicating that there are no artifacts introduced by the map-maker; a similar result is found for the simulated U input. Therefore, these maps qualitatively demonstrate the effectiveness of the algorithm in retrieving the polarization signal.

In addition, as a proof of concept of the naive binning technique for the BLAST-Pol polarized map-maker, we present *preliminary* intensity and polarization maps at $500 \mu\text{m}$ for a sample of three scientific targets observed by BLAST-Pol during its first Antarctic flight, completed in January 2011 (see Section 1.2.5). The original maps have been smoothed with a kernel of $3'$ (FWHM; about three times that of the nominal BLAST-Pol beam at $500 \mu\text{m}$) to mitigate the effects due to the uncertainty on the shape of the instrumental PSF, which are still being investigated.

The maps (shown in Figures 6.2, 6.4, and 6.6) are presented as contour levels of the intensity map I , upon which we superimpose vectors indicating the polarization direction in the sky; the length of each vector is proportional to the polarization degree (a vector corresponding to $p_{\%} = 5$ is shown for reference). The polarization degree is obtained as $p_{\%} = \sqrt{Q^2 + U^2}/I$, and the sky polarization angle is given by $\phi = \frac{1}{2} \arctan \frac{U}{Q}$. Because the absolute flux calibration has not

been finalized yet, we choose not to report here the intensity values corresponding to each contour level. These maps should not be considered of any scientific value as they are not calibrated in flux and the polarization angles may be rotated by an offset, as summarized later on in Section 6.7. Nonetheless, we note that the BLAST-Pol map of the Carina Nebula shown in Figure 6.4 bears a promising resemblance to the map produced by the Submillimeter Polarimeter for Antarctic Remote Observations (SPARO; Novak et al. 2003) at $450\ \mu\text{m}$, which is shown in Figure 1 of Li et al. (2006).

The polarization degree and position angle in the sky are two of the most important observables that BLAST-Pol will yield; in particular, as detailed in Section 1.2, the degree of dispersion in the polarization angle is an indicator of magnetic field strength, while the variation of the polarization amplitude as a function of wavelength can help constrain models of grain alignment. In addition to the maps, we show for each source *preliminary* histograms of the polarization degree and the polarization angle in the sky (Figures 6.3, 6.5, and 6.7), which are measured from the maps for each $3'$ resolution element.

6.6 Concluding Remarks

In this chapter we have introduced the problem of producing astronomical maps from raw bolometric data collected by an experiment with hundreds of detectors. We have focused on the mathematical formalism of map-making, and the algorithmic implementation of a naive binning technique for the case of BLAST-Pol, in the assumption of white and uncorrelated noise. By using a simulated polarized input synthesized from the timelines of a bright calibrator from the BLAST06 dataset, we have successfully tested the ability of the algo-

rithm to retrieve the correct polarization on the sky.

In addition, as a proof of concept, we have presented preliminary maps for a sample of three targets observed by BLAST-Pol. Although the reduction of this dataset has not yet been finalized, the maps presented here demonstrate the overall success of the mission.

6.7 Future Work

The polarization maps presented in this chapter are by all means preliminary and do not include several of the corrections relative to the HWP and the polarizing grids that we have derived in Chapter 5. In particular, we have highlighted that the most important correction is that due to the wavelength-dependent position of the equivalent axes of the sapphire plate stack, β_{ea} . Specifically, we have shown that its band-averaged values, $\overline{\beta}_{\text{ea}}$, are significantly affected by the spectral signature of input source, which can either be known or assumed. This dependence, if neglected, may lead to an arbitrary rotation of the retrieved polarization angle on the sky of magnitude $2\overline{\beta}_{\text{ea}} = 10\text{--}15^\circ$ ($3\text{--}5^\circ$) at 250 (500) μm . The 350 μm band, however, is minimally perturbed by this effect.

In addition, the optical and polarization efficiencies of each detector are still being measured as of this thesis' submission date, and will need to be combined with those due to the HWP that we have presented in Section 6.2.

Furthermore, during the BLAST-Pol integration and flight campaigns in Palestine (TX) and Antarctica, respectively, we have estimated for each detector the overall instrumental polarization (IP) of the receiver, by measuring the signal detected by the bolometers when exposed to a completely unpolarized calibration source. Prelim-

inary analysis of these datasets indicates very modest levels of IP, in the range of 0.5–1% (consistent with the levels of $I \rightarrow Q, U$ leakage and cross-pol estimated in this thesis for the HWP and the polarizing grids). Nonetheless, these corrections will be implemented in the data analysis pipeline; in particular, as a first instance, we are planning to simply subtract the IP contribution from the measured polarized signal. This technique has been successfully applied to other instruments (e.g., SPARO; Novak et al. 2003, Renbarger et al. 2004, Li et al. 2006) and is regarded as a very promising approach for BLAST-Pol, especially given the slightness of the IP effects.

Finally, it is our intention to develop a Monte Carlo approach to estimating the uncertainties on the $[I, Q, U]$ maps to account for the several biases inherent to a direct error propagation method.

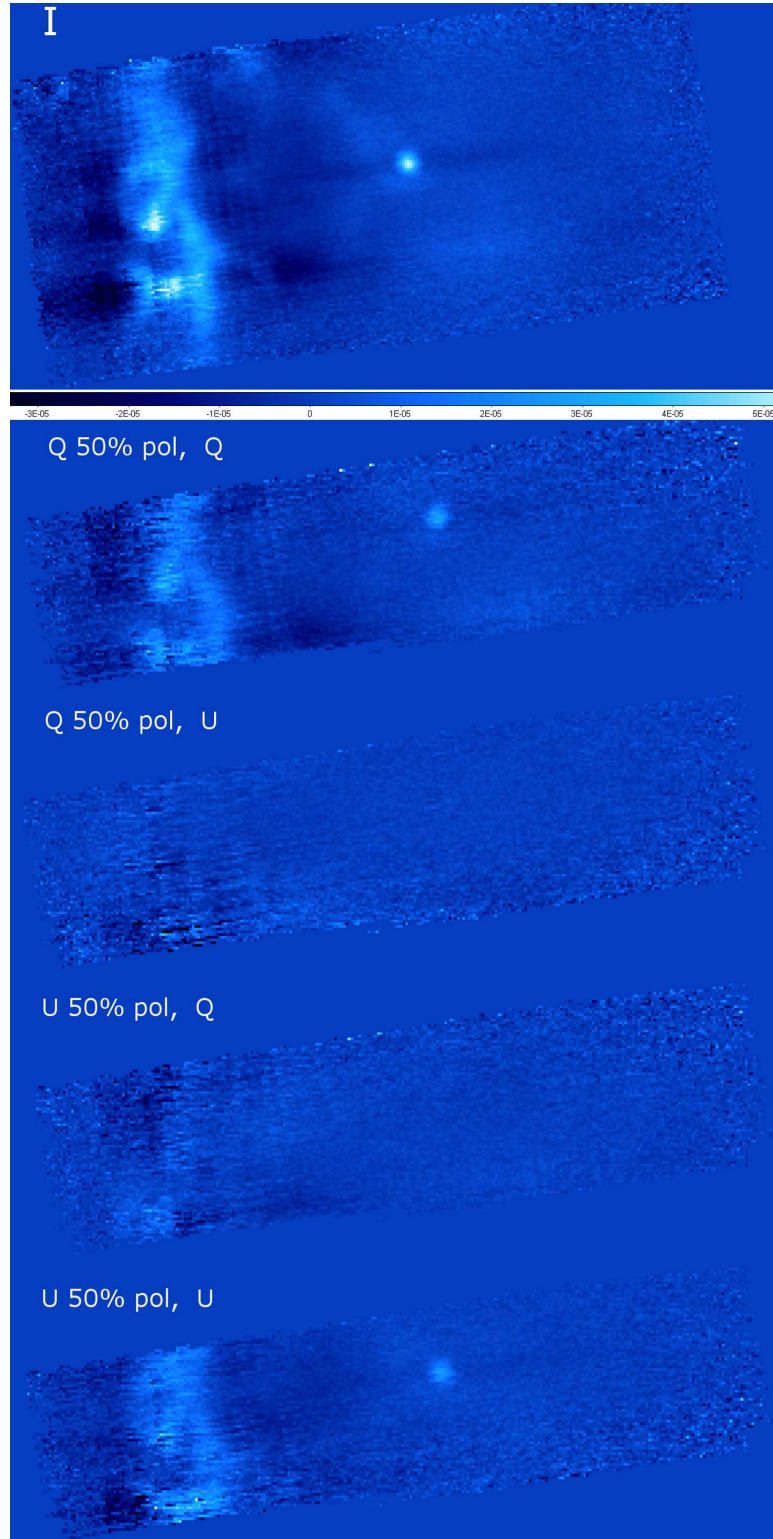


Fig. 6.1 Test maps generated from the timelines of BLAST06 observations of VY Canis Majoris (VY CMa). The top panel shows the intensity map, while the four panels beneath show Q, U test polarization maps produced by simulating a $p\% = 50$ Q and U input, obtained as $d_Q^{50\%} = d(1 + 0.5 \cos 2\gamma)$ and $d_U^{50\%} = d(1 + 0.5 \sin 2\gamma)$, respectively. The maps are on the same color scale, which is shown below the I map.

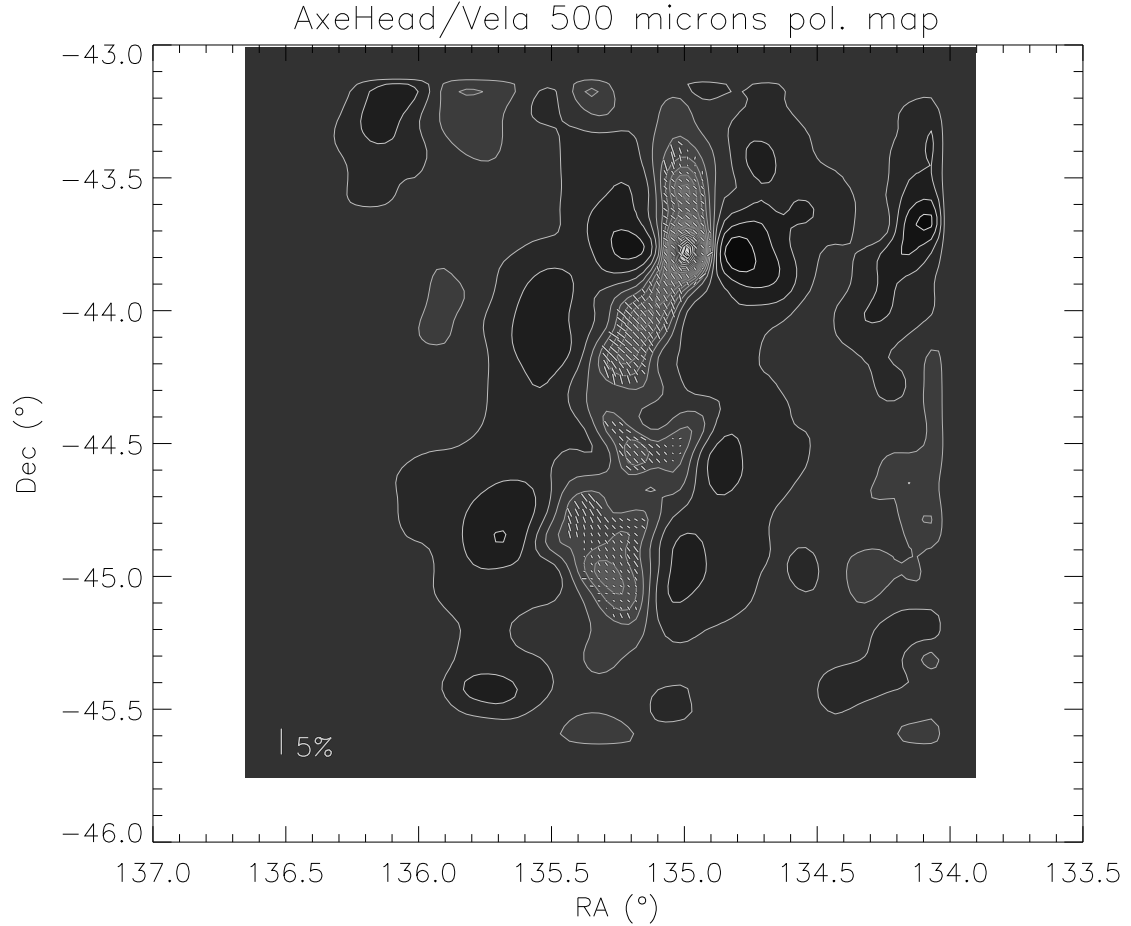
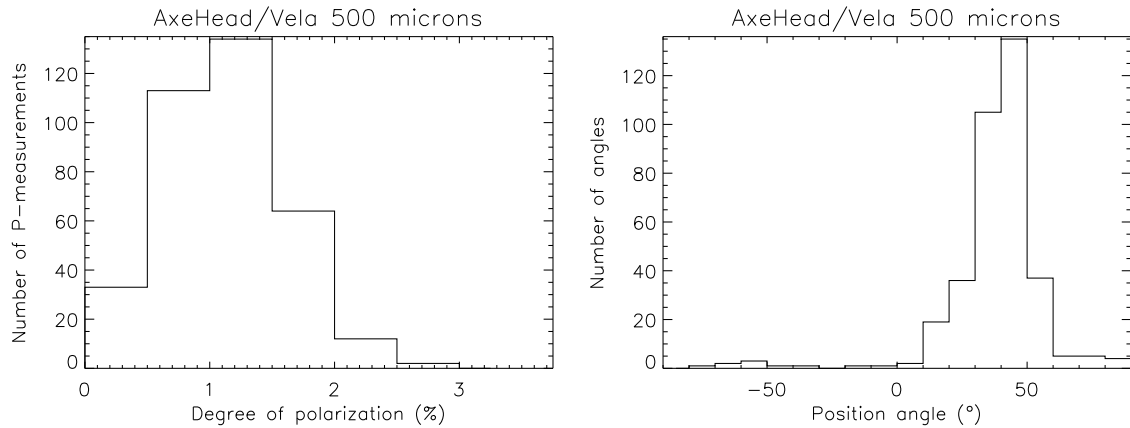


Fig. 6.2 Preliminary BLAST-Pol intensity and polarization map at $500\ \mu\text{m}$ of the “AxeHead” (Vela Molecular Ridge; Netterfield et al. 2009), approximately centered at coordinates $[09^{\text{h}}00^{\text{m}}49^{\text{s}}, -44^{\circ}25'10'']$. This map should not be considered of any scientific value as it is not calibrated in flux and the polarization angle may be rotated by an offset; the map is only shown as a proof of concept for the map-maker.



(a) Histogram of the polarization degree.

(b) Histogram of the sky polarization angle.

Fig. 6.3 Histograms for the “AxeHead”, shown in Figure 6.2.

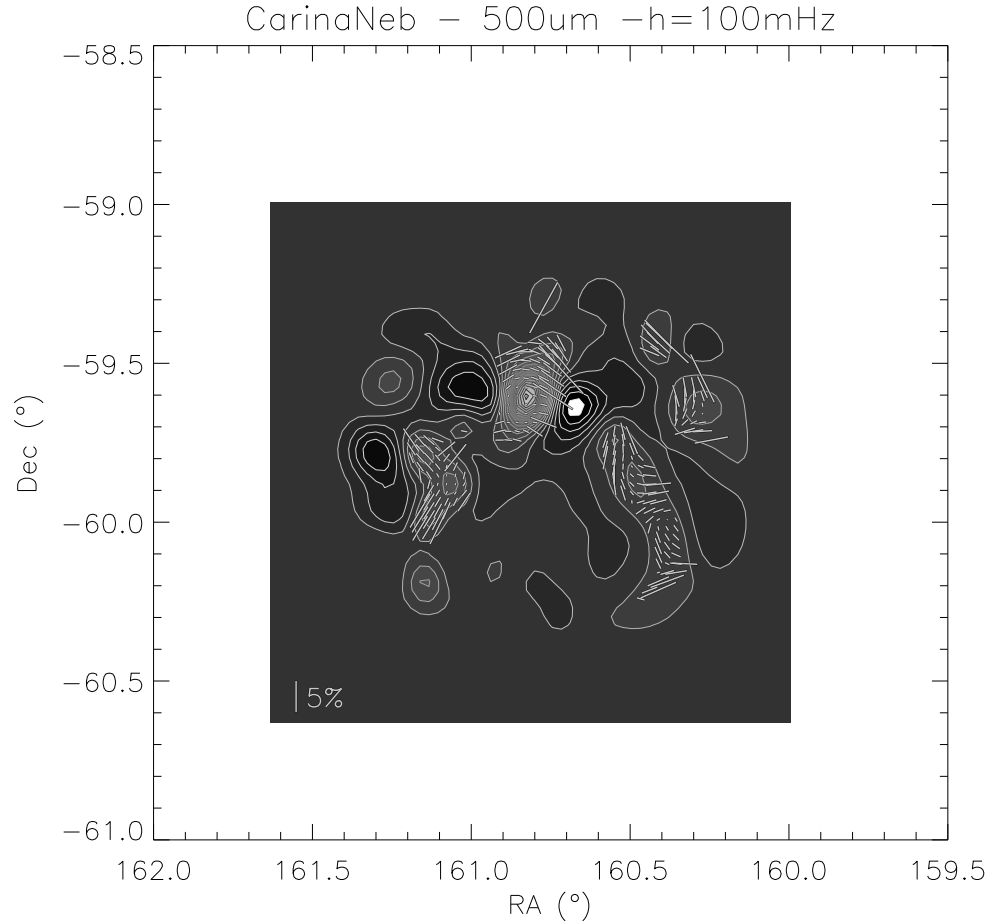
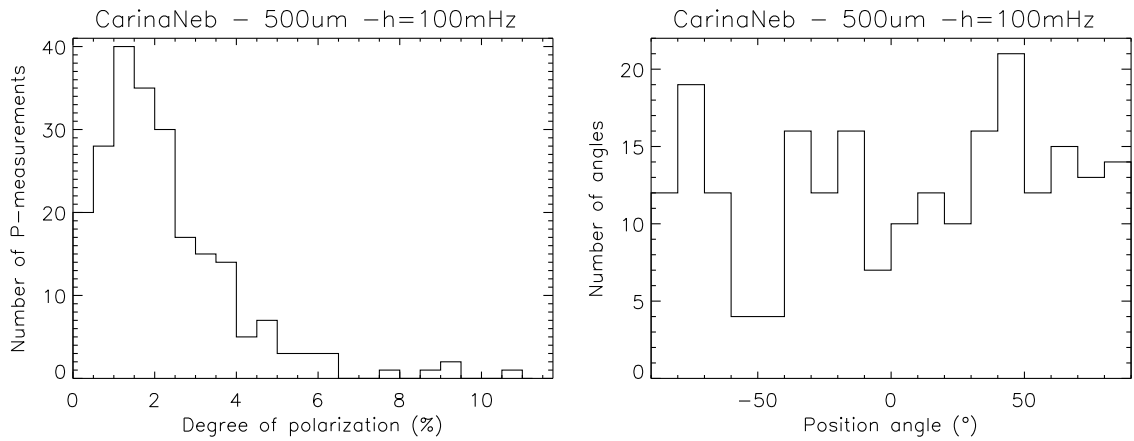


Fig. 6.4 Preliminary BLAST-Pol intensity and polarization map at $500\ \mu\text{m}$ of the Carina Nebula, a GMC approximately centered at coordinates $[10^{\text{h}}42^{\text{m}}35^{\text{s}}, -59^{\circ}42'15'']$. This map should not be considered of any scientific value as it is not calibrated in flux and the polarization angle may be rotated by an offset; the map is only shown as a proof of concept for the map-maker.



(a) Histogram of the polarization degree.

(b) Histogram of the sky polarization angle.

Fig. 6.5 Histograms for the Carina Nebula, shown in Figure 6.4.

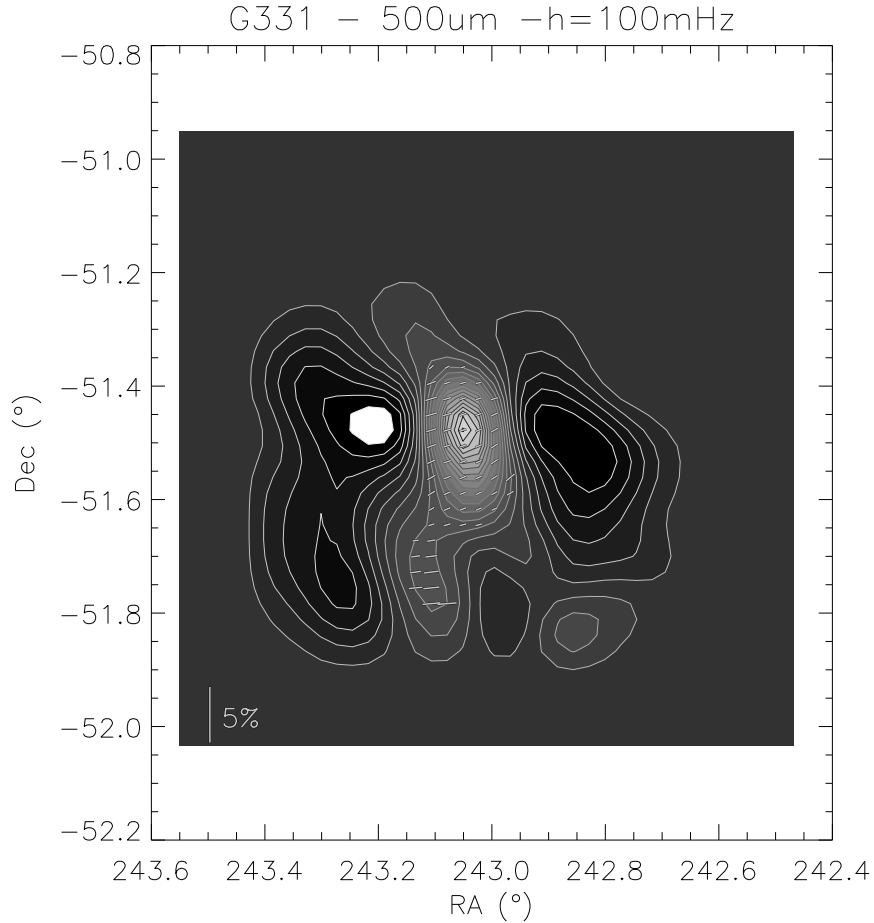
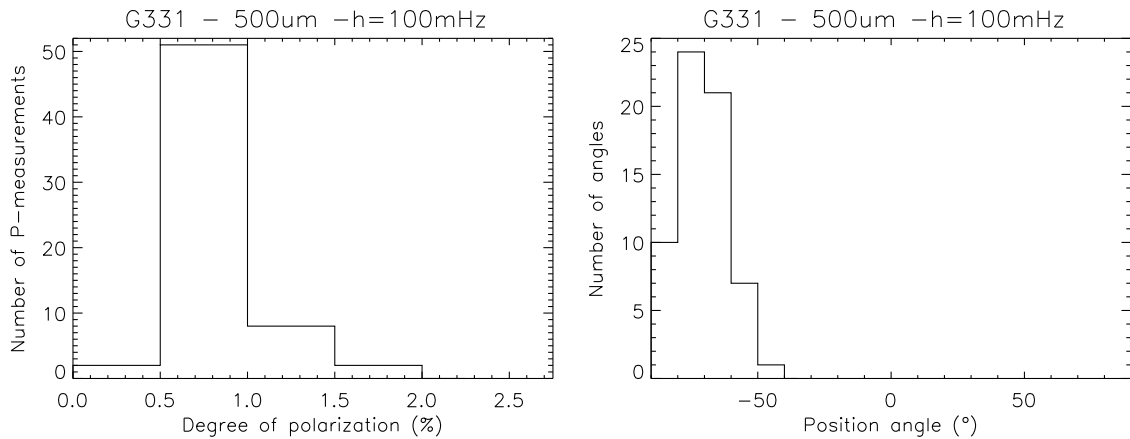


Fig. 6.6 Preliminary BLAST-Pol intensity and polarization map at $500\ \mu\text{m}$ of G331, a GMC approximately centered at coordinates $[16^{\text{h}}12^{\text{m}}10^{\text{s}}, -51^{\circ}27'51'']$. This map should not be considered of any scientific value as it is not calibrated in flux and the polarization angle may be rotated by an offset; the map is only shown as a proof of concept for the map-maker.



(a) Histogram of the polarization degree.

(b) Histogram of the sky polarization angle.

Fig. 6.7 Histograms for G331, shown in Figure 6.6.

7. CONCLUSIONS

The primary scientific motivation for this thesis is the study of the star-formation processes in galaxies at cosmological distances and in molecular clouds in our own Galaxy. We have discussed how fundamental it is to conduct surveys of the sky at FIR and submm wavelengths, in order to achieve a more complete understanding of the formation of stars and the evolution of galaxies in the Universe. In particular, we have introduced the reader to submm extragalactic and Galactic astronomy, referencing the leading theoretical models and observational findings as well as pinpointing the questions and issues that are still being debated. We have outlined the role that BLAST and its polarimetric upgrade, BLAST-Pol, respectively, has played and will play in making significant headway on these fronts, through large-area submm surveys conducted from long-duration stratospheric balloon platform.

In the first part of this thesis, we have presented a multi-wavelength study of a subset of the hundreds of distant, highly dust-obscured, and actively star-forming galaxies detected by BLAST in its survey of the Extended Chandra Deep-Field South (ECDFS), using data spanning the radio to the UV. We have developed a Monte Carlo method to account for flux boosting, source blending, and correlations among bands, which we have used to derive deboosted FIR luminosities for our sample. We have shown how crucial the BLAST/SPIRE photometry is to estimate the FIR luminosity of a galaxy without bias, especially at high redshift. We have estimated total (obscured plus unob-

scured) star-formation rates for the BLAST counterparts by combining their FIR and UV luminosities. We have shown that star formation is heavily obscured at $L_{\text{FIR}} \gtrsim 10^{11} L_{\odot}$, $z \gtrsim 0.5$, but the contribution from unobscured starlight cannot be neglected at $L_{\text{FIR}} \lesssim 10^{11} L_{\odot}$, $z \lesssim 0.25$. We have capitalized on the multi-wavelength data at our disposal to derive a broad morphological classification of our galaxies, their AGN fraction and stellar masses. We have assessed that about 20% of the galaxies in our sample harbor a type-1 AGN, but their submillimeter emission is mainly due to star formation in the host galaxy. We have used the combined estimates of SFRs and stellar masses to determine that the bulk of the BLAST counterparts at $z \lesssim 1$ are normal star-forming galaxies, typically spiral in shape, with intermediate stellar masses ($M_{\star} \sim 7 \times 10^{10} M_{\odot}$) and approximately constant SSFRs (τ_{SF} in the range 1–10 Gyr). On the other hand, the high- z tail of the BLAST counterparts significantly overlaps with the SCUBA starburst population, in terms of both SFRs and stellar masses, with observed trends of SSFRs that support strong evolution and downsizing.

In Part One of this thesis we have also presented a challenging measurement of the star-formation level in massive ($M_{\star} \geq 10^{11} M_{\odot}$), high-redshift ($1.7 < z < 2.9$) galaxies selected in the optical with the NICMOS camera on *HST*. Because the emission from each galaxy is too faint to be individually detected in the MIR–to–submm maps at our disposal, we have performed stacking analysis to unbiasedly measure their mean flux density. We have fitted a modified blackbody spectrum to the stacked flux densities and measured a median [interquartile] star-formation rate of $\text{SFR} = 63 [48, 81] M_{\odot} \text{yr}^{-1}$. When the galaxies are divided into two groups, disk-like and spheroid-like, according to their Sérsic indices, we have found evidence that most of the star formation is occurring in disk-like galaxies, with $\text{SFR} =$

122 [100, 150] $M_{\odot} \text{yr}^{-1}$; whereas the spheroid-like population seems to be forming stars at $\text{SFR} = 14$ [9, 20] $M_{\odot} \text{yr}^{-1}$, if at all. We have also shown that star formation is a plausible mechanism for size evolution in this population as a whole, but there is only marginal evidence that it is the main driver for the expansion of the spheroid-like galaxies.

In the second part of this thesis, we have presented the BLAST-Pol instrument, which is designed to probe the earliest stages of star formation by measuring the strength and morphology of magnetic fields in dust-enshrouded molecular clouds in our Galaxy. We have described the important subsystems of the gondola, including the optics, cryogenic system, bolometric detectors, polarization-sensitive elements, readout electronics, pointing sensors and control. In particular, we have focused on the primary pointing sensors for BLAST-Pol, two redundant daytime star cameras, detailing the principles of operation, design, and control software. The star cameras have been integrated with the BLAST-Pol gondola and successfully deployed in the 2010 Antarctic campaign. We have also presented preliminary results of the post-flight pointing reconstruction, which suggest that the overall pointing performance will reach that of BLAST06 ($\lesssim 3''$ rms).

In Part Two of this thesis we have also presented the polarization modulation scheme that has been successfully retrofitted on BLAST-Pol. We have illustrated in full detail the theoretical framework, principles of operation and manufacturing process for the optical components of the BLAST-Pol polarimeter, an achromatic cryogenic HWP and photolithographed polarizing grids acting as analyzers, as well as their pre-flight performance. We have highlighted the technical challenges of producing a broadband anti-reflection coating at submm wavelengths; the coating we have applied to the BLAST-Pol HWP represents the first successful application of a new-concept THz anti-

ficial dielectric metamaterial. We have identified and measured the parameters that characterize the optical properties and efficiency of these polarizing elements. In particular, using a pFTS we have performed a full spectral characterization, both at room and cryogenic temperatures, of the five-plate sapphire BLAST-Pol HWP, which is, to our knowledge, the most achromatic ever built at mm and submm wavelengths. We have found that most of the non-idealities of the HWP assembly can be accounted for by quantifying one wavelength-dependent parameter, the position of the equivalent axes of the HWP, possibly as a function of the spectral signature of a given astronomical source. We have subsequently included this parameter in the BLAST-Pol map-maker. We have measured the modulation efficiency of the HWP to be above 98% in all three BLAST-Pol bands. We have measured the efficiency the BLAST-Pol analyzers to be at least 97%, and their cross polarization to be at most 0.07%. We have also provided the nominal sensitivities for BLAST-Pol, and described the scanning strategy adopted to optimally recover the Stokes Q and U in the sky.

We have developed and implemented a polarized map-maker, which is used to transform raw detector time streams into usable sky maps of Stokes parameter $[I, Q, U]$. We have focused on the mathematical formalism of map-making, and the algorithmic implementation of a naive binning technique for the case of BLAST-Pol, in the assumption of white and uncorrelated noise. As a proof of concept, we have presented preliminary intensity and polarization maps for a sample of three targets observed by BLAST-Pol during its 9.5-day flight over Antarctica, completed in January 2011. In this first science campaign, BLAST-Pol has mapped ten star-forming regions with unprecedented combined mapping speed, sensitivity and resolution. Although the reduction of this dataset has not yet been finalized as of this thesis'

submission date, the maps we have presented here result as the culmination of the whole data analysis process and demonstrate the overall success of the mission. These maps comprise an exciting dataset for studying the role played by magnetic fields in star formation. The author of this thesis will continue to be involved in the BLAST-Pol data analysis and the subsequent scientific production.

7.1 Future Work

The analyses undertaken in Part One of this thesis with the BLAST06 dataset can naturally be extended and improved to include larger datasets with deeper and higher resolution observations from *Herschel*/SPIRE. In particular, the author of this thesis intends to carry-out a follow-up multi-wavelength study of the significantly larger sample of sources detected in the *Herschel* Astrophysical Terahertz Large Area Survey (H-ATLAS; Eales et al. 2010a). This will enable significantly reduced uncertainties and therefore much improved constraints on models of galaxy evolution and formation. Furthermore, we aim to further the stacking work with larger catalogs and better maps, which will enable more robust estimates of the SED, and will greatly increase our understanding of star formation in high-redshift massive galaxies.

As previously noted, LM will endeavor to produce high-quality polarization maps from the BLAST-Pol 2010 dataset, which will enable a promising study of the role played by magnetic fields in star formation. In particular, we aim at a more comprehensive account of the correlations in the noise, as well as a thorough assessment of the in-flight performance and calibrations of the instrument. LM will appear as co-author in all the BLAST-Pol scientific production, and will strive to lead a paper on the polarization spectrum described in Section 1.2.4.

APPENDIX

A. STACKING ANALYSIS

A.1 Introduction

Practically every map of the extragalactic sky ever produced to date at submillimeter (submm) wavelengths has a fundamental limitation in angular resolution with respect to most optical, near- to mid-IR, radio, and X-ray images. This simply arises as a consequence of the Rayleigh criterion at submm wavelengths, which dictates, for single-dish telescopes, diameters of the order of tens of meters to achieve an angular resolution of a few arcseconds. In addition, observations from the ground are impaired by the atmosphere being opaque over much of the wavelength range from $20\ \mu\text{m}$ to $1\ \text{mm}$, with only the $850\ \mu\text{m}$ atmospheric window having routine transmission of over 50%. Stratospheric and space observatories can only be equipped with a dish of limited size (2 m for BLAST, 3.5 m for *Herschel*), leading to angular resolutions no better than a few tens of arcseconds. Extragalactic sources detected in these maps are often confused, blended together, and in general difficult to isolate. Next generation instruments such as the ALMA interferometer or the Large Millimeter Telescope (LMT) will ultimately be able to match the resolution of optical imaging, albeit with limited mapping capabilities.

Although deriving the physical properties of individual galaxies at submm wavelengths can be challenging (see Chapter 2 of this thesis), one can use submm maps to study the ensemble properties of a population of sources detected at other wavelengths. Given a BLAST map

and an external catalog, we can estimate the average brightness of an externally-selected population of galaxies at the BLAST frequencies by taking postage-stamps of the BLAST map, at the positions of the external catalog, and stacking them together to form a unique, higher signal-to-noise image. This technique is often referred to as “stacking analysis”. As we will show in the following sections, not only does stacking naturally provide a way around the poor resolution of submm maps, but also greatly enhances the signal-to-noise ratio of objects too faint to be individually detected; the combination of these two virtues effectively allows stacking to push flux density measurements beyond the confusion limit. Technical questions often arise about the generalization of this technique to very high source density or about the exclusion of bright sources: we review the mathematical formalism in Section A.2, and find that many of these misconceptions are avoided when one realizes that the technique is really one of taking the covariance of the map with the catalog. In Section A.3, we formally show how aperture photometry can be safely performed to measure the stacked flux density. In Section A.4, we detail how to estimate uncertainties on the measured stacked values that include both instrumental and confusion noise. In Section A.5, we describe the catalogs used and present some of the stacked images. Finally, in Section A.6, we show how stacking analysis can provide additional information on the effective shape of the point-spread function (PSF) of BLAST, as well as being an effective diagnostic tool for pointing errors and astrometry registration.

For brevity, we choose not to report in this thesis all of the scientific results of this analysis, except for those presented in Chapter 3. In particular, we omit here the findings based on splitting up a catalog in bins of, e.g., $24\ \mu\text{m}$ flux density or redshift, which are extensively

described in Devlin et al. (2009), Pascale et al. (2009) and Marsden et al. (2009).

A.2 Mathematical Formalism

Imagine we have a map of the sky where M_j is the flux density in each pixel j . Suppose also that we have one or several independent catalogs of sources made from other experiments, potentially at different wavelengths; catalog C_α has N_α^j sources in pixel j , and we want to measure the mean flux density, S_α , of the sources in C_α . Let us denote the mean of N_α^j as μ_α , the average number of sources per pixel in list C_α . If objects in the catalog produce flux densities that are S_α on average, then, along with whatever else is in the sky, there will be a contribution $S_\alpha^j = S_\alpha N_\alpha^j$ to each pixel.

If a sky containing this signal were observed with BLAST, the resulting map would be the convolution of S_α^j with the instrumental PSF, and with a mean of zero (because BLAST is a relative photometer). We can write the flux density in the map as

$$M_j = n_j + \sum_{\alpha} S_{\alpha} (N_{\alpha}^j - \mu_{\alpha}), \quad (\text{A.1})$$

where n_j is the contribution of detector noise in pixel j , and, strictly speaking, the S_α form the complete set of all objects in the Universe. The mean in the map is removed by subtracting $S_\alpha \mu_\alpha$ for each catalog from every pixel. We additionally require that n_j has a mean of zero.

In order for stacking analysis to provide an unbiased estimate of the average brightness of an externally-selected population of galaxies at the BLAST wavelengths, we postulate that the sources in the catalog are not spatially correlated (or “clustered”, as often referred to in the literature), such that N_α^j is a random, Poisson-distributed

number¹. Furthermore, we assume that no two lists are correlated, so that $\langle (N_\alpha^j - \mu_\alpha) (N_\beta^j - \mu_\beta) \rangle = 0, \forall \alpha \neq \beta$.

We emphasize here that our goal is to determine the mean flux density per source in a catalog, from knowledge of the submm map, M_j , and the locations, N_α^j , of the sources in C_α , but without any other information. This problem can be approached by considering our map and our external catalog distribution as shapes on the sky; the amplitude, S_α , of N_α^j that matches M_j can be quantified by writing their covariance:

$$\begin{aligned} \text{Cov}(M_j, N_\alpha^j) &= \frac{1}{N_{\text{pix}}} \sum_j M_j N_\alpha^j \\ &= \frac{S_\alpha}{N_{\text{pix}}} \left[\sum_j (N_\alpha^j)^2 - \mu_\alpha \sum_j N_\alpha^j \right], \end{aligned} \quad (\text{A.2})$$

where N_{pix} is the total number of pixels in the map, and the terms in $N_\alpha^j N_\beta^j$ and $N_\alpha^j n_j$ vanish in the sum. We notice that the term in square parentheses in Equation (A.2) divided by N_{pix} is nothing else but the definition of variance for N_α^j , and therefore equals μ_α for a Poisson-distributed source list.

The net result is that the zero-lag cross-correlation (covariance) of a catalog with the map divided by the mean number of sources per pixel is an estimate of the average flux density per source. An additional re-arrangement of Equation (A.2) makes this result more useful. Notice that the sum runs over all pixels, with the weight of each pixel proportional to the number of catalog sources found in it, and that zero weight is given to pixels that do not contain a source ($N_\alpha^j = 0$). This can be written as a sum over all catalog entries with

¹ We refer to Section 3.3 and Figure 3 of Marsden et al. (2009) for an exhaustive test of this assumption. We also point out that the ‘‘catalog clustering’’ discussed here should not be confused with the source clustering detected in the BLAST maps by Viero et al. (2009).

unit weight:

$$\hat{S}_\alpha = \frac{\text{Cov}(M_j, N_\alpha^j)}{\mu_\alpha} = \frac{1}{N_{\text{pix}} \mu_\alpha} \sum_j M_j N_\alpha^j = \frac{1}{n_\alpha} \sum_k M_k, \quad (\text{A.3})$$

where k is the index of sources in catalog C_α , M_k is the measured flux density in the map pixel that contains the k^{th} catalog entry, and n_α is the total number of catalog entries, $n_\alpha = N_{\text{pix}} \mu_\alpha$. This expression is the simple average flux density in the map over all positions in the source catalog; as anticipated above, it can be used to probe the ensemble properties of sources much too crowded to be detected individually, and also those with flux densities that are much fainter than the typical thresholds of source catalogs derived only from the map itself.

Perhaps counterintuitively, in the absence of clustering of the source catalog, no additional correction is needed, even for cases in which the catalog has a very high source density (e.g., a few sources per submm beam). One other assumption made is that the instrumental noise is well-behaved, i.e. $\langle n_j = 0 \rangle$. Since the map pixel noises n_j are not uniform across the map, we weight the mean in Equation (A.3) by the inverse pixel variance to maximize the S/N ratio of \hat{S}_α . We will show in Section A.4 how to estimate the uncertainty on \hat{S}_α by repeating the stacking for a set of random locations in the map, and by measuring the sample standard deviation of the resulting stacks. This procedure accounts for uncertainties caused both by instrumental and confusion noise.

Equation (A.3) provides a robust estimate of the mean brightness per source even when there are other, possibly substantial, contributors to the flux density present, C_β . This is provided that N_α^j is Poisson distributed, and N_α^j is not correlated with either the detector

noise or sources in C_β . In other words, the effect of other sources on the estimator \hat{S}_α is to provide an additional source of noise. This noise may potentially be asymmetric, but it has a mean of zero, such that \hat{S}_α is unbiased. Similarly, a catalog C_α can be subdivided into disjoint subsets, and the mean brightness due to each subset can be measured without bias. We use this fact to split up our catalogs based on $24\ \mu\text{m}$ flux density or redshift (see Pascale et al. 2009).

We are now in a position to address the proper handling of sources that are bright enough to be easily recognized in the maps, for example the sources in a BLAST 5σ catalog. We have shown that \hat{S}_α , our estimate of S_α , is not affected by either the presence or the removal of flux density from other source lists C_β that are uncorrelated with C_α . However, since the sum of confusion noise and detector noise, $S_\alpha N_\alpha^j + n_j$, will cause sources near the threshold to be accidentally included or excluded from the BLAST catalog, any list made from the BLAST maps themselves will be artificially correlated with all the terms in Equation (A.1). Furthermore, since the BLAST-generated bright source catalog depends on the sum of the other terms in Equation (A.1), excision of the flux density from such a catalog will artificially correlate the remaining terms, such as $(N_\alpha^j - \mu_\alpha)$ and n_j . This introduces a bias in our estimator \hat{S}_α that is difficult to quantify. Therefore, stacking is performed on the full BLAST maps, including any bright sources they contain.

A.3 Aperture Photometry Method

In the previous section, we have outlined the mathematical formalism behind stacking analysis, starting from a catalog of sources and a map of the sky in units of flux density (Jy). Such a map is presumably the

result of the cross-correlation (convolution) of the raw map with the instrumental PSF: this operation is optimal for the case of an isolated point source in a field of statistically uncorrelated noise, and gives the maximum-likelihood flux density of a point-source fit to every position in the map (see, e.g., Stetson 1987). Alternatively, the flux density of a stack of postage-stamps, centered at the catalog positions and extracted from a raw submm map (with units of MJy/sr or Jy/pixel), can be measured via aperture photometry.

Let M_{ij} be our submm map and c_{ij}^α a list of positions from the catalog C_α . In the previous section, we have shown that the total flux, F , in M_{ij} associated with C_α can be written as

$$F = \sum_{\gamma\delta} \sum_{ij} c_{ij}^\alpha M_{i+\gamma, j+\delta}, \quad (\text{A.4})$$

where the indices $[\gamma, \delta]$ indicate the sum over a circular aperture of some radius (i.e., aperture photometry), while $[i, j]$ run over the map's pixels.

If the sources from C_α have a mean flux S_α in our map, then M_{ij} can be expressed as a PSF-convolution of the c_{ij}^α , as follows:

$$M_{ij} = S_\alpha \sum_{kw} c_{kw}^\alpha B_{i-k, j-w}, \quad (\text{A.5})$$

where B_{kw} is our best-estimate, pixelated instrumental PSF (or beam). Consequently, Equation (A.4) becomes

$$F = S_\alpha \sum_{\gamma\delta} \sum_{ij} \sum_{kw} c_{ij}^\alpha c_{kw}^\alpha B_{i+\gamma-k, j+\delta-w}. \quad (\text{A.6})$$

The mean flux, $\langle F \rangle$, is then

$$\begin{aligned}
\langle F \rangle &= S_\alpha \sum_{\gamma\delta} \sum_{ij} \sum_{kw} \langle c_{ij}^\alpha c_{kw}^\alpha \rangle B_{i+\gamma-k, j+\delta-w} \\
&= S_\alpha \sum_{\gamma\delta} \sum_{ij \neq kw} \langle c_{ij}^\alpha c_{kw}^\alpha \rangle B_{i+\gamma-k, j+\delta-w} + \\
&+ S_\alpha \sum_{\gamma\delta} \sum_{ij=kw} \langle c_{ij}^\alpha c_{kw}^\alpha \rangle B_{i+\gamma-k, j+\delta-w}, \tag{A.7}
\end{aligned}$$

which can be rearranged as

$$\begin{aligned}
\langle F \rangle &= S_\alpha \sum_{\gamma\delta} \sum_{ij \neq kw} \langle c_{ij}^\alpha c_{kw}^\alpha \rangle B_{i+\gamma-k, j+\delta-w} + \\
&+ S_\alpha \sum_{\gamma\delta} \sum_{ij=kw} \langle c_{ij}^\alpha c_{ij}^\alpha \rangle B_{\gamma\delta}. \tag{A.8}
\end{aligned}$$

In the assumption of no clustering, we have

$$\begin{aligned}
\langle c_{ij}^\alpha c_{kw}^\alpha \rangle &= \langle c_{ij}^\alpha \rangle \langle c_{kw}^\alpha \rangle = \mu_\alpha^2, \quad ij \neq kw, \\
\langle c_{ij}^\alpha c_{ij}^\alpha \rangle &= \text{Var}(c_{ij}^\alpha) + \langle c_{ij}^\alpha \rangle^2 = \mu_\alpha + \mu_\alpha^2, \quad ij = kw, \tag{A.9}
\end{aligned}$$

where $\mu_\alpha = \langle c_{ij}^\alpha \rangle$ is the expected value of the Poisson-distributed stochastic variable c_{ij}^α . Therefore Equation (A.8) becomes

$$\begin{aligned}
\langle F \rangle &= S_\alpha \mu_\alpha^2 \sum_{\gamma\delta} \sum_{ij \neq kw} B_{i+\gamma-k, j+\delta-w} + \\
&+ S_\alpha (\mu_\alpha + \mu_\alpha^2) \sum_{\gamma\delta} \sum_{ij=kw} B_{\gamma\delta} \\
&= S_\alpha \mu_\alpha^2 \sum_{\gamma\delta} \sum_{ij} \sum_{kw} B_{i+\gamma-k, j+\delta-w} + \\
&+ S_\alpha \mu_\alpha \sum_{\gamma\delta} \sum_{ij} B_{\gamma\delta}. \tag{A.10}
\end{aligned}$$

Because the beam integrates to unity, we obtain

$$\begin{aligned}\langle F \rangle &= S_\alpha \mu_\alpha^2 N_{\text{pix}} A + S_\alpha \mu_\alpha N_{\text{pix}} A_c \\ &= \mu_\alpha S_\alpha N_{\text{pix}} (\mu_\alpha A + A_c)\end{aligned}\quad (\text{A.11})$$

where A is the area size of the aperture (in pixel) and A_c the aperture correction (dimensionless number).

We can now account for the fact that BLAST maps have zero mean, by modifying Equation (A.4), which becomes

$$\langle F \rangle = \sum_{\gamma\delta} \sum_{ij} c_{ij}^\alpha \left[M_{i+\gamma, j+\delta} - \frac{1}{N_{\text{pix}}} \sum_{\iota\kappa} M_{\iota\kappa} \right] \quad (\text{A.12})$$

Equation (A.5) changes as follows:

$$\begin{aligned}M_{ij} - \frac{1}{N_{\text{pix}}} \sum_{\iota\kappa} M_{\iota\kappa} &= \\ &= S_\alpha \sum_{kw} c_{kw}^\alpha B_{i-k, j-w} - S_\alpha \frac{1}{N_{\text{pix}}} \sum_{\iota\kappa} \sum_{kw} c_{kw}^\alpha B_{\iota-k, \kappa-w} \\ &= S_\alpha \sum_{kw} c_{kw}^\alpha B_{i-k, j-w} - S_\alpha \mu_\alpha,\end{aligned}\quad (\text{A.13})$$

where the last equality holds, again, because the beam integrates to unity. Inserting Equation (A.13) into Equation (A.12), we easily obtain the equivalent of Equation (A.11), which now finally reads

$$\langle F \rangle = \mu_\alpha S_\alpha N_{\text{pix}} A_c. \quad (\text{A.14})$$

Equation (A.14), analogous and equally simple to Equation (A.3), gives the expression for the average flux density at submm wavelengths of an externally-selected population of sources as a function of the total stacked flux retrieved (and appropriately corrected) via aperture photometry.

Finally, there are a few important technicalities worth mentioning here about aperture photometry applied to our case. First, we deliberately set the value of the sky background to zero, since we have ensured that the region where the stacking is performed has zero mean. Second, the aperture radii chosen at the different channels are those maximizing the signal-to-noise² ratio, as computed by performing the stacking on BLAST noise maps, in a totally analogous way to the previously discussed signal maps. For BLAST, these turn out to be 30, 30, and 40'' at 250, 350, and 500 μm , respectively. Third, the aperture corrections are evaluated by performing aperture photometry on the PSFs themselves, with the same aperture radii as above. The resulting values are, 1.985, 1.906 and 1.966 at 250, 350, and 500 μm , respectively.

A.4 Uncertainties

In order to estimate the uncertainty of Equation (A.3) (and A.14) algebraically for a catalog C_α , one would need to know the scatter produced by the catalog of all sources not in C_α that contribute to the background (in addition to sources of instrumental noise) in the submm maps. In practice, such a catalog is not known, so we establish the uncertainties and possible biases of our measurements via a Monte Carlo technique, by generating random catalogs and stacking them on the submm maps under analysis. Namely, we stack N_α (the actual number of sources in the catalog or sub-catalog under analysis) postage-stamps centered at random positions within the region of sky under consideration; we then measure the mean flux density of such

² Note that here “noise” is just estimated by co-adding the BLAST variance map, which is not the most appropriate estimate of the noise associated with the measured average flux density, because it does not account for the confusion noise in the map (see Section A.4)

a stack using one of the two methods outlined in Sections A.2 and A.3. By repeating this procedure MC times (MC=10⁵ in our case), we can build a histogram of mock stacking measurements (see Figure 2 of Marsden et al. 2009). If such a histogram is Gaussian in shape, one is allowed to use the standard deviation of the distribution, σ_α , as the uncertainty associated with the measurement of flux density for the stack of real sources. Furthermore, if the histogram is centered on zero with high precision, these simulations also represent a very significant null test necessary to consolidate stacking analysis as an unbiased estimate of the average brightness of an externally-selected population of galaxies at submm wavelengths. Naturally, if a catalog is subdivided by flux or redshift bins into N_{bin} disjoint subsets, the whole procedure must be repeated N_{bin} times. This is obviously quite computationally expensive.

We find, as expected, that the uncertainties are Gaussian-distributed and scale as the map rms (including confusion noise) divided by the square root of the number of catalog entries, N_α . In practice, the whole process described above can be shortened, provided that the gaussianity of the histogram of random stacks has been verified at least once for every map under analysis. In fact, since the width of the above distribution scales as the map rms divided by the square root of the number of sources in the catalog, one can just produce a histogram of flux densities measured at MC random positions within the sky patch considered, with no stacking involved (shown in Figure A.1). If the resulting histogram is Gaussian and centered on zero, the uncertainty associated with the measured average flux density will be just the standard deviation of such distribution times $\sqrt{N_\alpha}$.

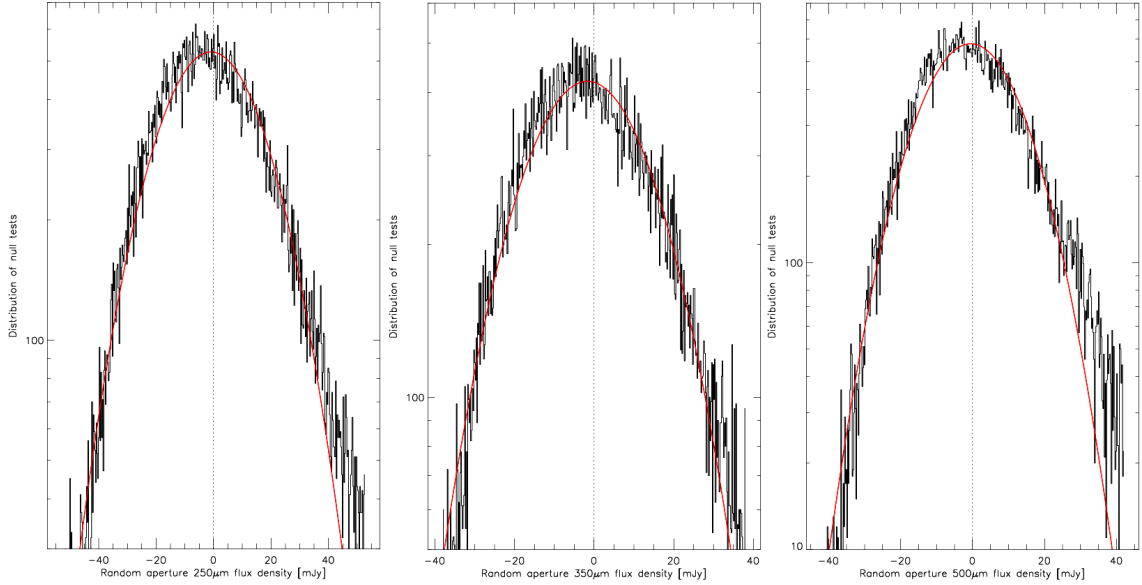


Fig. A.1 Quantification of errors in the stacking measurements from BLAST maps. We produce histograms of 10^5 flux density measurements at random positions within the survey area in consideration (see Figure A.2). The scale on the y -axis is the number of random apertures per $200 \mu\text{Jy}$ flux density bin. Clearly the histograms are very well described by Gaussians centered on zero. As detailed in the text, we can use the σ of each distribution, times the square root of the number of sources in the catalog under study, as the error in the stacked value. In addition, this figure shows a successful null test achieved with all three BLAST maps.

A.5 Catalogs

Here we briefly describe the five catalogs considered for stacking purposes.

1. SWIRE: $24 \mu\text{m}$ -selected catalog from the *Spitzer* Wide-Area Infrared Extragalactic Survey (Lonsdale et al. 2004). The survey area is $\simeq 8.5 \text{ deg}^2$, counting 21545 sources, with a minimum flux of $200 \mu\text{Jy}$.
2. FIDEL: $24 \mu\text{m}$ -selected catalog from the *Spitzer* Far-Infrared Deep Extragalactic Legacy survey (Magnelli et al. 2009). The survey area is $\simeq 0.206 \text{ deg}^2$, counting 9110 sources, with a minimum flux of $13 \mu\text{Jy}$ and a 80% completeness limit at $83 \mu\text{Jy}$.

3. ATLAS: 1.4 GHz-selected radio catalog from the Australia Telescope Large Area Survey (Norris et al. 2006). The survey area is $\simeq 3.45 \text{ deg}^2$, counting 726 sources, with a minimum flux of $150 \mu\text{Jy}$.
4. VLA: 1.4 GHz-selected radio catalog from the Very Large Array (VLA) survey of the Extended Chandra Deep-Field South (ECDFS Miller et al. 2008). The survey area is $\simeq 0.323 \text{ deg}^2$, counting 514 sources, with a minimum flux of $54 \mu\text{Jy}$. This catalog, as published, has a relatively conservative cut at 7σ . Therefore we extract our own catalog from the VLA map, using our own source finder (Devlin et al. 2009). This is a 3σ catalog, now counting 10474 sources, with a minimum flux of $20 \mu\text{Jy}$.
5. CHANDRA: X-ray-selected catalog from the 2Ms Chandra Deep-Field South (Luo et al. 2008; CDFS) survey. The survey area is $\simeq 0.121 \text{ deg}^2$, counting 462 X-ray sources in the two bands 0.5–2.0 and 2–8 keV.

All the sources in the listed catalogs lie within the area of the BLAST survey, as shown by a combination of Figure A.2 and Figure 2.1.

Figure A.3 shows an example of the quality of the stacked images for the FIDEL catalog.

A.6 Post-flight Pointing Verification

Stacking embodies a powerful diagnostic tool for pointing errors and astrometry registration, as briefly discussed in Marsden et al. (2008). In fact, we can we perform a stacking analysis on the BLAST extragalactic maps to check the absolute pointing performance and to give

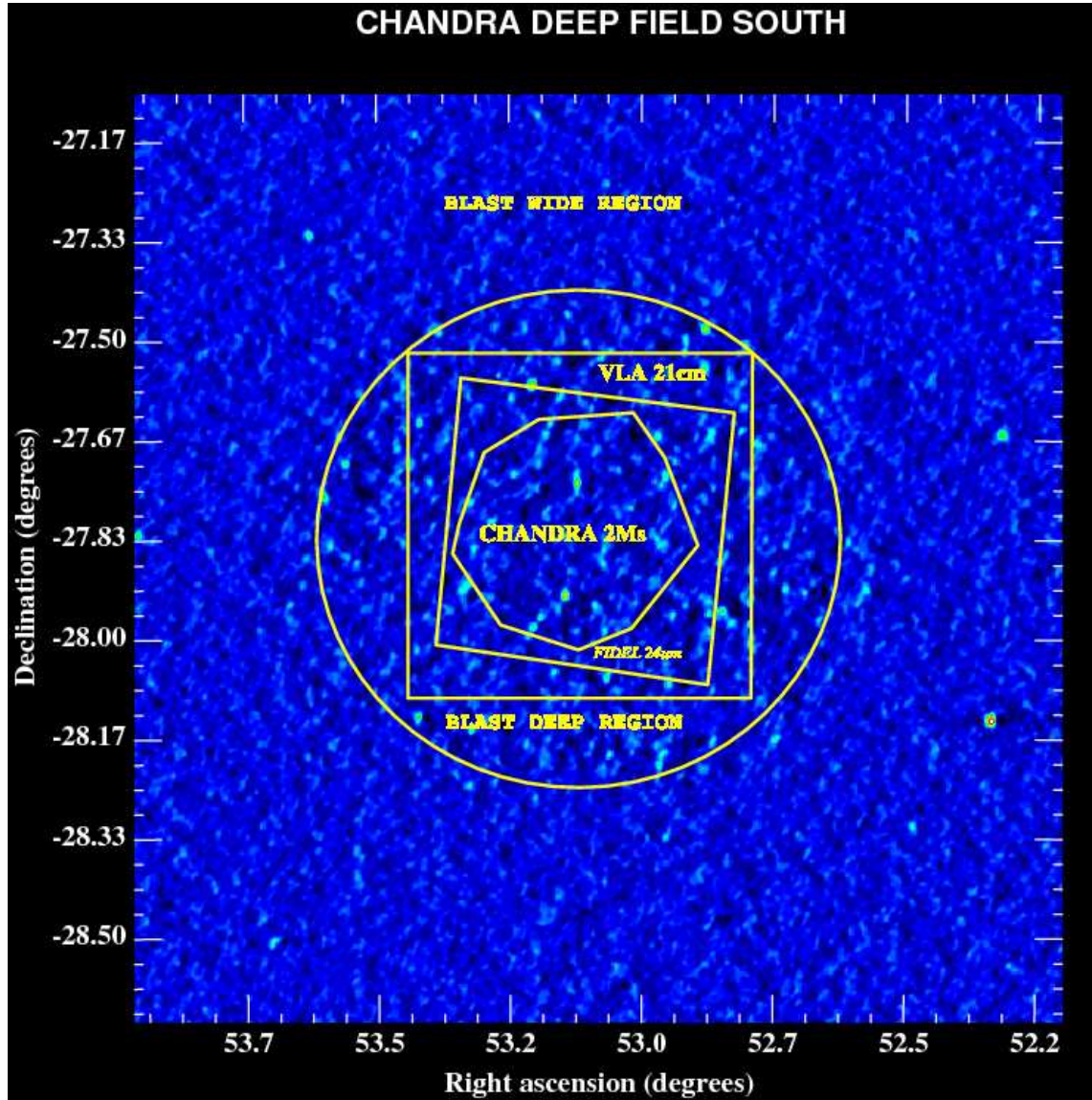


Fig. A.2 Distribution of the sources for the catalogs taken into account. They cover a noteworthy fraction of the BLAST Deep region.

an estimate of potential random pointing errors. We use sources detected in the deep radio VLA survey (see Section A.5), because of the sub-arcsecond accuracy achieved by radio interferometry. We find that the peak in the stacked map is located within $2''$ from the nominal position of the catalog, indicating that the absolute pointing accuracy is at least 15 times smaller than the BLAST beam size (see Figure A.4). Moreover, assuming random Gaussian pointing errors, we superimpose

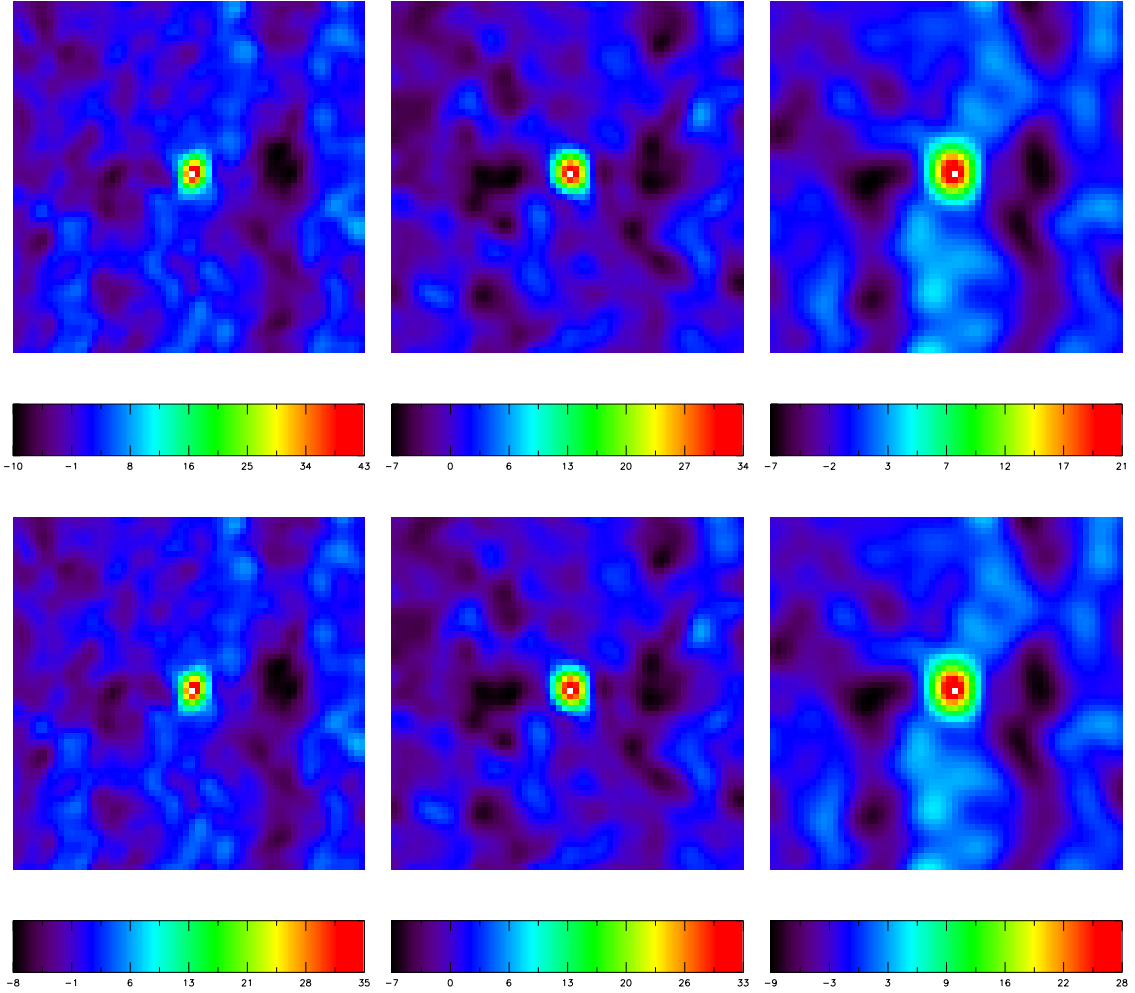


Fig. A.3 Example of stacked images obtained by co-adding $10' \times 10'$ postage-stamps of the BLAST maps (*left* 250 μm ; *center* 350 μm ; *right* 500 μm), centered at the positions of the FIDEL catalog. *Top row*: flux images in Jy. *Bottom row*: signal-to-noise² ratio images (dimensionless).

the synthetic scaled PSF to the stacked map and convolve it with a Gaussian profile, modeling the broadening of the PSF due to a potential pointing jitter. By varying the jitter width, we compute the χ^2 of the convolved PSF over the stacked data; this analysis yields an estimated upper limit for potential random pointing errors of $3''$.

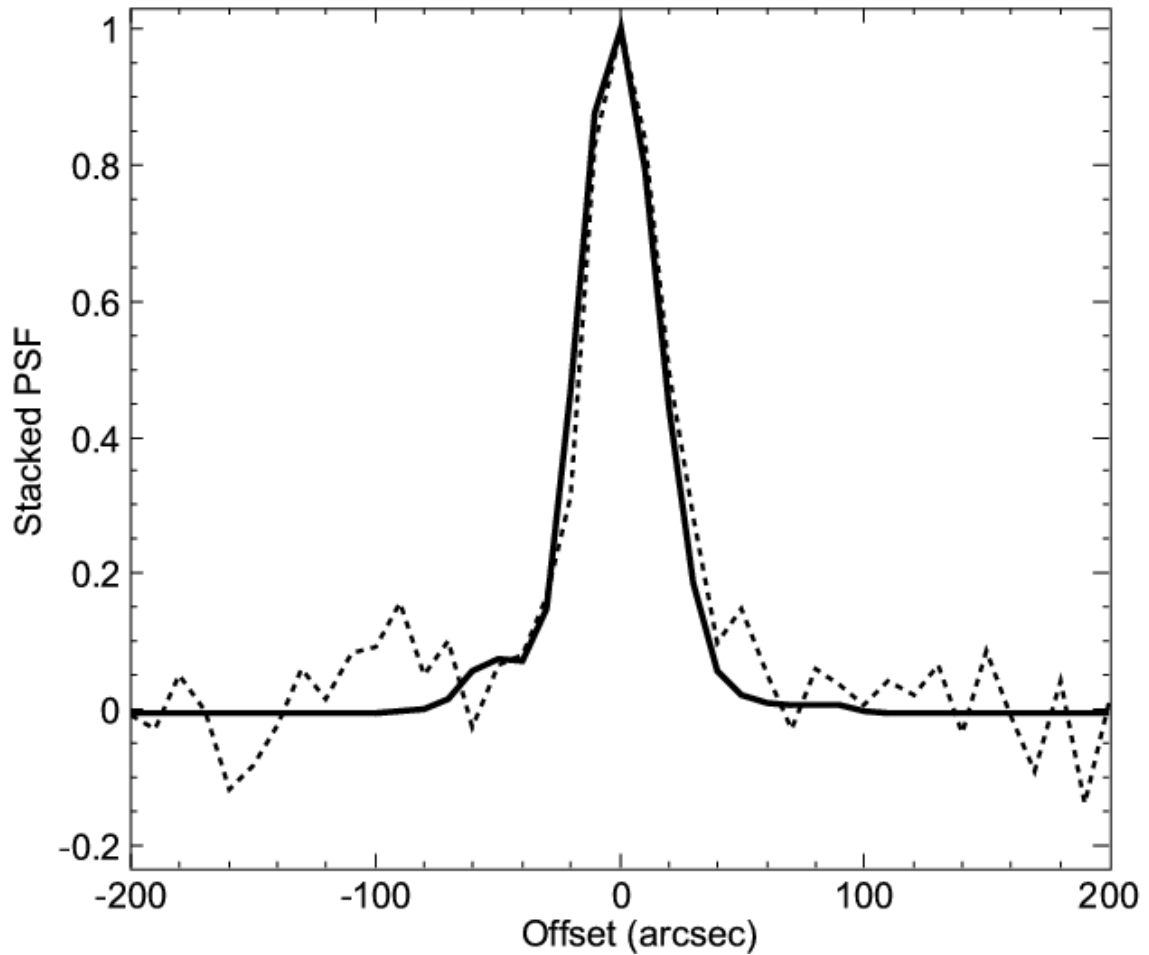


Fig. A.4 A cut through the stacked BLAST $250\ \mu\text{m}$ flux at the positions of VLA 1.4 GHz radio sources (Miller et al. 2008; dashed line) and through the $250\ \mu\text{m}$ PSF (solid line). We see that the stack is very well described by the PSF, in both position and width. We conclude that our absolute pointing is good to $< 2''$ and that random pointing errors are $< 3''$ rms.

B. POSTAGE STAMPS OF BLAST COUNTERPARTS

The broad morphological classification of the BLAST IDs presented in this work is based upon visual inspection of UV, optical, and MIR postage-stamp images (see Sections 2.2.5 and 2.7). A selection of $2' \times 2'$ cutouts is shown in Figure B1. The complete set of full-color cutouts can be found at:

http://blastexperiment.info/results_images/moncelsi/.

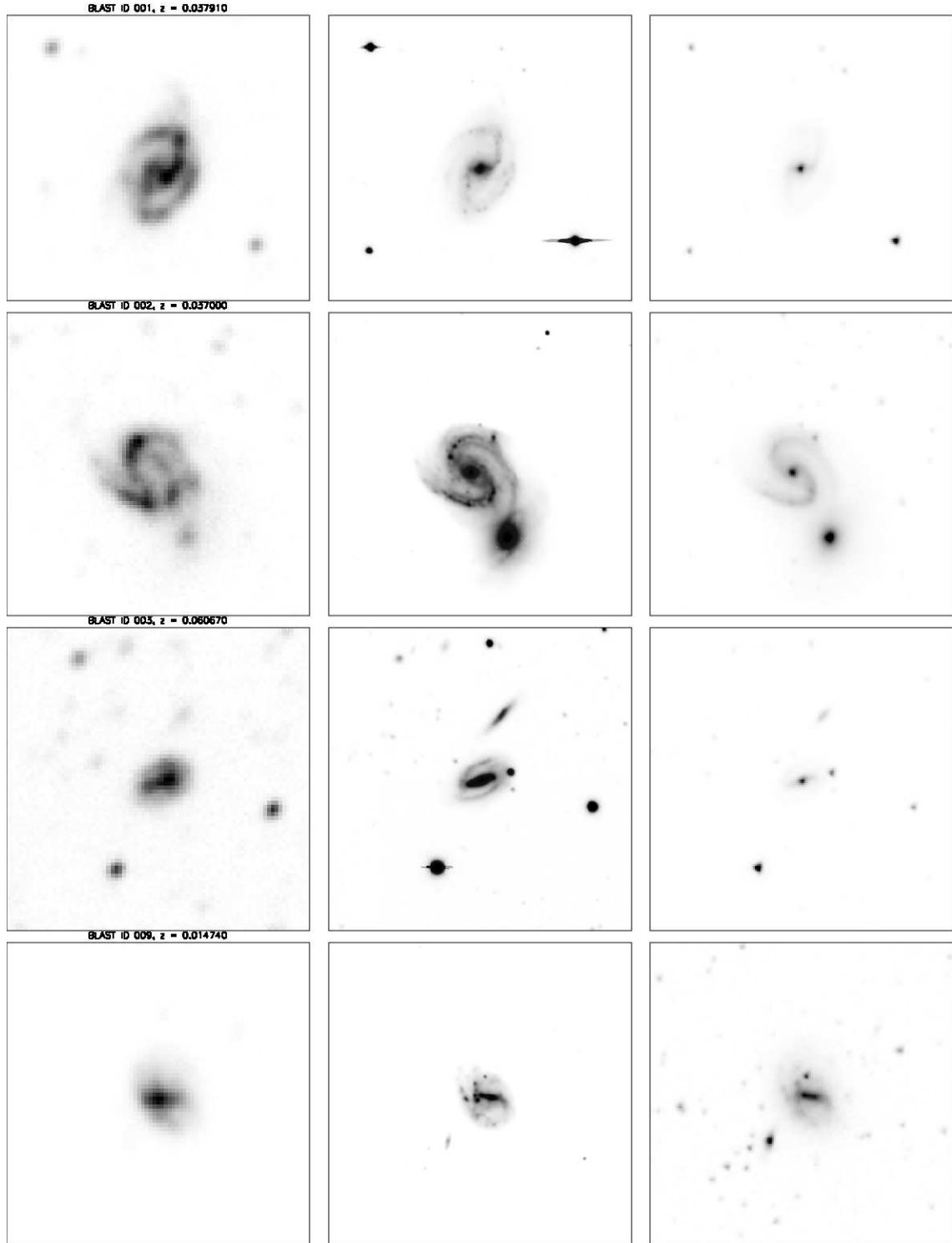


Fig. B1 Postage-stamp images for a selection of low redshift BLAST IDs. The images are all $2' \times 2'$ in size. Every row shows a BLAST source, imaged at three different bands: *left*, GALEX NUV filter (centered at 2315 \AA); *center*, RGB combination of the Ugr filters from the SWIRE optical survey; *right*, $3.6 \mu\text{m}$ IRAC band. The complete set of full-color cut-outs can be found at http://blastexperiment.info/results_images/moncelsi/

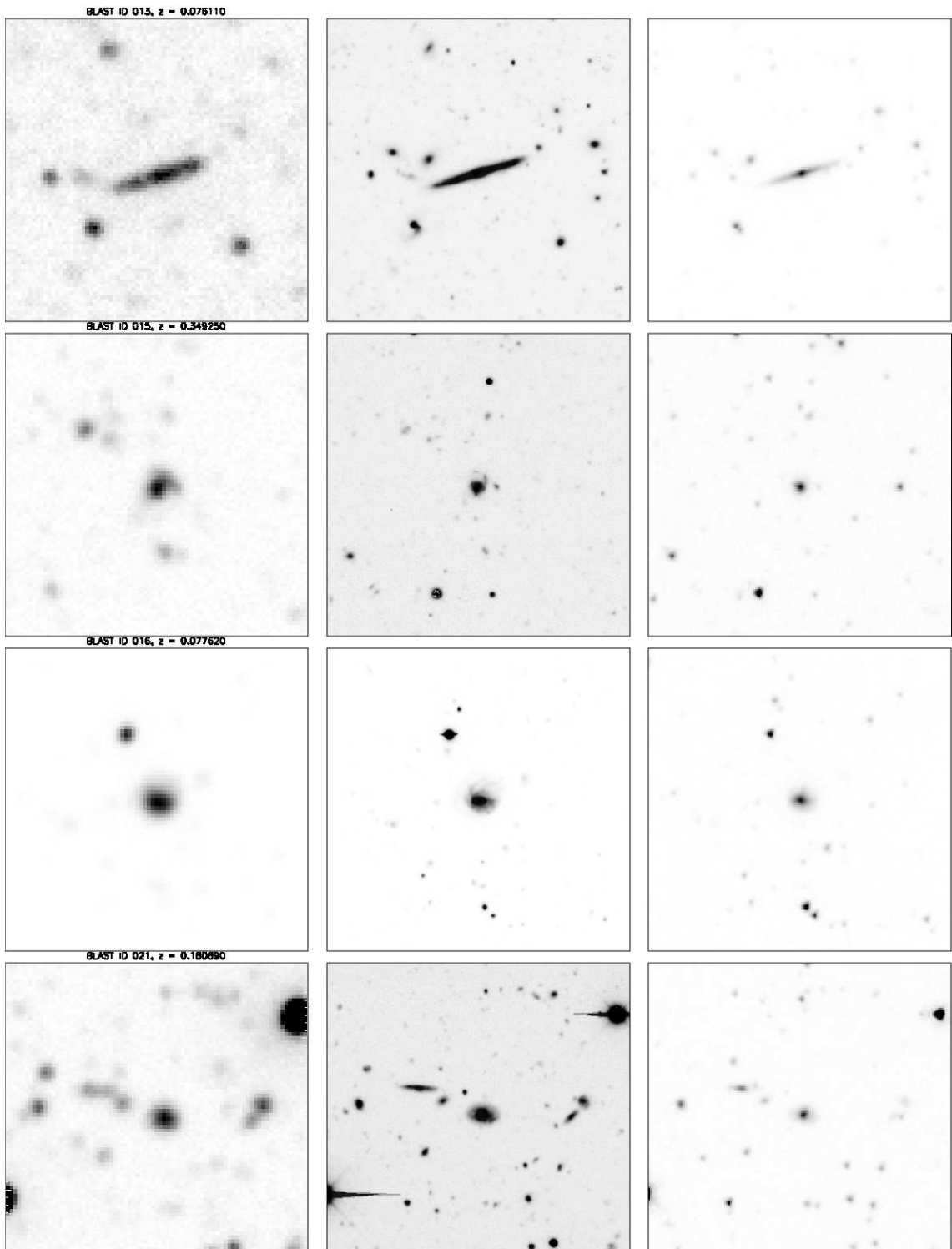


Fig. B1 continued.

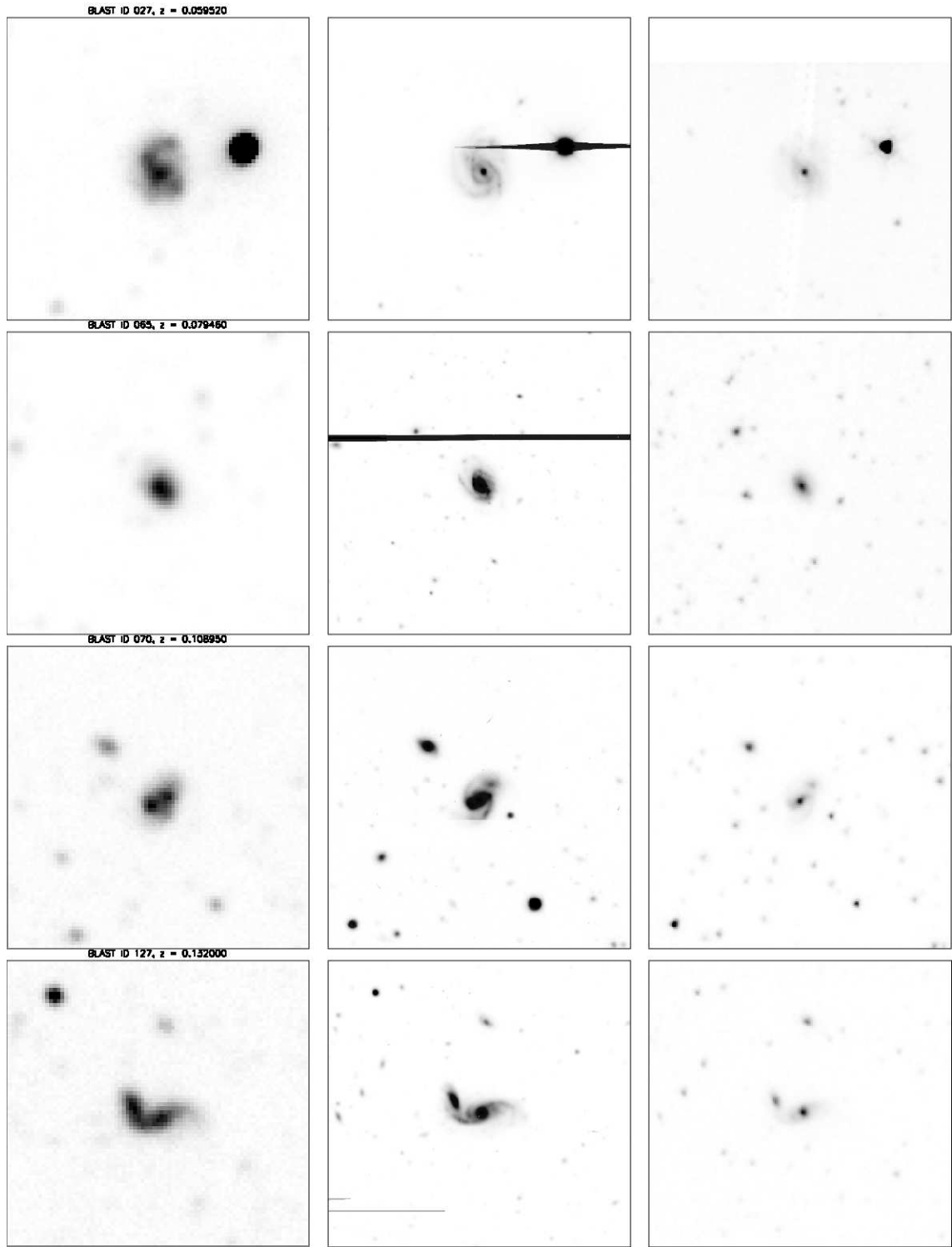


Fig. B1 continued.

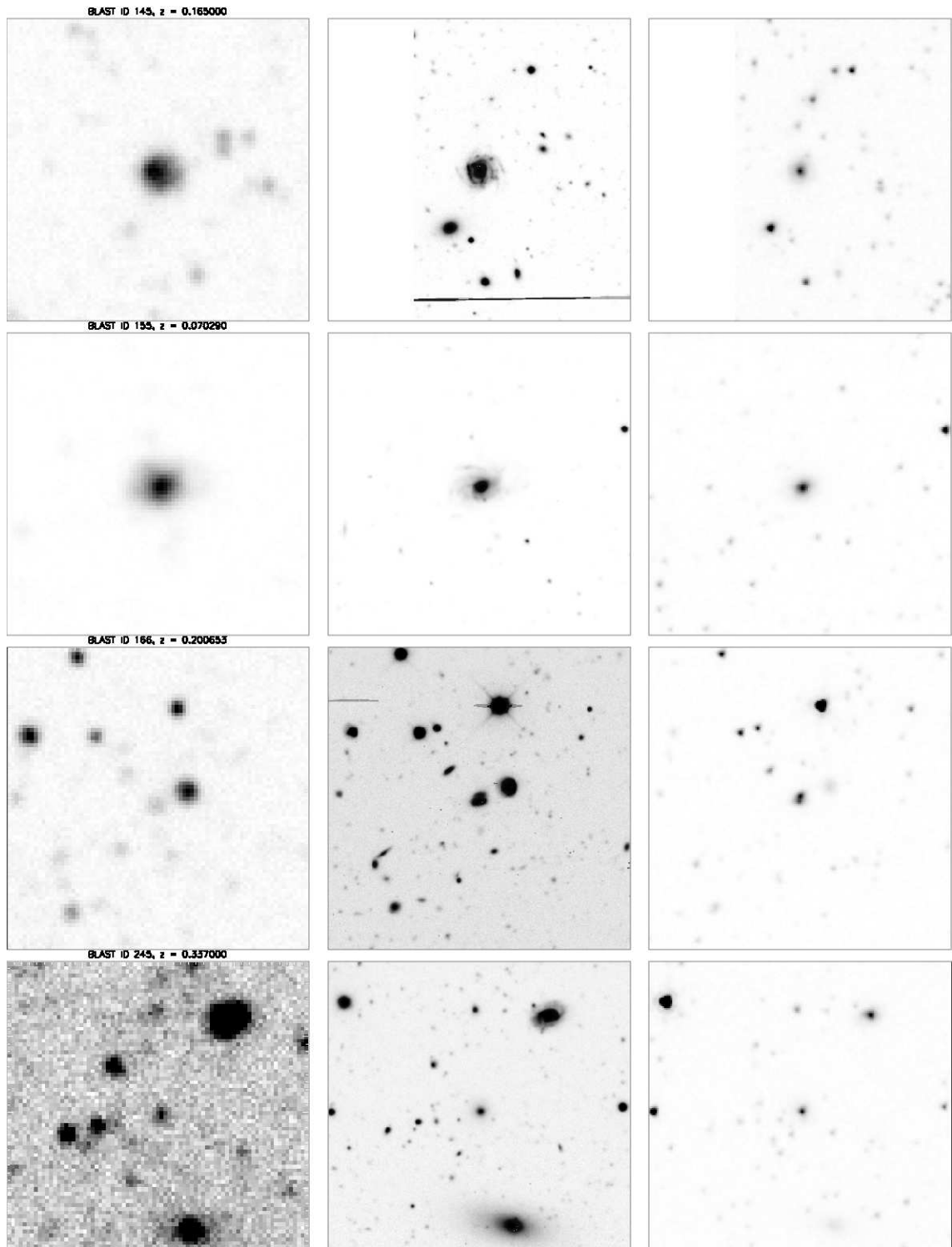


Fig. B1 continued.

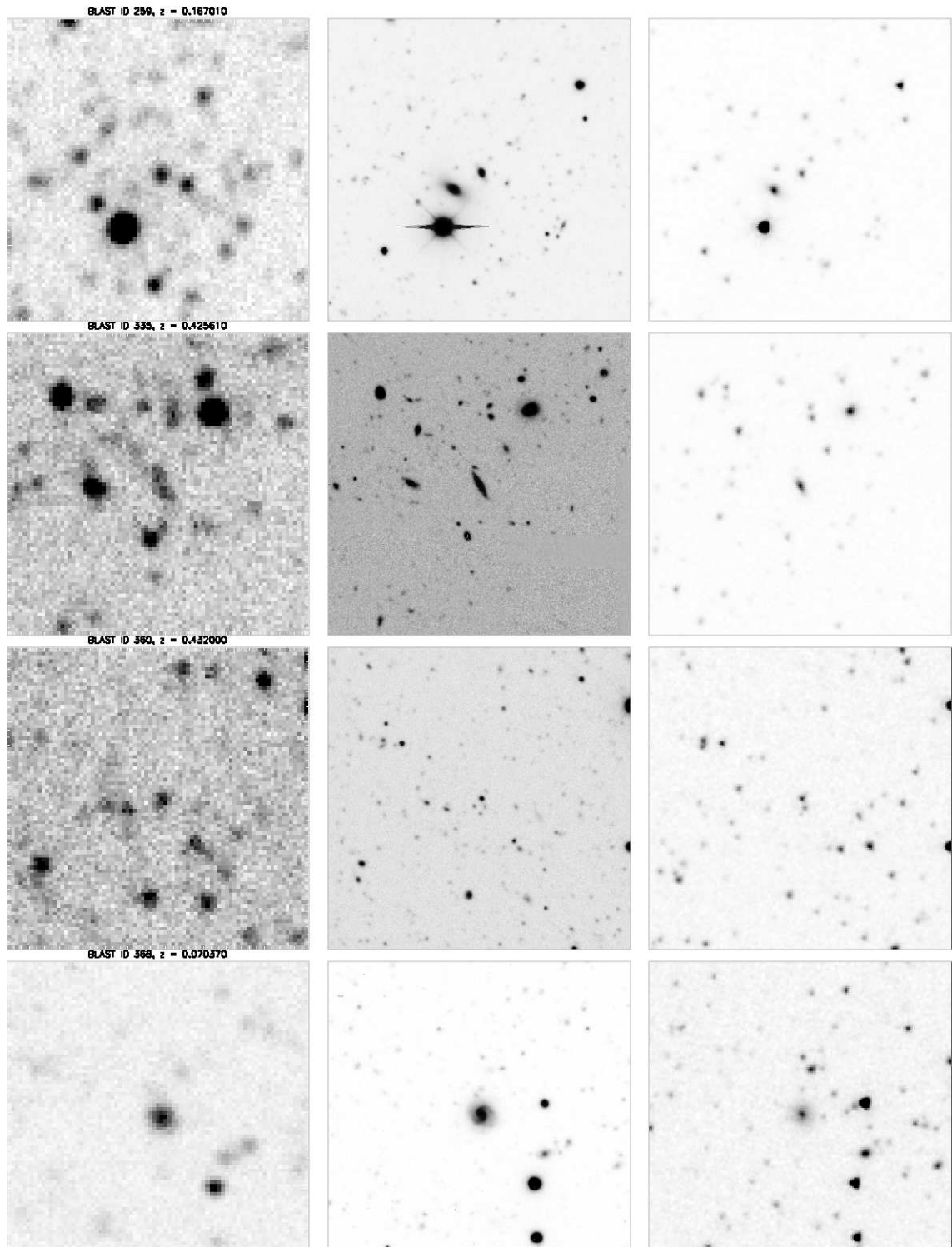


Fig. B1 continued.

C. CATALOGS OF BLAST COUNTERPARTS

We present here the catalogs of the primary counterparts to $\geq 5\sigma$ BLAST sources. Table C1 contains the redshifts, the spectral information and the morphology while Table C2 lists the UV and FIR properties.

Table C1 (continued)

| ID | BLAST Name | α_{BLAST} | δ_{BLAST} | Deep | z | Flag spec- z | Provenance | H α EW $_{\text{rf}}$ | [N II]/H α | AGN flag | Q flag | Morphology |
|----|----------------------|-------------------------|-------------------------|------|----------|----------------|------------------|------------------------------|-------------------|-------------------------|--------|------------|
| 61 | BLAST J033148–280424 | 52.952355 | –28.076205 | 1 | ... | ... | ... | ... | ... | ... | ... | ... |
| 62 | BLAST J033119–275822 | 52.83376 | –27.97194 | 1 | 0.898 | 0 | COMBO17 | ... | ... | ... | ... | BC |
| 63 | BLAST J033316–275045 | 53.318815 | –27.844285 | 1 | 0.0874 | 1 | AAO | 14.9 \pm 3.1 | 0.51 | ... | ... | S |
| 64 | BLAST J033240–280310 | 53.16542 | –28.05305 | 1 | ... | ... | ... | ... | ... | ... | ... | ... |
| 65 | BLAST J033018–275500 | 52.57593 | –27.91682 | 1 | 0.07946 | 1 | AAO | 9.9 \pm 2.3 | 0.42 | ... | ... | S |
| 66 | BLAST J033205–274648 | 53.020375 | –27.779815 | 1 | 2.019 | 0 | EAZY | ... | ... | ... | Q? | C |
| 68 | BLAST J033146–275732 | 52.944085 | –27.9597 | 1 | 0.3645 | 1 | AAO | ... | ... | ... | ... | S |
| 69 | BLAST J033153–281036 | 52.97797 | –28.1766 | 1 | 0.21472 | 1 | AAO | 34.6 \pm 3.9 | 0.40 | ... | ... | S |
| 70 | BLAST J033111–284835 | 52.79579 | –28.80925 | 0 | 0.10895 | 1 | AAO | 1.5 \pm 2.5 | 1.60 | AGN | ... | S |
| 71 | BLAST J033140–272937 | 52.91928 | –27.493975 | 1 | 0.06728 | 1 | AAO | 5.5 \pm 1.9 | 0.60 | AGN (broad H α) | ... | S |
| 72 | BLAST J033120–273344 | 52.834745 | –27.56287 | 1 | 0.19504 | 1 | AAO | 15.1 \pm 4.8 | 0.50 | ... | ... | S |
| 73 | BLAST J033158–273519 | 52.99226 | –27.58947 | 1 | 2.034 | 0 | EAZY | ... | ... | ... | Q | C |
| 75 | BLAST J033115–273905 | 52.810675 | –27.651895 | 1 | 0.31183 | 1 | AAO | 7.6 \pm 4.3 | 0.44 | ... | ... | E |
| 76 | BLAST J033328–273949 | 53.37102 | –27.66589 | 1 | 0.808 | 0 | EAZY | ... | ... | ... | ... | ... |
| 77 | BLAST J033218–273138 | 53.07989 | –27.52747 | 1 | 0.22716 | 1 | AAO | 16.4 \pm 3.8 | 0.41 | ... | ... | S? |
| 78 | BLAST J033401–274759 | 53.50673 | –27.79859 | 1 | ... | ... | ... | ... | ... | ... | ... | ... |
| 80 | BLAST J033156–284241 | 52.99144 | –28.70857 | 0 | ... | ... | ... | ... | ... | AGN (NED) | Q? | C |
| 83 | BLAST J033633–284223 | 54.14349 | –28.70855 | 0 | 0.19754 | 1 | AAO | 26.1 \pm 3.9 | 0.41 | ... | ... | S |
| 84 | BLAST J033318–281436 | 53.329275 | –28.242505 | 1 | 0.10287 | 1 | AAO | 12.6 \pm 2.7 | 0.48 | ... | ... | S |
| 85 | BLAST J033153–274950 | 52.97289 | –27.83057 | 1 | 0.8409 | 1 | AAO | ... | ... | ... | ... | C? |
| 86 | BLAST J033447–283013 | 53.700025 | –28.502715 | 0 | 0.04139 | 1 | AAO | 28.0 \pm 2.1 | 0.47 | ... | ... | S |
| 87 | BLAST J032746–265801 | 51.94289 | –26.96452 | 0 | 0.043304 | 1 | NED ^a | ... | ... | ... | ... | S? |
| 88 | BLAST J033636–284115 | 54.15564 | –28.6873 | 0 | 0.06828 | 1 | AAO | 36.3 \pm 2.4 | 0.43 | ... | ... | S |
| 90 | BLAST J032818–274311 | 52.07546 | –27.719205 | 0 | 0.24845 | 1 | AAO | 4.8 \pm 9.0 | 1.38 | AGN | ... | S? |
| 92 | BLAST J033241–280557 | 53.1742 | –28.09777 | 1 | 0.29663 | 1 | AAO | 25.5 \pm 16.1 | 0.45 | ... | ... | S |
| 93 | BLAST J033408–273514 | 53.5334 | –27.59049 | 1 | ... | ... | ... | ... | ... | ... | ... | ... |
| 94 | BLAST J033351–274357 | 53.46998 | –27.72938 | 1 | 0.22496 | 1 | AAO | 14.7 \pm 3.2 | ... | ... | ... | ... |
| 95 | BLAST J033343–270918 | 53.4297 | –27.15331 | 0 | 0.0685 | 1 | AAO | 4.0 \pm 2.5 | 0.65 | AGN? | ... | S |

Table C1 (continued)

| ID | BLAST Name | α_{BLAST} | δ_{BLAST} | Deep | z | Flag spec- z | Provenance | $H\alpha$ EW _{rf} | [N II]/ $H\alpha$ | AGN flag | Q flag | Morphology |
|-----|----------------------|-------------------------|-------------------------|------|----------|----------------|------------------|----------------------------|-------------------|-----------|--------|------------|
| 96 | BLAST J033336–272854 | 53.40486 | –27.48539 | 1 | 0.14489 | 1 | AAO | 14.9 ± 9.4 | 0.49 | ... | ... | S |
| 97 | BLAST J033317–280220 | 53.317655 | –28.03985 | 1 | 0.34897 | 1 | AAO | ... | ... | ... | ... | S? |
| 98 | BLAST J033214–273053 | 53.0595 | –27.51728 | 1 | ... | ... | ... | ... | ... | ... | ... | ... |
| 99 | BLAST J033247–270716 | 53.19616 | –27.11917 | 0 | ... | ... | ... | ... | ... | ... | ... | ... |
| 100 | BLAST J033203–281015 | 53.01636 | –28.17114 | 1 | 1.432 | 0 | RR | ... | ... | ... | Q | C |
| 101 | BLAST J033127–281009 | 52.86677 | –28.16924 | 1 | ... | ... | ... | ... | ... | ... | Q? | C |
| 102 | BLAST J033124–275207 | 52.85381 | –27.868845 | 1 | 1.182 | 0 | RR | ... | ... | AGN (NED) | Q | C |
| 103 | BLAST J032707–270516 | 51.78465 | –27.09038 | 0 | ... | ... | ... | ... | ... | ... | ... | ... |
| 106 | BLAST J032704–280713 | 51.76851 | –28.12049 | 0 | 0.089978 | 1 | NED ^a | ... | ... | ... | ... | S |
| 109 | BLAST J033408–275415 | 53.53403 | –27.90217 | 1 | ... | ... | ... | ... | ... | ... | ... | S |
| 110 | BLAST J033217–275054 | 53.074425 | –27.849725 | 1 | 0.12275 | 1 | AAO | 7.9 ± 6.5 | 0.55 | ... | ... | S |
| 112 | BLAST J033241–273818 | 53.17499 | –27.63874 | 1 | 0.832 | 0 | COMBO17 | ... | ... | ... | ... | ... |
| 113 | BLAST J033347–273848 | 53.4544 | –27.64381 | 1 | ... | ... | ... | ... | ... | AGN (NED) | ... | ... |
| 115 | BLAST J033128–280508 | 52.86134 | –28.08199 | 1 | ... | ... | ... | ... | ... | ... | ... | S |
| 118 | BLAST J033238–273151 | 53.158495 | –27.53339 | 1 | ... | ... | ... | ... | ... | ... | ... | ... |
| 119 | BLAST J033606–272311 | 54.0313 | –27.38652 | 0 | ... | ... | ... | ... | ... | ... | Q | ... |
| 120 | BLAST J032703–282950 | 51.76878 | –28.49448 | 0 | ... | ... | ... | ... | ... | ... | ... | ... |
| 122 | BLAST J033025–275014 | 52.60716 | –27.83824 | 1 | 0.12152 | 1 | AAO | 35.4 ± 2.7 | 0.35 | ... | ... | S |
| 123 | BLAST J033112–265716 | 52.8017 | –26.95459 | 0 | ... | ... | ... | ... | ... | ... | ... | ... |
| 125 | BLAST J033229–273505 | 53.12247 | –27.58556 | 1 | 0.52 | 0 | EAZY | ... | ... | ... | ... | C |
| 126 | BLAST J033211–283251 | 53.05272 | –28.54705 | 0 | 0.69385 | 1 | AAO | ... | ... | ... | ... | S? |
| 127 | BLAST J033224–291707 | 53.10425 | –29.28513 | 0 | 0.132 | 0 | RR | ... | ... | ... | ... | IS |
| 128 | BLAST J033100–275310 | 52.75566 | –27.8887 | 1 | 0.959 | 0 | RR | ... | ... | ... | ... | RC |
| 129 | BLAST J033225–284148 | 53.11398 | –28.6995 | 0 | 0.17159 | 1 | AAO | 30.7 ± 3.7 | 0.47 | ... | ... | S |
| 130 | BLAST J033505–274027 | 53.76858 | –27.6737 | 0 | 0.472 | 0 | RR | ... | ... | ... | ... | C |
| 131 | BLAST J033200–273604 | 53.00352 | –27.59926 | 1 | 0.767 | 0 | EAZY | ... | ... | AGN (NED) | Q? | C |
| 132 | BLAST J033225–273818 | 53.104395 | –27.63964 | 1 | 0.772 | 0 | EAZY | ... | ... | ... | ... | RC |
| 134 | BLAST J032813–270453 | 52.05436 | –27.08062 | 0 | 0.037356 | 1 | NED ^b | ... | ... | ... | ... | S |

Table C1 (continued)

| ID | BLAST Name | α_{BLAST} | δ_{BLAST} | Deep | z | Flag spec- z | Provenance | H α EW $_{\text{rf}}$ | [N II]/H α | AGN flag | Q flag | Morphology |
|-----|----------------------|-------------------------|-------------------------|------|---------|----------------|------------|------------------------------|-------------------|----------|--------|------------|
| 280 | BLAST J033351–273306 | 53.46829 | –27.55235 | 1 | ... | ... | ... | ... | ... | ... | ... | ... |
| 288 | BLAST J033507–275242 | 53.78062 | –27.88157 | 0 | ... | ... | ... | ... | ... | ... | ... | ... |
| 289 | BLAST J033102–273948 | 52.75508 | –27.66077 | 1 | 0.24165 | 0 | RR | ... | ... | ... | ... | BC? |
| 294 | BLAST J033324–273432 | 53.354965 | –27.57337 | 1 | 0.504 | 0 | COMBO17 | ... | ... | ... | ... | ... |
| 302 | BLAST J033552–275511 | 53.97283 | –27.91971 | 0 | 1.884 | 0 | RR | ... | ... | ... | ... | ... |
| 303 | BLAST J033121–275803 | 52.84267 | –27.965485 | 1 | 0.52975 | 1 | AAO | ... | ... | ... | ... | E |
| 304 | BLAST J033231–280437 | 53.1321 | –28.07667 | 1 | ... | ... | ... | ... | ... | ... | ... | ... |
| 307 | BLAST J033210–270531 | 53.04573 | –27.09132 | 0 | ... | ... | ... | ... | ... | ... | ... | ... |
| 309 | BLAST J033113–273016 | 52.80434 | –27.50111 | 1 | ... | ... | ... | ... | ... | ... | Q | ... |
| 311 | BLAST J033017–283020 | 52.57364 | –28.50466 | 0 | 2.565 | 0 | RR | ... | ... | ... | ... | C? |
| 318 | BLAST J033210–280711 | 53.04041 | –28.12135 | 1 | 0.9805 | 1 | AAO | ... | ... | ... | ... | ... |
| 319 | BLAST J033036–273717 | 52.64954 | –27.62388 | 1 | ... | ... | ... | ... | ... | ... | ... | ... |
| 320 | BLAST J032656–291615 | 51.74249 | –29.27044 | 0 | ... | ... | ... | ... | ... | ... | Q | C |
| 322 | BLAST J033321–280333 | 53.34598 | –28.05703 | 1 | 1.1365 | 0 | EAZY | ... | ... | ... | ... | ... |
| 323 | BLAST J033557–283540 | 53.98524 | –28.59187 | 0 | 0.4388 | 0 | RR | ... | ... | ... | ... | IS? |
| 329 | BLAST J033332–281348 | 53.39012 | –28.23444 | 1 | 1.37631 | 1 | AAO | ... | ... | Quasar | Q | C |
| 332 | BLAST J033038–274738 | 52.66361 | –27.79376 | 1 | ... | ... | ... | ... | ... | ... | Q | C |
| 333 | BLAST J033649–275932 | 54.20814 | –27.99234 | 0 | 0.698 | 0 | RR | ... | ... | ... | ... | ... |
| 335 | BLAST J033611–290528 | 54.05066 | –29.08868 | 0 | 0.42561 | 0 | RR | ... | ... | ... | ... | S |
| 339 | BLAST J033018–285124 | 52.57649 | –28.85588 | 0 | 0.47231 | 0 | RR | ... | ... | ... | ... | S |
| 341 | BLAST J033445–275038 | 53.69046 | –27.84443 | 1 | ... | ... | ... | ... | ... | ... | ... | ... |
| 342 | BLAST J032745–292408 | 51.9383 | –29.39774 | 0 | ... | ... | ... | ... | ... | ... | ... | ... |
| 343 | BLAST J033430–273704 | 53.62629 | –27.61929 | 1 | ... | ... | ... | ... | ... | ... | ... | ... |
| 344 | BLAST J033239–280553 | 53.16118 | –28.09707 | 1 | ... | ... | ... | ... | ... | ... | ... | ... |
| 346 | BLAST J032702–281055 | 51.7626 | –28.18012 | 0 | ... | ... | ... | ... | ... | ... | ... | ... |
| 355 | BLAST J033117–272006 | 52.8241 | –27.33796 | 0 | 0.1064 | 1 | AAO | 15.1 \pm 5.0 | 0.37 | ... | ... | ... |
| 359 | BLAST J033545–272937 | 53.94254 | –27.49272 | 0 | ... | ... | ... | ... | ... | ... | ... | ... |
| 360 | BLAST J032735–285902 | 51.89937 | –28.98942 | 0 | 0.432 | 0 | RR | ... | ... | ... | Q | C |

Table C1 (continued)

| ID | BLAST Name | α_{BLAST} | δ_{BLAST} | Deep | z | Flag spec- z | Provenance | H α EW $_{\text{rf}}$ | [N II]/H α | AGN flag | Q flag | Morphology |
|-----|----------------------|-------------------------|-------------------------|------|---------|----------------|------------|------------------------------|-------------------|----------|--------|------------|
| 368 | BLAST J032957–290321 | 52.48499 | –29.05382 | 0 | 0.07037 | 1 | AAO | ... | ... | ... | ... | S |
| 369 | BLAST J033359–293715 | 53.49599 | –29.62169 | 0 | ... | ... | ... | ... | ... | ... | ... | S |
| 376 | BLAST J033031–264922 | 52.63121 | –26.82185 | 0 | ... | ... | ... | ... | ... | ... | ... | ... |

Note. — Reading from the left, the columns are: the BLAST identification number; the full IAU name of the BLAST source; the position of the counterpart (the arithmetic mean between the two sets of coordinates if both the radio and 24 μm counterparts are present); flag indicating whether the source is located within BGS-Deep; the redshift; flag indicating whether the redshift is spectroscopic or photometric; the provenance of the redshift (see Section 2.2.6 for details); the H α rest-frame equivalent width (EW $_{\text{rf}}$) from AAOmega spectra, in \AA , with uncertainty; the ratio of the flux in the [N II] 658.3 line to the flux in the H α line, from AAOmega spectra; column assessing the presence of an AGN in the host galaxy, based on line ratios ([N II]/H α > 0.6, Kauffmann et al. 2003, Miller et al. 2003), or of a quasar, based solely on the broadness of the lines (we also indicate with “NED” objects flagged as AGN in NED); column assessing whether the objects is a quasar (Q), based solely on optical and mid-IR (IRAC) colors (see Section 2.6 for details); morphological classification: S=spiral, IS = interacting system, E = elliptical, C = compact, RC = red compact, BC = blue compact (see Section 2.7 for details).

^aColless et al. (2003)

^bRatcliffe et al. (1998)

^cRavikumar et al. (2007)

Table C2 (continued)

| ID | GALEX Name | α_{GALEX} | δ_{GALEX} | FUV | NUV | E(B - V) | SFR _{FUV} | SFR _{NUV} | L_{FIR} | M_{\star} |
|----|------------------------|------------------|------------------|--------------|----------------|----------|--------------------|--------------------|--|----------------|
| 31 | GALEX J033414.4-274221 | 53.560362 | -27.706052 | 21.78 ± 0.12 | 20.954 ± 0.068 | 0.00844 | 0.23 ± 0.03 | 0.53 ± 0.03 | 3.33 ^{+0.65} _{-0.58} | ... |
| 32 | GALEX J033332.1-272917 | 53.383843 | -27.488205 | 21.15 ± 0.12 | 20.51 ± 0.068 | 0.0083 | 0.83 ± 0.09 | 1.57 ± 0.1 | 5.22 ^{+1.29} _{-0.93} | ... |
| 34 | GALEX J033149.6-274325 | 52.956886 | -27.723754 | ... | 22.887 ± 0.083 | 0.00904 | ... | 3.48 ± 0.27 | 46.3 ^{+46.1} _{-10.4} | 15.243 ± 2.493 |
| 35 | ... | ... | ... | ... | ... | ... | ... | ... | 1229 ⁺⁵⁹⁹ ₋₄₃₆ | 4.604 ± 0.784 |
| 36 | ... | ... | ... | ... | ... | ... | ... | ... | 1344 ⁺³⁶⁵ ₋₆₇₀ | 12.073 ± 2.149 |
| 37 | ... | ... | ... | ... | ... | ... | ... | ... | ... | ... |
| 38 | GALEX J033215.7-280348 | 53.065624 | -28.063464 | ... | 23.01 ± 0.1 | 0.00764 | ... | 2.11 ± 0.19 | 59.2 ^{+8.1} _{-29.8} | 21.382 ± 3.922 |
| 39 | ... | ... | ... | ... | ... | ... | ... | ... | ... | ... |
| 40 | GALEX J032821.0-292631 | 52.087587 | -29.442053 | 19.67 ± 0.12 | 19.146 ± 0.067 | 0.00854 | 0.78 ± 0.09 | 1.37 ± 0.08 | 4.34 ^{+0.92} _{-0.31} | ... |
| 41 | GALEX J033430.6-271914 | 53.627691 | -27.320708 | 22.18 ± 0.13 | 20.743 ± 0.069 | 0.01122 | 0.16 ± 0.02 | 0.66 ± 0.04 | 14.6 ^{+1.2} _{-1.1} | ... |
| 42 | ... | ... | ... | ... | ... | ... | ... | ... | ... | ... |
| 43 | GALEX J033309.7-274800 | 53.290632 | -27.800154 | 22.38 ± 0.12 | 21.741 ± 0.07 | 0.00814 | 0.43 ± 0.05 | 0.79 ± 0.05 | 7.78 ^{+0.73} _{-3.28} | ... |
| 44 | GALEX J033131.2-273236 | 52.879954 | -27.543585 | ... | 23.862 ± 0.105 | 0.00871 | ... | ... | ... | ... |
| 45 | GALEX J033150.9-281120 | 52.96221 | -28.18901 | 21.02 ± 0.12 | 20.68 ± 0.068 | 0.00938 | 2.17 ± 0.24 | 2.97 ± 0.19 | 8.89 ^{+2.67} _{-1.89} | 11.915 ± 1.891 |
| 46 | GALEX J033110.5-265740 | 52.79395 | -26.961304 | 18.9 ± 0.12 | 18.524 ± 0.067 | 0.00774 | ... | ... | ... | ... |
| 47 | GALEX J033110.8-275552 | 52.795045 | -27.931179 | 22.53 ± 0.12 | 21.851 ± 0.07 | 0.0086 | ... | ... | ... | ... |
| 48 | GALEX J033055.6-275501 | 52.732045 | -27.917032 | ... | 21.0 ± 0.068 | 0.0090 | ... | ... | ... | ... |
| 49 | GALEX J033032.8-273539 | 52.636808 | -27.594438 | 21.19 ± 0.12 | 20.536 ± 0.069 | 0.00936 | 0.43 ± 0.05 | 0.84 ± 0.05 | 4.63 ^{+0.57} _{-0.77} | 4.769 ± 0.916 |
| 50 | ... | ... | ... | ... | ... | ... | ... | ... | 70.1 ^{+7.3} _{-6.3} | 34.049 ± 6.752 |
| 51 | GALEX J033046.2-275518 | 52.692639 | -27.921688 | 25.13 ± 0.32 | 23.015 ± 0.105 | 0.0090 | 0.49 ± 0.15 | 2.17 ± 0.21 | 212 ⁺¹² ₋₄₁ | ... ± ... |
| 52 | ... | ... | ... | ... | ... | ... | ... | ... | 86.6 ^{+13.3} _{-29.6} | 6.812 ± 1.202 |
| 53 | GALEX J033419.6-265318 | 53.581519 | -26.888353 | 19.08 ± 0.12 | 18.701 ± 0.067 | 0.00995 | ... | ... | ... | ... |
| 54 | ... | ... | ... | ... | ... | ... | ... | ... | 195 ⁺⁷¹ ₋₁₁₄ | 2.177 ± 0.349 |
| 55 | GALEX J033130.0-275602 | 52.87525 | -27.933952 | 24.46 ± 0.19 | 22.243 ± 0.078 | 0.00828 | 137.04 ± 24.31 | 288.87 ± 20.78 | 106 ⁺⁵² ₋₂₇ | 20.026 ± 3.013 |
| 56 | GALEX J033034.4-274328 | 52.643648 | -27.72453 | ... | 24.576 ± 0.194 | 0.00846 | ... | ... | ... | ... |
| 57 | GALEX J033432.9-275148 | 53.637466 | -27.863358 | 23.54 ± 0.14 | 22.283 ± 0.076 | 0.00905 | ... | ... | ... | ... |
| 58 | ... | ... | ... | ... | ... | ... | ... | ... | ... | ... |
| 60 | GALEX J033422.1-275042 | 53.592338 | -27.845121 | ... | 22.939 ± 0.094 | 0.00871 | ... | ... | ... | ... |

Table C2 (continued)

| ID | GALEX Name | α_{GALEX} | δ_{GALEX} | FUV | NUV | E(B - V) | SFR _{FUV} | SFR _{NUV} | L_{FIR} | M_{\star} |
|----|------------------------|------------------|------------------|--------------|----------------|----------|--------------------|--------------------|--|----------------|
| 61 | ... | ... | ... | ... | ... | ... | ... | ... | ... | ... |
| 62 | GALEX J033120.1-275819 | 52.833759 | -27.971939 | ... | 24.442 ± 0.504 | 0.0080 | ... | 1.14 ± 0.53 | 176 ⁺⁶⁷ ₋₅₆ | ... |
| 63 | GALEX J033316.4-275039 | 53.318678 | -27.844186 | 21.93 ± 0.12 | 21.247 ± 0.069 | 0.00738 | 0.14 ± 0.02 | 0.29 ± 0.02 | 1.76 ^{+0.25} _{-0.55} | 3.845 ± 0.65 |
| 64 | ... | ... | ... | ... | ... | ... | ... | ... | ... | ... |
| 65 | GALEX J033018.2-275500 | 52.575918 | -27.916683 | 18.88 ± 0.12 | 18.508 ± 0.067 | 0.00827 | 1.96 ± 0.22 | 2.99 ± 0.18 | 2.40 ^{+0.26} _{-0.56} | 1.911 ± 0.381 |
| 66 | ... | ... | ... | ... | ... | ... | ... | ... | 835 ⁺²⁵⁶ ₋₄₃₂ | 15.543 ± 2.356 |
| 68 | GALEX J033146.6-275734 | 52.944236 | -27.959632 | 24.44 ± 0.19 | 22.748 ± 0.099 | 0.00818 | 0.31 ± 0.05 | 1.31 ± 0.12 | 46.9 ^{+7.4} _{-12.2} | 11.692 ± 1.66 |
| 69 | GALEX J033154.6-281035 | 52.977711 | -28.176491 | 22.74 ± 0.23 | 21.844 ± 0.12 | 0.00909 | 0.45 ± 0.1 | 1.03 ± 0.11 | 5.40 ^{+4.82} _{-1.83} | 4.392 ± 0.85 |
| 70 | GALEX J033110.9-284832 | 52.795552 | -28.80897 | 19.06 ± 0.12 | 18.7 ± 0.067 | 0.01024 | 3.21 ± 0.36 | 4.79 ± 0.3 | 6.51 ^{+0.13} _{-1.44} | 10.717 ± 2.23 |
| 71 | GALEX J033140.6-272938 | 52.919358 | -27.494078 | 21.62 ± 0.12 | 20.574 ± 0.068 | 0.00888 | 0.11 ± 0.01 | 0.32 ± 0.02 | 1.22 ^{+0.39} _{-0.22} | ... |
| 72 | GALEX J033120.3-273346 | 52.834738 | -27.562779 | 21.31 ± 0.12 | 20.713 ± 0.069 | 0.00973 | 1.37 ± 0.16 | 2.41 ± 0.15 | 5.50 ^{+2.60} _{-1.44} | 8.098 ± 1.493 |
| 73 | ... | ... | ... | ... | ... | ... | ... | ... | 497 ⁺⁵⁷³ ₋₂₀₄ | 11.63 ± 1.93 |
| 75 | GALEX J033114.5-273906 | 52.810475 | -27.651857 | 22.46 ± 0.12 | 21.119 ± 0.07 | 0.00914 | 1.32 ± 0.15 | 4.31 ± 0.28 | 10.1 ^{+7.2} _{-3.0} | 38.27 ± 7.201 |
| 76 | ... | ... | ... | ... | ... | ... | ... | ... | 66.5 ^{+59.3} _{-24.3} | 8.598 ± 1.161 |
| 77 | GALEX J033219.1-273138 | 53.079817 | -27.527321 | 21.62 ± 0.12 | 21.032 ± 0.068 | 0.00952 | 1.44 ± 0.16 | 2.45 ± 0.15 | 6.11 ^{+2.90} _{-3.01} | 12.134 ± 2.735 |
| 78 | GALEX J033401.5-274754 | 53.506405 | -27.798424 | ... | 23.327 ± 0.504 | 0.00754 | ... | ... | ... | ... |
| 80 | ... | ... | ... | ... | ... | ... | ... | ... | ... | ... |
| 83 | GALEX J033634.3-284230 | 54.143208 | -28.708474 | 21.53 ± 0.12 | 20.353 ± 0.07 | 0.01355 | 1.18 ± 0.13 | 3.55 ± 0.23 | 28.2 ^{+0.6} _{-5.7} | 10.255 ± 2.071 |
| 84 | GALEX J033318.9-281434 | 53.329027 | -28.242794 | 21.3 ± 0.12 | 20.741 ± 0.069 | 0.00852 | 0.36 ± 0.04 | 0.64 ± 0.04 | 3.82 ^{+0.23} _{-1.06} | 6.028 ± 1.128 |
| 85 | GALEX J033153.4-274950 | 52.972841 | -27.830587 | ... | 23.772 ± 0.102 | 0.00798 | ... | 2.17 ± 0.2 | 105 ⁺³¹ ₋₅₈ | ... |
| 86 | GALEX J033447.9-283009 | 53.699655 | -28.502527 | 19.8 ± 0.12 | 19.295 ± 0.068 | 0.00847 | 0.23 ± 0.03 | 0.39 ± 0.02 | 0.98 ^{+0.20} _{-0.08} | 0.815 ± 0.129 |
| 87 | GALEX J032746.7-265745 | 51.944804 | -26.962548 | 19.37 ± 0.12 | 19.027 ± 0.067 | 0.01328 | ... | ... | 1.16 ^{+0.03} _{-0.25} | ... |
| 88 | GALEX J033637.3-284112 | 54.155408 | -28.686825 | 19.89 ± 0.12 | 19.342 ± 0.068 | 0.01355 | 0.59 ± 0.07 | 1.06 ± 0.07 | 3.79 ^{+0.52} _{-0.19} | ... |
| 90 | GALEX J032818.0-274307 | 52.07511 | -27.718748 | 22.99 ± 0.16 | 21.647 ± 0.073 | 0.01206 | 0.51 ± 0.07 | 1.7 ± 0.12 | 60.0 ^{+5.4} _{-6.9} | ... |
| 92 | GALEX J033241.8-280550 | 53.17437 | -28.097491 | 23.45 ± 0.14 | 22.624 ± 0.079 | 0.00717 | 0.47 ± 0.06 | 0.96 ± 0.07 | 6.51 ^{+8.38} _{-1.36} | 3.142 ± 0.674 |
| 93 | ... | ... | ... | ... | ... | ... | ... | ... | ... | ... |
| 94 | GALEX J033352.8-274347 | 53.470297 | -27.729779 | 22.21 ± 0.12 | 21.255 ± 0.069 | 0.0071 | 0.8 ± 0.09 | 1.92 ± 0.12 | 4.89 ^{+4.45} _{-1.38} | ... |
| 95 | GALEX J033343.0-270910 | 53.429287 | -27.153012 | 20.0 ± 0.12 | 19.456 ± 0.067 | 0.01134 | 0.53 ± 0.06 | 0.95 ± 0.06 | 3.33 ^{+0.47} _{-0.23} | ... |

Table C2 (continued)

| ID | GALEX Name | α_{GALEX} | δ_{GALEX} | FUV | NUV | E(B - V) | SFR _{FUV} | SFR _{NUV} | L_{FIR} | M_{\star} |
|-----|------------------------|------------------|------------------|--------------|----------------|----------|--------------------|--------------------|---|-----------------|
| 96 | GALEX J033337.1-272906 | 53.404714 | -27.485016 | 21.35 ± 0.12 | 20.749 ± 0.068 | 0.00896 | 0.69 ± 0.08 | 1.27 ± 0.08 | 4.40 ^{+1.42} _{-1.04} | ... |
| 97 | GALEX J033316.2-280223 | 53.317712 | -28.039773 | 23.1 ± 0.13 | 22.024 ± 0.072 | 0.00675 | 0.93 ± 0.11 | 2.32 ± 0.15 | 6.97 ^{+5.74} _{-2.85} | ... |
| 98 | GALEX J033214.3-273102 | 53.059692 | -27.517126 | 22.98 ± 0.15 | 22.574 ± 0.091 | 0.00924 | ... | ... | ... | ... |
| 99 | GALEX J033247.0-270708 | 53.195852 | -27.11912 | 19.86 ± 0.12 | 19.29 ± 0.067 | 0.00891 | ... | ... | ... | ... |
| 100 | GALEX J033203.8-281015 | 53.016063 | -28.17096 | ... | 23.483 ± 0.094 | 0.00843 | ... | 25.3 ± 2.19 | 337 ⁺²⁶² ₋₉₄ | 31.822 ± 14.775 |
| 101 | ... | ... | ... | ... | ... | ... | ... | ... | ... | ... |
| 102 | GALEX J033125.1-275211 | 52.85488 | -27.869679 | 23.83 ± 0.13 | 22.265 ± 0.073 | 0.00772 | 48.93 ± 6.04 | 32.23 ± 2.16 | 378 ⁺⁵⁰ ₋₁₉₇ | 19.499 ± 2.896 |
| 103 | GALEX J032708.3-270524 | 51.784617 | -27.090199 | 20.55 ± 0.12 | 19.824 ± 0.068 | 0.01335 | ... | ... | ... | ... |
| 106 | GALEX J032704.4-280713 | 51.768423 | -28.120328 | 23.8 ± 0.19 | 22.645 ± 0.099 | 0.00944 | ... | ... | 2.15 ^{+0.45} _{-0.70} | ... |
| 109 | GALEX J033408.0-275407 | 53.533691 | -27.902007 | 21.4 ± 0.12 | 20.924 ± 0.068 | 0.00744 | ... | ... | ... | ... |
| 110 | GALEX J033217.7-275058 | 53.07384 | -27.84969 | 23.95 ± 0.17 | 23.043 ± 0.097 | 0.00776 | 0.04 ± 0.01 | 0.11 ± 0.01 | 1.78 ^{+0.94} _{-0.66} | 2.402 ± 0.384 |
| 112 | ... | ... | ... | ... | ... | ... | ... | ... | 106 ⁺⁷⁹ ₋₅₃ | 0.402 ± 0.183 |
| 113 | GALEX J033349.0-273843 | 53.454251 | -27.645331 | ... | 22.678 ± 0.088 | 0.00802 | ... | ... | ... | ... |
| 115 | ... | ... | ... | ... | ... | ... | ... | ... | ... | ... |
| 118 | ... | ... | ... | ... | ... | ... | ... | ... | ... | ... |
| 119 | ... | ... | ... | ... | ... | ... | ... | ... | ... | ... |
| 120 | ... | ... | ... | ... | ... | ... | ... | ... | ... | ... |
| 122 | GALEX J033025.7-275017 | 52.607255 | -27.838082 | 20.98 ± 0.12 | 20.351 ± 0.067 | 0.00826 | 0.68 ± 0.08 | 1.28 ± 0.08 | 3.60 ^{+0.97} _{-0.95} | 3.238 ± 0.628 |
| 123 | ... | ... | ... | ... | ... | ... | ... | ... | ... | ... |
| 125 | ... | ... | ... | ... | ... | ... | ... | ... | 30.3 ^{+14.5} _{-12.7} | 1.672 ± 0.598 |
| 126 | GALEX J033212.5-283248 | 53.052314 | -28.546836 | 23.26 ± 0.18 | 22.781 ± 0.1 | 0.0082 | 10.69 ± 1.82 | 4.83 ± 0.45 | 53.0 ^{+25.0} _{-29.6} | 10.32 ± 3.849 |
| 127 | GALEX J033225.7-291709 | 53.107192 | -29.285858 | 19.14 ± 0.12 | 18.734 ± 0.067 | 0.00979 | 4.43 ± 0.49 | 6.8 ± 0.42 | 7.06 ^{+1.07} _{-1.46} | 8.745 ± 1.719 |
| 128 | ... | ... | ... | ... | ... | ... | ... | ... | 58.5 ^{+120.5} _{-56.2} | 48.841 ± 9.912 |
| 129 | GALEX J033227.3-284157 | 53.113772 | -28.699345 | 22.89 ± 0.14 | 21.648 ± 0.072 | 0.00999 | 0.24 ± 0.03 | 0.79 ± 0.05 | 8.86 ^{+1.87} _{-1.67} | 4.049 ± 0.806 |
| 130 | ... | ... | ... | ... | ... | ... | ... | ... | 20.6 ^{+20.3} _{-3.0} | 5.854 ± 1.023 |
| 131 | ... | ... | ... | ... | ... | ... | ... | ... | 28.0 ^{+71.3} _{-19.5} | 9.677 ± 1.357 |
| 132 | ... | ... | ... | ... | ... | ... | ... | ... | 84.0 ^{+33.1} _{-52.5} | 3.939 ± 0.763 |
| 134 | GALEX J032813.0-270449 | 52.054388 | -27.080549 | 18.37 ± 0.12 | 18.001 ± 0.067 | 0.01253 | ... | ... | 0.86 ^{+0.10} _{-0.11} | ... |

Table C2 (continued)

| ID | GALEX Name | α_{GALEX} | δ_{GALEX} | FUV | NUV | E(B - V) | SFR _{FUV} | SFR _{NUV} | L_{FIR} | M_* |
|-----|------------------------|------------------|------------------|--------------|----------------|----------|--------------------|--------------------|--|-----------------|
| 135 | GALEX J033133.9-282403 | 52.891282 | -28.400861 | 23.29 ± 0.14 | 22.015 ± 0.07 | 0.0087 | 0.48 ± 0.06 | 1.5 ± 0.1 | 24.3 ^{+5.6} _{-6.3} | 6.369 ± 1.671 |
| 136 | GALEX J033228.5-273536 | 53.11883 | -27.593592 | 25.92 ± 0.3 | 23.828 ± 0.121 | 0.0097 | 0.89 ± 0.24 | 1.82 ± 0.2 | 15.4 ^{+11.2} _{-2.9} | 37.782 ± 12.281 |
| 137 | GALEX J032821.5-280811 | 52.089837 | -28.136439 | 20.49 ± 0.12 | 19.866 ± 0.068 | 0.00842 | 3.69 ± 0.41 | 6.55 ± 0.41 | 22.4 ^{+2.9} _{-4.5} | ... |
| 138 | GALEX J033348.9-275014 | 53.453949 | -27.837456 | ... | 25.064 ± 0.252 | 0.00622 | ... | ... | ... | ... |
| 139 | ... | ... | ... | ... | ... | ... | ... | ... | 59.3 ^{+7.7} _{-4.2} | ... |
| 140 | ... | ... | ... | ... | ... | ... | ... | ... | ... | ... |
| 143 | GALEX J033147.9-281007 | 52.949911 | -28.168868 | 24.71 ± 0.24 | 21.189 ± 0.07 | 0.00939 | 0.2 ± 0.04 | 4.75 ± 0.31 | 41.1 ^{+12.0} _{-13.5} | 16.095 ± 3.185 |
| 145 | GALEX J033211.1-275858 | 53.046532 | -27.982875 | 20.08 ± 0.12 | 19.678 ± 0.067 | 0.00852 | 7.45 ± 0.83 | 10.53 ± 0.65 | 2.80 ^{+1.92} _{-0.76} | 11.444 ± 1.915 |
| 146 | GALEX J033000.4-275346 | 52.501809 | -27.896302 | 21.02 ± 0.12 | 20.379 ± 0.068 | 0.00844 | 0.91 ± 0.1 | 1.74 ± 0.11 | 4.90 ^{+1.64} _{-0.79} | 13.495 ± 2.621 |
| 147 | ... | ... | ... | ... | ... | ... | ... | ... | ... | ... |
| 148 | ... | ... | ... | ... | ... | ... | ... | ... | ... | ... |
| 149 | ... | ... | ... | ... | ... | ... | ... | ... | 10.3 ^{+3.8} _{-1.1} | 6.664 ± 1.246 |
| 152 | GALEX J033649.0-271938 | 54.204385 | -27.327469 | 22.28 ± 0.13 | 21.756 ± 0.078 | 0.01227 | 0.31 ± 0.04 | 0.52 ± 0.04 | 11.8 ^{+0.8} _{-2.9} | ... |
| 153 | ... | ... | ... | ... | ... | ... | ... | ... | ... | ... |
| 154 | GALEX J033541.2-285521 | 53.921886 | -28.922714 | 20.12 ± 0.12 | 19.681 ± 0.068 | 0.00957 | 1.53 ± 0.17 | 2.44 ± 0.15 | 4.65 ^{+0.33} _{-1.50} | 2.386 ± 0.537 |
| 155 | GALEX J032929.4-284218 | 52.372851 | -28.705028 | 18.09 ± 0.12 | 17.747 ± 0.067 | 0.01159 | 3.26 ± 0.36 | 4.83 ± 0.3 | 3.30 ^{+0.47} _{-0.45} | 1.821 ± 0.392 |
| 157 | GALEX J033609.1-280944 | 54.037984 | -28.162246 | 23.24 ± 0.19 | 21.793 ± 0.094 | 0.01055 | 0.67 ± 0.12 | 2.4 ± 0.21 | 51.6 ^{+6.4} _{-10.8} | 18.643 ± 3.62 |
| 158 | GALEX J033307.3-281409 | 53.280691 | -28.235987 | 19.82 ± 0.12 | 19.343 ± 0.067 | 0.00824 | 0.19 ± 0.02 | 0.32 ± 0.02 | 0.30 ^{+0.09} _{-0.07} | 0.389 ± 0.081 |
| 160 | GALEX J032843.6-274409 | 52.182047 | -27.735859 | 22.57 ± 0.13 | 21.426 ± 0.07 | 0.00847 | ... | ... | ... | ... |
| 162 | ... | ... | ... | ... | ... | ... | ... | ... | 37.7 ^{+68.2} _{-39.8} | 3.452 ± 0.616 |
| 163 | GALEX J033114.1-273411 | 52.809126 | -27.569857 | 23.38 ± 0.13 | 21.643 ± 0.073 | 0.00979 | 2.63 ± 0.33 | 7.99 ± 0.54 | 29.7 ^{+20.2} _{-11.2} | 8.753 ± 1.525 |
| 165 | GALEX J033605.9-293413 | 54.024817 | -29.570388 | 22.86 ± 0.16 | 21.547 ± 0.102 | 0.01119 | 0.78 ± 0.12 | 2.51 ± 0.23 | 20.2 ^{+20.4} _{-3.8} | 14.919 ± 2.152 |
| 166 | GALEX J033055.0-293426 | 52.729487 | -29.574 | 23.39 ± 0.15 | 22.279 ± 0.075 | 0.01019 | 0.39 ± 0.06 | 1.07 ± 0.07 | 20.5 ^{+3.3} _{-1.9} | 11.484 ± 2.099 |
| 167 | GALEX J033247.9-274232 | 53.199576 | -27.709084 | ... | 23.291 ± 0.093 | 0.00866 | ... | 6.65 ± 0.57 | 76.6 ^{+86.0} _{-60.1} | ... |
| 168 | GALEX J033111.4-275257 | 52.797751 | -27.882512 | 21.24 ± 0.12 | 20.616 ± 0.068 | 0.00836 | 220.07 ± 24.58 | 60.6 ± 3.79 | 18.5 ^{+30.1} _{-9.1} | 5.826 ± 1.729 |
| 169 | ... | ... | ... | ... | ... | ... | ... | ... | 190 ⁺²⁴³ ₋₈₉ | 58.348 ± 8.475 |
| 170 | GALEX J033038.4-275748 | 52.660132 | -27.963382 | 25.29 ± 0.24 | 23.346 ± 0.09 | 0.00808 | 0.12 ± 0.03 | 0.64 ± 0.05 | 14.0 ^{+3.5} _{-9.3} | 4.535 ± 0.814 |
| 173 | GALEX J033131.7-281304 | 52.882415 | -28.21781 | ... | 23.887 ± 0.145 | 0.00964 | ... | ... | ... | ... |

Table C2 (continued)

| ID | GALEX Name | α_{GALEX} | δ_{GALEX} | FUV | NUV | $E(B - V)$ | SFR_{FUV} | SFR_{NUV} | L_{FIR} | M_{\star} |
|-----|------------------------|------------------|------------------|------------------|--------------------|------------|-----------------|------------------|-------------------------|---------------------|
| 280 | GALEX J033352.3-273313 | 53.468291 | -27.553668 | ... | 23.359 ± 0.101 | 0.00898 | ... | ... | ... | ... |
| 288 | ... | ... | ... | ... | ... | ... | ... | ... | ... | ... |
| 289 | GALEX J033101.4-273934 | 52.756057 | -27.659615 | ... | 23.94 ± 0.138 | 0.00861 | ... | 0.22 ± 0.03 | $2.15^{+2.15}_{-1.57}$ | 0.034 ± 0.011 |
| 294 | GALEX J033325.1-273421 | 53.35491 | -27.572659 | 22.46 ± 0.12 | 21.921 ± 0.07 | 0.00693 | 4.91 ± 0.56 | 5.37 ± 0.35 | $4.78^{+20.84}_{-5.10}$ | 0.105 ± 0.038 |
| 302 | ... | ... | ... | ... | ... | ... | ... | ... | 278^{+758}_{-124} | 23.653 ± 3.354 |
| 303 | GALEX J033122.2-275755 | 52.842805 | -27.965377 | 24.3 ± 0.16 | 22.897 ± 0.089 | 0.00851 | 1.09 ± 0.16 | 2.45 ± 0.2 | $39.3^{+27.1}_{-14.5}$ | ... |
| 304 | ... | ... | ... | ... | ... | ... | ... | ... | ... | ... |
| 307 | ... | ... | ... | ... | ... | ... | ... | ... | ... | ... |
| 309 | ... | ... | ... | ... | ... | ... | ... | ... | ... | ... |
| 311 | ... | ... | ... | ... | ... | ... | ... | ... | ... | ... |
| 318 | GALEX J033209.5-280716 | 53.039879 | -28.121257 | ... | 24.553 ± 0.174 | 0.0078 | ... | 2.07 ± 0.33 | 853^{+115}_{-31} | 50.648 ± 8.308 |
| 319 | ... | ... | ... | ... | ... | ... | ... | ... | $29.7^{+10.6}_{-32.4}$ | 6.636 ± 2.516 |
| 320 | ... | ... | ... | ... | ... | ... | ... | ... | ... | ... |
| 322 | ... | ... | ... | ... | ... | ... | ... | ... | ... | ... |
| 323 | GALEX J033556.4-283531 | 53.98499 | -28.591981 | ... | 24.087 ± 0.147 | 0.01151 | ... | 0.22 ± 0.03 | $17.4^{+149.1}_{-59.8}$ | 2.625 ± 0.397 |
| 329 | GALEX J033333.6-281403 | 53.390188 | -28.234378 | 25.3 ± 0.31 | 23.153 ± 0.12 | 0.00909 | 19.92 ± 5.7 | 28.16 ± 3.12 | $39.3^{+15.8}_{-7.4}$ | 17.128 ± 2.448 |
| 332 | ... | ... | ... | ... | ... | ... | ... | ... | 179^{+94}_{-103} | 44.785 ± 14.422 |
| 333 | ... | ... | ... | ... | ... | ... | ... | ... | ... | ... |
| 335 | GALEX J033612.1-290520 | 54.05074 | -29.089025 | 23.03 ± 0.17 | 22.304 ± 0.09 | 0.01016 | 0.69 ± 0.11 | 1.29 ± 0.11 | $29.2^{+3.6}_{-3.6}$ | 10.517 ± 1.675 |
| 339 | GALEX J033018.2-285120 | 52.576305 | -28.855675 | 24.8 ± 0.37 | 22.842 ± 0.107 | 0.00979 | 0.18 ± 0.06 | 1.0 ± 0.1 | $44.7^{+16.9}_{-7.9}$ | 29.11 ± 4.433 |
| 341 | ... | ... | ... | ... | ... | ... | ... | ... | $48.5^{+25.9}_{-8.1}$ | 6.416 ± 1.152 |
| 342 | GALEX J032745.1-292350 | 51.93792 | -29.397395 | ... | 22.528 ± 0.143 | 0.00822 | ... | ... | ... | ... |
| 343 | ... | ... | ... | ... | ... | ... | ... | ... | ... | ... |
| 344 | ... | ... | ... | ... | ... | ... | ... | ... | ... | ... |
| 346 | ... | ... | ... | ... | ... | ... | ... | ... | ... | ... |
| 355 | GALEX J033117.7-272016 | 52.824134 | -27.337986 | 19.84 ± 0.12 | 19.571 ± 0.068 | 0.00994 | 1.49 ± 0.17 | 2.04 ± 0.13 | $1.76^{+0.71}_{-0.54}$ | ... |
| 359 | ... | ... | ... | ... | ... | ... | ... | ... | ... | ... |
| 360 | GALEX J032735.8-285921 | 51.899171 | -28.989387 | 23.39 ± 0.16 | 23.418 ± 0.125 | 0.00902 | 1.25 ± 0.18 | 1.01 ± 0.12 | $7.57^{+3.33}_{-3.03}$ | ... |

Table C2 (continued)

| ID | GALEX Name | α_{GALEX} | δ_{GALEX} | FUV | NUV | $E(B - V)$ | SFR_{FUV} | SFR_{NUV} | L_{FIR} | M_* |
|-----|------------------------|------------------|------------------|------------------|--------------------|------------|-----------------|-----------------|------------------------|------------------|
| 368 | GALEX J032956.2-290313 | 52.484512 | -29.053836 | 21.28 ± 0.12 | 20.769 ± 0.069 | 0.00904 | 0.44 ± 0.05 | 0.75 ± 0.05 | $0.37^{+0.10}_{-0.19}$ | 0.25 ± 0.048 |
| 369 | ... | ... | ... | ... | ... | ... | ... | ... | ... | ... |
| 376 | ... | ... | ... | ... | ... | ... | ... | ... | ... | ... |

Note. — Reading from the left, the columns are: the BLAST identification number; the full IAU name of the *GALEX* counterpart to the BLAST source; the position of the *GALEX* counterpart; the flux in the FUV filter, in magnitudes, with uncertainty; the flux in the NUV filter, in magnitudes, with uncertainty; Galactic extinction correction as from Schlegel et al. (1998), in magnitudes; star-formation rate as estimated from the FUV flux (see Equation 2.3), in $M_{\odot} \text{ yr}^{-1}$, with uncertainty (note that we listed SFR_{FUV} for all FUV sources, even if only those with $z < 0.36$ are to be considered reliable, see Section 2.4.2); star-formation rate as estimated from the NUV flux (see Equation 2.3), in $M_{\odot} \text{ yr}^{-1}$, with uncertainty (note that we listed SFR_{NUV} for all NUV sources, even if only those with $z < 0.91$ are to be considered reliable, see Section 2.4.2); rest-frame bolometric FIR luminosity of the BLAST ID, in $10^{10} L_{\odot}$, with upper and lower uncertainties (note that we quote the mode, and 68% c.l. of the distribution obtained, see Section 2.3.2 for details); stellar mass of the BLAST ID, in $10^{10} M_{\odot}$ (see Section 2.8 for details), with uncertainty.

BIBLIOGRAPHY

- Ade, P. A. R., Pisano, G., Tucker, C., & Weaver, S. 2006, in Proceedings of SPIE, Vol. 6275, Society of Photo-Optical Instrumentation Engineers (SPIE) Conference Series
- Alexander, C. D., Swift, W. R., Ghosh, K., & Ramsey, B. D. 1999, in Proceedings of SPIE, Vol. 3779, Society of Photo-Optical Instrumentation Engineers (SPIE) Conference Series, 47–54
- Allen, A., Li, Z.-Y., & Shu, F. H. 2003, *ApJ*, 599, 363
- Alves, J., Lombardi, M., & Lada, C. J. 2007, *A&A*, 462, L17
- Amblard, A., Cooray, A., et al. 2011, *Nature*, 470, 510
- André, P., Men'shchikov, A., et al. 2010, *A&A*, 518, L102+
- Aretxaga, I., Hughes, D. H., Chapin, E. L., Gaztañaga, E., Dunlop, J. S., & Ivison, R. J. 2003, *MNRAS*, 342, 759
- Aretxaga, I., Hughes, D. H., & Dunlop, J. S. 2005, *MNRAS*, 358, 1240
- Attard, M., Houde, M., Novak, G., Li, H.-b., Vaillancourt, J. E., Dowell, C. D., Davidson, J., & Shinnaga, H. 2009, *ApJ*, 702, 1584
- Balogh, M., Eke, V., et al. 2004, *MNRAS*, 348, 1355
- Barger, A. J., Cowie, L. L., Sanders, D. B., Fulton, E., Taniguchi, Y., Sato, Y., Kawara, K., & Okuda, H. 1998, *Nature*, 394, 248

- Bastien, P., Bissonnette, É., Ade, P., Pisano, G., Savini, G., Jenness, T., Johnstone, D., & Matthews, B. 2005, *JRASC*, 99, 133
- Basu, S. 2000, *ApJ*, 540, L103
- Basu, S. & Mouschovias, T. C. 1994, *ApJ*, 432, 720
- Bauer, A. E., Conselice, C. J., Pérez-González, P. G., Grützbauch, R., Bluck, A. F. L., Buitrago, F., & Mortlock, A. 2011, *MNRAS*, 417, 289
- Bell, E. F. 2003, *ApJ*, 586, 794
- Bell, E. F., Wolf, C., et al. 2004, *ApJ*, 608, 752
- Bernard, J.-P., Ade, P., et al. 2007, in *EAS Publications Series*, Vol. 23, *EAS Publications Series*, ed. M.-A. Miville-Deschênes & F. Boulanger, 189–203
- Bernstein, R. A., Freedman, W. L., & Madore, B. F. 2002, *ApJ*, 571, 56
- Bethell, T. J., Chepurinov, A., Lazarian, A., & Kim, J. 2007, *ApJ*, 663, 1055
- Béthermin, M., Dole, H., Beelen, A., & Aussel, H. 2010, *A&A*, 512, A78+
- Bezanson, R., van Dokkum, P. G., Tal, T., Marchesini, D., Kriek, M., Franx, M., & Coppi, P. 2009, *ApJ*, 697, 1290
- Bianchi, S., Gonçalves, J., Albrecht, M., Caselli, P., Chini, R., Galli, D., & Walmsley, M. 2003, *A&A*, 399, L43
- Bintley, D., Macintosh, M. J., et al. 2010, in *Proceedings of SPIE*, Vol. 7741, *Society of Photo-Optical Instrumentation Engineers (SPIE) Conference Series*

- Blain, A. W. 1999, *MNRAS*, 304, 669
- Blain, A. W., Barnard, V. E., & Chapman, S. C. 2003, *MNRAS*, 338, 733
- Blain, A. W., Kneib, J., Ivison, R. J., & Smail, I. 1999a, *ApJ*, 512, L87
- Blain, A. W., Smail, I., Ivison, R. J., & Kneib, J.-P. 1999b, *MNRAS*, 302, 632
- Blain, A. W., Smail, I., Ivison, R. J., Kneib, J.-P., & Frayer, D. T. 2002, *Phys. Rep.*, 369, 111
- Bluck, A. F. L., Conselice, C. J., Bouwens, R. J., Daddi, E., Dickinson, M., Papovich, C., & Yan, H. 2009, *MNRAS*, 394, L51
- Bock, J. J., Glenn, J., Grannan, S. M., Irwin, K. D., Lange, A. E., Leduc, H. G., & Turner, A. D. 1998, in *Proceedings of SPIE*, Vol. 3357, Society of Photo-Optical Instrumentation Engineers (SPIE) Conference Series, 297–304
- Boggess, N. W., Mather, J. C., et al. 1992, *ApJ*, 397, 420
- Borys, C., Smail, I., Chapman, S. C., Blain, A. W., Alexander, D. M., & Ivison, R. J. 2005, *ApJ*, 635, 853
- Bournaud, F., Chapon, D., et al. 2011, *ApJ*, 730, 4
- Bournaud, F. & Elmegreen, B. G. 2009, *ApJ*, 694, L158
- Braglia, F. G., Ade, P. A. R., et al. 2011, *MNRAS*, 412, 1187
- Brammer, G. B., van Dokkum, P. G., & Coppi, P. 2008, *ApJ*, 686, 1503

- Brinchmann, J., Charlot, S., White, S. D. M., Tremonti, C., Kauffmann, G., Heckman, T., & Brinkmann, J. 2004, *MNRAS*, 351, 1151
- Bruzual, G. 2010, in *IAU Symposium*, Vol. 262, *IAU Symposium*, ed. G. Bruzual & S. Charlot, 55–64
- Bryan, S. A., Ade, P. A. R., et al. 2010a, in *Proceedings of SPIE*, Vol. 7741, *Society of Photo-Optical Instrumentation Engineers (SPIE) Conference Series*
- Bryan, S. A., Montroy, T. E., & Ruhl, J. E. 2010b, *Appl. Opt.*, 49, 6313
- Buat, V., Boissier, S., et al. 2008, *A&A*, 483, 107
- Buat, V., Giovannoli, E., et al. 2010, *MNRAS*, 409, L1
- Buat, V., Takeuchi, T. T., et al. 2007, *ApJS*, 173, 404
- Buitrago, F., Trujillo, I., Conselice, C. J., Bouwens, R. J., Dickinson, M., & Yan, H. 2008, *ApJ*, 687, L61
- Bundy, K., Ellis, R. S., et al. 2006, *ApJ*, 651, 120
- Calzetti, D., Armus, L., Bohlin, R. C., Kinney, A. L., Koornneef, J., & Storchi-Bergmann, T. 2000, *ApJ*, 533, 682
- Calzetti, D., Kennicutt, R. C., et al. 2007, *ApJ*, 666, 870
- Cantalupo, C. M., Borrill, J. D., Jaffe, A. H., Kisner, T. S., & Stompor, R. 2010, *ApJS*, 187, 212
- Caputi, K. I., Dole, H., et al. 2006, *ApJ*, 637, 727
- Cava, A., Rodighiero, G., et al. 2010, *MNRAS*, 409, L19
- Chabrier, G. 2003, *PASP*, 115, 763

- Chandrasekhar, S. & Fermi, E. 1953, *ApJ*, 118, 113
- Chapin, E. L., Ade, P. A. R., et al. 2008, *ApJ*, 681, 428
- Chapin, E. L., Chapman, S. C., et al. 2011, *MNRAS*, 411, 505
- Chapman, S. C., Blain, A. W., Ivison, R. J., & Smail, I. R. 2003, *Nature*, 422, 695
- Chapman, S. C., Blain, A. W., Smail, I., & Ivison, R. J. 2005, *ApJ*, 622, 772
- Chary, R. & Elbaz, D. 2001, *ApJ*, 556, 562
- Chattopadhyay, G., Glenn, J., Bock, J. J., Rownd, B. K., Caldwell, M., & Griffin, M. J. 2003, *IEEE Transactions on Microwave Theory Techniques*, 51, 2139
- Cho, J. & Lazarian, A. 2005, *ApJ*, 631, 361
- Cid Fernandes, R., Stasińska, G., Schlickmann, M. S., Mateus, A., Vale Asari, N., Schoenell, W., & Sodré, L. 2010, *MNRAS*, 403, 1036
- Cole, S., Lacey, C. G., Baugh, C. M., & Frenk, C. S. 2000, *MNRAS*, 319, 168
- Colless, M., Peterson, B. A., et al. 2003, *ArXiv astro-ph/0306581*
- Collett, E. 1993, *Polarized light: fundamentals and applications* (Marcel Dekker)
- Conroy, C. & Gunn, J. E. 2010, *ApJ*, 712, 833
- Conselice, C. J., Bluck, A. F. L., et al. 2011, *MNRAS*, 413, 80
- Conselice, C. J., Bundy, K., et al. 2007, *MNRAS*, 381, 962
- Cook, W. B. & Perkowitz, S. 1985, *Appl. Opt.*, 24, 1773

- Coppin, K., Chapin, E. L., et al. 2006, *MNRAS*, 372, 1621
- Coppin, K., Halpern, M., Scott, D., Borys, C., & Chapman, S. 2005, *MNRAS*, 357, 1022
- Coppin, K., Halpern, M., et al. 2008, *MNRAS*, 384, 1597
- Coppin, K., Pope, A., et al. 2010, *ApJ*, 713, 503
- Coppin, K. E. K., Greaves, J. S., Jenness, T., & Holland, W. S. 2000, *A&A*, 356, 1031
- Crutcher, R. M. 1999, *ApJ*, 520, 706
- . 2004, *Ap&SS*, 292, 225
- Crutcher, R. M., Nutter, D. J., Ward-Thompson, D., & Kirk, J. M. 2004, *ApJ*, 600, 279
- Daddi, E., Dickinson, M., et al. 2005, *ApJ*, 631, L13
- . 2007, *ApJ*, 670, 156
- Dale, D. A. & Helou, G. 2002, *ApJ*, 576, 159
- Damen, M., Labbé, I., Franx, M., van Dokkum, P. G., Taylor, E. N., & Gawiser, E. J. 2009, *ApJ*, 690, 937
- Damjanov, I., McCarthy, P. J., et al. 2009, *ApJ*, 695, 101
- Davé, R., Finlator, K., Oppenheimer, B. D., Fardal, M., Katz, N., Kereš, D., & Weinberg, D. H. 2010, *MNRAS*, 404, 1355
- Davis, Jr., L. & Greenstein, J. L. 1951, *ApJ*, 114, 206
- Dekel, A., Birnboim, Y., et al. 2009, *Nature*, 457, 451
- Della Valle, A., Mazzei, P., Bettoni, D., Aussel, H., & de Zotti, G. 2006, *A&A*, 454, 453

- Devlin, M. J., Ade, P. A. R., et al. 2009, *Nature*, 458, 737
- Devlin, M. J., Ade, P. A. R., et al. 2004, in *Proceedings of SPIE*, Vol. 5498, Society of Photo-Optical Instrumentation Engineers (SPIE) Conference Series, 42–54
- Dickinson, M. & FIDEL team. 2007, in *Bulletin of the American Astronomical Society*, Vol. 38, BAAS, 822–+
- Dickinson, M., Giavalisco, M., & The Goods Team. 2003, in *The Mass of Galaxies at Low and High Redshift*, 324–+
- Dole, H., Lagache, G., et al. 2006, *A&A*, 451, 417
- Dowell, C. D., Cook, B. T., et al. 2010, in *Proceedings of SPIE*, Vol. 7735, Society of Photo-Optical Instrumentation Engineers (SPIE) Conference Series
- Draine, B. T. 2003, *ARA&A*, 41, 241
- Draine, B. T. & Fraisse, A. A. 2009, *ApJ*, 696, 1
- Dunlop, J. S., Ade, P. A. R., et al. 2010, *MNRAS*, 408, 2022
- Dunne, L., Eales, S., Edmunds, M., Ivison, R., Alexander, P., & Clements, D. L. 2000, *MNRAS*, 315, 115
- Dunne, L. & Eales, S. A. 2001, *MNRAS*, 327, 697
- Dwek, E., Arendt, R. G., et al. 1998, *ApJ*, 508, 106
- Dye, S. 2008, *MNRAS*, 389, 1293
- Dye, S., Ade, P. A. R., et al. 2009, *ApJ*, 703, 285
- Dye, S., Dunne, L., et al. 2010a, *A&A*, 518, L10+

- Dye, S., Eales, S., Moncelsi, L., & Pascale, E. 2010b, MNRAS, 407, L69
- Dye, S., Eales, S. A., et al. 2008, MNRAS, 386, 1107
- Dye, S., Eales, S. A., Ashby, M. L. N., Huang, J., Egami, E., Brodwin, M., Lilly, S., & Webb, T. 2007, MNRAS, 375, 725
- Eales, S., Chapin, E. L., et al. 2009, ApJ, 707, 1779
- Eales, S., Dunne, L., et al. 2010a, PASP, 122, 499
- Eales, S. A., Raymond, G., et al. 2010b, A&A, 518, L23+
- Elbaz, D., Daddi, E., et al. 2007, A&A, 468, 33
- Elbaz, D., Hwang, H. S., et al. 2010, A&A, 518, L29+
- Elmegreen, B. G. & Scalo, J. 2004, ARA&A, 42, 211
- Engel, H., Tacconi, L. J., et al. 2010, ApJ, 724, 233
- Falceta-Gonçalves, D., Lazarian, A., & Kowal, G. 2008, ApJ, 679, 537
- Fazio, G. G., Hora, J. L., et al. 2004, ApJS, 154, 10
- Fioc, M. & Rocca-Volmerange, B. 1997, A&A, 326, 950
- Fissel, L. M., Ade, P. A. R., et al. 2010, in Proceedings of SPIE, Vol. 7741, Society of Photo-Optical Instrumentation Engineers (SPIE) Conference Series
- Fixsen, D. J., Dwek, E., Mather, J. C., Bennett, C. L., & Shafer, R. A. 1998, ApJ, 508, 123
- Foucaud, S., Conselice, C. J., Hartley, W. G., Lane, K. P., Bamford, S. P., Almaini, O., & Bundy, K. 2010, MNRAS, 406, 147

- Frayser, D. T., Reddy, N. A., Armus, L., Blain, A. W., Scoville, N. Z., & Smail, I. 2004, *AJ*, 127, 728
- Frayser, D. T., Sanders, D. B., et al. 2009, *AJ*, 138, 1261
- Galli, D. & Shu, F. H. 1993a, *ApJ*, 417, 220
- . 1993b, *ApJ*, 417, 243
- Gardner, J. P., Mather, J. C., et al. 2006, *Space Sci. Rev.*, 123, 485
- Gawiser, E., van Dokkum, P. G., et al. 2006, *ApJS*, 162, 1
- Genzel, R., Lutz, D., et al. 1998, *ApJ*, 498, 579
- Genzel, R., Tacconi, L. J., et al. 2006, *Nature*, 442, 786
- Girart, J. M., Rao, R., & Marrone, D. P. 2006, *Science*, 313, 812
- Gispert, R., Lagache, G., & Puget, J. L. 2000, *A&A*, 360, 1
- Goldsmith, P. F. & Li, D. 2005, *ApJ*, 622, 938
- González, J. E., Lacey, C. G., Baugh, C. M., & Frenk, C. S. 2011, *MNRAS*, 413, 749
- Grazian, A., Fontana, A., et al. 2006, *A&A*, 449, 951
- Greve, T. R., Ivison, R. J., Bertoldi, F., Stevens, J. A., Dunlop, J. S., Lutz, D., & Carilli, C. L. 2004, *MNRAS*, 354, 779
- Griffin, M. J., Abergel, A., et al. 2010, *A&A*, 518, L3+
- Griffin, M. J., Bock, J. J., & Gear, W. K. 2002, *Appl. Opt.*, 41, 6543
- Guiderdoni, B., Hivon, E., Bouchet, F. R., & Maffei, B. 1998, *MNRAS*, 295, 877

- Hanany, S., Hubmayr, J., Johnson, B. R., Matsumura, T., Oxley, P., & Thibodeau, M. 2005, *Appl. Opt.*, 44, 4666
- Harman, R. R. 2005, Wilkinson Microwave Anisotropy Probe (WMAP) Attitude Estimation Filter Comparison, Tech. Rep. 20060002447
- Hatton, S., Devriendt, J. E. G., Ninin, S., Bouchet, F. R., Guiderdoni, B., & Vibert, D. 2003, *MNRAS*, 343, 75
- Hatziminaoglou, E., Omont, A., et al. 2010, *A&A*, 518, L33+
- Hatziminaoglou, E., Pérez-Fournon, I., et al. 2005, *AJ*, 129, 1198
- Hauser, M. G., Arendt, R. G., et al. 1998, *ApJ*, 508, 25
- Hauser, M. G. & Dwek, E. 2001, *ARA&A*, 39, 249
- Heavens, A., Panter, B., Jimenez, R., & Dunlop, J. 2004, *Nature*, 428, 625
- Helou, G., Soifer, B. T., & Rowan-Robinson, M. 1985, *ApJ*, 298, L7
- Hennebelle, P. & Chabrier, G. 2008, *ApJ*, 684, 395
- Hildebrand, R. H. 1983, *QJRAS*, 24, 267
- Hildebrand, R. H., Davidson, J. A., Dotson, J. L., Dowell, C. D., Novak, G., & Vaillancourt, J. E. 2000, *PASP*, 112, 1215
- Hildebrand, R. H., Dotson, J. L., Dowell, C. D., Schleuning, D. A., & Vaillancourt, J. E. 1999, *ApJ*, 516, 834
- Hildebrand, R. H. & Vaillancourt, J. E. 2009, in *Revista Mexicana de Astronomia y Astrofisica*, vol. 27, Vol. 36, *Revista Mexicana de Astronomia y Astrofisica Conference Series*, 137–141

- Hinshaw, G., Weiland, J. L., et al. 2009, *ApJS*, 180, 225
- Hirashita, H., Buat, V., & Inoue, A. K. 2003, *A&A*, 410, 83
- Ho, P. T. P., Moran, J. M., & Lo, K. Y. 2004, *ApJ*, 616, L1
- Holland, W., MacIntosh, M., et al. 2006, in *Proceedings of SPIE*, Vol. 6275, Society of Photo-Optical Instrumentation Engineers (SPIE) Conference Series
- Holland, W. S., Robson, E. I., et al. 1999, *MNRAS*, 303, 659
- Hopkins, A. M., Miller, C. J., et al. 2003, *ApJ*, 599, 971
- Hopkins, P. F., Bundy, K., Murray, N., Quataert, E., Lauer, T. R., & Ma, C. 2009, *MNRAS*, 398, 898
- Hubble, E. 1929, *Proceedings of the National Academy of Science*, 15, 168
- Hubble, E. P. 1926, *ApJ*, 64, 321
- Hughes, D. H., Serjeant, S., et al. 1998, *Nature*, 394, 241
- Iglesias-Páramo, J., Buat, V., Donas, J., Boselli, A., & Milliard, B. 2004, *A&A*, 419, 109
- Iglesias-Páramo, J., Buat, V., et al. 2006, *ApJS*, 164, 38
- Inoue, A. K. 2002, *ApJ*, 570, L97
- Iverson, R. J., Alexander, D. M., et al. 2010a, *MNRAS*, 402, 245
- Iverson, R. J., Magnelli, B., et al. 2010b, *A&A*, 518, L31+
- Jeans, J. H. 1902, *Royal Society of London Philosophical Transactions Series A*, 199, 1

- Johansson, P. H., Naab, T., & Ostriker, J. P. 2009, *ApJ*, 697, L38
- Johnson, B. R., Collins, J., et al. 2007, *ApJ*, 665, 42
- Johnstone, D., Wilson, C. D., Moriarty-Schieven, G., Joncas, G., Smith, G., Gregersen, E., & Fich, M. 2000, *ApJ*, 545, 327
- Jones, C. E. & Basu, S. 2002, *ApJ*, 569, 280
- Jones, W. C., Bhatia, R., Bock, J. J., & Lange, A. E. 2003, in *Proceedings of SPIE, Vol. 4855, Society of Photo-Optical Instrumentation Engineers (SPIE) Conference Series*, 227–238
- Kauffmann, G., Heckman, T. M., et al. 2003, *MNRAS*, 346, 1055
- Kauffmann, G., White, S. D. M., & Guiderdoni, B. 1993, *MNRAS*, 264, 201
- Kennicutt, Jr., R. C. 1983, *ApJ*, 272, 54
- . 1998, *ARA&A*, 36, 189
- Kennicutt, Jr., R. C., Hao, C.-N., et al. 2009, *ApJ*, 703, 1672
- Kereš, D., Katz, N., Fardal, M., Davé, R., & Weinberg, D. H. 2009, *MNRAS*, 395, 160
- Kessler, M. F., Steinz, J. A., et al. 1996, *A&A*, 315, L27
- Khochfar, S. & Burkert, A. 2003, *ApJ*, 597, L117
- Khochfar, S. & Silk, J. 2006, *ApJ*, 648, L21
- Kimble, R. A., MacKenty, J. W., O’Connell, R. W., & Townsend, J. A. 2008, in *Proceedings of SPIE, Vol. 7010, Society of Photo-Optical Instrumentation Engineers (SPIE) Conference Series*

- Kirk, J. M., Ward-Thompson, D., & Crutcher, R. M. 2006, *MNRAS*, 369, 1445
- Könyves, V., André, P., et al. 2010, *A&A*, 518, L106+
- Kreysa, E., Gemuend, H.-P., et al. 1998, in *Proceedings of SPIE*, Vol. 3357, Society of Photo-Optical Instrumentation Engineers (SPIE) Conference Series, ed. T. G. Phillips, 319–325
- Kriek, M., van Dokkum, P. G., Franx, M., Illingworth, G. D., & Magee, D. K. 2009a, *ApJ*, 705, L71
- Kriek, M., van Dokkum, P. G., et al. 2008, *ApJ*, 677, 219
- . 2006, *ApJ*, 649, L71
- Kriek, M., van Dokkum, P. G., Labbé, I., Franx, M., Illingworth, G. D., Marchesini, D., & Quadri, R. F. 2009b, *ApJ*, 700, 221
- Kroupa, P. 2001, *MNRAS*, 322, 231
- Lacey, C. G., Baugh, C. M., Frenk, C. S., Silva, L., Granato, G. L., & Bressan, A. 2008, *MNRAS*, 385, 1155
- Lacy, M., Storrie-Lombardi, L. J., et al. 2004, *ApJS*, 154, 166
- Lada, C. J. 2005, *Progress of Theoretical Physics Supplement*, 158, 1
- Lasker, B. M., Jenkner, H., & Russell, J. L. 1987, *NASA STI/Recon Technical Report N*, 88, 30547
- Lazarian, A. 2007, *J. Quant. Spec. Radiat. Transf.*, 106, 225
- Lazarian, A. & Cho, J. 2005, in *Astronomical Society of the Pacific Conference Series*, Vol. 343, *Astronomical Polarimetry: Current Status and Future Directions*, ed. A. Adamson, C. Aspin, C. Davis, & T. Fujiyoshi, 333–+

- Le Floc'h, E., Papovich, C., et al. 2005, *ApJ*, 632, 169
- Leitherer, C., Schaerer, D., et al. 1999, *ApJS*, 123, 3
- Li, H., Dowell, C. D., Kirby, L., Novak, G., & Vaillancourt, J. E. 2008, *Appl. Opt.*, 47, 422
- Li, H., Griffin, G. S., Krejny, M., Novak, G., Loewenstein, R. F., Newcomb, M. G., Calisse, P. G., & Chuss, D. T. 2006, *ApJ*, 648, 340
- Li, H. & Houde, M. 2008, *ApJ*, 677, 1151
- Loewenstein, E. V., Smith, D. R., & Morgan, R. L. 1973, *Appl. Opt.*, 12, 398
- Lonsdale, C., Polletta, M. d. C., et al. 2004, *ApJS*, 154, 54
- Luo, B., Bauer, F. E., et al. 2008, *ApJS*, 179, 19
- Lutz, D., Poglitsch, A., et al. 2011, *A&A*, 532, A90+
- Mac Low, M.-M. & Klessen, R. S. 2004, *Reviews of Modern Physics*, 76, 125
- Magnelli, B., Elbaz, D., Chary, R. R., Dickinson, M., Le Borgne, D., Frayer, D. T., & Willmer, C. N. A. 2009, *A&A*, 496, 57
- Maraston, C. 2005, *MNRAS*, 362, 799
- Marchesini, D., van Dokkum, P. G., Förster Schreiber, N. M., Franx, M., Labbé, I., & Wuyts, S. 2009, *ApJ*, 701, 1765
- Markley, F. L. 2003, *Journal of Guidance, Control, and Dynamics*, 26, 311

- Marsden, G., Ade, P. A. R., et al. 2008, in Proceedings of SPIE, Vol. 7020, Society of Photo-Optical Instrumentation Engineers (SPIE) Conference Series
- Marsden, G., Ade, P. A. R., et al. 2009, *ApJ*, 707, 1729
- Marsden, G., Chapin, E. L., et al. 2011, *MNRAS*, 417, 1192
- Martin, D. C., Fanson, J., et al. 2005, *ApJ*, 619, L1
- Martin, D. H. & Puplett, E. 1970, *Infrared Physics*, 10, 105
- Masi, S., Ade, P. A. R., et al. 2006, *A&A*, 458, 687
- Masi, S., Brienza, D., et al. 2007, in 18th ESA Symposium on European Rocket and Balloon Programmes and Related Research (ESA)
- Mathis, J. S. 1990, *ARA&A*, 28, 37
- Matsumura, T., Hanany, S., Ade, P. A. R., Johnson, B. R., Jones, T. J., Jonnalagadda, P., & Savini, G. 2009, *Appl. Opt.*, 48, 3614
- Mazzei, P., Della Valle, A., & Bettoni, D. 2007, *A&A*, 462, 21
- McKee, C. F. & Ostriker, E. C. 2007, *ARA&A*, 45, 565
- Men'shchikov, A., André, P., et al. 2010, *A&A*, 518, L103+
- Mentuch, E., Abraham, R. G., & Zibetti, S. 2010, *ApJ*, 725, 1971
- Mihos, J. C. & Hernquist, L. 1994, *ApJ*, 431, L9
- . 1996, *ApJ*, 464, 641
- Miller, C. J., Nichol, R. C., Gómez, P. L., Hopkins, A. M., & Bernardi, M. 2003, *ApJ*, 597, 142
- Miller, G. E. & Scalo, J. M. 1979, *ApJS*, 41, 513

- Miller, N. A., Fomalont, E. B., Kellermann, K. I., Mainieri, V., Norman, C., Padovani, P., Rosati, P., & Tozzi, P. 2008, *ApJS*, 179, 114
- Molinari, S., Swinyard, B., et al. 2010, *A&A*, 518, L100+
- Moncelsi, L. 2007, Master thesis, La Sapienza University, Rome, Italy, a pdf version of the thesis can be found here: www.astro.cardiff.ac.uk/pub/Lorenzo.Moncelsi/Master_Thesis.pdf
- Moncelsi, L., Ade, P. A. R., et al. 2011, *ApJ*, 727, 83
- Morrissey, P., Conrow, T., et al. 2007, *ApJS*, 173, 682
- Mortari, D., Samaan, M. A., & Bruccoleri, C. 2004, *Navigation*, 51, 171–183
- Motte, F., Andre, P., & Neri, R. 1998, *A&A*, 336, 150
- Mouschovias, T. C. 1976, *ApJ*, 207, 141
- Müller, T., Nielbock, M., Balog, Z., Klaas, U., & Vilenius, E. 2011a, PACS Photometer - Point-Source Flux Calibration, Tech. Rep. PICC-ME-TN-037 v1.0
- Müller, T., Okumura, K., & Klaas, U. 2011b, PACS Photometer - Passbands and Colour Correction Factors for Various Source SEDs, Tech. Rep. PICC-ME-TN-038 v1.0
- Murphy, E. J., Chary, R., Alexander, D. M., Dickinson, M., Magnelli, B., Morrison, G., Pope, A., & Teplitz, H. I. 2009, *ApJ*, 698, 1380
- Murray, A. G., Nartallo, R., Haynes, C. V., Gannaway, F., & Ade, P. A. R. 1997, in *ESA Special Publication*, Vol. 401, *The Far Infrared and Submillimetre Universe.*, ed. A. Wilson, 405–+

- Murray, N. 2011, *ApJ*, 729, 133
- Muzzin, A., van Dokkum, P., Franx, M., Marchesini, D., Kriek, M., & Labbé, I. 2009, *ApJ*, 706, L188
- Muzzin, A., van Dokkum, P., Kriek, M., Labbé, I., Cury, I., Marchesini, D., & Franx, M. 2010, *ApJ*, 725, 742
- Naab, T., Johansson, P. H., & Ostriker, J. P. 2009, *ApJ*, 699, L178
- Nakamura, F. & Li, Z.-Y. 2008, *ApJ*, 687, 354
- Narayanan, D., Hayward, C. C., Cox, T. J., Hernquist, L., Jonsson, P., Younger, J. D., & Groves, B. 2010, *MNRAS*, 401, 1613
- Natoli, P., Botti, M., de Gasperis, G., De Troia, G., & Massaioli, F. 2009, *Memorie della Societa Astronomica Italiana Supplementi*, 13, 84
- Natoli, P., de Gasperis, G., Gheller, C., & Vittorio, N. 2001, *A&A*, 372, 346
- Netterfield, C. B., Ade, P. A. R., et al. 2009, *ApJ*, 707, 1824
- Neugebauer, G., Habing, H. J., et al. 1984, *ApJ*, 278, L1
- Nguyen, H. T., Schulz, B., et al. 2010, *A&A*, 518, L5+
- Nordon, R., Lutz, D., et al. 2010, *A&A*, 518, L24+
- Norris, R. P., Afonso, J., et al. 2006, *AJ*, 132, 2409
- Novak, G., Chuss, D. T., et al. 2003, *ApJ*, 583, L83
- Novak, G., Dotson, J. L., & Li, H. 2009, *ApJ*, 695, 1362
- Nutter, D. & Ward-Thompson, D. 2007, *MNRAS*, 374, 1413

- Olmi, L. 2002, in Proceedings of SPIE, Vol. 4849, Society of Photo-Optical Instrumentation Engineers (SPIE) Conference Series, 245–256
- Oser, L., Ostriker, J. P., Naab, T., Johansson, P. H., & Burkert, A. 2010, *ApJ*, 725, 2312
- Ostriker, E. C., Stone, J. M., & Gammie, C. F. 2001, *ApJ*, 546, 980
- Ott, S. 2010, in Astronomical Society of the Pacific Conference Series, Vol. 434, Astronomical Data Analysis Software and Systems XIX, 139–+
- Padoan, P., Goodman, A., Draine, B. T., Juvela, M., Nordlund, Å., & Rögnvaldsson, Ö. E. 2001, *ApJ*, 559, 1005
- Padoan, P., Jimenez, R., Juvela, M., & Nordlund, Å. 2004, *ApJ*, 604, L49
- Pancharatnam, S. 1955, *Memoirs of the Raman Research Institute Bangalore*, 71, 137
- Papovich, C., Moustakas, L. A., et al. 2006, *ApJ*, 640, 92
- Papovich, C., Rudnick, G., et al. 2007, *ApJ*, 668, 45
- Pascale, E., Ade, P. A. R., et al. 2008, *ApJ*, 681, 400
- . 2009, *ApJ*, 707, 1740
- Pascale, E., Auld, R., et al. 2011, *MNRAS*, 415, 911
- Patanchon, G., Ade, P. A. R., et al. 2008, *ApJ*, 681, 708
- . 2009, *ApJ*, 707, 1750
- Pelkonen, V.-M., Juvela, M., & Padoan, P. 2007, *A&A*, 461, 551

- Peng, C. Y., Ho, L. C., Impey, C. D., & Rix, H. 2002, *AJ*, 124, 266
- Pérez-González, P. G., Rieke, G. H., et al. 2005, *ApJ*, 630, 82
- Pérez-González, P. G., Trujillo, I., Barro, G., Gallego, J., Zamorano, J., & Conselice, C. J. 2008, *ApJ*, 687, 50
- Pilbratt, G. L., Riedinger, J. R., et al. 2010, *A&A*, 518, L1+
- Pisano, G., Savini, G., Ade, P. A. R., & Haynes, V. 2008, *Appl. Opt.*, 47, 6251
- Pisano, G., Savini, G., Ade, P. A. R., Haynes, V., & Gear, W. K. 2006, *Appl. Opt.*, 45, 6982
- Planck Collaboration. 2011, *ArXiv* 1101.2022
- Poglitsch, A., Waelkens, C., et al. 2010, *A&A*, 518, L2+
- Pope, A., Borys, C., Scott, D., Conselice, C., Dickinson, M., & Mobasher, B. 2005, *MNRAS*, 358, 149
- Pope, A., Scott, D., et al. 2006, *MNRAS*, 370, 1185
- Prescott, M. K. M., Kennicutt, Jr., R. C., et al. 2007, *ApJ*, 668, 182
- Press, W. H. & Schechter, P. 1974, *ApJ*, 187, 425
- Press, W. H., Teukolsky, S. A., Vetterling, W. T., & Flannery, B. P. 1992, *Numerical recipes in C (2nd ed.): the art of scientific computing* (New York, NY, USA: Cambridge University Press)
- Puget, J.-L., Abergel, A., Bernard, J.-P., Boulanger, F., Burton, W. B., Desert, F.-X., & Hartmann, D. 1996, *A&A*, 308, L5+
- Ratcliffe, A., Shanks, T., Parker, Q. A., Broadbent, A., Watson, F. G., Oates, A. P., Collins, C. A., & Fong, R. 1998, *MNRAS*, 300, 417

- Ravikumar, C. D., Puech, M., et al. 2007, *A&A*, 465, 1099
- Ravindranath, S., Ferguson, H. C., et al. 2004, *ApJ*, 604, L9
- Reichborn-Kjennerud, B., Aboobaker, A. M., et al. 2010, in *Proceedings of SPIE*, Vol. 7741, Society of Photo-Optical Instrumentation Engineers (SPIE) Conference Series
- Reid, M. A. & Wilson, C. D. 2006, *ApJ*, 650, 970
- Renbarger, T., Chuss, D. T., et al. 2004, *PASP*, 116, 415
- Rex, M. 2007, PhD thesis, University of Pennsylvania
- Rex, M., Chapin, E., Devlin, M. J., Gundersen, J., Klein, J., Pascale, E., & Wiebe, D. 2006, in *Proceedings of SPIE*, Vol. 6269, Society of Photo-Optical Instrumentation Engineers (SPIE) Conference Series
- Rieke, G. H., Young, E. T., et al. 2004, *ApJS*, 154, 25
- Rodighiero, G., Cimatti, A., et al. 2010, *A&A*, 518, L25+
- Rowan-Robinson, M. 1986, *MNRAS*, 219, 737
- . 2001, *ApJ*, 549, 745
- Rowan-Robinson, M., Babbedge, T., et al. 2008, *MNRAS*, 386, 697
- Rowan-Robinson, M., Broadhurst, T., et al. 1991, *Nature*, 351, 719
- Rowan-Robinson, M., Mann, R. G., et al. 1997, *MNRAS*, 289, 490
- Rownd, B., Bock, J. J., Chattopadhyay, G., Glenn, J., & Griffin, M. J. 2003, in *Proceedings of SPIE*, Vol. 4855, Society of Photo-Optical Instrumentation Engineers (SPIE) Conference Series, 510–519
- Salpeter, E. E. 1955, *ApJ*, 121, 161

- Santini, P., Fontana, A., et al. 2009, *A&A*, 504, 751
- Savage, B. D. & Mathis, J. S. 1979, *ARA&A*, 17, 73
- Savini, G., Ade, P. A. R., House, J., Pisano, G., Haynes, V., & Bastien, P. 2009, *Appl. Opt.*, 48, 2006
- Savini, G., Pisano, G., & Ade, P. A. R. 2006, *Appl. Opt.*, 45, 8907
- Schlegel, D. J., Finkbeiner, D. P., & Davis, M. 1998, *ApJ*, 500, 525
- Schleuning, D. A. 1998, *ApJ*, 493, 811
- Schneider, G. 2004, *Advances in Space Research*, 34, 543
- Schulz, B., Pearson, C. P., et al. 2010, *A&A*, 518, L32+
- Scott, S. E., Fox, M. J., et al. 2002, *MNRAS*, 331, 817
- Serjeant, S., Dye, S., et al. 2008, *MNRAS*, 386, 1907
- Sersic, J. L. 1968, *Atlas de galaxias australes (Observatorio Astronómico)*
- Shao, L., Lutz, D., et al. 2010, *A&A*, 518, L26+
- Sharp, R., Saunders, W., et al. 2006, in *Proceedings of SPIE, Vol. 6269, Society of Photo-Optical Instrumentation Engineers (SPIE) Conference Series*
- Shu, F. H., Adams, F. C., & Lizano, S. 1987, *ARA&A*, 25, 23
- Silverman, J. D., Lamareille, F., et al. 2009, *ApJ*, 696, 396
- Siringo, G., Kreysa, E., et al. 2009, *A&A*, 497, 945
- Smail, I., Ivison, R. J., & Blain, A. W. 1997, *ApJ*, 490, L5+
- Somerville, R. S. & Primack, J. R. 1999, *MNRAS*, 310, 1087

- Stern, D., Eisenhardt, P., et al. 2005, *ApJ*, 631, 163
- Stetson, P. B. 1987, *PASP*, 99, 191
- Stokes, G. G. 1852, *Annalen der Physik*, 163, 480
- Surace, J. A. & SWIRE Team. 2005, in *Bulletin of the American Astronomical Society*, Vol. 37, BAAS, 1246–+
- Swinbank, A. M., Lacey, C. G., et al. 2008, *MNRAS*, 391, 420
- Swinyard, B. & Nakagawa, T. 2009, *Experimental Astronomy*, 23, 193
- Tacconi, L. J., Genzel, R., et al. 2010, *Nature*, 463, 781
- . 2008, *ApJ*, 680, 246
- Tacconi, L. J., Neri, R., et al. 2006, *ApJ*, 640, 228
- Takeuchi, T., Yamamoto, H., et al. 2010a, *PASJ*, 62, 557
- Takeuchi, T. T., Buat, V., Heinis, S., Giovannoli, E., Yuan, F., Iglesias-Páramo, J., Murata, K. L., & Burgarella, D. 2010b, *A&A*, 514, A4+
- Tassis, K. & Mouschovias, T. C. 2004, *ApJ*, 616, 283
- Taylor, E. N., Franx, M., et al. 2009, *ApJS*, 183, 295
- Title, A. M. & Rosenberg, W. J. 1981, in *Proceedings of SPIE*, Vol. 307, Society of Photo-Optical Instrumentation Engineers (SPIE) Conference Series, ed. G. Trapani, 120
- Truch, M. D. P. 2007, PhD thesis, Brown University
- Truch, M. D. P., Ade, P. A. R., et al. 2009, *ApJ*, 707, 1723
- Trujillo, I., Cenarro, A. J., de Lorenzo-Cáceres, A., Vazdekis, A., de la Rosa, I. G., & Cava, A. 2009, *ApJ*, 692, L118

- Trujillo, I., Conselice, C. J., Bundy, K., Cooper, M. C., Eisenhardt, P., & Ellis, R. S. 2007, *MNRAS*, 382, 109
- Trujillo, I., Ferreras, I., & de La Rosa, I. G. 2011, *MNRAS*, 415, 3903
- Trujillo, I., Feulner, G., et al. 2006, *MNRAS*, 373, L36
- Tucker, C. & Ade, P. 2007, in *IR/mm Waves and 15th International Conference on THz Electronics, IRMMW-THz*, 973 –975
- Vaillancourt, J. E. 2002, *ApJS*, 142, 53
- . 2009, *ArXiv* 0904.1979
- Vaillancourt, J. E., Dowell, C. D., et al. 2008, *ApJ*, 679, L25
- van Dokkum, P. G., Whitaker, K. E., et al. 2010, *ApJ*, 709, 1018
- Vázquez-Semadeni, E., Ryu, D., Passot, T., González, R. F., & Gazol, A. 2006, *ApJ*, 643, 245
- Viero, M. P., Ade, P. A. R., et al. 2009, *ApJ*, 707, 1766
- Viero, M. P., Moncelsi, L., et al. 2011, *ArXiv* 1008.4359
- Vlahakis, C., Dunne, L., & Eales, S. 2005, *MNRAS*, 364, 1253
- Vollmann, K. & Eversberg, T. 2006, *Astronomische Nachrichten*, 327, 862
- Wang, W., Cowie, L. L., & Barger, A. J. 2006, *ApJ*, 647, 74
- Ward-Thompson, D., Kirk, J. M., et al. 2010, *A&A*, 518, L92+
- Ward-Thompson, D., Kirk, J. M., Crutcher, R. M., Greaves, J. S., Holland, W. S., & André, P. 2000, *ApJ*, 537, L135
- Ward-Thompson, D., Sen, A. K., Kirk, J. M., & Nutter, D. 2009, *MNRAS*, 398, 394

- Weiß, A., Kovács, A., et al. 2009, *ApJ*, 707, 1201
- Werner, M. W., Roellig, T. L., et al. 2004, *ApJS*, 154, 1
- White, S. D. M. & Frenk, C. S. 1991, *ApJ*, 379, 52
- Whittet, D. C. B., Gerakines, P. A., Hough, J. H., & Shenoy, S. S. 2001, *ApJ*, 547, 872
- Whittet, D. C. B., Hough, J. H., Lazarian, A., & Hoang, T. 2008, *ApJ*, 674, 304
- Wiebe, D. V. 2008, PhD thesis, University of Toronto, Canada
- Wiebe, D. V., Ade, P. A. R., et al. 2009, *ApJ*, 707, 1809
- Wolf, C., Hildebrandt, H., Taylor, E. N., & Meisenheimer, K. 2008, *A&A*, 492, 933
- Wolf, C., Meisenheimer, K., et al. 2004, *A&A*, 421, 913
- Wootten, A. & Thompson, A. R. 2009, *IEEE Proceedings*, 97, 1463
- Wu, J. H. P., Zuntz, J., et al. 2007, *ApJ*, 665, 55
- Wuyts, S., Labbé, I., Schreiber, N. M. F., Franx, M., Rudnick, G., Brammer, G. B., & van Dokkum, P. G. 2008, *ApJ*, 682, 985
- Wyder, T. K., Martin, D. C., et al. 2007, *ApJS*, 173, 293
- Yan, H., Dickinson, M., et al. 2004, *ApJ*, 616, 63
- Zeeman, P. 1897, *ApJ*, 5, 332
- Zhang, J., Ade, P. A. R., Mauskopf, P., Moncelsi, L., Savini, G., & Whitehouse, N. 2009, *Appl. Opt.*, 48, 6635
- Zhang, J., Ade, P. A. R., Mauskopf, P., Savini, G., Moncelsi, L., & Whitehouse, N. 2011, *Appl. Opt.*, 50, 3750